PHOTOPRODUCTION OF CHARGED PION PAIRS AND $N^*(1238)^{++}$ IN HYDROGEN FROM 0.9 TO 1.3 GeV

Thesis by
Michael George Hauser

In Partial Fulfillment of the Requirements

For the Degree of
Doctor of Philosophy

California Institute of Technology
Pasadena, California
1967
(Submitted January 23, 1967)

ACKNOWLEDGMENTS

The experiment described here was originally suggested by my advisor, Professor Robert L. Walker. His continuing interest, helpful suggestions, and active participation in the early stages of data collection were deeply appreciated.

Dr. H. A. Thiessen was a collaborator in all phases of this investigation. The periods of synchrotron time used for my experiment alternated with the periods used for his study of π^+ photoproduction, and we shared the many tasks of data collection, particularly those related to use of the 600 MeV/c spectrometer. This experiment benefited from his ingenuity and hard work in innumerable ways. I am also grateful to the other members of the "spectrometer group", Dr. S. D. Ecklund and Mr. F. B. Wolverton, for numerous informative discussions.

I wish to thank Professor Jon Mathews for many helpful discussions and calculations relating to interpretation of the data.

During the long days and nights of running this experiment, I had the able assistance of Mr. R. H. Ault, Mr. J. E. Downum, Mr. C. D. Maxwell, and Miss J. Bruce. Their dedication to the job, often above and beyond the call of duty, was greatly appreciated.

I am deeply grateful to the crew of the synchrotron, headed by Mr. L. Loucks, and the beam tuners, headed by Mr. A. Neubeiser, for their efforts in maintaining and getting the best possible performance from an aging machine. Mr. E. Emory maintained the hydrogen target, and designed and maintained the helium bags.

I am indebted to the National Science Foundation, Atomic Energy Commission, and California Institute of Technology for financial support.

Finally, I want to acknowledge the immense support provided by my wife and parents, whose love and understanding have sustained and inspired me through this first quarter century of my informal and formal education.

ABSTRACT

The momentum spectrum and angular distribution of negative pions produced in the reaction $\gamma + p \rightarrow \pi^- + \pi^+ + p$ have been measured at eight incident photon energies from 0.9 to 1.3 GeV. The reaction was produced in a liquid hydrogen target illuminated by a bremsstrahlung beam from the Caltech synchrotron. Negative pions were detected and momentum analyzed with a magnetic spectrometer employing a combination of scintillation counters and Cherenkov counters. The incident photon energy was fixed by using the technique of bremsstrahlung subtraction. The cross section for the pseudo-two-body reaction $\gamma + p \rightarrow \pi^- + N^*(1238)^{++}$ was obtained by fitting the π^- momentum spectrum at each angle and energy with a linear combination of a resonance term and a three-body phase space term. The angular distribution of the π^- in N^* production is in good qualitative and fair quantitative agreement with predictions of the Drell (OPE) model. Gauge invariant models are in poorer agreement with the data. The total cross section for pion pair production decreases smoothly from $78.9 \pm 2.9\,\mu b$ at .93 GeV to $59.1 \pm 5.2\,\mu b$ at 1.29 GeV, whereas the N^* part of the cross section decreases from $45.0 \pm 2.4\,\mu b$ to $18.2 \pm 3.5\,\mu b$ over the same range. A slight shoulder in each of these cross sections suggests formation of the $N^*(1688)$ as an intermediate state.

TABLE OF CONTENTS

LIST OF FIGURES

LIST OF TABLES

To Mim, Karen, et al.

I. INTRODUCTION

The photoproduction of two charged pions from hydrogen,

$$\gamma + p \rightarrow \pi^- + \pi^+ + p \ ,$$

was first observed in 1954,[1] almost as soon as photon beams energetic enough to produce the reaction were available. Although numerous experimental investigations of this process have since been made,[2-20] only in the past two or three years have sufficiently detailed data been obtained to permit serious attempts at interpretation in terms of specific dynamical models. This paper describes an experiment in which angular and momentum distributions of negative pions produced by the above reaction were measured over an energy range from 0.9 to 1.3 GeV for the incident photon. These measurements can be used to test the predictions of some models which have been proposed for the reaction, and provide a basis for further theoretical investigations.

In order to put the motivation for this work in perspective, we shall review briefly the results of some previous studies. Discussion of the most recent results from other laboratories, however, will be postponed until our data have been presented. One of the distinctive features of pion pair production which was noticed in the early work was the important role played by final state interactions. Friedman and Crowe[4] observed that at 60° in the laboratory the yield of 76 MeV positive pions from pair production was about three times larger than that of negative pions of the same energy. The spectrum of negative pions was peaked at low kinetic

energy, and the excitation function at fixed pion momentum and angle had a slow initial rise from threshold. These features were in agreement with calculations made by Cutkosky and Zachariasen[21] using a cutoff static theory, and suggested the presence of a strong P wave interaction between the positive pion and the nucleon. Bloch and Sands[7] measured the π^- spectrum for c. m. angles greater than 90° at photon energies of .67, .83, and 1.01 GeV. Their results showed reasonable agreement with the Cutkosky-Zachariasen calculations at .67 GeV. Lacking a theory applicable to the higher energies, and noting that three-body phase space did not adequately describe their results, they calculated the π^- spectrum on the assumption that the reaction proceeded through one of the following quasi-two-body processes:

$$\gamma + p \rightarrow N^*(1238)^{++} + \pi^-$$

$$\gamma + p \rightarrow N^*(1238)^{0} + \pi^+ \ .$$

The neutral isobar model was in better agreement with their data than the doubly charged isobar model, but they were not able to draw any strong conclusions in favor of the isobar model. Sellen et al.[9, 10] studied pion pair production in a diffusion cloud chamber, where for the first time all particles in the final state were observed. Examination of the mass distributions of the various pairs of particles in the final state showed that the reaction occurred predominantly through production of the $N^*(1238)^{++}$ for photon energies from 0.5 to 0.7 GeV; the same isobar was present to a lesser degree from 0.7 to 0.9 GeV. There was virtually no

evidence for production of the N^* in its neutral charge state. Evidence for strong pion-pion interactions in the final state was first reported by McLeod, Richert, and Silverman,[12] who observed an enhancement in the reaction probability when the $\pi-\pi$ mass was about 720 MeV/c^2, near the ρ^o meson mass. DelFabbro et al.[13,14] interpreted an enhancement at a dipion mass of 380 MeV/c^2 in terms of a σ^o meson.

A second striking characteristic of pion pair production was the dependence of the total cross section on photon energy. Sellen et al. found that the cross section increased quite slowly from threshold (321 MeV) up to about 450 MeV, but then rose quite sharply to a peak of 80 μb between 500 and 600 MeV. At higher energies (up to 1000 MeV) the cross section decreased slowly and smoothly. This group described the reaction as a multistep process

$$\gamma + p \rightarrow C \rightarrow N + \pi + \pi$$

or

$$\gamma + p \rightarrow C \rightarrow \begin{array}{l} N^* + \pi \\ \quad \lfloor\!\rightarrow N + \pi \end{array}$$

where C denoted an intermediate system which might include several states of different isotopic spin and angular momentum. They considered Wilson's suggestion that C might be predominantly the $N^*(1512)$ state.[22] The observed predominance of the $N^*(1238)^{++}$ over the $N^*(1238)^o$ would be explained by this model, since a branching ratio of 9:1 is expected for these two modes if an isotopic

spin 1/2 state were dominant. However, one would expect the total cross section to peak around a photon energy of 750 MeV, and the cross section seemed quite flat in this region. They concluded that more than one intermediate state must be making a strong contribution.

A specific model for the reaction mechanism was proposed by Drell in an investigation of the production of beams of high energy particles.[23] The Drell model, or one pion exchange (OPE) model, is based upon the amplitude given by the Feynman diagram shown in Figure 1. This model predicts that the angular distribution of the π^- will be peaked strongly forward, but that the cross section must be zero at 0^o. To the extent that the exchanged pion is not too far off the mass shell, the lower vertex in Figure 1 is approximately described by the π^+-p scattering amplitude for real pions, which is dominated by the $N^*(1238)$ state at low excitation energies. The interesting features predicted by this model prompted Kilner, Diebold, and Walker to study π^- production from hydrogen at small angles at an incident photon energy of 1.23 GeV.[11] They found that the cross section exhibited the qualitative features of the Drell model, but the measured cross sections were a factor of 2-3 larger than the prediction.

The above summary shows that pion pair photoproduction is a complex process, rich in information concerning the basic pion-nucleon and pion-pion interactions, yet hopefully not so complex that this information cannot be extracted. The cross section calculated by Drell from the one pion exchange diagram was expected to give reasonable results only in the limit of high photon energy and for negative pions produced at small angles to the photon beam. The striking qualitative agreement between Drell's predictions and the

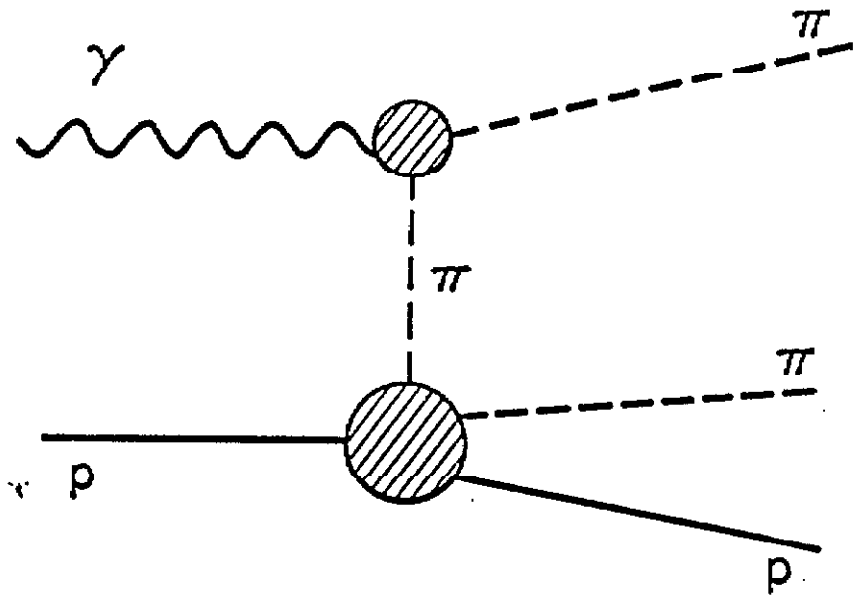

Figure 1. Diagram for the one pion exchange model

data of Kilner et al. suggested that it would be very interesting to extend the measurements over a greater energy and angular range. In particular, one would expect the Drell model to be more successful in describing events of the type $\gamma + p \rightarrow \pi^- + N^*(1238)^{++}$ than in describing all charged pion pair photoproduction. The investigation reported here was planned to study primarily this quasi-two-body process in order to make possible a detailed comparison with the Drell model and its refinements. A similar investigation was being completed by Allaby, Lynch, and Ritson[18] at Stanford at the time this work was beginning; because they covered the photon energy range from 575 to 950 MeV, our attention was confined to the range from 900 to 1300 MeV. In this energy range we could also look for evidence of the effect of excitation of the third pion-nucleon resonance, $N^*(1688)$, on pion pair production.

Because both the method and the apparatus used in this work have been used in previous studies, most experimental details are given in the Appendices. Section II summarizes the experimental method and procedures. The reduction of data is discussed in Section III, where the data are also presented. The results of this and other recent experiments are discussed in Section IV, and Section V contains conclusions.

II. EXPERIMENTAL METHOD

A. Reaction Identification

The photoproduction of a negative pion from a proton has the general form

$$\gamma + p \rightarrow \pi^- + X \ . \qquad (1)$$

The system represented by X must have charge +2 and hypercharge +1. Since there is no single particle with these quantum numbers which is stable with respect to strong interactions, there is no final state for the above reaction consisting of only two particles of sharply defined mass. There are only two reactions of the above form having three particles in the final state. These reactions, together with those having four-and five-body final states which can be produced by photons with energy less than 1.35 GeV, are tabulated below:

Reaction	k_t (GeV)	M_{min} (GeV/c^2)	
$\gamma + p \rightarrow \pi^- + \pi^+ + p$	.32	1.08	(2a)
$\rightarrow \pi^- + K^+ + \Sigma^+$	1.31	1.68	(2b)
$\rightarrow \pi^- + \pi^+ + \pi^o + p$	.51	1.21	(2c)
$\rightarrow \pi^- + \pi^+ + \pi^+ + n$	.52	1.22	(2d)
$\rightarrow \pi^- + \pi^+ + \pi^o + \pi^o + p$	.71	1.35	(2e)
$\rightarrow \pi^- + \pi^+ + \pi^+ + \pi^o + n$	.72	1.35	(2f)
$\rightarrow \pi^- + \pi^- + \pi^+ + \pi^+ + p$	.73	1.36	(2g)

k_t is the laboratory photon energy at threshold, and M_{min} is the minimum possible invariant mass of the final state particles comprising the X. In the present investigation, the photon laboratory energy varied from 0.93 to 1.29 GeV, and the π^- momentum was chosen to cover the "missing mass" (invariant mass of the X) range from 1.08 to about 1.30 GeV/c^2. This missing mass constraint excluded reactions (2b) and (2e) - (2g) as possible sources of the pions detected. Reactions (2c) and (2d) were expected to make only a small contribution because the photon energies involved never exceeded their threshold by very much. This expectation was supported by bubble chamber measurements of the total cross sections for these reactions, as discussed in Section III.D. Thus, the negative pions observed in this experiment were essentially all produced in the process of interest, reaction (2a).

For reactions of the above type, measurement of only the photon energy (k), the π^- momentum (p), and the π^- direction with respect to the photon beam (θ,φ) leaves unspecified at least two of the kinematic variables needed to describe the final state completely. However, the following properties of the system are determined: (a) the total energy (W) in the center of mass (c.m.) system; (b) the momentum (p') and angle (θ') of the π^- in the c.m. system; and (c) the invariant mass (M) of the X. Thus, measurement of these variables does not completely determine the state of the constituents of the X, but it does permit study of the angular distribution of the π^-, the mass distribution of the X, and the total cross section as functions of the total center of mass energy. Such an approach is particularly well suited to investigation of the contribution of the quasi-two-body channel

$$\gamma + p \rightarrow \pi^- + N^*(1238)^{++} \qquad (3)$$

to pion pair photoproduction.

B. Procedure

The method used to measure π^- yields in the present experiment was the same as that used by Kilner, Diebold, and Walker.[11] Negative pions photoproduced in a liquid hydrogen target by a bremsstrahlung beam from the synchrotron were identified and their momentum and direction were measured with a magnetic spectrometer. Because this information alone does not suffice to determine the photon energy, data were taken in such a way that a bremsstrahlung subtraction could be performed. Subtraction of the π^- yields obtained at a fixed angle and momentum but slightly different synchrotron energies gave a net yield of pions produced by photons whose energy was known to lie in a relatively narrow band. The increment in synchrotron energy used in this experiment, chosen as a compromise between the desire to minimize random errors and the desire to obtain the best possible resolution in total c.m. energy and missing mass, was 50 MeV. The rms width of the net bremsstrahlung spectrum was of the order of 30 MeV, implying about 1-1/2% resolution in total c.m. energy, and 2-1/2% resolution in missing mass. The uncertainty in photon energy was the dominant source of uncertainty in the missing mass.

The basic laboratory cross section measured as outlined above is differential in both pion momentum and angle. At fixed photon energy and pion angle, this cross section is essentially a spectrum of the missing mass. This can be visualized by considering

the kinematics for the reaction as shown in Figure 2, where contours of constant missing mass are plotted in the k-p plane for a fixed π^- angle. For each angle at which the cross section was measured, a set of standard momentum values, separated by slightly more than the acceptance of the spectrometer, was selected. The yield of negative pions was measured at synchrotron energies ranging from 922 to 1330 MeV in steps of 50 MeV, and at a subset of these standard momentum values such that after the bremsstrahlung subtraction the missing mass varied from threshold to about 1.30 GeV/c^2. The bremsstrahlung subtraction was performed on the yields at each pair of adjacent synchrotron energies, giving π^- momentum spectra at eight values of average photon energy from 934 to 1289 MeV. The regions blocked out in Figure 2 show the points selected in a typical case. The cross section was measured in this manner at laboratory angles of 4°, 12°, 20°, 44°, 56°, and 84°. Additional measurements were made at 30° for average photon energies of 934 and 985 MeV, and at 120° for energies of 1086 to 1289 MeV in steps of 50 MeV. A complete list of the kinematic conditions for which data were obtained is included in Table I (see Section III. A).

The apparatus used in the experiment was the same as that employed recently by Thiessen[24] and Ecklund[25] to study photoproduction of single positive pions from hydrogen. Figure 3 shows a laboratory floor plan. After initial collimation and sweeping, the south bremsstrahlung beam from the synchrotron traversed nearly seventeen feet of air and the hydrogen target for another experiment before reaching our hydrogen target. Scraping walls were inserted at several places along the beam line to remove charged particles diverging from the beam. The sweeping magnet just upstream of our hydrogen target and the helium bag in the beam line from this magnet

Figure 2

Typical Kinematics Curves

The curves show the relationship between photon energy, π^- lab momentum, and missing mass (M) for a π^- lab angle of 20^o. The blocked out regions indicate the range covered in a single bremsstrahlung subtraction and setting of the spectrometer central momentum. All kinematic settings used at 20^o are shown.

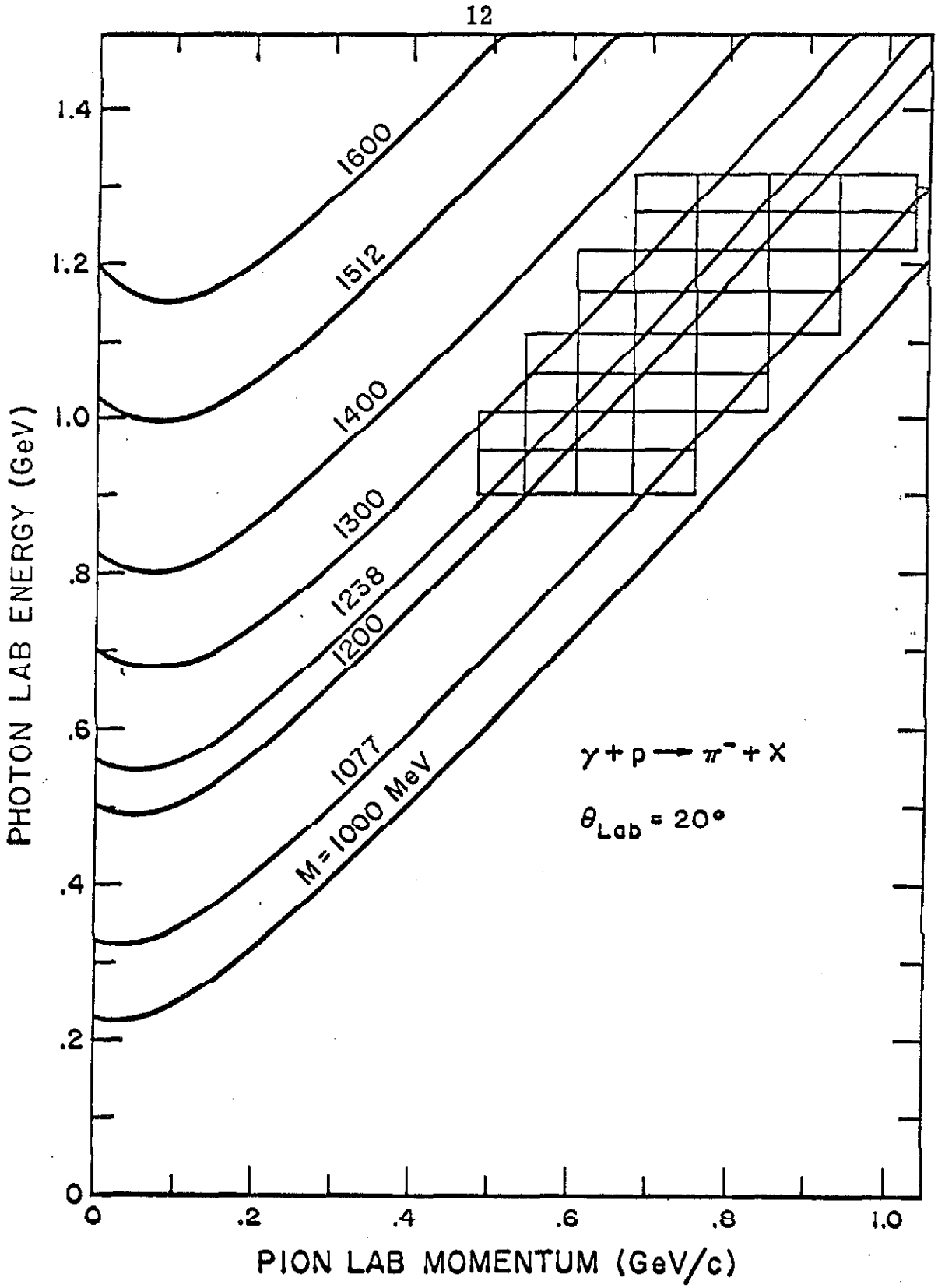
1600
1512
1400
1300
1238
1200
1077
M=1000 MeV
γ + p → π⁻ + X
θ_Lab = 20°
PHOTON LAB ENERGY (GeV)
PION LAB MOMENTUM (GeV/c)
0
.2
.4
.6
.8
1.0
1.2
1.4

Figure 2

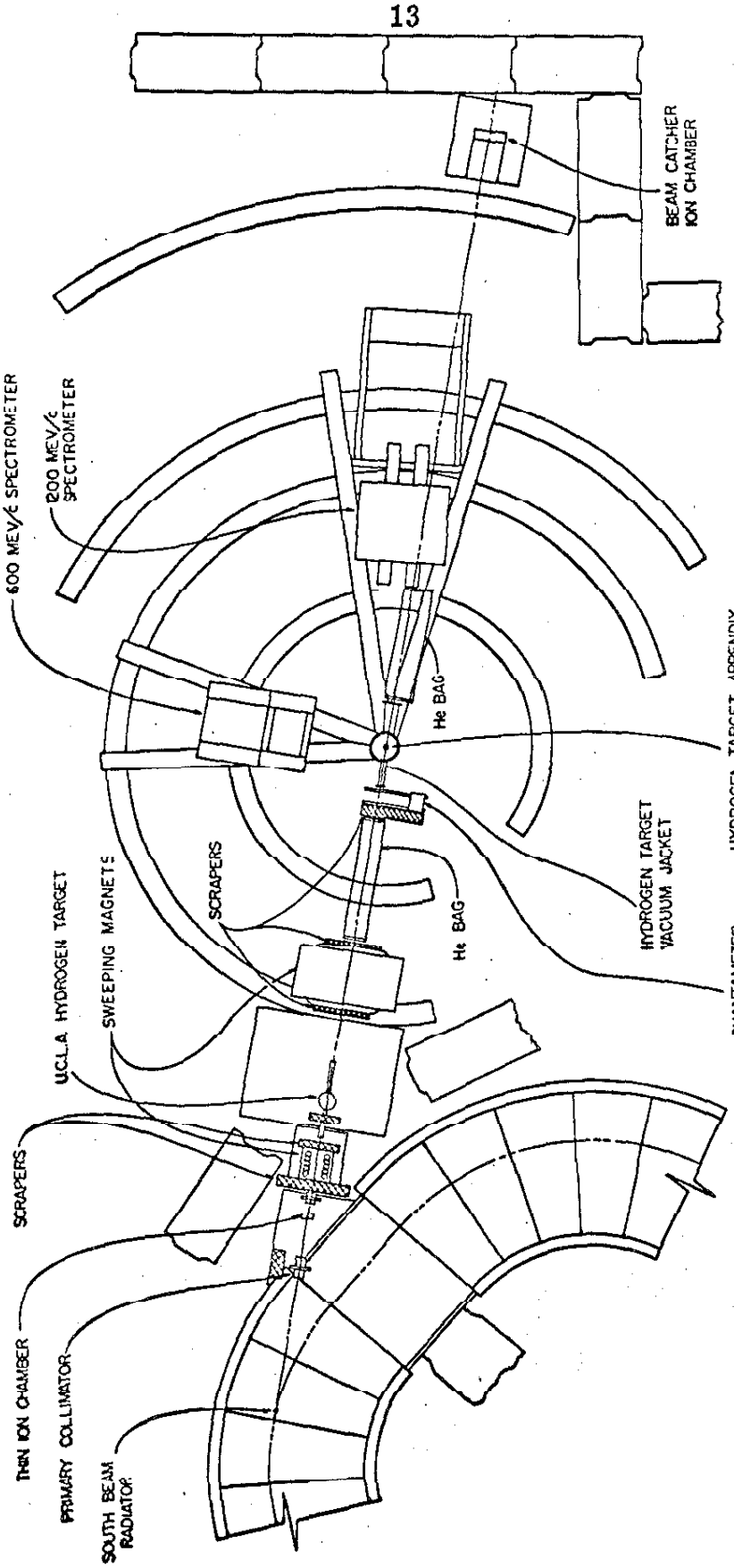

Figure 3. Floor plan of apparatus

to the hydrogen target were not present during the 1965 phase of the experiment: they were added in 1966, primarily to reduce the electron flux at small angles. The helium bag from the hydrogen target to the 1200 MeV/c spectrometer was used only while taking data at 4^{o} and 12^{o} during 1966.

Two magnetic spectrometers viewed the hydrogen target; they were used independently to measure the π^- yields at two angles simultaneously. The 1200 MeV/c spectrometer was used to measure yields from 4^{o} to 44^{o} in the laboratory, covering a momentum range of 450 to 1200 MeV/c. The counter system on this magnet included a freon threshold Cherenkov counter which provided virtually 100% discrimination against the large electron flux encountered at small angles. The 600 MeV/c spectrometer was used to measure the yield from 30^{o} to 120^{o} in the laboratory, covering a momentum range of 250 to 600 MeV/c. A counter sensitive only to electrons was not included in this spectrometer. The error produced in the cross sections measured with this spectrometer by e^- contamination was estimated to be less than 5% in the worst cases (see Section VI. D. 1). The counter systems and fast electronics used with each spectrometer were described fully by Ecklund and Thiessen; a summary of the properties of each system needed to analyze the data is given in Section VI. B. 3. It should be noted that the resolution functions of the spectrometers were known accurately, enabling us to make an absolute cross section measurement.

The total energy of the bremsstrahlung beam in each run was monitored simultaneously by as many as four independent secondary monitors. These monitors included: (1) a "thin" (.005 in. Al) ionization chamber located just downstream from the primary

collimator; (2) a counter telescope consisting of two scintillation counters mounted beneath the hydrogen target looking at particles produced at 90° to the beam; (3) a probe in the synchrotron monitoring the number of electrons accelerated in each machine cycle; and (4) a copper plate ionization chamber located in the beam catcher. The absolute calibration of these beam monitors as a function of synchrotron energy and time was determined by comparison with a Wilson quantameter[26] before and after every run.

Because the entire detection system used in this experiment consisted of counters, analysis of the data was relatively simple and rapid. In fact, the number of pions accumulated during a run was displayed on a scaler so the experimenter could see immediately the nature of the results. However, conversion of these numbers into cross sections, with all corrections included, required a considerable amount of data manipulation. For this reason, the raw data were punched onto cards, and all data handling was done with the aid of an IBM 7094 computer.

A more detailed description of the apparatus and procedures discussed above is given in Sections VI. B and C.

III. DATA REDUCTION AND RESULTS

A. Yield

The first steps in the evaluation of cross sections from the yields measured in this experiment followed closely the procedure used by Bloch and Sands.[7] The negative pion counting rate is related to the laboratory cross section by

$$C(E_o, p_o, \theta_o) = \eta\, \rho_H\, D\, \Delta\Omega \Delta p \int_{k_m}^{E_o} dk N(k, E_o) \frac{d^2\sigma}{dp d\Omega}(k, p_o, \theta_o) \tag{4}$$

where $C(E_o, p_o, \theta_o)$ = number of π^- counted per unit energy of the photon beam,

E_o = energy of the synchrotron,

p_o = central momentum of the momentum resolution function,

θ_o = central angle of the spectrometer,

η = efficiency factor which includes electronic effects (such as dead time, accidental coincidences, and accidental vetoes) and absorption of pions by matter in the system,

ρ_H = number of protons per unit volume of the target,

D = diameter of the target (note: a correction for the cylindrical geometry of the hydrogen target was included in the calculation of the effective bremsstrahlung spectrum, as discussed in Section VI. B. 1),

$\Delta\Omega$ = total angular aperture of the spectrometer,

Δp = total momentum acceptance of the spectrometer,

k_m = minimum photon energy required to produce a π^- of momentum p_o at angle θ_o,

$N(k, E_o)dk$ = number of photons with energy in the interval k to k + dk per unit energy of the beam,

$\frac{d^2\sigma}{dpd\Omega}(k, p_o, \theta_o)$ = laboratory cross section for π^- production per unit momentum and unit solid angle by a photon of energy k.

In writing equation (4), we have already performed integrations over the momentum and angular resolution functions, so that $d^2\sigma/dpd\Omega$ is actually the cross section averaged over these functions. We define the yield per equivalent quantum as follows:

$$\sigma^*(E_o, p_o, \theta_o) = E_o \int_{k_m}^{E_o} dk\, N(k, E_o)\, \frac{d^2\sigma}{dpd\Omega}(k, p_o, \theta_o)\,. \qquad (5)$$

This quantity, which has the dimensions of a cross section per unit momentum and unit solid angle, was determined directly from the

counting rates and instrumental parameters:

$$\sigma^*(E_o, p_o, \theta_o) = \frac{E_o C(E_o, p_o, \theta_o)}{\eta \rho_H D \Delta\Omega \Delta p} \quad . \tag{6}$$

A number of corrections were included in the factors appearing in equation (6): (1) The spectrometer acceptance was corrected for pion decay and the indistinguishability of pions and muons. These effects, evaluated by Monte Carlo calculations, typically altered the acceptance by about 10%. (2) Nuclear scattering of pions in matter along their flight path caused a loss of events. The correction for this loss, based upon transmission measurements and known pion scattering cross sections, varied from 5% to 10% for the 600 MeV/c spectrometer and from 10% to 13% for the 1200 MeV/c spectrometer. (3) Accidental coincidences, dead time losses, and other electronic inefficiencies were quite negligible.

The yields thus obtained were corrected for pions produced in sources other than the liquid hydrogen by subtracting yields measured with liquid hydrogen removed from the target. The empty target yield varied from 100% of the full target yield for points near threshold to as low as about 10% at most angles. For the 4° measurements, the empty target yield was never less than 30% of the full target yield because the spectrometer could detect pions produced in the windows of the hydrogen target vacuum jacket. A detailed discussion of all corrections is given in Section VI. D.

The yields per equivalent quantum measured in this experiment, averaged over all momentum channels at a given central momentum setting, are shown in Table I. The errors given include the statistical counting errors and additional random errors of 1.4%

TABLE I

Summary of π^- Yields at all Kinematic Points

P0 is the central momentum of the spectrometer (MeV/c)

E0 is the synchrotron energy (MeV)

LAB ANG is the π^- angle, θ_o (degrees).

The table entries are the yield per equivalent quantum, $\sigma^*(E_o, p_o, \theta_o)$, averaged over all momentum channels of the spectrometer, in units of 10^{-34} cm^2/sr-MeV/c. The errors include counting errors and random errors of 1.4% from beam monitoring and synchrotron energy fluctuations.

				EO					
PO	922	974	1025	1076	1127	1179	1230	1281	1332
LAB ANG = 4.0		BATCH 1							
542	136.5+- 8.4	188.0+- 9.7	215.8+- 9.5	229.6+-12.5					
612	42.2+- 5.9	98.5+- 6.9	145.8+- 7.8	178.1+-10.0	193.4+-10.9				
687	13.6+- 3.8	31.7+- 3.9	86.8+- 4.7	123.3+- 6.0	171.1+- 9.3	194.8+- 9.0	206.3+-11.5	210.7+-12.9	
772		13.8+- 2.6	15.7+- 3.7	48.6+- 4.8	108.5+- 6.0	169.7+- 8.4	200.0+- 9.4	215.7+-11.4	244.8+- 7.1
867				10.7+- 2.7	25.4+- 2.8	62.4+- 5.3	127.7+- 6.5	171.8+- 6.8	235.4+- 7.1
972						16.6+- 2.3	27.4+- 2.7	68.7+- 4.3	141.6+- 4.7
1072								11.4+- 3.3	33.8+- 2.1
LAB ANG = 4.0		BATCH 2							
542	132.6+- 5.1	185.0+- 6.2	199.8+- 6.3						
612	48.2+- 3.3	100.5+- 3.8	148.8+- 4.6	188.8+- 9.0	198.8+- 9.1				
687	6.6+- 2.3	32.3+- 2.8	73.3+- 3.6	127.7+- 7.9	163.2+- 6.8	189.2+- 9.0	207.5+- 9.4	191.3+-10.2	
772	-1.1+- 2.4	5.5+- 1.9	14.2+- 2.3	42.5+- 4.6	97.9+- 5.4	146.9+- 7.0	185.8+- 8.1	189.7+- 8.7	
LAB ANG = 4.0		BATCH 3							
867				3.8+- 2.1	86.5+- 4.3	145.6+- 5.1	176.7+- 6.2	212.4+- 8.1	
972					7.0+- 2.5	32.9+- 2.9	73.3+- 5.1	127.9+- 6.0	
1072							8.3+- 1.8	28.8+- 2.9	
B ANG = 12.0		BATCH 1							
62	232.0+- 6.9	257.1+- 7.3	291.6+- 8.4						
527	159.4+- 5.4	237.7+- 7.8	252.3+- 6.3	267.2+- 8.5					
597	52.0+- 4.5	138.6+- 4.9	185.5+- 6.2	241.0+- 5.4	240.9+- 6.9	277.9+- 7.5			
672	10.2+- 2.4	29.7+- 2.5	92.6+- 3.8	154.5+- 5.2	211.1+- 5.7	232.5+- 6.6	250.3+- 6.7	279.7+- 6.9	
757		-0.3+- 2.8	7.7+- 3.2	39.5+- 2.8	105.0+- 4.5	159.0+- 4.9	204.0+- 5.5	225.2+- 6.2	242.6+- 6.5
852				0.5+- 2.3	13.2+- 2.3	51.0+- 3.0	94.6+- 3.8	149.3+- 4.6	182.9+- 5.1
957						1.5+- 1.3	11.7+- 1.2	30.5+- 2.3	69.8+- 2.5
LAB ANG = 12.0		BATCH 2							
462	231.5+- 8.3	276.9+- 9.3	279.3+- 7.6						
527	170.2+- 6.5	211.6+- 7.8	250.2+- 8.5						
597	56.1+- 4.0	124.6+- 5.0	186.0+- 5.7						
672	6.1+- 2.4	29.6+- 3.2	87.4+- 4.0						
757	3.8+- 2.1	-0.4+- 1.7	11.7+- 2.2						
LAB ANG = 20.0		BATCH 1							
512	136.5+- 5.3	191.3+- 6.3	234.8+- 7.2						
572	55.1+- 3.8	120.5+- 5.0	175.9+- 4.5	214.8+- 6.5					
642	4.6+- 2.2	26.2+- 2.6	76.9+- 3.0	137.0+- 4.0	181.5+- 6.0				
717		0.9+- 1.5	13.4+- 1.8	40.7+- 2.1	87.6+- 2.8	130.6+- 4.2	153.7+- 4.6	171.5+- 4.8	
802				2.5+- 1.3	16.8+- 1.6	37.2+- 2.5	68.7+- 3.0	103.8+- 2.7	116.8+- 4.0
897					1.3+- 1.2	2.2+- 1.2	8.1+- 1.5	25.7+- 1.5	48.0+- 2.4
982								3.5+- 1.2	10.8+- 1.3

Table I.1. Summary of π^- yields

				EO					
PO	922	974	1025	1076	1127	1179	1230	1281	1332
LAB ANG = 20.0		BATCH 2							
512	129.5+- 4.5	184.0+- 5.5	217.0+- 7.2						
572	51.9+- 3.0	118.9+- 4.4	166.6+- 5.5	206.5+- 5.4					
642	8.8+- 1.3	30.6+- 2.1	84.4+- 3.3	134.1+- 4.5	179.0+- 5.2	198.3+- 4.2	210.9+- 5.7		
717	1.8+- 0.9	2.7+- 1.1	11.8+- 1.4	49.1+- 2.4	90.1+- 3.2	131.5+- 4.0	154.7+- 4.5	177.5+- 3.7	184.5+- 4.1
802			1.0+- 0.7	5.6+- 0.8	17.5+- 1.4	42.3+- 2.1	75.2+- 2.8	102.1+- 3.4	118.3+- 3.1
897					0.6+- 0.7	3.9+- 0.9	10.6+- 1.0	28.8+- 1.4	53.5+- 1.6
982							1.4+- 0.6	5.0+- 0.9	12.3+- 0.9
LAB ANG = 20.0		BATCH 3							
512	134.6+- 4.4	194.1+- 5.4	220.6+- 6.0						
572	55.2+- 2.8	117.8+- 3.8	171.3+- 4.9						
642	8.2+- 1.4	35.6+- 2.1	78.8+- 3.3						
717	0.5+- 1.1	1.3+- 1.2	14.2+- 1.6						
LAB ANG = 30.0		BATCH 1							
416	156.2+- 3.0	178.4+- 3.4							
471	121.2+- 2.3	154.1+- 2.4	176.0+- 2.6						
536	42.5+- 1.3	86.8+- 1.8	129.5+- 1.9						
LAB ANG = 30.0		BATCH 2							
537	45.5+- 2.3	91.3+- 2.8	132.3+- 4.2						
602	6.2+- 1.2	25.5+- 1.5	54.2+- 2.1						
672	3.3+- 1.1	2.1+- 1.0	8.8+- 1.3						
LAB ANG = 44.0		BATCH 1							
416	84.7+- 2.4	108.7+- 2.7	122.9+- 3.4	135.6+- 3.7					
466	42.0+- 1.4	71.5+- 1.6	98.5+- 2.0	110.9+- 2.4	116.2+- 3.0				
521	11.8+- 1.2	25.3+- 1.3	48.2+- 1.3	71.6+- 1.8	86.2+- 1.7	96.0+- 2.1	103.4+- 2.9	111.1+- 3.2	
576		4.6+- 1.1	10.8+- 1.3	26.7+- 1.2	45.8+- 1.4	61.5+- 2.1	71.8+- 1.8	76.2+- 1.9	85.1+- 1.9
LAB ANG = 44.0		BATCH 2							
657					5.0+- 1.3	10.5+- 1.4	21.8+- 1.7	29.1+- 2.3	
737						0. +- 0.7	0.6+- 0.8	3.8+- 1.1	
LAB ANG = 44.0		BATCH 3							
416	77.8+- 2.2	97.5+- 2.5	118.6+- 2.5	131.9+- 4.9					
466	35.5+- 2.0	67.7+- 2.6	93.2+- 3.1	103.2+- 2.9					
521	9.8+- 1.1	24.1+- 1.4	45.4+- 1.9	68.4+- 2.3	83.6+- 1.9	90.4+- 1.5	98.6+- 1.5	107.3+- 1.7	111.2+- 3.4
576	0.2+- 1.0	6.4+- 0.7	13.2+- 1.0	25.8+- 1.0	44.6+- 1.7	59.1+- 1.9	68.9+- 1.7	75.9+- 1.7	79.8+- 1.2
LAB ANG = 44.0		BATCH 4							
577				23.1+- 1.9	43.1+- 2.4	51.5+- 2.7			
657				0.8+- 0.8	5.8+- 1.0	13.7+- 1.3	22.1+- 1.9	29.0+- 1.4	38.4+- 2.3
737						0.2+- 0.5	2.0+- 0.5	3.4+- 0.9	10.2+- 1.2

Table I. 2. Summary of π^- yields

PO	922	974	1025	1076	1127	1179	1230	1281	1332
				EO					
LAB ANG = 44.0		BATCH 5							
467		75.0+- 5.4	92.1+- 5.6						
522	8.6+- 1.8	24.5+- 2.2	44.8+- 2.8						
571	0.7+- 1.4	3.3+- 1.4	9.8+- 1.9						
LAB ANG = 56.0		BATCH 1							
351				99.2+- 3.0	103.3+- 3.1				
379				91.2+- 2.6	97.1+- 2.6				
421				71.2+- 2.3	78.8+- 2.4				
463				41.9+- 1.6	53.2+- 1.6	61.1+- 2.1	71.2+- 2.1		
511				16.9+- 1.8	28.7+- 2.0	38.0+- 1.8	48.8+- 1.9		
553									
567						15.4+- 1.2	21.8+- 1.3		
LAB ANG = 56.0		BATCH 2							
331	79.2+- 3.2	83.6+- 3.4	95.4+- 3.1						
371	56.2+- 1.7	78.1+- 3.1	86.1+- 2.3	97.0+- 3.2	98.5+- 2.8	103.8+- 3.6			
416	22.4+- 2.3	44.7+- 1.9	58.9+- 2.0	71.5+- 2.0	77.4+- 2.5	85.8+- 2.7			
466	5.2+- 1.4	13.1+- 1.3	27.7+- 1.5	39.4+- 1.8	52.4+- 1.9	60.6+- 2.2	65.1+- 1.7	70.0+- 2.1	73.6+- 2.4
526				11.3+- 1.4	19.0+- 1.1	28.6+- 1.5	39.2+- 1.1	41.9+- 2.0	45.0+- 2.1
576							16.5+- 1.4	21.1+- 1.4	23.4+- 1.0
LAB ANG = 56.0		BATCH 3							
331	75.0+- 1.9	85.3+- 1.9	92.1+- 2.1						
371	57.1+- 1.4	73.4+- 1.8	83.8+- 1.7	90.6+- 3.1	104.0+- 3.5				
416	26.3+- 1.0	46.1+- 1.3	60.6+- 1.2	71.3+- 2.8	73.9+- 2.4	83.5+- 2.8	83.8+- 2.9		
466	6.2+- 0.6	15.0+- 0.7	27.7+- 0.9	42.4+- 2.0	54.1+- 2.0	63.1+- 2.4	67.7+- 2.6	69.3+- 2.6	71.9+- 2.5
LAB ANG = 56.0		BATCH 4							
526				11.0+- 0.9	20.8+- 1.4	29.4+- 1.6	40.0+- 1.9	40.7+- 1.0	43.6+- 1.4
576					6.7+- 0.7	10.2+- 0.7	15.9+- 0.8	19.4+- 1.2	24.5+- 1.2
LAB ANG = 84.0		BATCH 1							
334						39.2+- 2.8	36.5+- 2.8		
371						22.4+- 2.0	26.3+- 2.1		
407						11.1+- 1.8	14.7+- 1.8		
431						5.6+- 1.8	7.6+- 1.9		
LAB ANG = 84.0		BATCH 2							
271	39.7+- 2.8	50.8+- 3.0	55.6+- 3.0						
301	20.0+- 2.0	29.2+- 2.1	40.6+- 2.2	42.7+- 2.2	48.0+- 3.0				
336	7.6+- 1.6	10.6+- 1.6	16.1+- 1.4	25.4+- 1.6	32.2+- 1.7	34.5+- 2.0	42.2+- 2.1	44.2+- 2.1	
376		4.7+- 1.4	7.7+- 1.4	10.3+- 1.3	14.4+- 1.2	20.2+- 1.3	24.6+- 1.4	26.9+- 1.3	27.0+- 1.4
421					5.4+- 1.3	7.9+- 1.2	9.6+- 1.2	12.7+- 1.2	15.9+- 1.3
471								3.7+- 1.2	5.3+- 1.2

Table I. 3. Summary of π^- yields

			E3					
PO	922	974	1025	1076	1127	1179	1230	1281	1332
LAB ANG = 84.0		BATCH 3							
271	38.4+- 1.7	47.7+- 2.2	53.6+- 2.0						
301	21.8+- 1.7	29.4+- 1.7	33.9+- 1.9						
336	6.8+- 1.0	12.1+- 1.0	20.2+- 1.0						
376	1.8+- 0.6	3.8+- 0.6	6.3+- 0.7						
LAB ANG = 84.0		BATCH 4							
271	40.0+- 2.4	48.5+- 2.9	51.6+- 2.7						
301	21.1+- 1.2	29.8+- 2.2	36.2+- 1.5						
336	9.2+- 1.0	12.2+- 2.1	20.6+- 1.3						
LAB ANG = 120.0		BATCH 1							
241				22.4+- 2.4	27.8+- 2.4	27.5+- 2.3	30.8+- 2.9	30.2+- 2.6	
271				8.3+- 1.5	9.5+- 1.6	12.9+- 1.4	16.1+- 2.0	16.4+- 1.9	20.7+- 2.2
301							6.0+- 1.9	8.1+- 1.9	9.1+- 1.5
336									2.7+- 1.3

Table I. 4. Summary of π^- yields

arising from the beam monitoring and fluctuations in synchrotron energy (see Section VI. E. 1). Several determinations of σ^* were made at almost all kinematic points, and these different "batches" of data were treated separately until after the bremsstrahlung subtraction was performed to minimize the effects of systematic shifts. A key to the data batch assignments is provided in Table II, where the time when each batch was obtained and the spectrometer which was used are specified. A typical pair of yield curves obtained at a fixed angle in one batch is plotted in Figure 4. These curves are for a point where the cross section was large and the bremsstrahlung subtraction was easily made. Note that as the π^- momentum decreased (missing mass increased), the bremsstrahlung subtraction became more difficult. This behavior set a practical limit to the largest missing mass which could be observed.

B. Laboratory Cross Section

Subtraction of the expressions for the yields at two synchrotron energies $E_2 > E_1$ gives the following integral equation for the cross section:

$$\sigma^*(E_2, p_o, \theta_o) - \sigma^*(E_1, p_o, \theta_o) = \int_{k_m}^{E_2} dk\, R(k, E_1, E_2) \frac{d^2\sigma}{dp d\Omega}(k, p_o, \theta_o) \quad (7)$$

where $R(k, E_1, E_2) = E_2 N(k, E_2) - E_1 N(k, E_1)$.

TABLE II

Data Batch Information

Angle	Batch	Time	Spectrometer	Aperture
4°	1	Sept. 1965	1200 MeV/c*	3 in. x 6 in.
	2	June-July 1966	1200 MeV/c*	2 3/4 in. x 6 in.
	3	Aug. 1966	1200 MeV/c	"
12°	1	Aug.-Sept. 1965	"	3 in. x 9 in.
	2	July 1966	"	2 3/4 in. x 9 in.
20°	1	Sept.-Oct. 1965	"	3 in. x 9 in.
	2	May-June 1966	"	2 3/4 in. x 12 in.
	3	Aug. 1966	"	"
30°	1	July-Aug. 1966	600 MeV/c	2 3/4 in. x 9 1/2 in.
	2	"	1200 MeV/c	2 3/4 in. x 12 in.
44°	1	Sept. 1965	600 MeV/c	2 3/4 in. x 9 1/2 in.
	2	"	1200 MeV/c	3 in. x 9 in.
	3	May-June 1966	600 MeV/c	2 3/4 in. x 9 1/2 in.
	4	June 1966	1200 MeV/c	2 3/4 in. x 12 in.
	5	Aug. 1966	"	"
56°	1	May 1965	600 MeV/c	2 3/4 in. x 9 1/2 in.
	2	Aug.-Sept. 1965	"	"
	3	June-July 1966	"	"
	4	Aug. 1966	"	"
84°	1	May 1965	"	"
	2	Sept.-Oct. 1965	"	"
	3	July 1966	"	"
	4	Aug. 1966	"	"
120°	1	June 1966	"	"

* The FAN counters were turned off during all or part of this time.

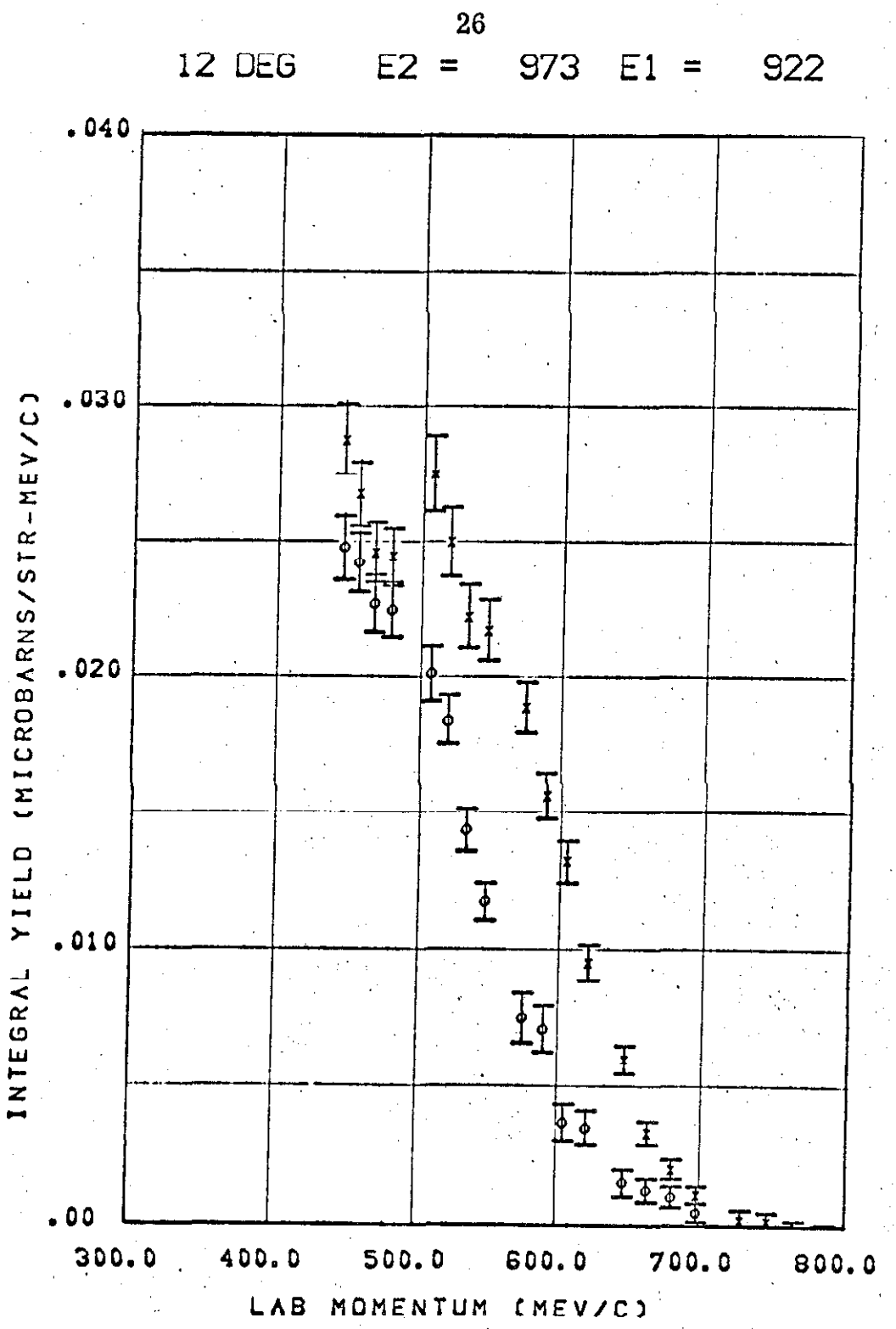

Figure 4. Typical π^- yield curves. All data were obtained at 12^o in batch 1. The lower set of points (o) are for synchrotron energy E1, the upper set (x) for E2.

The function $N(k, E_o)$ was written in the conventional form:

$$N(k, E_o) = \frac{1}{E_o} \frac{\bar{B}(k, E_o)}{k} \quad . \tag{8}$$

$\bar{B}(k, E_o)$ is essentially a constant for $k < E_o$, drops rapidly to zero as k increases to E_o, and is to a very good approximation a function only of k/E_o. The shape of $\bar{B}(k, E_o)$ for our radiator and collimator, including correction for the nonuniform thickness of our hydrogen target (see Section VI. B. 1), was obtained from a theory of thick radiator bremsstrahlung by Wolverton,[27] and is shown in Figure 5(a). The kernel of integral equation (7) which results when E_2 and E_1 differ by 50 MeV is shown in Figure 5(b). It is worth noting that the lower limit on the integral, k_m, was typically a few hundred MeV or less below E_2 under the conditions of this experiment, so that the long, low energy tail of $R(k, E_1, E_2)$ did not make an appreciable contribution to the integral.

Assuming that the cross section varies slowly with k over the region where $R(k, E_1, E_2)$ is large, we obtain the approximate solution of equation (7):

$$\frac{d^2\sigma}{dp d\Omega}(k_o, p_o, \theta_o) \cong \frac{\sigma^*(E_2, p_o, \theta_o) - \sigma^*(E_1, p_o, \theta_o)}{I(E_2, E_1, p_o, \theta_o)} \tag{9}$$

where $$I(E_2, E_1, p_o, \theta_o) = \int_{k_m(p_o, \theta_o)}^{E_2} dk\, R(k, E_1, E_2)$$

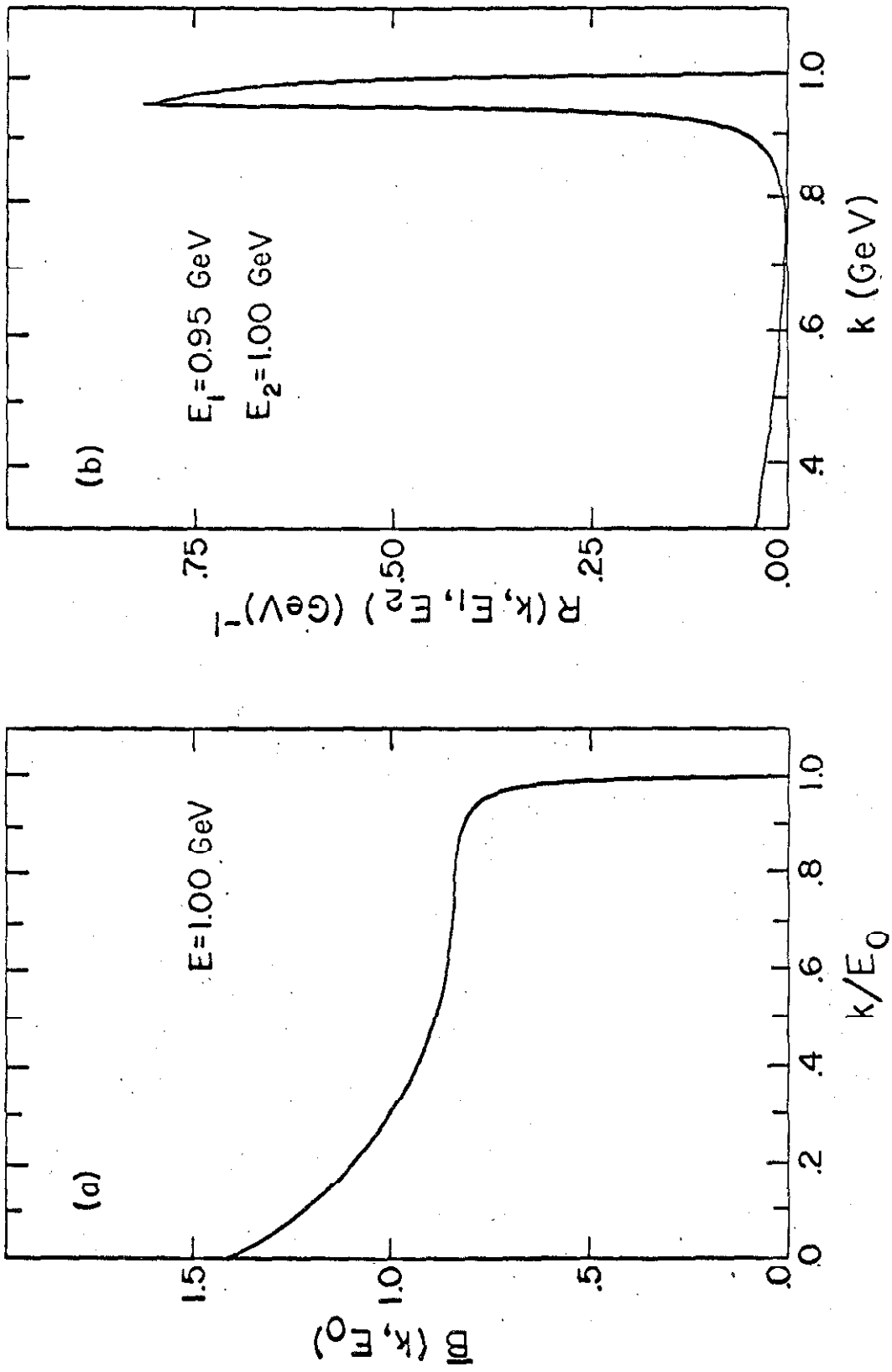

Figure 5. Bremsstrahlung beam spectrum functions: (a) $\bar{B}(k, E_0)$ including correction for the cylindrical geometry of the hydrogen target. (b) Beam spectrum after 50 MeV bremsstrahlung subtraction, normalized to equal numbers of equivalent quanta at each synchrotron energy.

$$k_o(E_2, E_1, p_o, \theta_o) = \frac{\int_{k_m(p_o,\theta_o)}^{E_2} dk\, k\, R(k, E_1, E_2)}{I(E_2, E_1, p_o, \theta_o)} \quad .$$

Note that equation (9) is the result of expanding the cross section in a power series about some central energy, k_o, and that with the choice of k_o made here, equation (9) is an exact solution if the cross section varies linearly with k in the region where $R(k, E_1, E_2)$ is large. For reasons which will be discussed below, no attempt was made to evaluate the error incurred as a result of using equation (9) to evaluate the laboratory cross section differential in angle and momentum.

The cross sections obtained using $E_2 - E_1 = 50$ MeV are plotted in Figure 6. The cross sections were first computed separately with the σ^* data from each batch. Weighted averages over batches were then formed at each kinematic point to give the results shown in Figure 6. The smooth curves in these plots are discussed in the next section. A complete list of the cross sections is also given in Table III. The data at 120^o are obviously of poorer quality than the rest; a limited set of measurements was made at this angle simply to be sure the cross section did not become large again at the most backward angle we could readily observe.

Figure 6

Laboratory Cross Sections

The measured cross sections, $\frac{d^2\sigma}{dpd\Omega}(k_o, p_o, \theta_o)$, are plotted as a function of π^- lab momentum, p_o. The π^- lab angle, θ_o, and average photon energy, k_o, are shown at the top of each plot. The upper smooth curve is the least squares fit of an N^{*++} resonance term and a 3-body phase space term to the data; the lower curve is the phase space term alone.

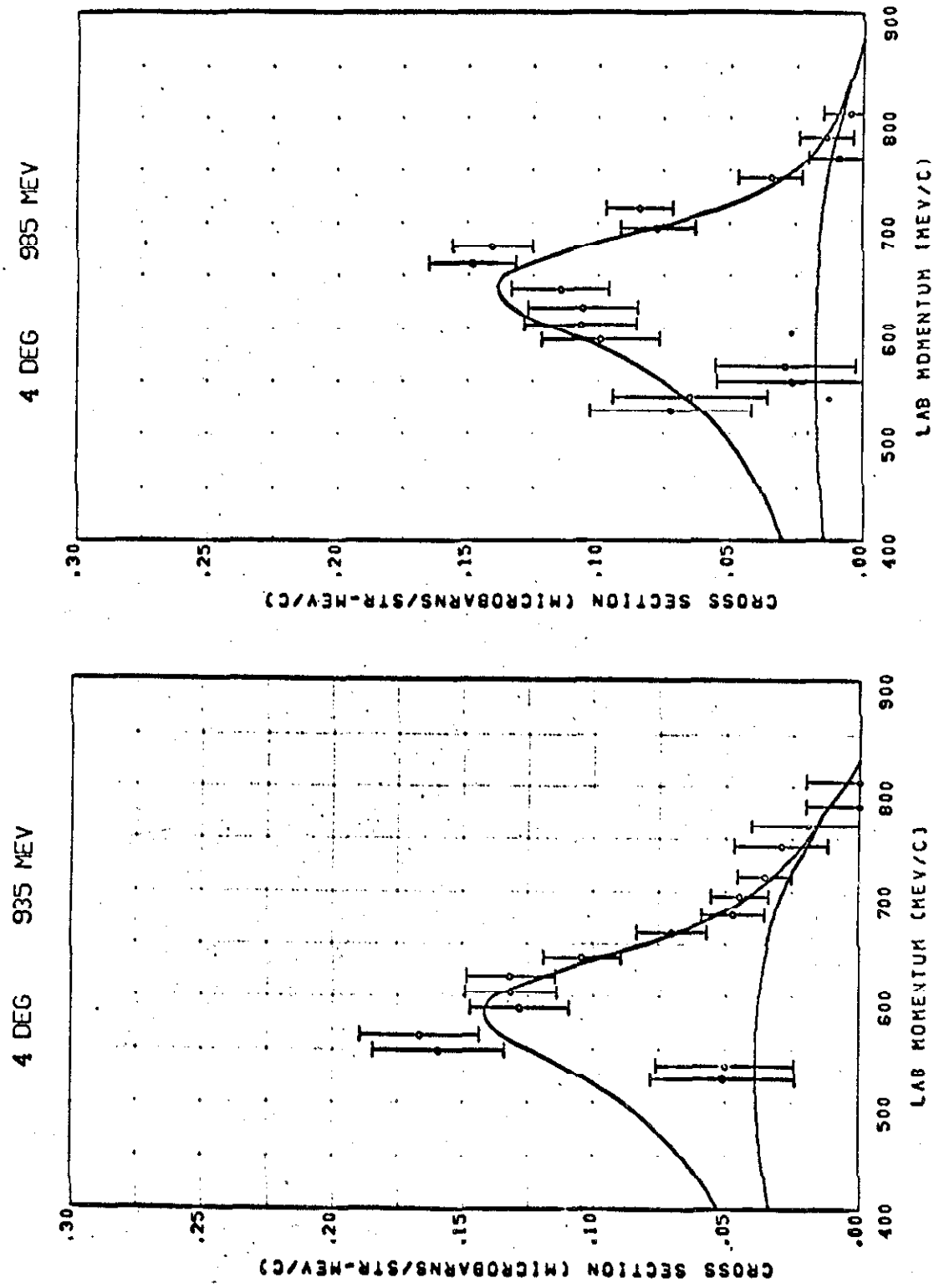

Figure 6.1. Laboratory cross section.

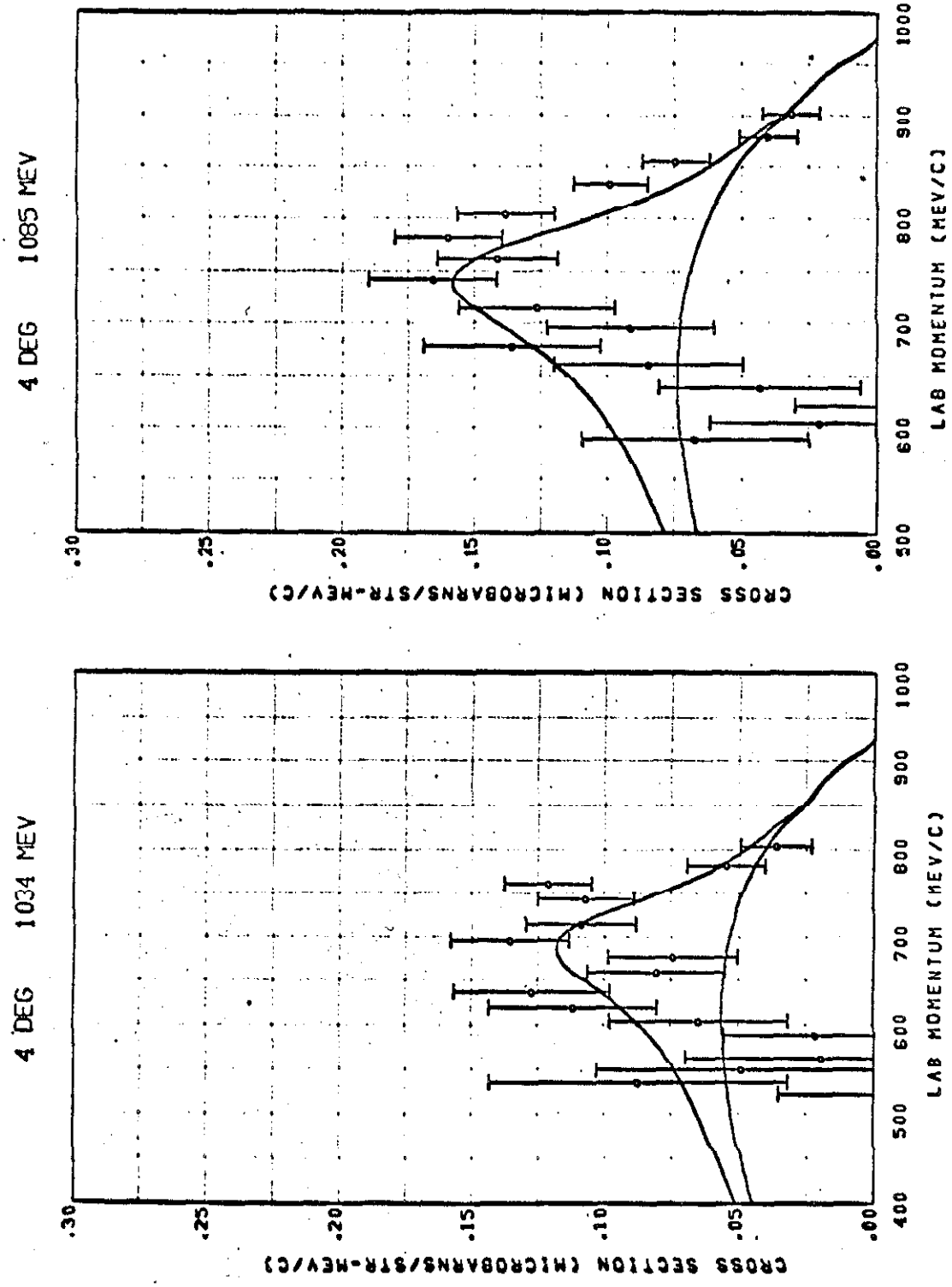

Figure 6.2. Laboratory cross section.

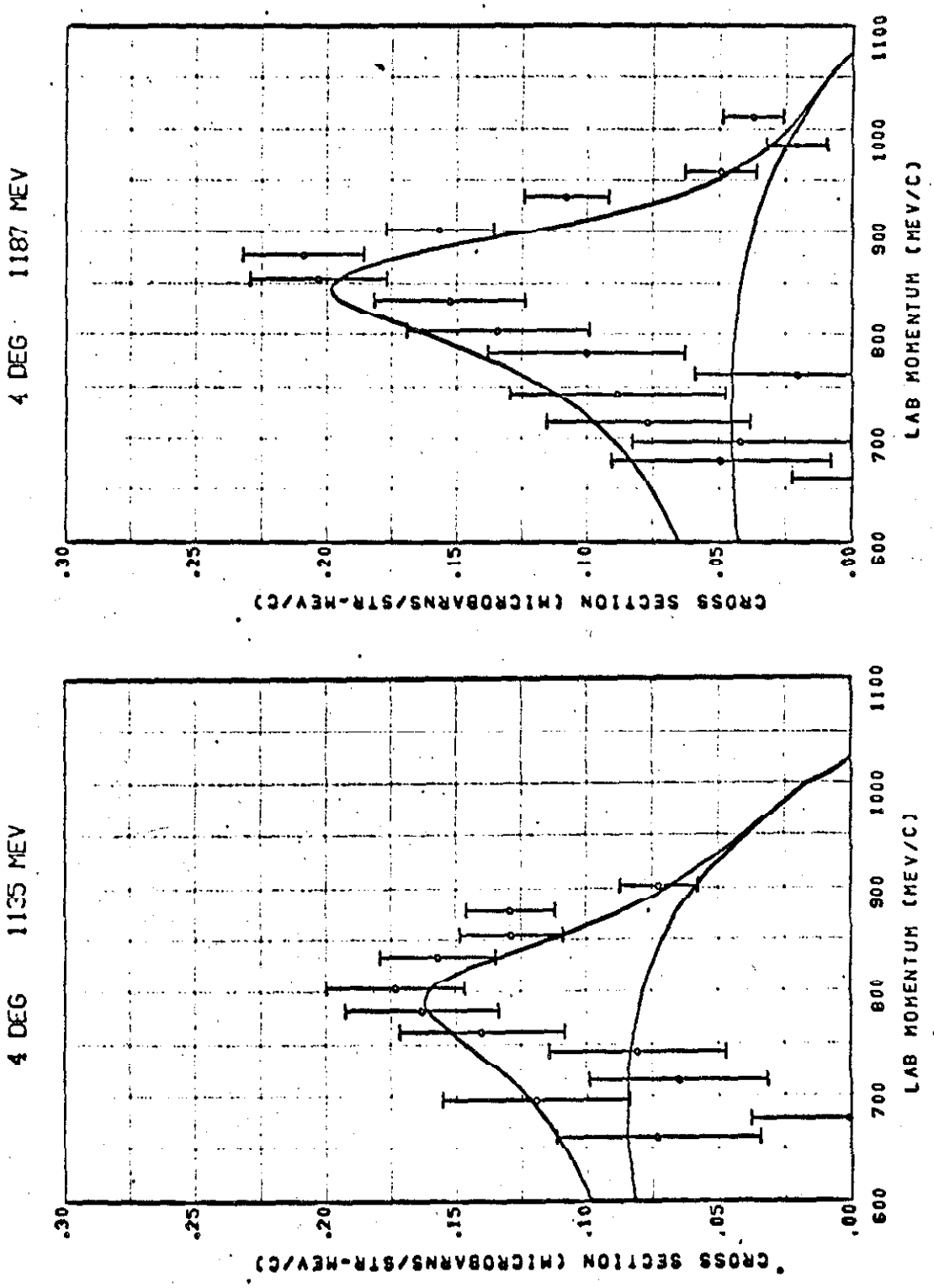

Figure 6.3. Laboratory cross section.

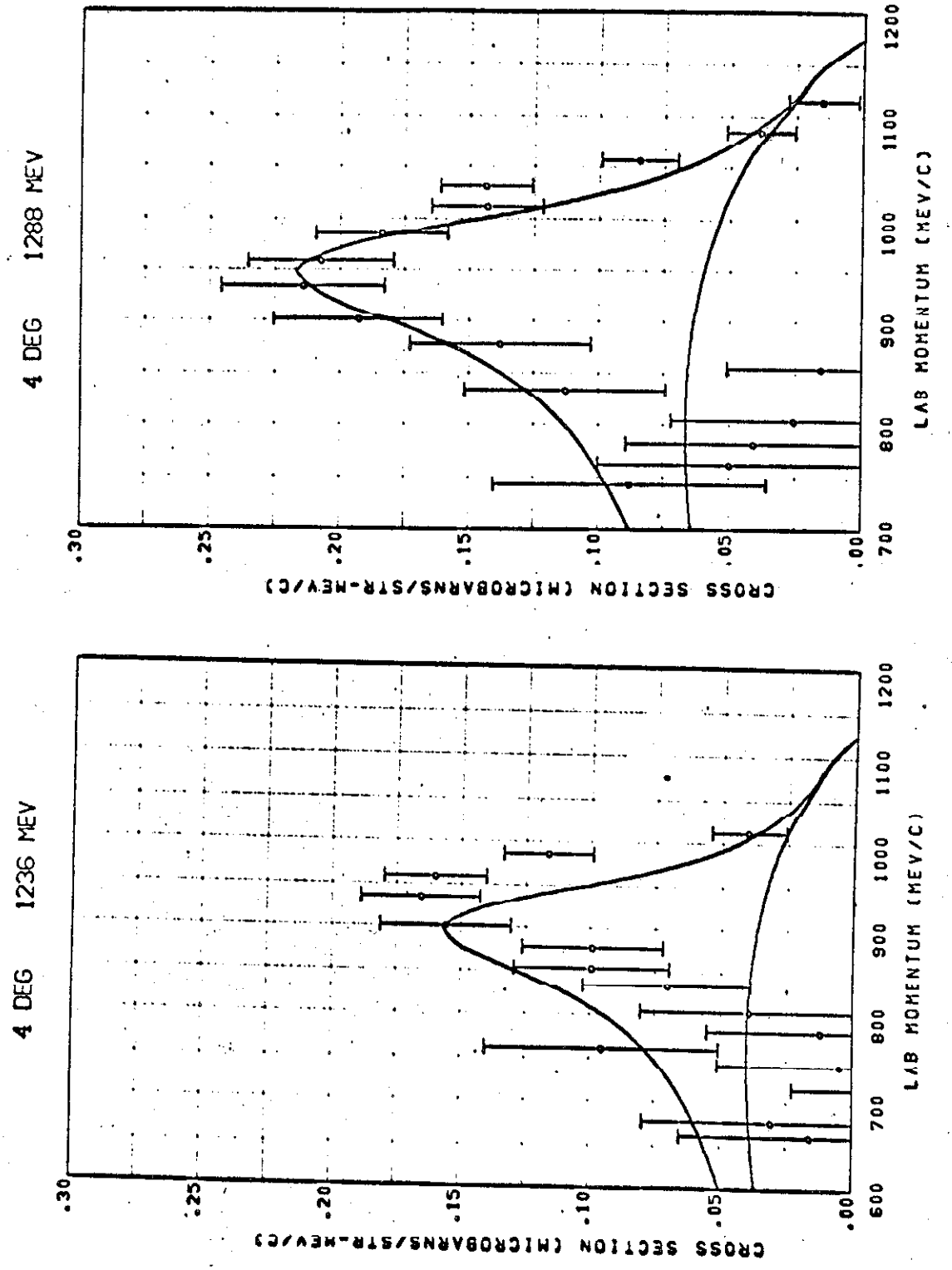

Figure 6.4. Laboratory cross section.

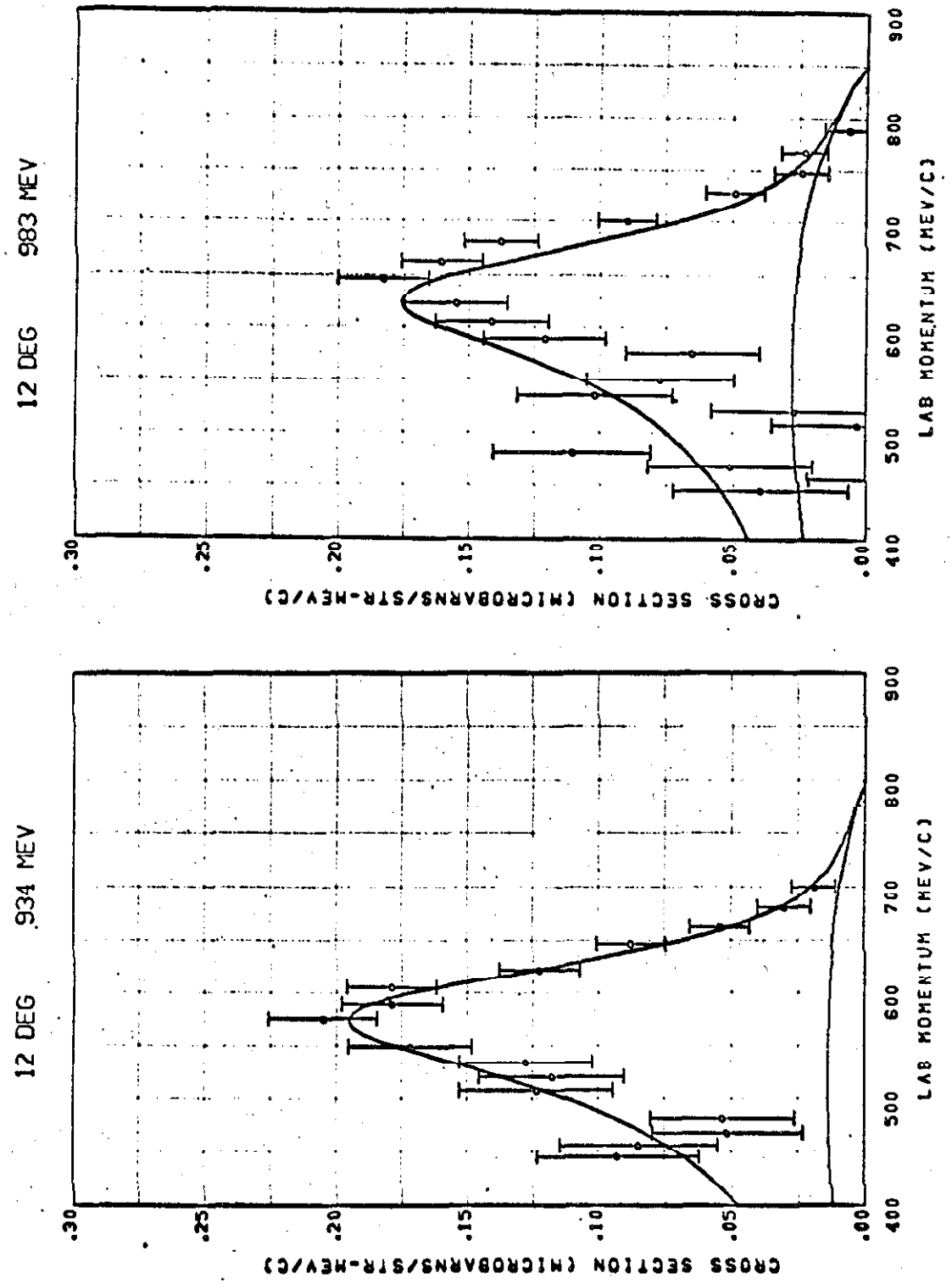

Figure 6.5. Laboratory cross section.

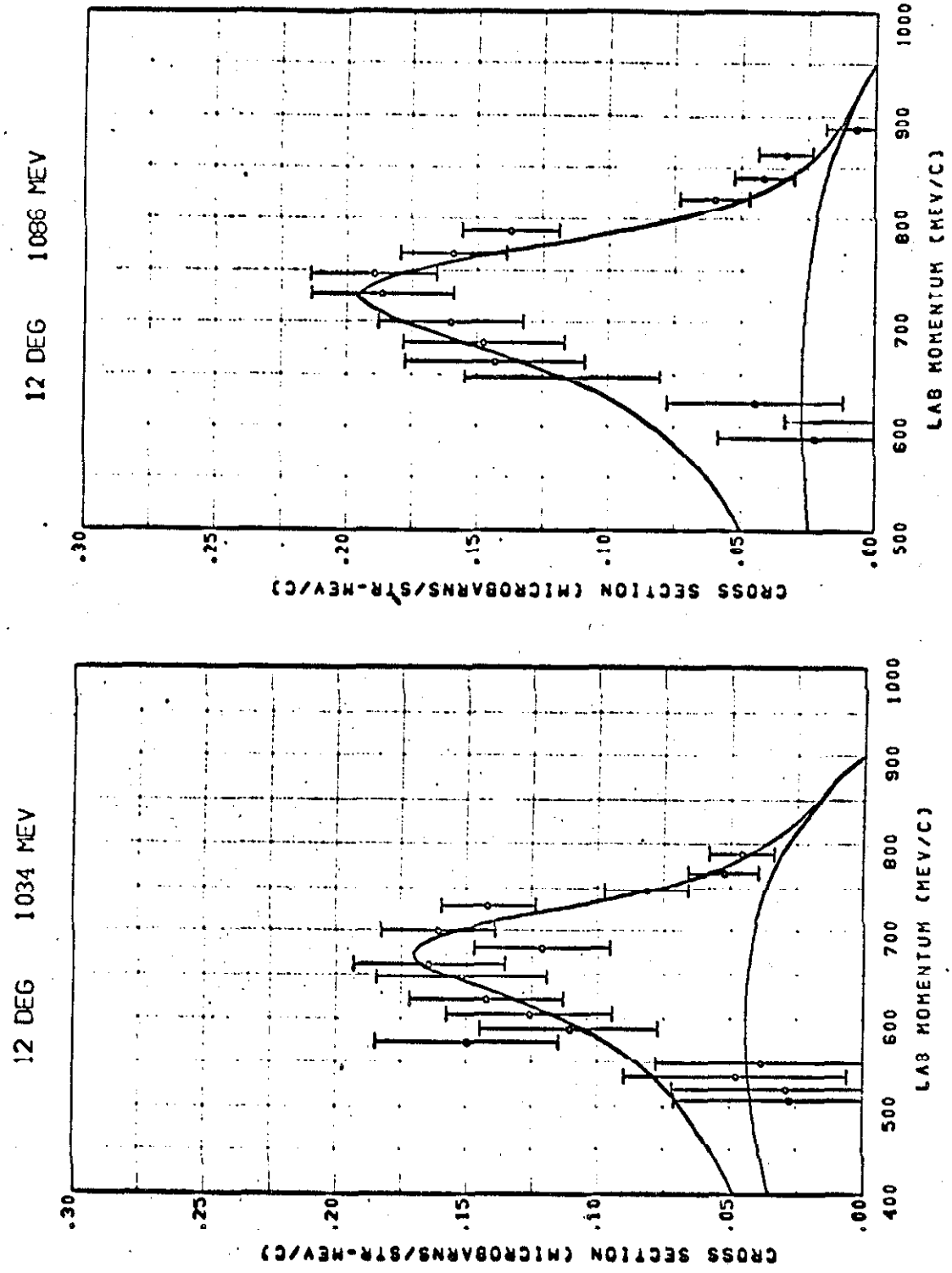

Figure 6.6. Laboratory cross section.

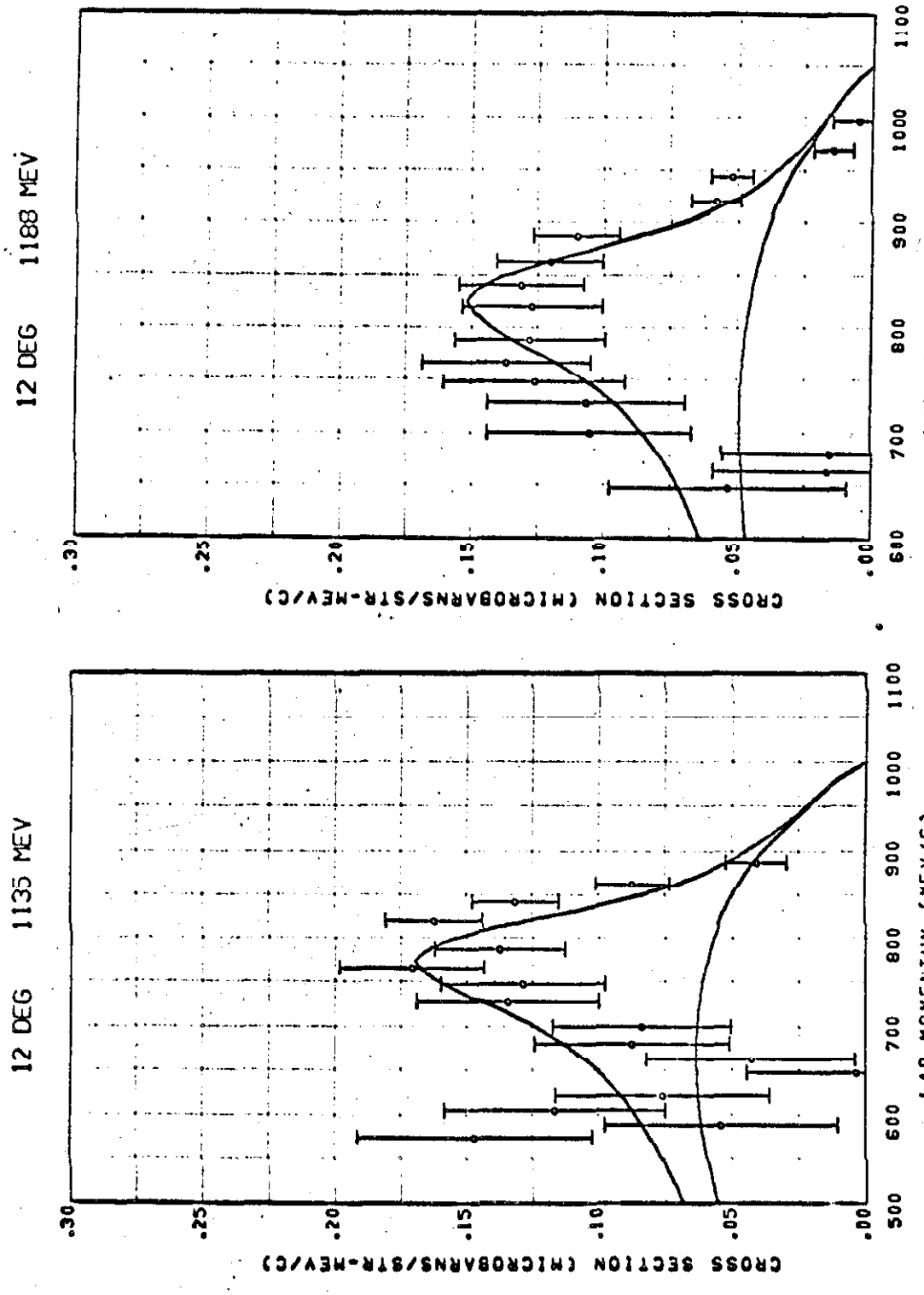

Figure 6.7. Laboratory cross section.

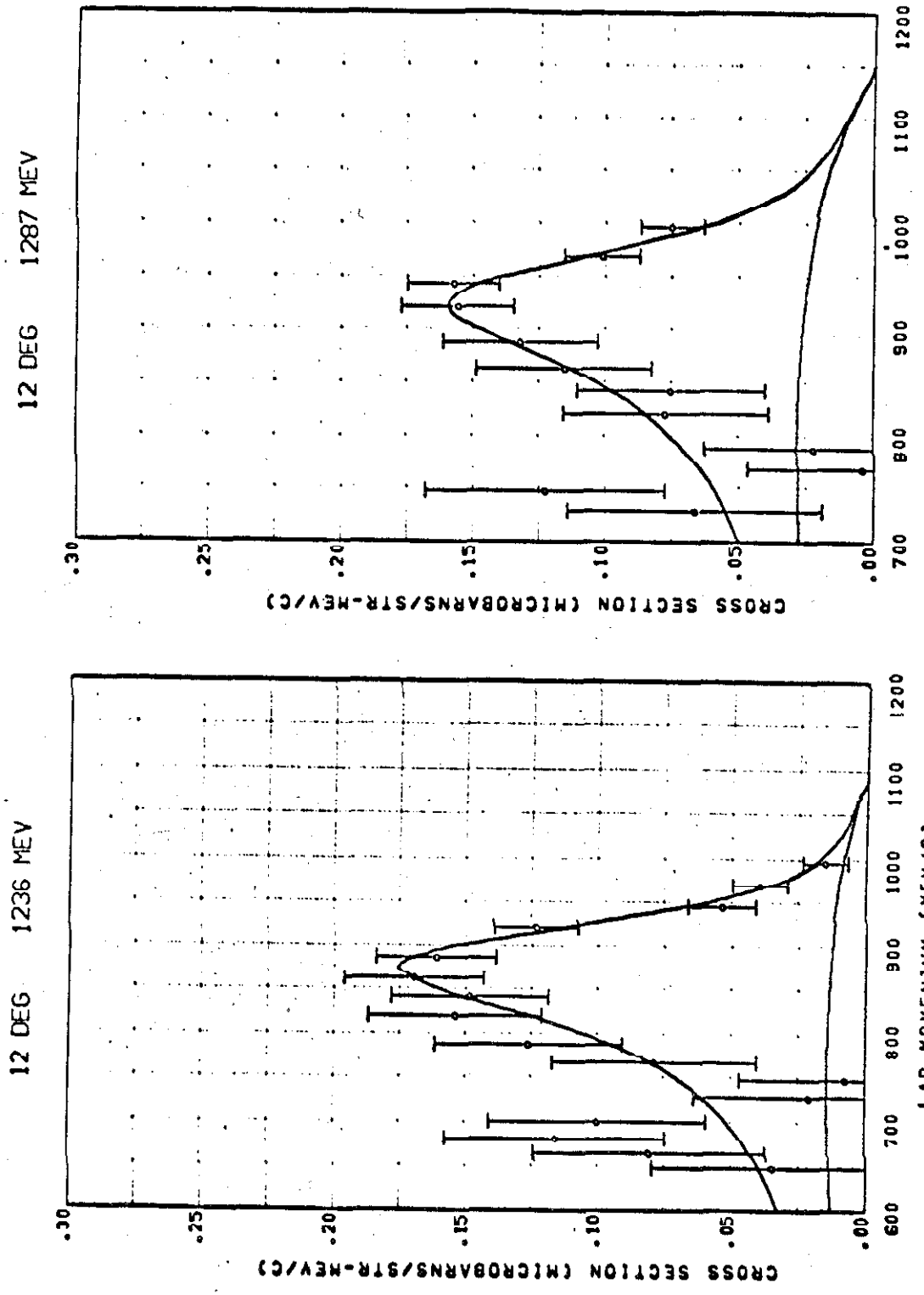

Figure 6.8. Laboratory cross section.

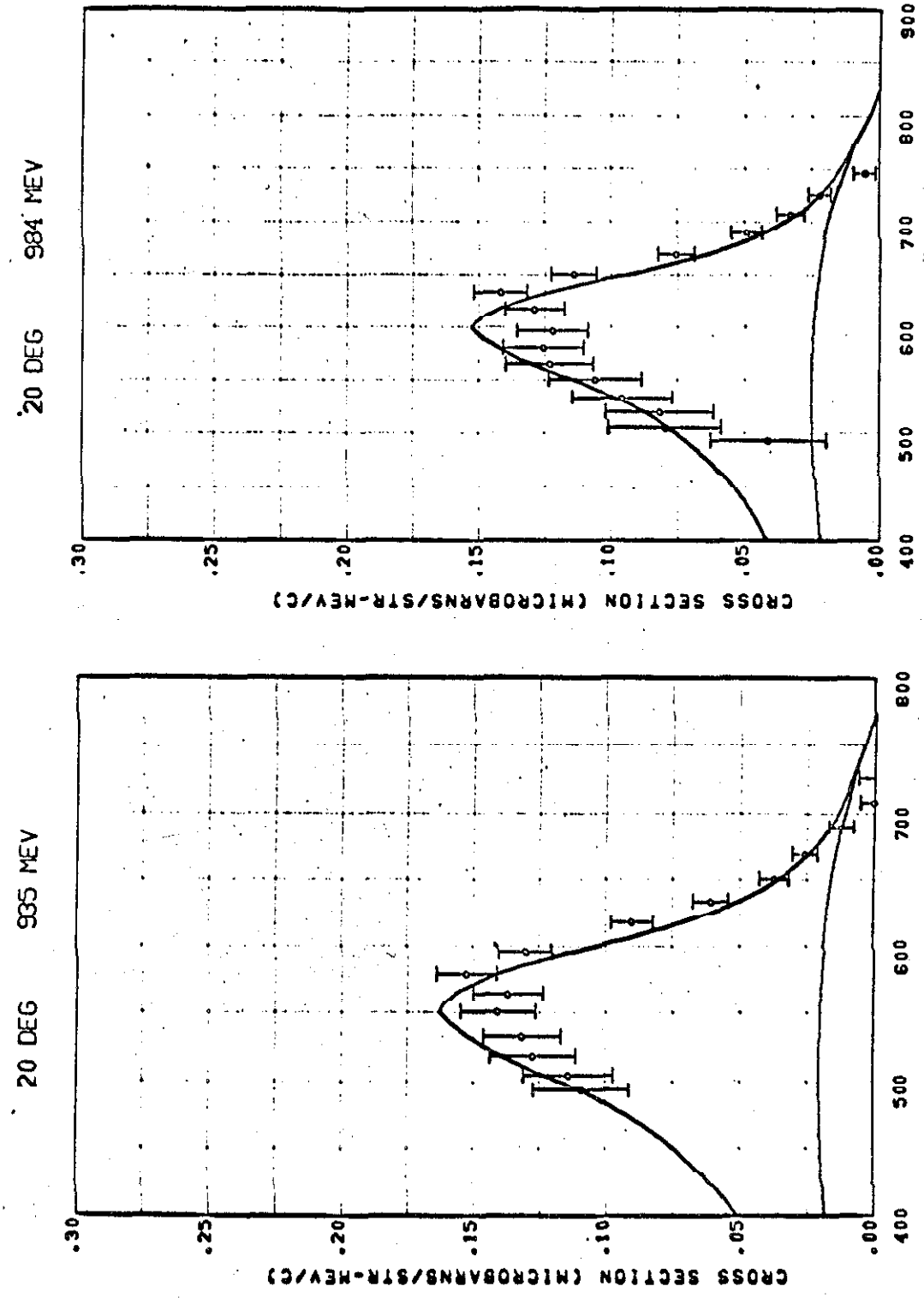

Figure 6.9. Laboratory cross section.

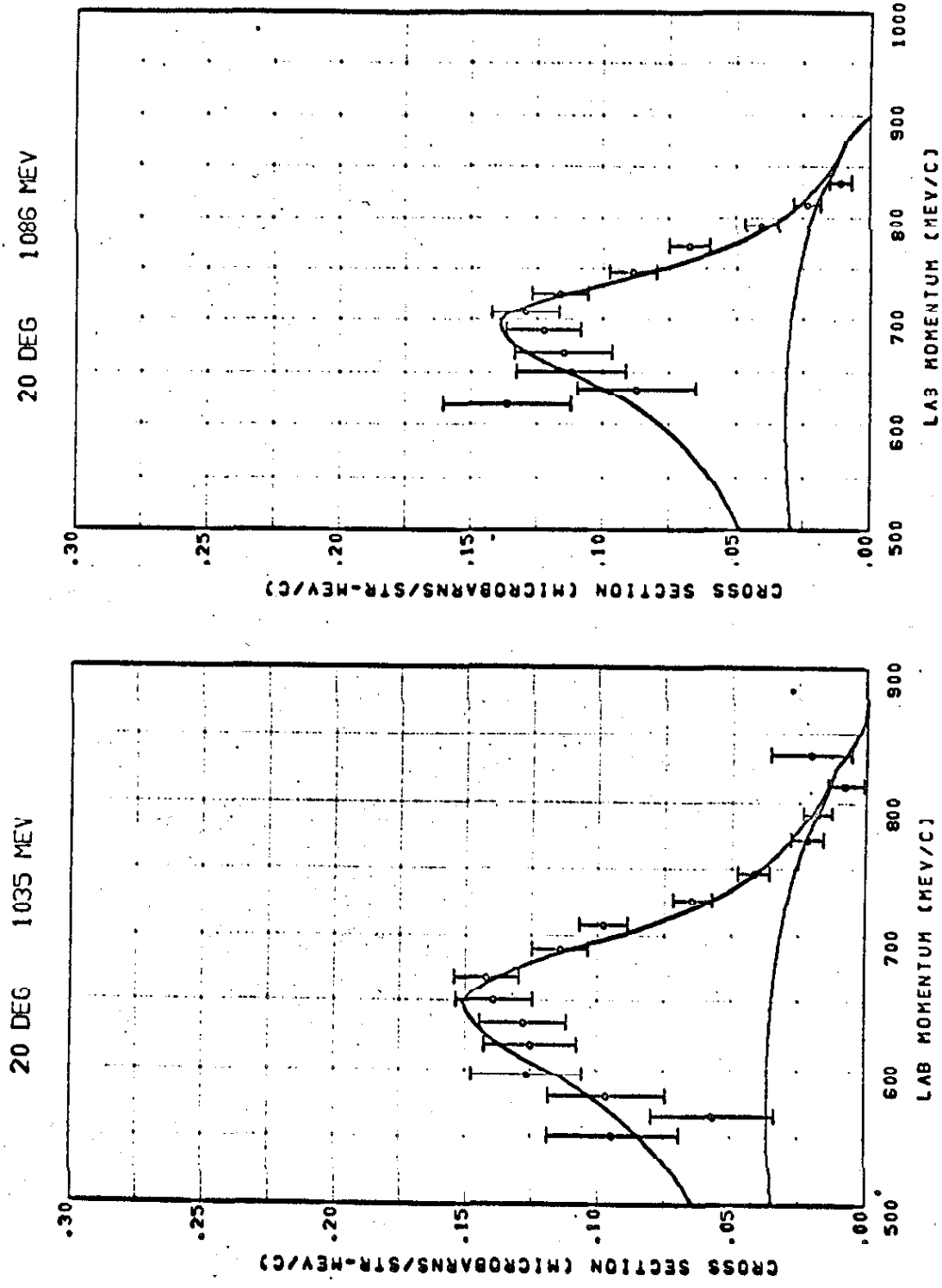

Figure 6.10. Laboratory cross section.

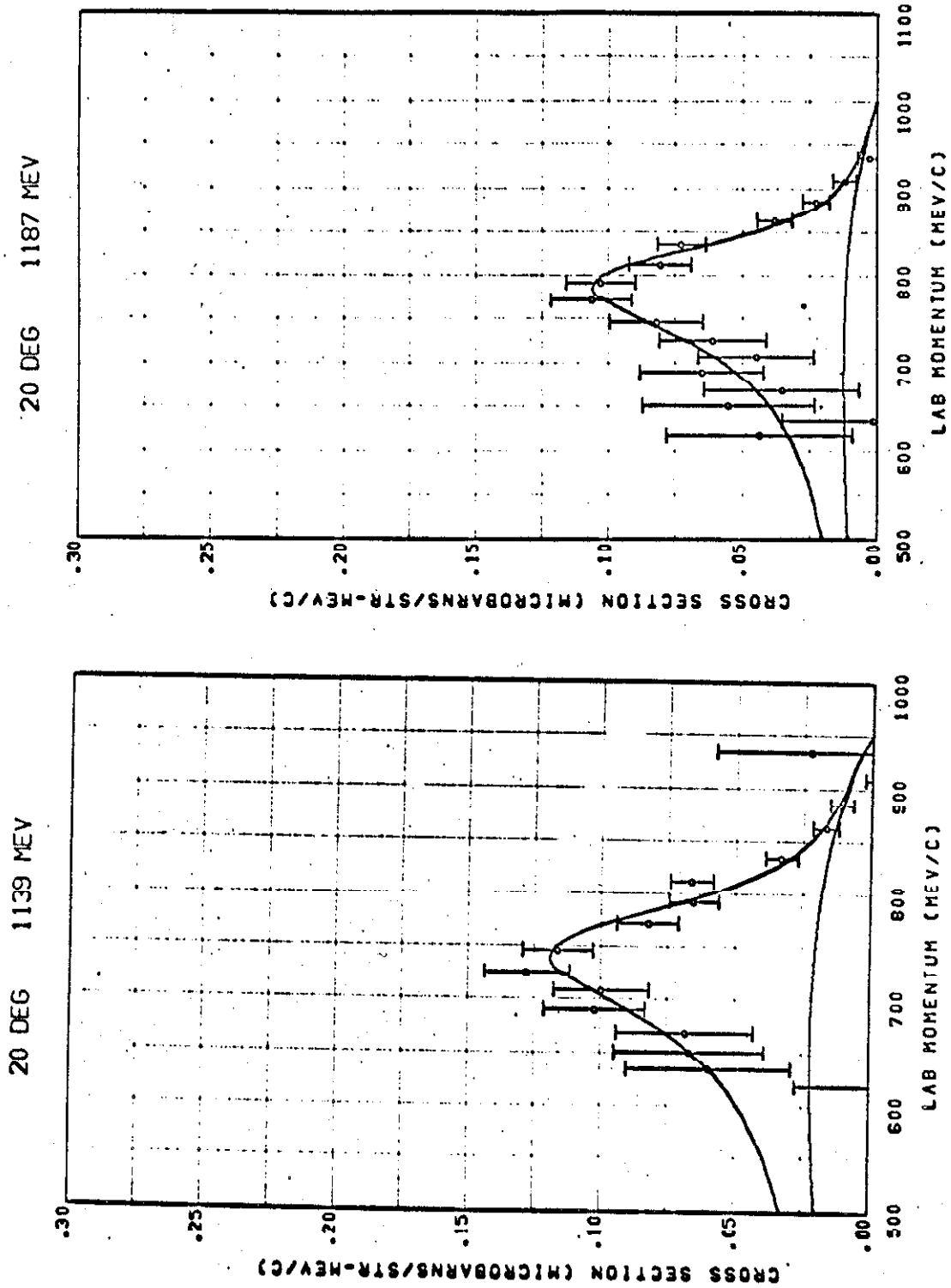

Figure 6.11. Laboratory cross section.

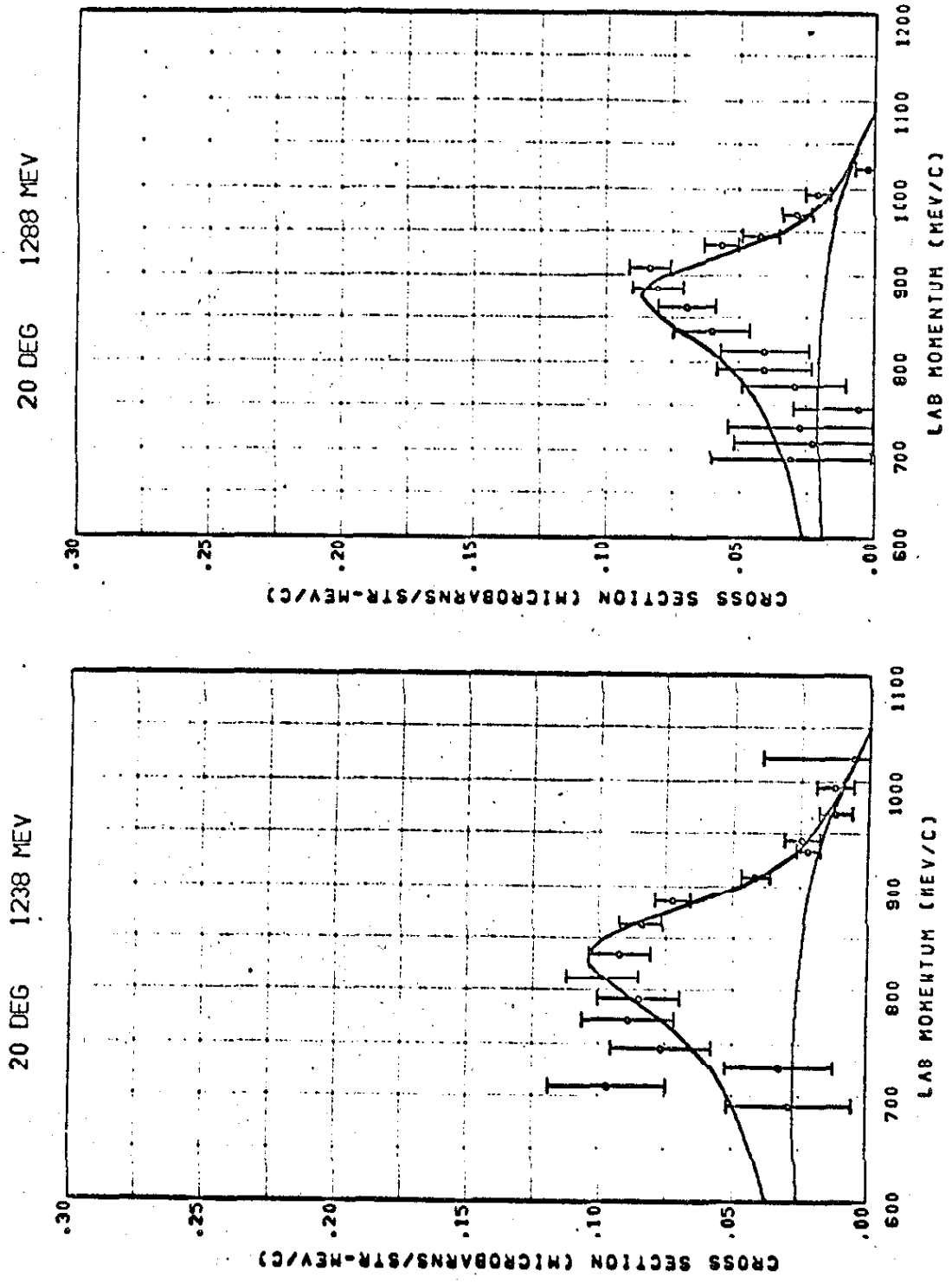

Figure 6.12. Laboratory cross section.

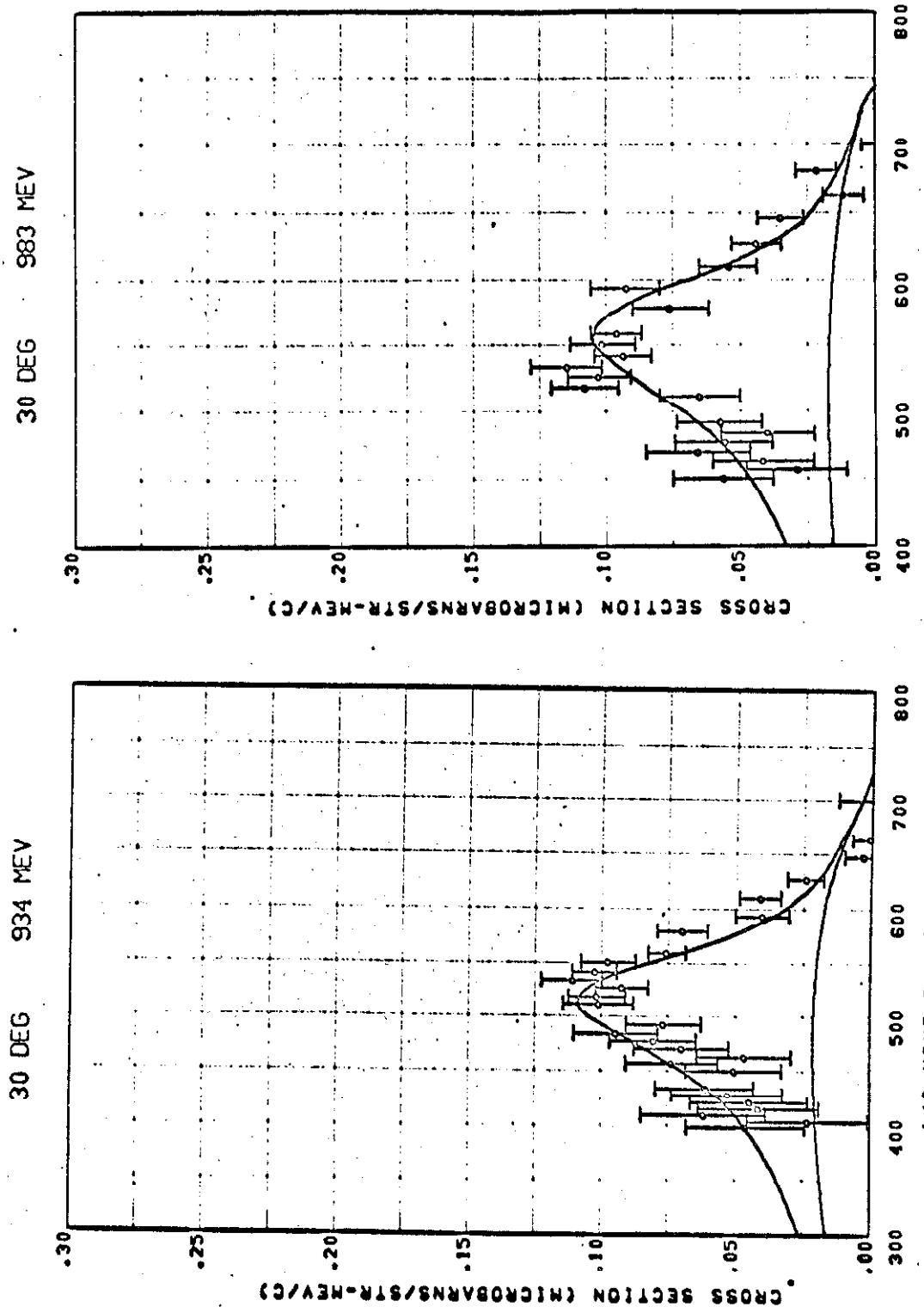

Figure 6.13. Laboratory cross section.

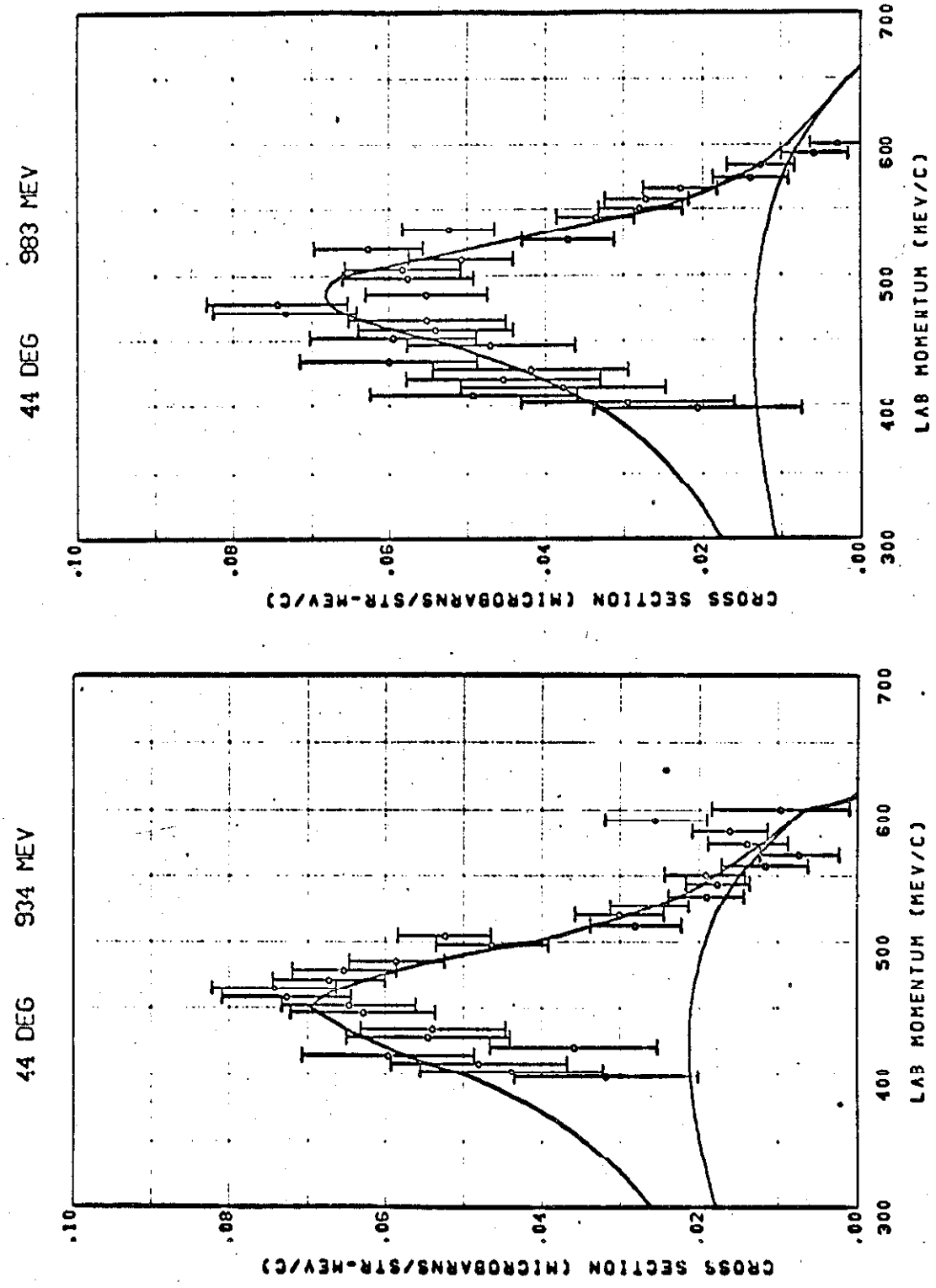

Figure 6.14. Laboratory cross section.

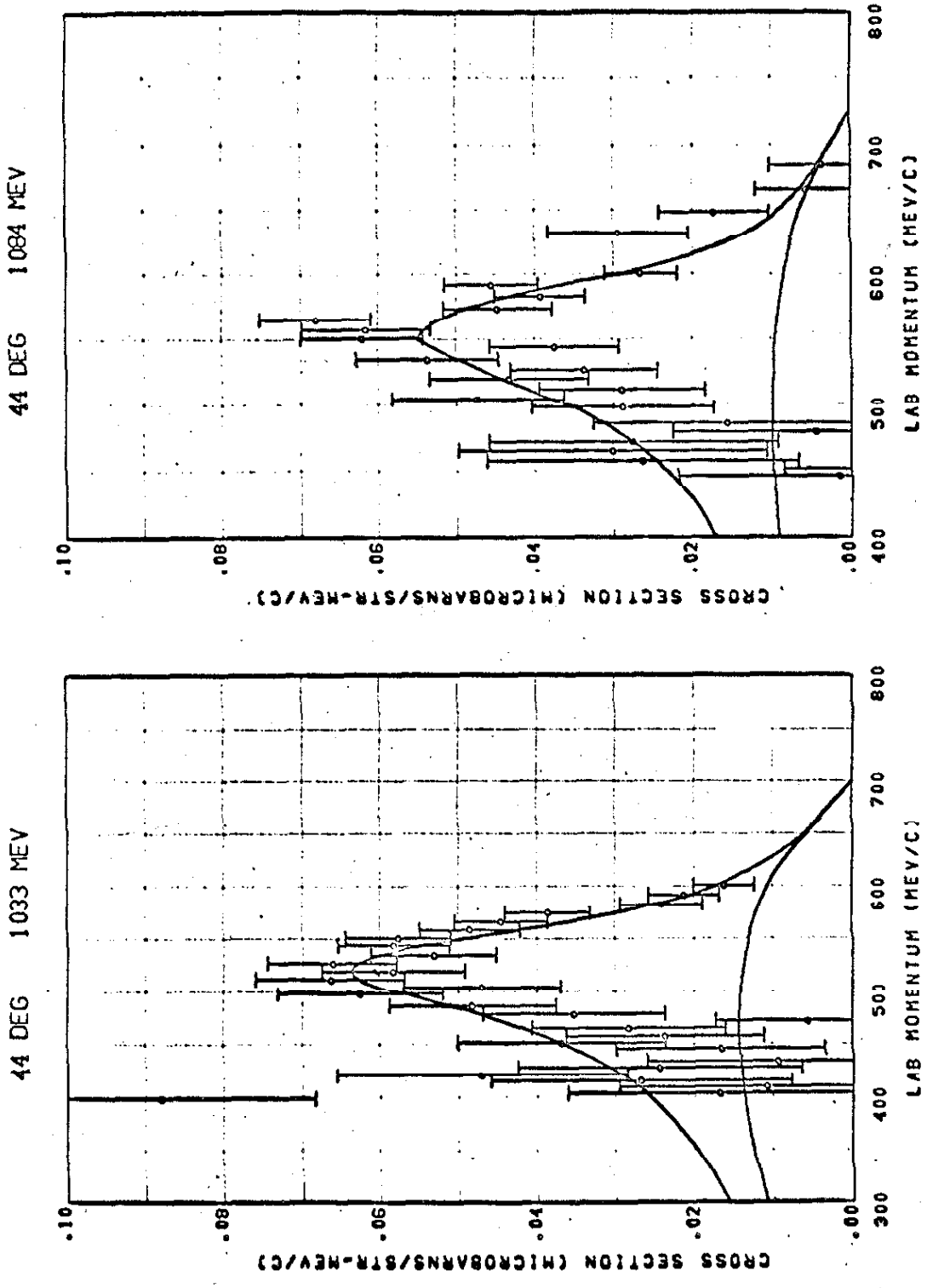

Figure 6.15. Laboratory cross section.

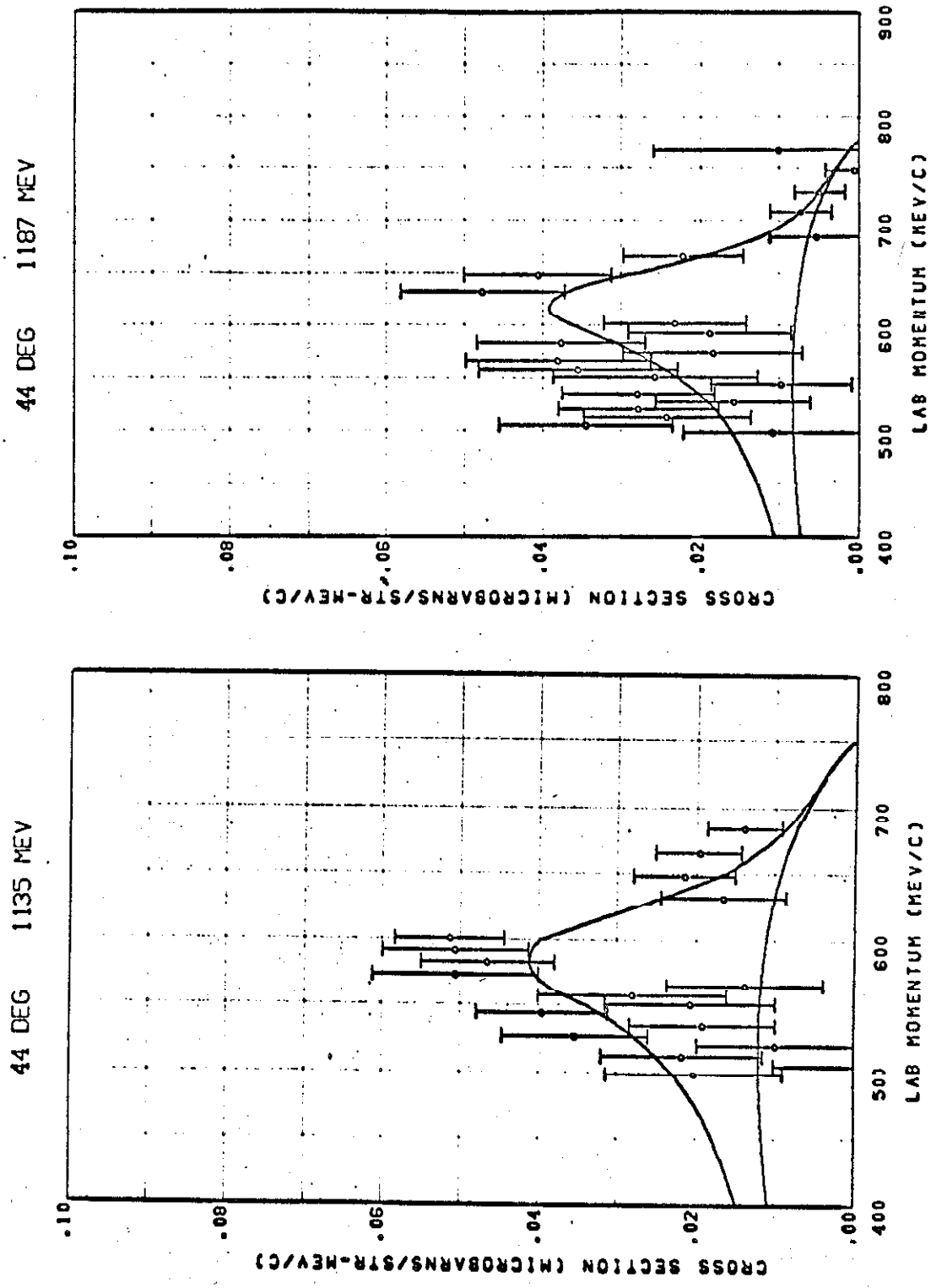

Figure 6.16. Laboratory cross section.

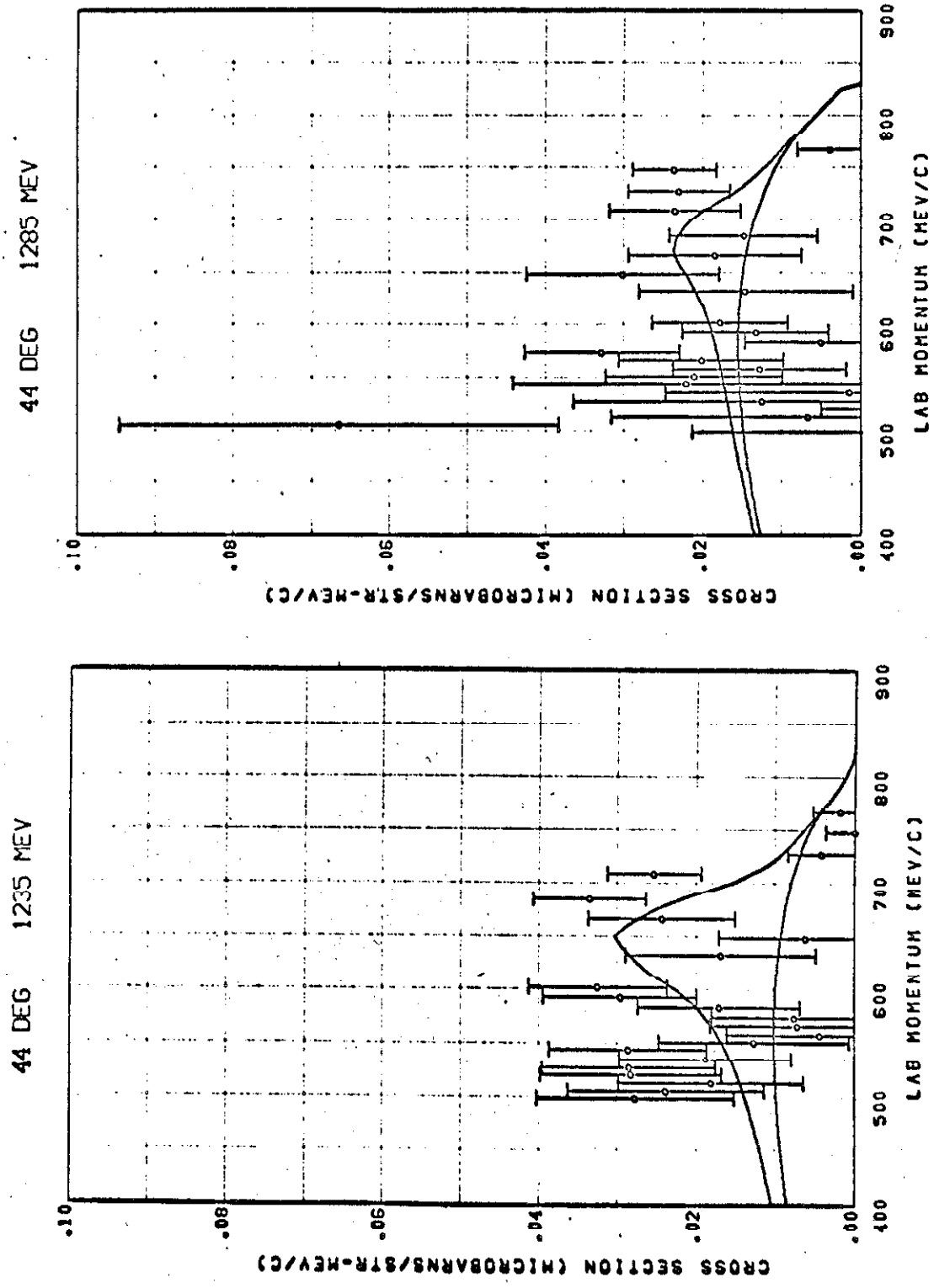

Figure 6.17. Laboratory cross section.

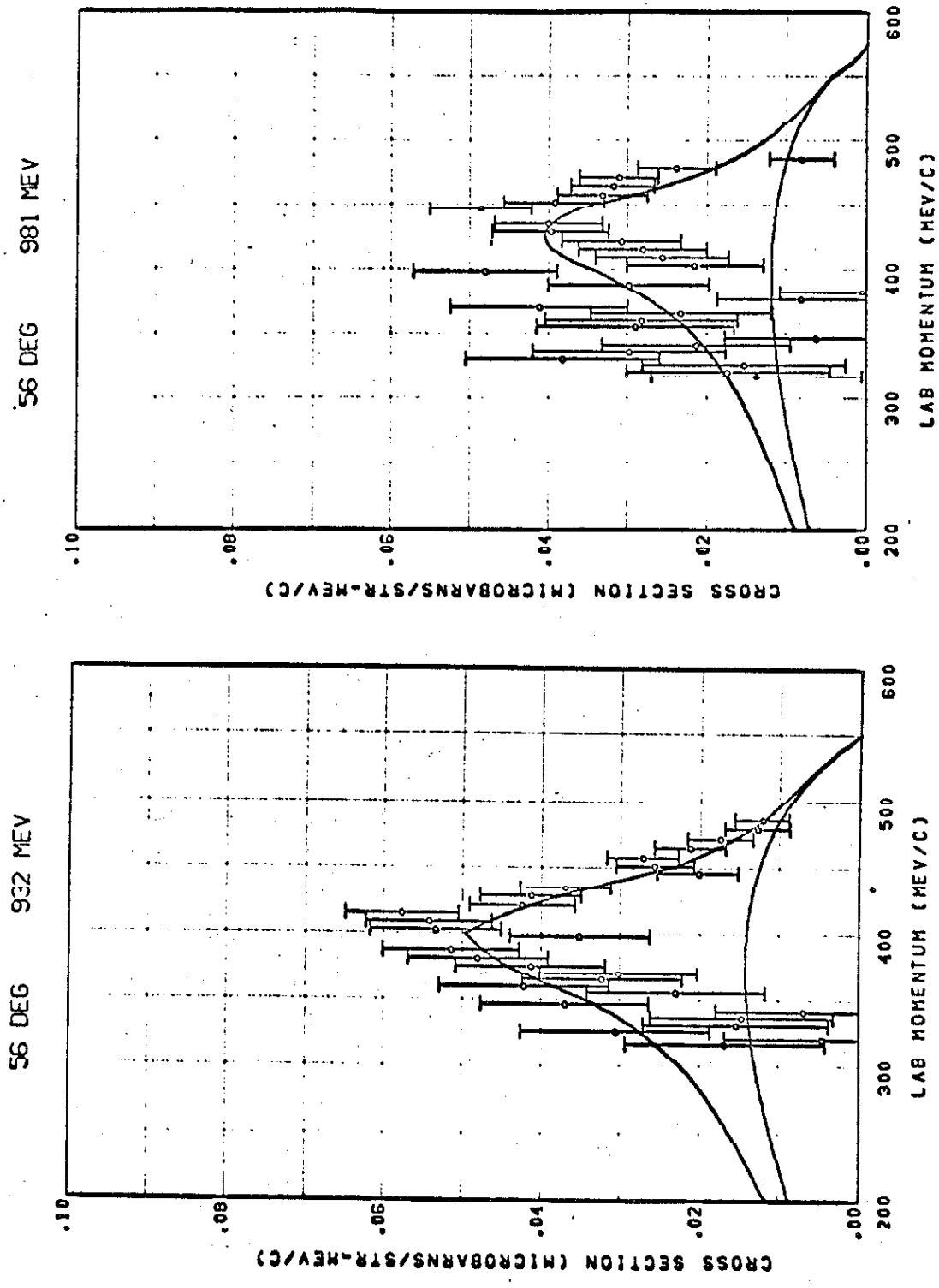

Figure 6.18. Laboratory cross section.

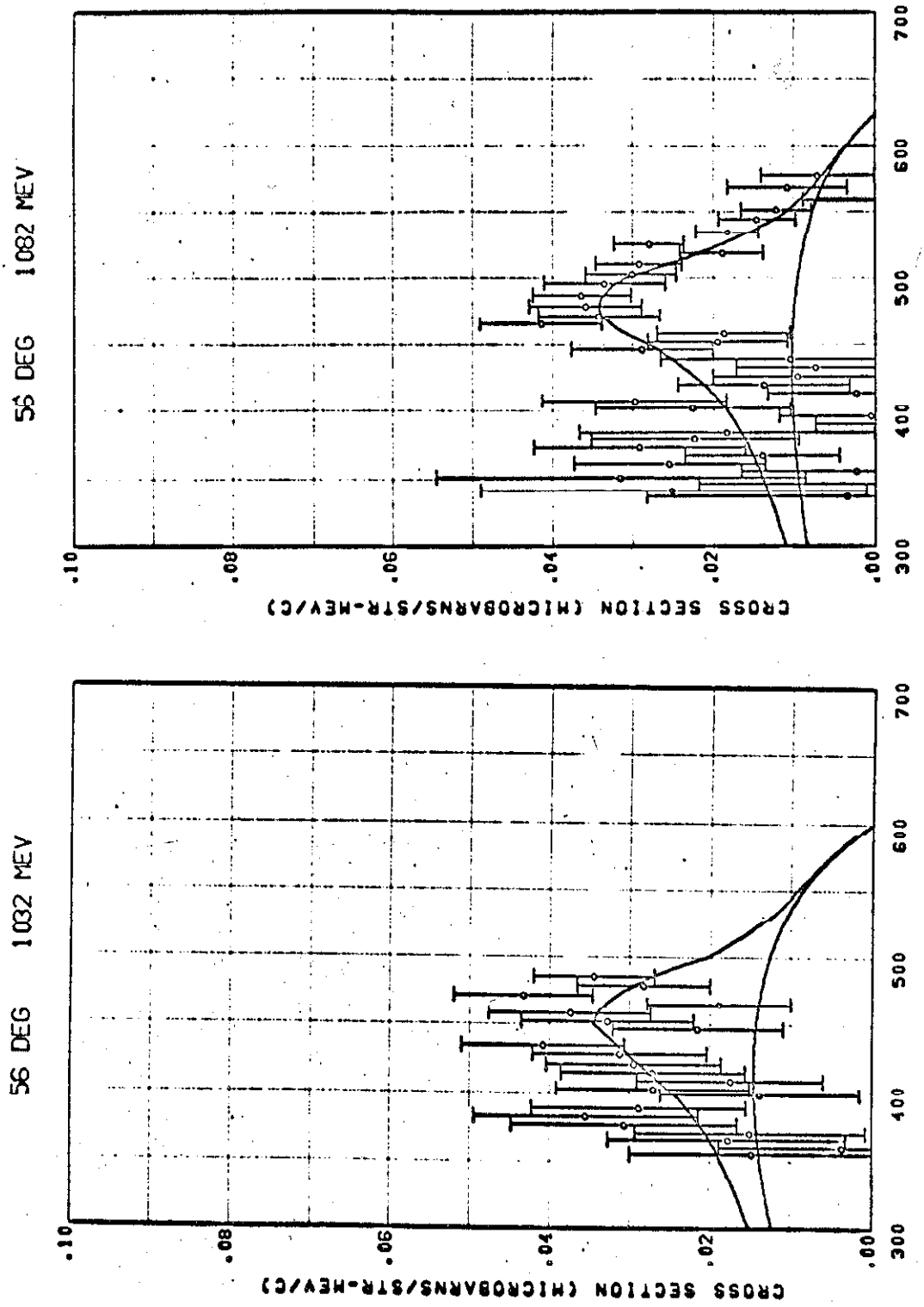

Figure 6.19. Laboratory cross section.

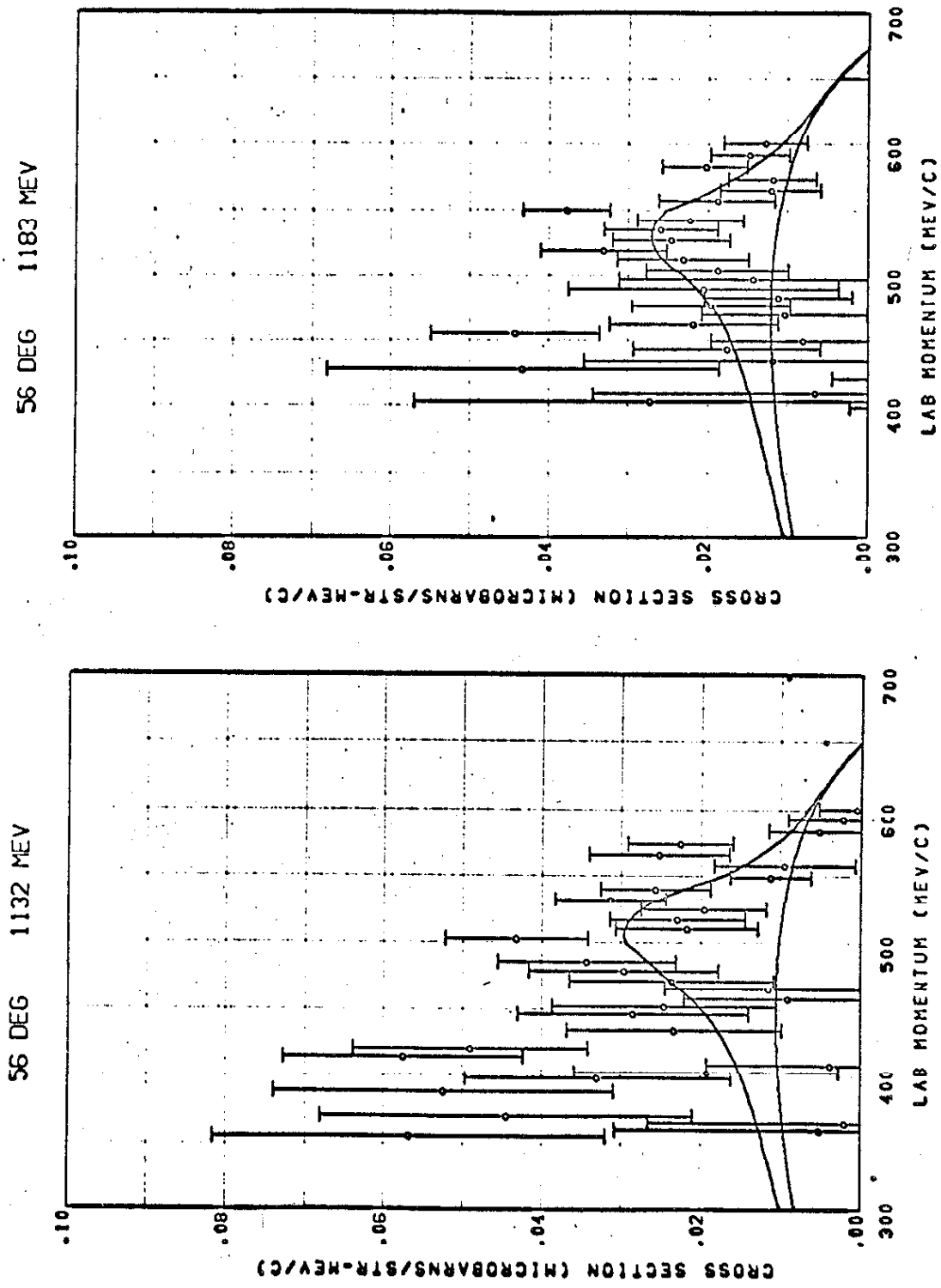

Figure 6.20. Laboratory cross section.

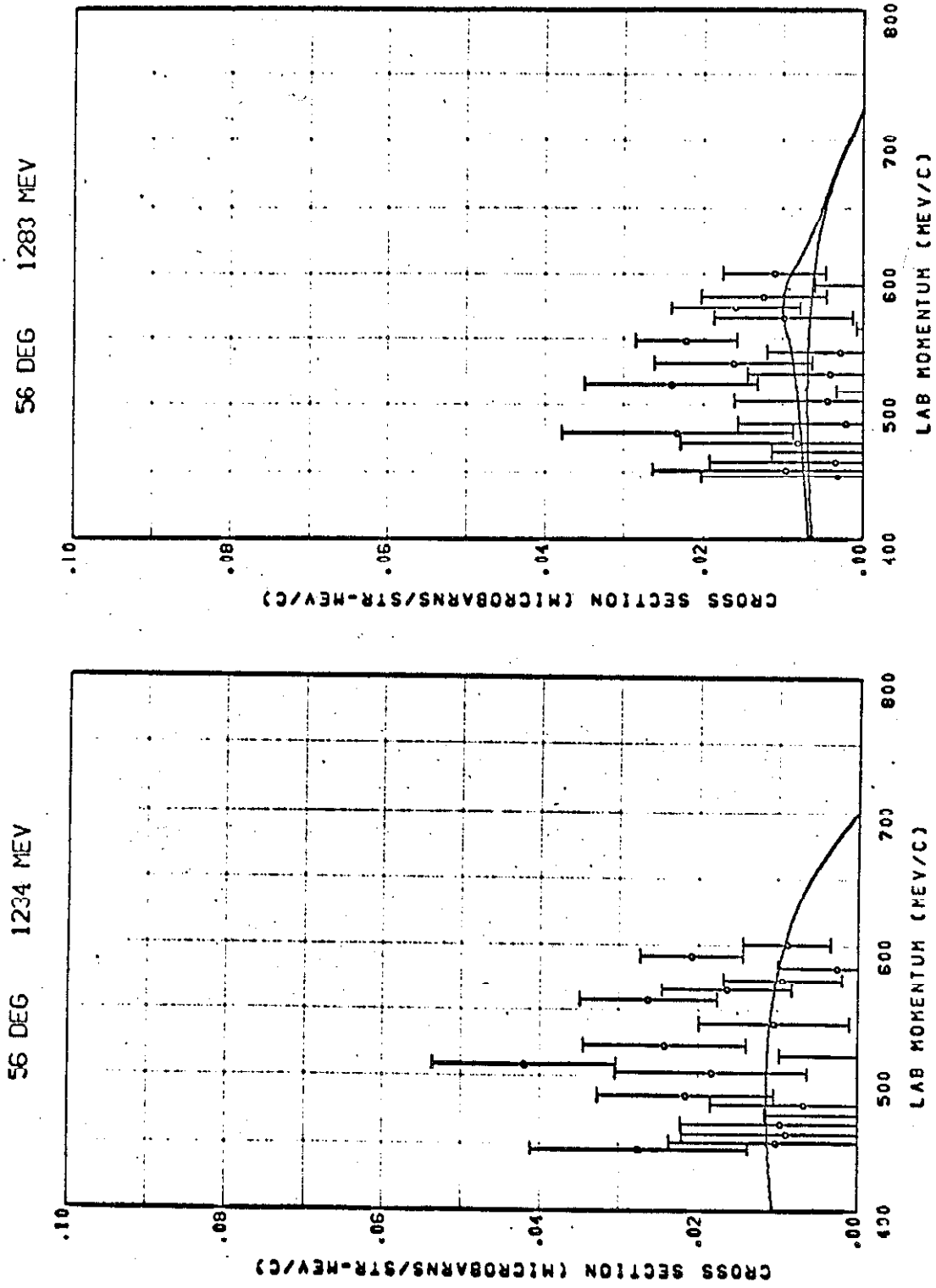

Figure 6.21. Laboratory cross section.

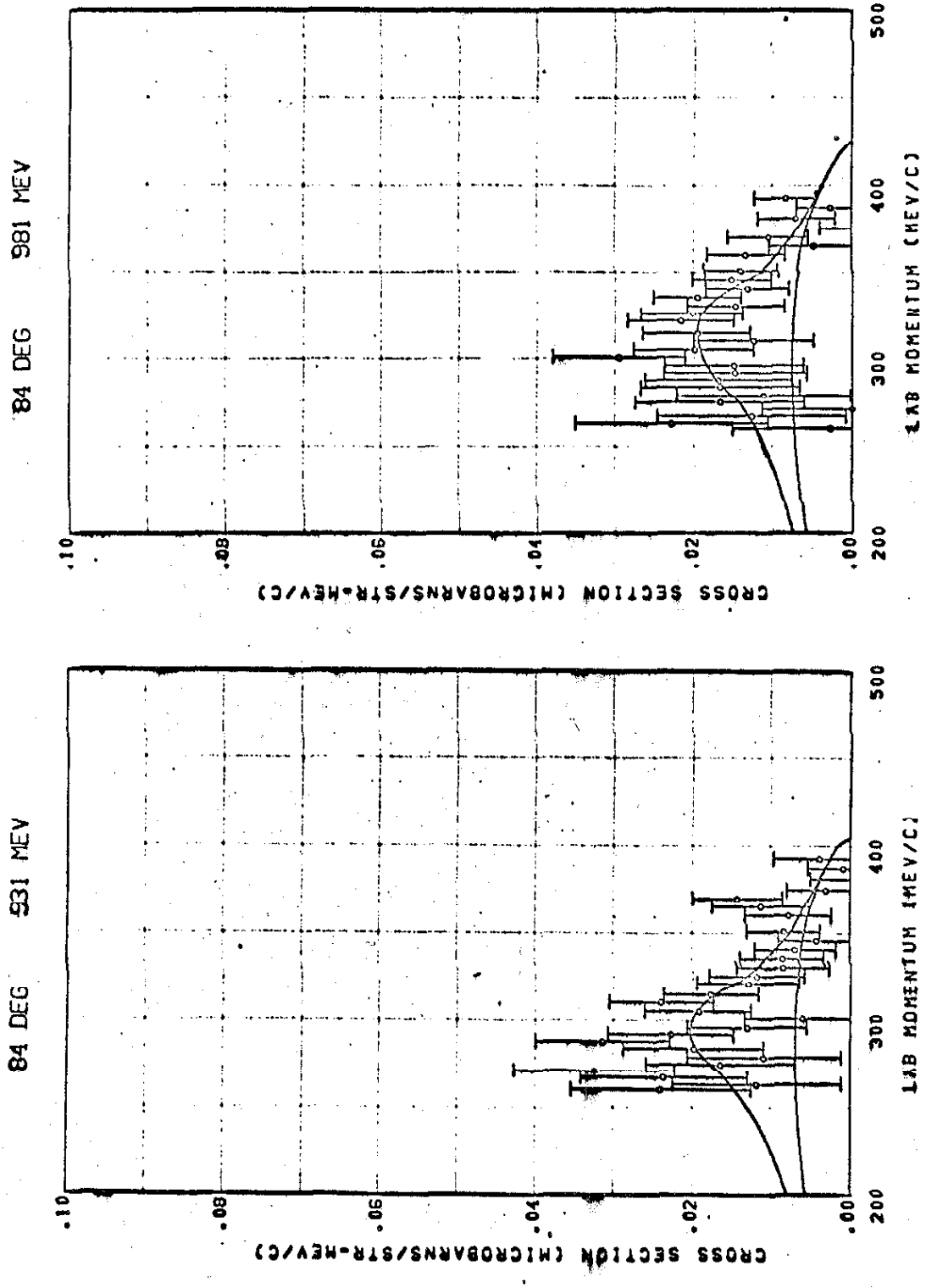

Figure 6.22. Laboratory cross section.

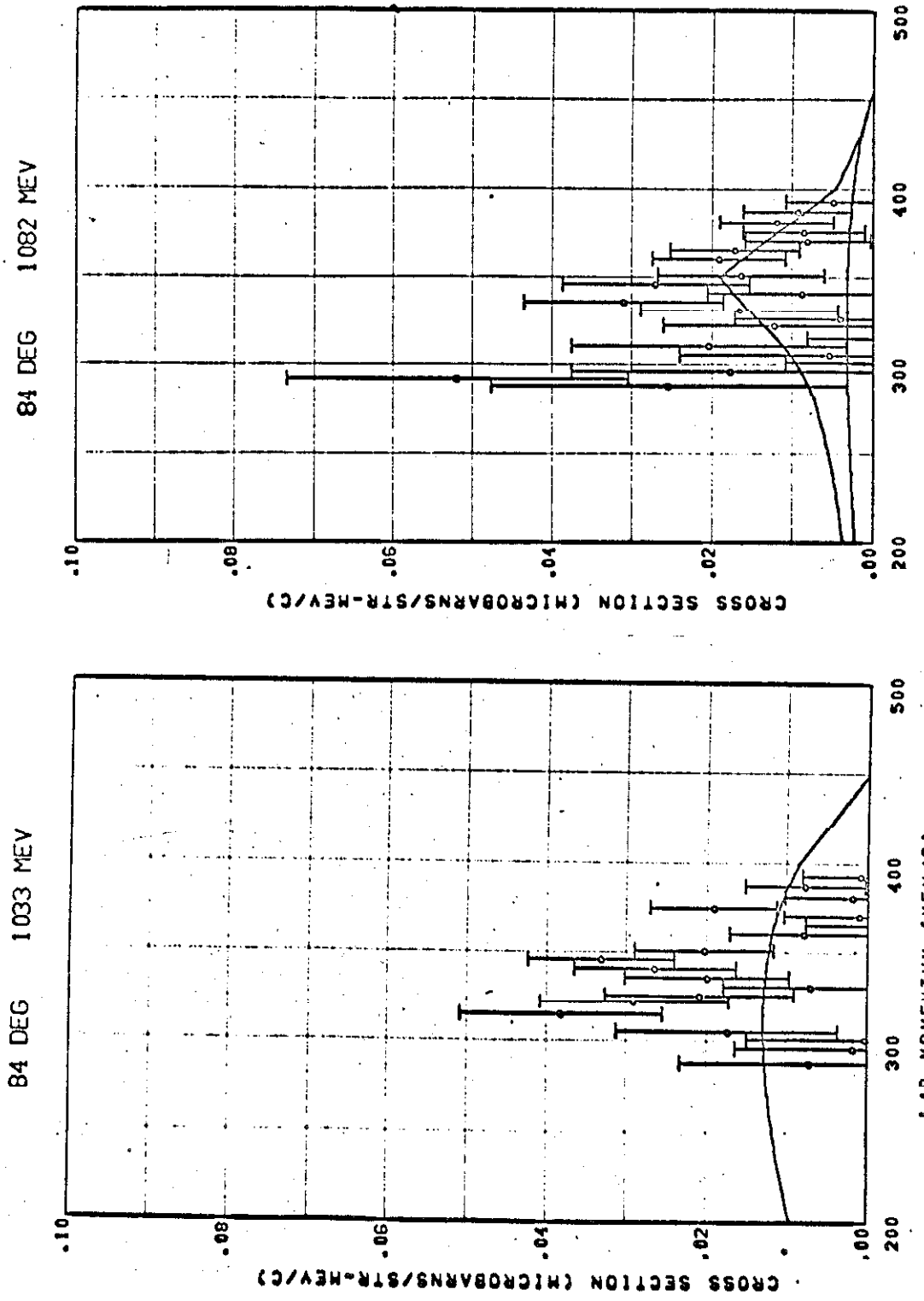

Figure 6.23. Laboratory cross section.

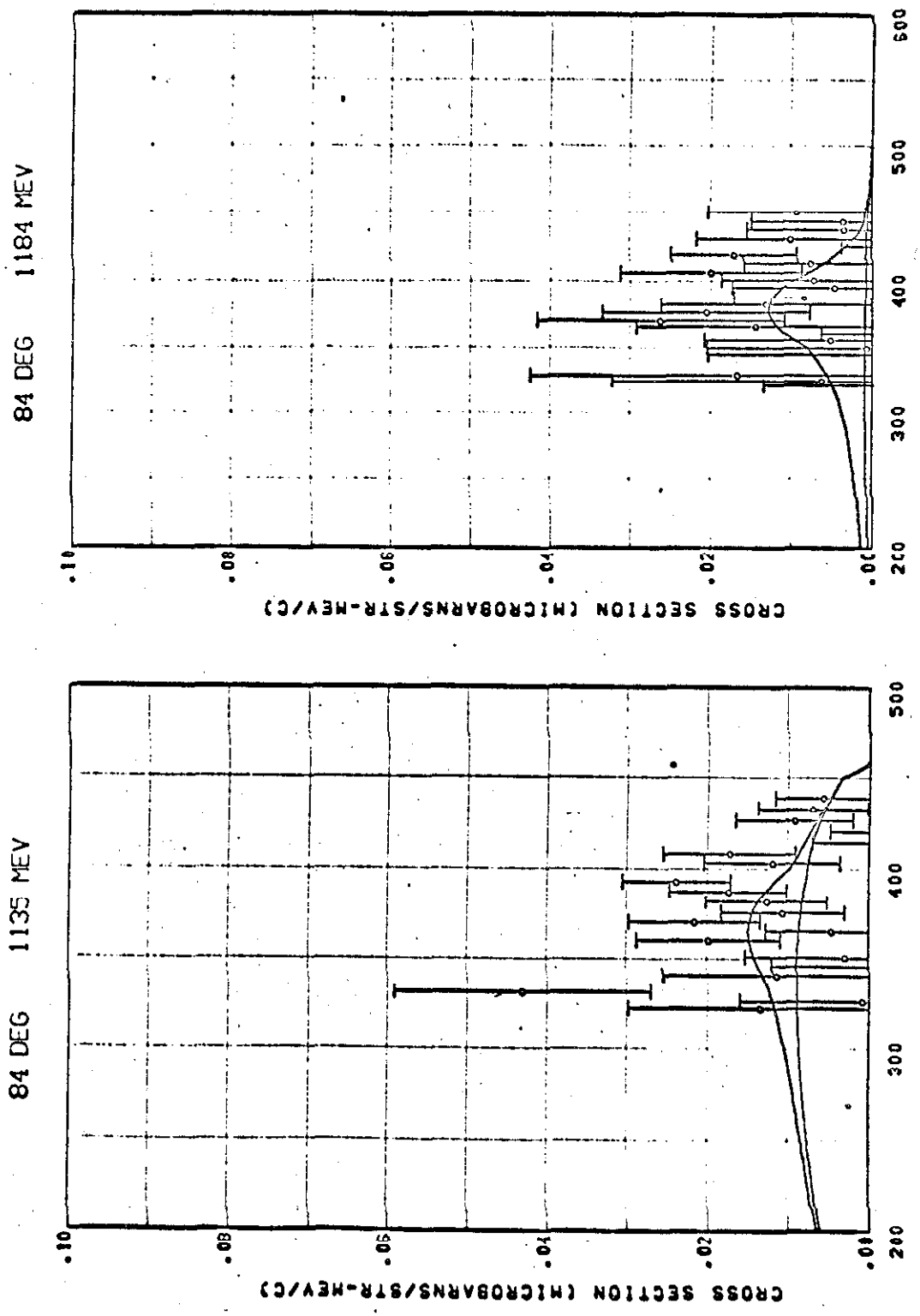

Figure 6.24. Laboratory cross section.

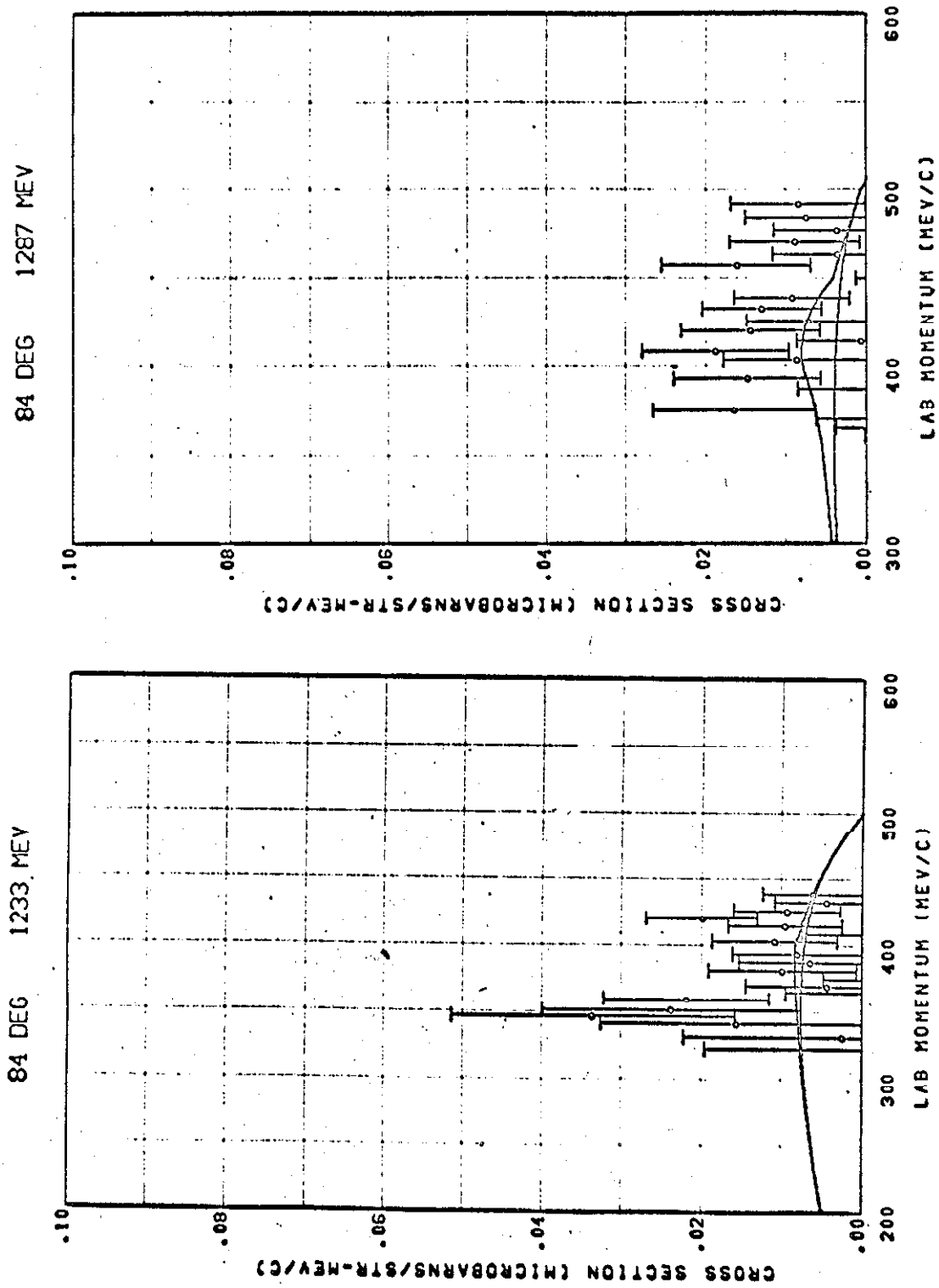

Figure 6.25. Laboratory cross section.

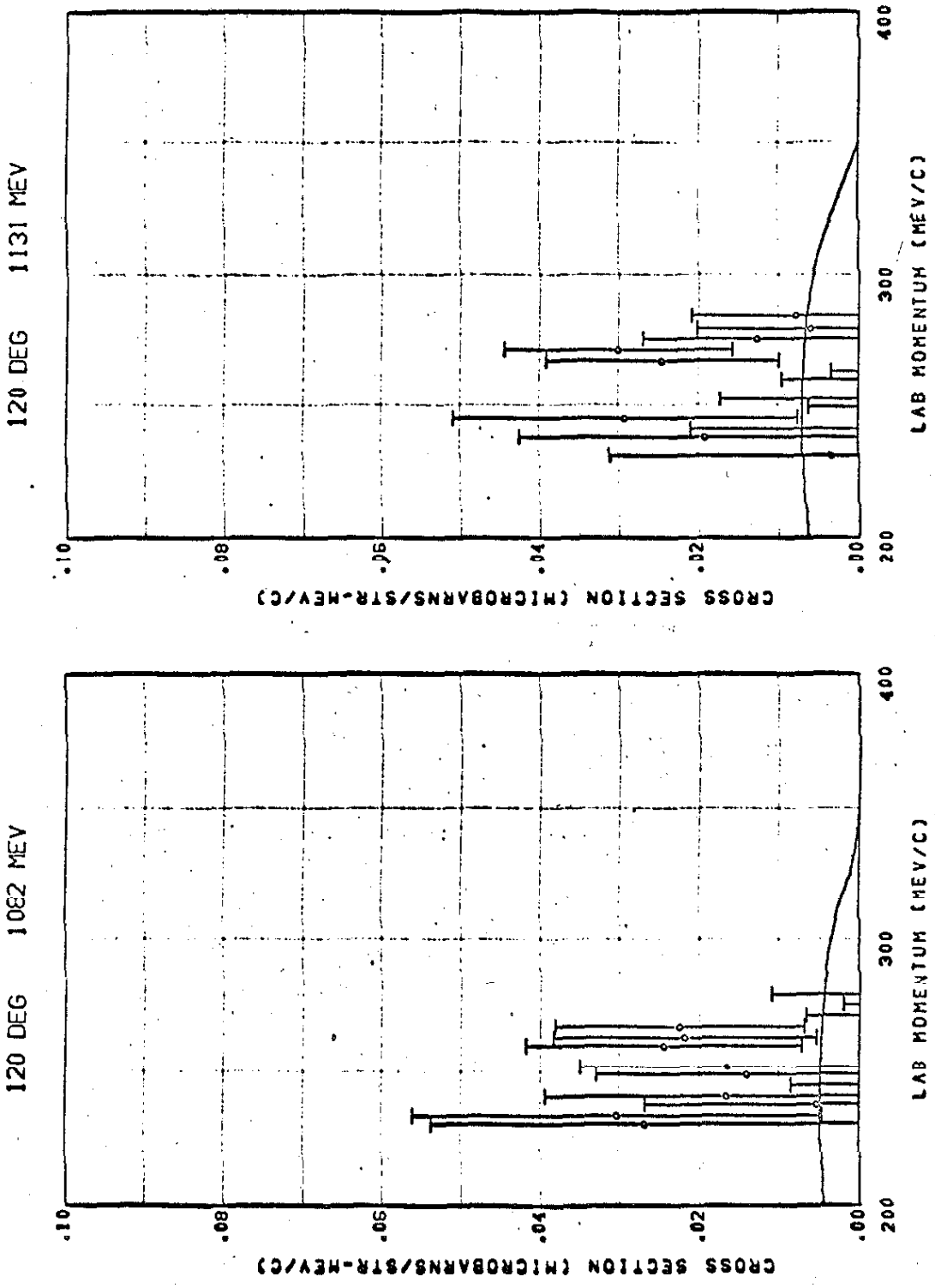

Figure 6.26. Laboratory cross section.

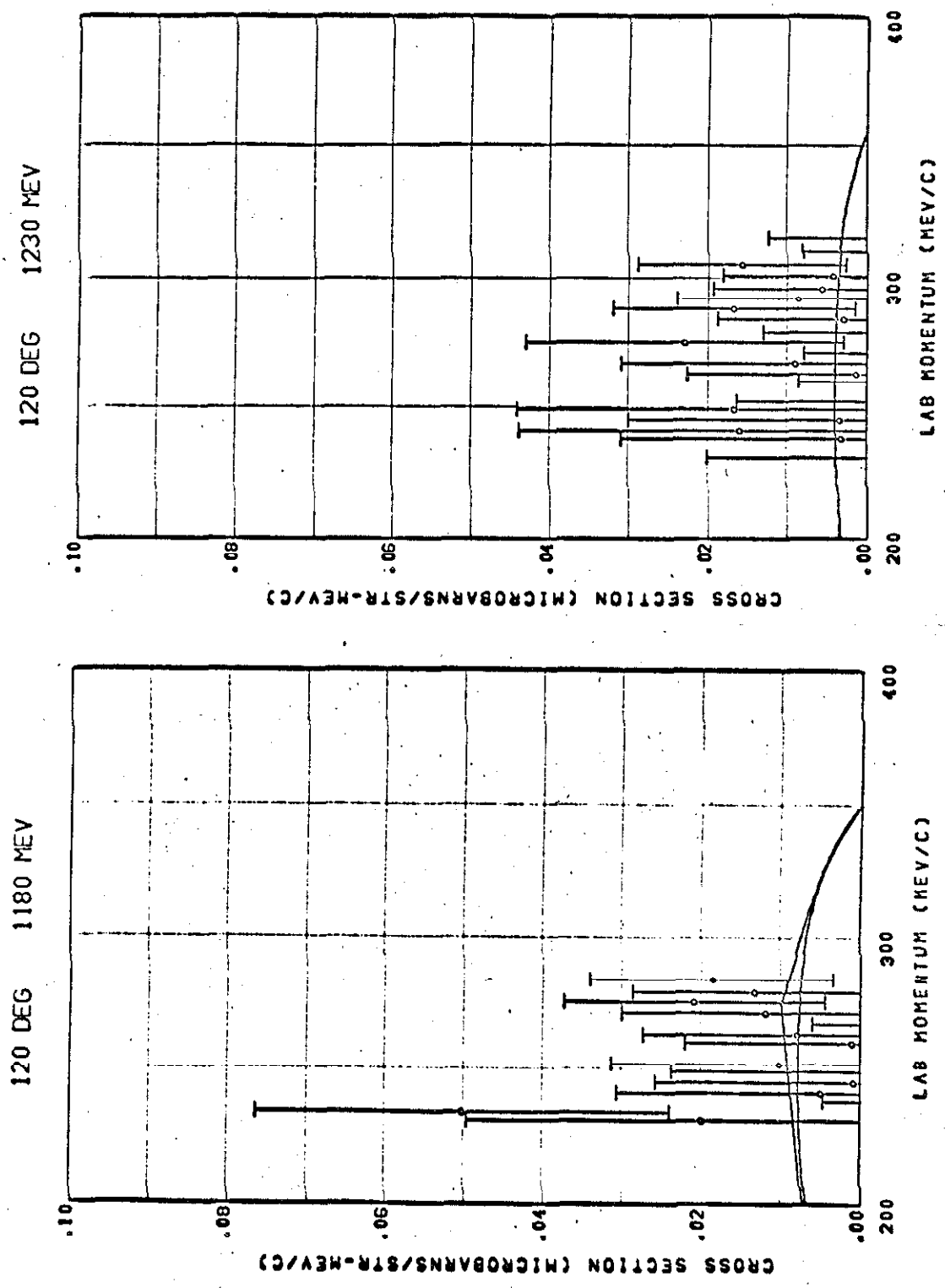

Figure 6.27. Laboratory cross section.

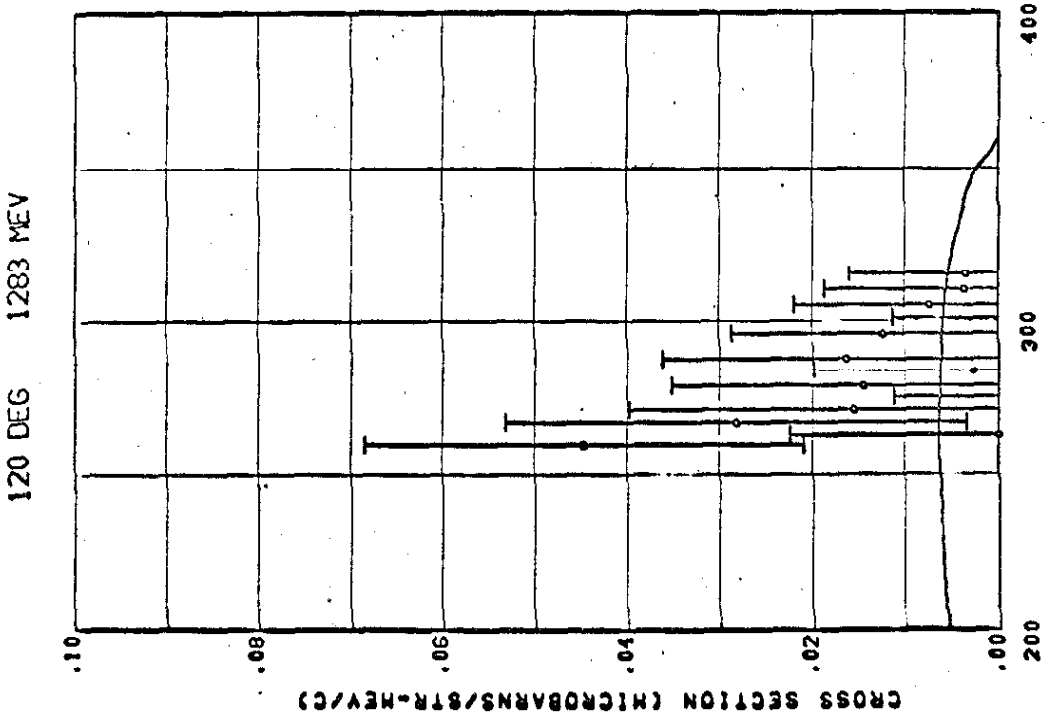

Figure 6.28. Laboratory cross section.

TABLE III

Laboratory Cross Sections

LAB ANG is the π^- lab angle (degrees)

CM ANG is the approximate π^- c. m. angle (degrees)

k is the average photon lab energy (MeV)

p is the π^- lab momentum (MeV/c).

The tabulated quantities are the laboratory cross sections, $\frac{d^2\sigma}{dpd\Omega}(k, p, \theta)$, in units of 10^{-32} cm^2/sr-MeV/c. The errors shown are the random errors only, including counting statistics, beam monitoring, and synchrotron energy fluctuations.

LAB ANG = 4.0 CM ANG = 7.5

P	934	983	1034	1084	1134	1185	1235	1285
522	5.1+- 2.7	7.2+- 3.1	-2.2+- 5.7					
535	5.0+- 2.6	6.5+- 2.9	8.8+- 5.6					
549	15.9+- 2.5	2.7+- 2.8	4.9+- 5.4					
564	16.7+- 2.3	2.3+- 2.7	2.0+- 5.0					
589	12.8+- 1.9	9.3+- 2.3	2.2+- 3.4	6.8+- 4.2				
604	13.2+- 1.8	10.7+- 2.1	6.5+- 3.3	2.1+- 4.1				
620	13.2+- 1.7	10.6+- 2.1	11.2+- 3.2	-0.9+- 3.9				
637	10.5+- 1.5	11.5+- 1.9	12.7+- 2.9	4.3+- 3.7				
661	7.0+- 1.3	14.8+- 1.7	8.1+- 2.6	8.5+- 3.5	7.3+- 3.9	-2.0+- 4.1	1.6+- 5.0	
678	4.7+- 1.2	14.0+- 1.5	7.5+- 2.4	13.6+- 3.3	0.1+- 3.7	5.0+- 4.2	3.1+- 4.9	
696	4.5+- 1.1	7.7+- 1.4	13.6+- 2.2	9.2+- 3.1	12.0+- 3.6	4.2+- 4.1	-6.8+- 4.7	
715	3.5+- 1.0	8.4+- 1.3	10.9+- 2.0	12.6+- 3.0	6.5+- 3.4	7.7+- 3.9	-2.2+- 4.5	
743	2.9+- 1.8	3.5+- 1.2	10.7+- 1.8	16.6+- 2.4	8.1+- 3.4	8.9+- 4.1	0.5+- 4.7	8.8+- 5.2
762	1.9+- 2.2	0.9+- 1.1	12.1+- 1.7	14.2+- 2.3	14.0+- 3.2	2.0+- 3.9	9.6+- 4.5	5.0+- 5.0
782	0. +- 2.0	1.4+- 1.0	5.5+- 1.5	16.0+- 2.0	16.3+- 2.9	10.1+- 3.7	1.2+- 4.4	4.1+- 4.9
804	0. +- 2.0	0.5+- 1.0	3.6+- 1.3	13.9+- 1.8	17.3+- 2.7	13.5+- 3.5	3.9+- 4.2	2.6+- 4.7
834				9.9+- 1.4	15.7+- 2.2	15.3+- 2.9	7.1+- 3.2	11.3+- 3.9
855				7.5+- 1.3	12.9+- 2.0	20.3+- 2.6	10.0+- 3.0	1.5+- 3.6
878				4.0+- 1.1	12.9+- 1.7	20.9+- 2.3	9.9+- 2.7	13.8+- 3.5
902				3.2+- 1.1	7.3+- 1.5	15.7+- 2.1	15.6+- 2.5	19.3+- 3.3
935						10.8+- 1.6	16.6+- 2.3	21.4+- 3.2
959						5.0+- 1.4	16.0+- 2.0	20.7+- 2.8
985						2.1+- 1.1	11.7+- 1.7	18.4+- 2.6
1012						3.7+- 1.2	4.0+- 1.4	14.3+- 2.1
1031								14.4+- 1.8
1057								8.5+- 1.5
1085								3.9+- 1.3
1115								1.5+- 1.3

Table III. 1. Laboratory cross sections at 4^{o}.

LAB ANG = 12.0 CM ANG = 22.3

P	K 934	983	1034	1084	1134	1185	1235	1285
445	9.3+- 3.1	4.0+- 3.3						
456	8.5+- 3.0	-1.0+- 3.2						
468	5.2+- 2.8	5.1+- 3.1						
481	5.3+- 2.7	11.1+- 3.0						
507	12.4+- 2.9	0.3+- 3.2	2.7+- 4.4					
520	11.8+- 2.8	2.7+- 3.1	2.9+- 4.3					
534	12.8+- 2.5	10.2+- 2.9	4.8+- 4.2					
549	17.2+- 2.4	7.8+- 2.8	3.8+- 4.0					
575	20.5+- 2.1	6.5+- 2.5	15.0+- 3.5	-7.4+- 3.7	14.7+- 4.5			
589	17.9+- 1.9	12.1+- 2.3	11.1+- 3.4	2.2+- 3.7	5.4+- 4.4			
605	17.9+- 1.7	14.1+- 2.2	12.6+- 3.2	-0.1+- 3.5	11.7+- 4.2			
622	12.3+- 1.5	15.5+- 2.0	14.3+- 2.9	4.5+- 3.3	7.6+- 4.0			
647	8.8+- 1.3	18.3+- 1.8	15.2+- 3.2	11.8+- 3.7	0.4+- 4.1	5.3+- 4.4	3.5+- 4.5	
663	5.4+- 1.1	16.1+- 1.6	16.5+- 2.9	14.3+- 3.4	4.3+- 3.9	1.6+- 4.3	8.0+- 4.3	
681	3.0+- 1.0	13.8+- 1.4	12.1+- 2.6	14.8+- 3.1	8.8+- 3.7	1.5+- 4.1	11.6+- 4.2	
700	1.9+- 0.8	9.0+- 1.1	16.1+- 2.2	16.0+- 2.8	8.4+- 3.4	10.5+- 3.9	10.0+- 4.1	
728		4.9+- 1.1	14.2+- 1.8	18.7+- 2.7	13.5+- 3.5	10.7+- 3.7	2.1+- 4.3	6.7+- 4.8
747		2.4+- 1.0	8.1+- 1.6	19.0+- 2.4	12.9+- 3.1	12.6+- 3.4	0.7+- 4.0	12.3+- 4.5
767		2.3+- 0.9	5.2+- 1.3	15.9+- 2.0	17.1+- 2.8	13.7+- 3.2	7.9+- 3.8	0.4+- 4.3
788		0.6+- 0.9	4.6+- 1.2	13.8+- 1.9	13.8+- 2.5	12.8+- 2.9	12.6+- 3.5	2.2+- 4.1
820				6.0+- 1.3	16.2+- 1.9	12.7+- 2.7	15.4+- 3.3	7.7+- 3.9
841				4.1+- 1.1	13.1+- 1.6	13.2+- 2.4	14.9+- 3.0	7.5+- 3.5
863				3.3+- 1.0	8.7+- 1.4	12.1+- 2.0	17.0+- 2.7	11.6+- 3.3
887				0.7+- 1.1	4.1+- 1.1	11.1+- 1.6	16.1+- 2.3	13.2+- 2.9
921						5.8+- 0.9	12.4+- 1.6	15.6+- 2.1
944						5.2+- 0.8	5.3+- 1.3	15.8+- 1.8
969						1.4+- 0.7	3.9+- 1.0	10.1+- 1.4
996						0.5+- 0.9	1.5+- 0.9	7.5+- 1.2

Table III. 2. Laboratory cross sections at 12^{o}.

LAB ANG = 20.0 CM ANG = 36.6

P	934	983	1034	1084	1134	1185	1235	1285
493	10.9+- 1.8	4.1+- 2.2						
505	11.4+- 1.7	8.0+- 2.1						
519	12.8+- 1.6	8.2+- 2.0						
533	13.2+- 1.4	9.6+- 1.9						
551	14.1+- 1.4	10.6+- 1.7	9.4+- 2.5					
565	13.7+- 1.3	12.3+- 1.6	5.7+- 2.3					
580	15.3+- 1.1	12.6+- 1.5	9.7+- 2.2					
596	13.1+- 1.0	12.2+- 1.3	12.7+- 2.1					
618	9.0+- 0.8	12.9+- 1.1	12.5+- 1.7	13.6+- 2.4	-0.4+- 3.2	4.4+- 3.5		
636	6.1+- 0.6	14.2+- 1.0	12.8+- 1.6	8.7+- 2.2	6.0+- 3.1	0.1+- 3.4		
651	3.7+- 0.6	11.4+- 0.9	13.9+- 1.4	11.2+- 2.1	6.7+- 2.8	5.5+- 3.2		
669	2.6+- 0.5	7.6+- 0.7	14.2+- 1.2	11.5+- 1.8	6.9+- 2.5	3.5+- 2.9		
690	1.2+- 0.5	4.9+- 0.6	11.4+- 1.1	12.3+- 1.4	10.2+- 1.9	6.5+- 2.3	2.9+- 2.3	3.1+- 3.0
708	0.0+- 0.5	3.3+- 0.5	9.8+- 0.9	12.9+- 1.3	10.0+- 1.8	4.5+- 2.1	9.7+- 2.2	2.2+- 2.9
726	-0.2+- 0.8	2.2+- 0.4	6.5+- 0.7	11.6+- 1.1	12.8+- 1.6	6.1+- 2.0	3.2+- 2.0	2.7+- 2.7
746	-2.8+- 2.4	0.5+- 0.4	4.2+- 0.6	8.9+- 0.9	11.6+- 1.3	8.2+- 1.8	7.7+- 1.9	0.5+- 2.5
772			2.2+- 0.6	6.8+- 0.7	8.3+- 1.1	10.7+- 1.5	8.9+- 1.7	3.0+- 2.0
792			1.8+- 0.5	4.0+- 0.6	6.6+- 0.9	10.3+- 1.3	8.5+- 1.5	4.1+- 1.8
813			0.8+- 0.7	2.3+- 0.5	6.6+- 0.8	8.1+- 1.2	9.9+- 1.4	4.1+- 1.7
835			2.1+- 1.5	1.1+- 0.4	3.3+- 0.6	7.3+- 0.9	9.3+- 1.1	6.0+- 1.4
863					1.7+- 0.5	3.8+- 0.6	8.4+- 0.8	7.0+- 1.1
885					1.1+- 0.4	2.3+- 0.5	7.2+- 0.7	8.1+- 1.0
909					-0.4+- 0.7	1.2+- 0.4	4.2+- 0.5	8.4+- 0.8
934					2.3+- 3.5	0.3+- 0.4	2.2+- 0.5	5.7+- 0.6
944							2.5+- 0.7	4.2+- 0.7
969							1.2+- 0.6	2.9+- 0.6
995							1.2+- 0.7	2.1+- 0.5
1022							0.6+- 3.4	0.3+- 0.4

Table III. 3. Laboratory cross sections at 20^{o}.

LAB ANG = 30.0 CM ANG = 51.5

P	K 934	983	1034	1084	1134	1185	1235	1285
398	4.6+- 2.2							
403	2.3+- 2.2							
409	6.2+- 2.3							
415	4.1+- 2.2							
421	4.5+- 2.2							
428	5.3+- 2.1							
434	6.1+- 1.8							
450	5.1+- 1.8	5.7+- 1.8						
457	7.4+- 1.7	2.9+- 1.9						
463	4.7+- 1.8	4.2+- 1.9						
470	7.0+- 1.8	6.6+- 1.9						
477	8.1+- 1.6	5.6+- 1.8						
484	9.5+- 1.6	4.0+- 1.7						
492	7.7+- 1.4	5.8+- 1.6						
512	10.1+- 1.3	6.5+- 1.5						
519	10.2+- 1.1	10.8+- 1.3						
527	9.3+- 1.0	10.3+- 1.2						
534	11.1+- 1.1	11.5+- 1.3						
542	10.3+- 0.8	9.4+- 1.1						
551	9.8+- 1.0	10.2+- 1.2						
559	7.6+- 0.7	9.6+- 0.9						
579	7.0+- 0.9	7.6+- 1.4						
596	4.0+- 1.0	9.3+- 1.3						
610	4.1+- 0.8	5.5+- 1.1						
627	2.4+- 0.7	4.4+- 0.9						
647	0.3+- 0.6	3.5+- 0.8						
663	0.1+- 0.6	1.2+- 0.8						
681	-2.4+- 1.4	2.2+- 0.8						
700	-5.3+- 6.5	-0.2+- 0.7						

Table III. 4. Laboratory cross sections at 30^{o}.

LAB ANG = 44.0 CM ANG = 74.6

P	934	983	1034	1084	1134	1185	1235	1285
398	3.2+- 1.2	2.1+- 1.3	8.8+- 2.0					
403	4.4+- 1.2	3.0+- 1.4	1.7+- 1.9					
409	4.8+- 1.1	4.9+- 1.3	1.1+- 1.9					
415	6.0+- 1.1	3.8+- 1.3	2.7+- 1.9					
421	3.6+- 1.1	4.5+- 1.2	4.7+- 1.9					
428	5.5+- 1.1	4.2+- 1.2	2.4+- 1.8					
434	5.4+- 0.9	6.0+- 1.1	0.9+- 1.7					
446	6.3+- 0.9	4.7+- 1.1	1.7+- 1.3	0.2+- 2.0				
452	6.5+- 0.9	6.0+- 1.1	3.7+- 1.3	-1.2+- 2.0				
458	7.3+- 0.8	5.4+- 1.0	2.4+- 1.3	2.6+- 2.0				
465	7.4+- 0.8	5.5+- 1.0	2.8+- 1.2	1.0+- 2.0				
472	6.7+- 0.7	7.3+- 0.9	0.5+- 1.2	2.7+- 1.8				
479	6.5+- 0.7	7.4+- 0.9	3.5+- 1.2	0.4+- 1.8				
486	5.9+- 0.6	5.5+- 0.8	4.8+- 1.1	1.6+- 1.7				
498	4.6+- 0.7	5.8+- 0.8	6.3+- 1.1	2.9+- 1.1	2.0+- 1.1	1.1+- 1.1	2.8+- 1.3	-0.5+- 2.6
505	5.2+- 0.6	5.8+- 0.7	4.7+- 1.0	4.7+- 1.1	-0.1+- 1.1	3.5+- 1.1	2.4+- 1.2	6.7+- 2.8
512	2.8+- 0.6	5.1+- 0.7	6.6+- 1.0	2.9+- 1.1	2.2+- 1.0	2.4+- 1.1	1.8+- 1.2	0.7+- 2.5
520	3.0+- 0.6	6.3+- 0.7	5.8+- 0.9	4.3+- 1.0	1.0+- 1.0	2.8+- 1.0	2.3+- 1.2	-1.9+- 2.4
527	2.6+- 0.5	3.7+- 0.6	6.6+- 0.8	3.4+- 0.9	3.5+- 0.9	1.6+- 1.0	2.9+- 1.1	1.3+- 2.4
535	1.9+- 0.5	5.2+- 0.6	5.3+- 0.8	5.4+- 0.9	1.9+- 0.9	2.8+- 1.0	1.9+- 1.1	0.1+- 2.3
544	1.8+- 0.4	3.4+- 0.5	5.8+- 0.7	3.7+- 0.8	4.0+- 0.8	1.0+- 0.9	2.9+- 1.0	2.2+- 2.2
551	1.9+- 0.5	2.8+- 0.5	5.8+- 0.7	6.2+- 0.8	2.1+- 1.1	2.6+- 1.3	1.3+- 1.2	2.1+- 1.1
558	1.2+- 0.6	2.7+- 0.5	4.8+- 0.6	6.2+- 0.8	2.8+- 1.2	3.6+- 1.3	0.4+- 1.2	1.3+- 1.1
566	0.7+- 0.5	2.3+- 0.5	4.5+- 0.6	6.8+- 0.7	1.4+- 1.0	3.8+- 1.2	0.7+- 1.1	2.0+- 1.0
574	1.4+- 0.5	1.4+- 0.5	3.9+- 0.5	4.5+- 0.7	5.1+- 1.1	1.8+- 1.1	0.8+- 1.0	3.3+- 1.0
583	1.6+- 0.5	1.1+- 0.4	2.4+- 0.5	3.9+- 0.6	4.7+- 0.9	3.8+- 1.1	1.7+- 1.0	0.5+- 1.0
592	2.6+- 0.6	0.6+- 0.4	2.1+- 0.4	4.6+- 0.6	5.1+- 0.9	1.9+- 1.0	3.0+- 1.0	1.3+- 0.9
601	1.0+- 0.9	0.1+- 0.3	1.6+- 0.4	2.7+- 0.5	5.1+- 0.7	2.3+- 0.9	3.1+- 0.9	1.8+- 0.9
632				2.9+- 0.9	1.7+- 0.8	4.8+- 1.1	1.7+- 1.2	1.5+- 1.3
648				1.7+- 0.7	2.2+- 0.6	4.1+- 0.9	0.6+- 1.1	3.0+- 1.2
666				0.5+- 0.7	2.0+- 0.5	2.2+- 0.8	2.4+- 0.9	1.8+- 1.1
684				0.4+- 0.7	1.4+- 0.5	0.5+- 0.6	3.4+- 0.7	1.5+- 0.9
709						0.7+- 0.4	2.5+- 0.6	2.4+- 0.8
727						0.5+- 0.3	0.4+- 0.4	2.3+- 0.6
747						0.1+- 0.4	-0.0+- 0.4	2.4+- 0.5
767						1.0+- 1.6	0.2+- 0.3	0.4+- 0.4

Table III. 5. Laboratory cross sections at 44^{o}.

LAB ANG = 56.0 CM ANG = 90.6

K

P	934	983	1034	1084	1134	1185	1235	1285
317	1.7+- 1.3	1.4+- 1.3						
321	0.4+- 1.2	1.7+- 1.3						
326	3.1+- 1.2	1.5+- 1.3						
331	1.5+- 1.2	3.8+- 1.2						
336	1.5+- 1.2	3.0+- 1.2		0.3+- 2.5				
341	0.7+- 1.1	2.1+- 1.2		2.5+- 2.4				
346	3.7+- 1.1	0.6+- 1.2		-0.2+- 2.4				
351				3.2+- 2.3				
355	2.3+- 1.1	2.9+- 1.2	1.5+- 1.5	0.2+- 1.4	5.7+- 2.5			
360	4.2+- 1.1	2.8+- 1.2	0.3+- 1.5	2.5+- 1.2	0.5+- 2.6			
365	3.2+- 1.0	2.3+- 1.1	1.8+- 1.5	1.4+- 1.0	0.2+- 2.5			
370	3.0+- 1.0	4.1+- 1.1	1.5+- 1.4	2.9+- 1.3	4.5+- 2.4			
376	4.1+- 1.0	0.8+- 1.1	3.1+- 1.4	2.2+- 1.3	-2.5+- 2.4			
382	4.8+- 0.9	0.1+- 1.0	3.5+- 1.4	1.8+- 1.8	-4.1+- 2.2			
388	5.1+- 0.9	3.0+- 1.0	2.9+- 1.3	-0.5+- 1.2	5.3+- 2.2			
396	3.5+- 0.9	4.8+- 0.9	1.4+- 1.2	0.1+- 1.1	3.3+- 1.7	-2.7+- 2.9		
402	5.3+- 0.8	2.2+- 0.9	2.7+- 1.2	2.3+- 1.2	1.9+- 1.7	2.7+- 3.0		
408	5.4+- 0.8	2.6+- 0.8	1.8+- 1.2	3.0+- 1.1	0.4+- 1.6	0.6+- 2.8		
414	5.8+- 0.7	2.8+- 0.8	2.7+- 1.2	0.2+- 1.1	5.1+- 1.5	-3.8+- 2.8		
420	4.2+- 0.7	3.1+- 0.8	3.0+- 1.1	1.4+- 1.1	4.9+- 1.5	-2.3+- 2.7		
426	4.1+- 0.6	4.0+- 0.7	3.1+- 1.1	1.0+- 1.0	-2.3+- 1.4	4.3+- 2.5		
433	3.7+- 0.6	4.0+- 0.7	4.1+- 1.0	0.7+- 1.0	2.3+- 1.4	1.2+- 2.4		
439				1.1+- 1.6				
443	2.0+- 0.5	4.9+- 0.6	2.2+- 1.1	2.9+- 0.9	2.8+- 1.5	1.8+- 1.2	2.7+- 1.4	0.3+- 1.7
449	2.6+- 0.5	3.9+- 0.6	3.3+- 1.1	1.9+- 0.9	2.5+- 1.4	0.8+- 1.1	1.0+- 1.3	1.0+- 1.7
455	2.7+- 0.5	3.3+- 0.6	3.7+- 1.0	1.9+- 0.8	0.9+- 1.3	4.4+- 1.1	0.9+- 1.3	0.3+- 1.6
462	2.1+- 0.4	3.2+- 0.5	1.9+- 0.9	4.1+- 0.8	1.2+- 1.3	2.2+- 1.1	1.0+- 1.3	-0.4+- 1.5
469	1.7+- 0.4	3.1+- 0.5	4.3+- 0.9	3.4+- 0.8	2.4+- 1.3	1.0+- 1.0	-0.1+- 1.2	0.8+- 1.5
476	1.3+- 0.4	2.4+- 0.5	2.8+- 0.8	3.6+- 0.7	3.0+- 1.2	2.0+- 1.0	0.7+- 1.2	2.3+- 1.5
483	1.2+- 0.3	0.8+- 0.4	3.4+- 0.8	3.6+- 0.6	3.4+- 1.1	1.1+- 0.9	2.2+- 1.1	0.2+- 1.4
490						2.1+- 1.7		
496				3.4+- 0.8		1.4+- 1.7		
503				3.0+- 0.6	4.3+- 0.9	1.9+- 0.9	1.8+- 1.2	0.4+- 1.2
510				2.9+- 0.5	2.2+- 0.9	2.3+- 0.8	4.2+- 1.2	-0.8+- 1.2
517				1.9+- 0.5	2.3+- 0.9	3.3+- 0.8	-0.1+- 1.1	2.4+- 1.1
524				2.8+- 0.4	2.0+- 0.8	2.5+- 0.7	2.4+- 1.0	0.4+- 1.0
532				1.8+- 0.4	3.1+- 0.7	2.6+- 0.7	-1.2+- 1.0	1.6+- 1.0
540				1.5+- 0.5	2.6+- 0.7	2.2+- 0.7	1.1+- 0.9	0.3+- 0.9
549				1.2+- 0.4	1.1+- 0.5	3.8+- 0.5	-0.8+- 0.6	2.2+- 0.6
558				-0.0+- 0.9	1.0+- 0.9	1.9+- 0.7	2.6+- 0.9	-0.8+- 0.9
566				1.1+- 0.7	2.3+- 0.9	1.2+- 0.6	1.6+- 0.8	1.0+- 0.9
574				0.7+- 0.7	2.3+- 0.7	1.2+- 0.6	0.9+- 0.7	1.6+- 0.8
583					0.5+- 0.6	2.0+- 0.5	0.3+- 0.7	1.2+- 0.8
592					0.2+- 0.7	1.5+- 0.5	2.1+- 0.7	-0.1+- 0.7
601					0.1+- 0.5	1.3+- 0.5	0.9+- 0.6	1.1+- 0.6

Table III.6. Laboratory cross sections at 56^{o}.

LAB ANG = 84.0 CM ANG = 119.7

P	K 934	983	1034	1084	1134	1185	1235	1285
260	2.4+- 1.1	0.3+- 1.2						
263	1.2+- 1.1	2.3+- 1.2						
267	2.4+- 1.1	1.3+- 1.2						
271	3.2+- 1.0	-0.0+- 1.1						
275	1.6+- 0.9	1.7+- 1.1						
279	1.1+- 1.0	1.1+- 1.1						
284	2.0+- 0.9	1.7+- 1.0						
288	3.1+- 0.9	1.7+- 0.9	0.7+- 1.6	2.5+- 2.2				
292	2.3+- 0.8	1.5+- 0.9	-1.7+- 1.5	5.2+- 2.2				
296	1.3+- 0.8	1.5+- 0.9	0.2+- 1.5	1.8+- 2.0				
301	0.6+- 0.7	3.0+- 0.8	0.0+- 1.5	-0.8+- 1.9				
305	1.9+- 0.7	2.0+- 0.8	1.7+- 1.4	0.5+- 1.9				
310	2.4+- 0.7	1.2+- 0.8	-1.8+- 1.3	2.0+- 1.7				
315	1.8+- 0.6	2.0+- 0.7	3.8+- 1.3	-0.9+- 1.7				
320	1.3+- 0.7	2.2+- 0.7	2.9+- 1.2	1.2+- 1.4	1.3+- 1.7	-1.2+- 2.6	-0.2+- 2.1	
324	1.2+- 0.6	2.0+- 0.6	2.1+- 1.2	0.4+- 1.3	0.1+- 1.5	0.6+- 2.6	-2.1+- 2.0	
329	0.9+- 0.6	1.5+- 0.6	0.7+- 1.1	1.7+- 1.2	4.3+- 1.6	1.7+- 2.6	0.2+- 2.0	
334	0.8+- 0.5	2.0+- 0.6	2.0+- 1.0	3.1+- 1.2	-1.7+- 1.5	-3.2+- 2.5	-2.0+- 1.8	
339	0.7+- 0.5	1.3+- 0.5	2.6+- 1.0	0.9+- 1.2	1.1+- 1.4	-2.9+- 2.1	1.6+- 1.7	
344	0.4+- 0.5	1.5+- 0.5	3.3+- 0.9	2.7+- 1.2	-0.2+- 1.4	-0.3+- 2.3	3.4+- 1.8	
349	0.8+- 0.5	1.4+- 0.5	2.0+- 0.9	1.6+- 1.0	0.3+- 1.2	0.1+- 2.0	2.4+- 1.6	
355						0.5+- 1.6		
360	0.8+- 0.5	1.3+- 0.5	0.8+- 0.9	1.9+- 0.8	2.0+- 0.9	-0.9+- 1.5	2.2+- 1.0	-1.1+- 1.1
365	1.1+- 0.6	0.5+- 0.6	-0.2+- 1.0	1.7+- 0.8	0.4+- 0.8	1.4+- 1.5	-0.1+- 1.0	-0.7+- 1.1
370	1.4+- 0.6	1.0+- 0.5	0.1+- 0.9	0.8+- 0.8	2.2+- 0.8	2.6+- 1.5	0.4+- 1.0	-0.4+- 1.1
375	0.3+- 0.5	-0.1+- 0.5	1.9+- 0.8	0.9+- 0.8	1.1+- 0.8	2.1+- 1.3	-0.5+- 0.9	1.6+- 1.0
381	-0.0+- 0.5	0.7+- 0.5	0.2+- 0.8	1.2+- 0.7	1.3+- 0.8	1.3+- 1.3	1.0+- 0.9	-1.0+- 1.0
387	0.1+- 0.4	0.3+- 0.4	0.8+- 0.7	0.9+- 0.7	1.7+- 0.7	0.8+- 0.9	0.6+- 0.9	-0.1+- 1.0
393	0.4+- 0.6	0.8+- 0.4	0.1+- 0.7	0.5+- 0.6	2.4+- 0.7	0.5+- 1.3	0.8+- 0.8	1.5+- 0.9
401					1.2+- 0.9	0.7+- 1.1	1.1+- 0.8	0.9+- 0.9
406					1.7+- 0.8	2.0+- 1.1	-0.0+- 0.8	1.9+- 0.9
413					-0.2+- 0.9	0.8+- 0.8	1.0+- 0.7	0.1+- 0.8
419					-0.3+- 0.8	1.7+- 0.8	2.0+- 0.7	1.4+- 0.9
425					0.9+- 0.7	-0.4+- 0.8	0.9+- 0.7	0.7+- 0.8
430					0.7+- 0.7	1.0+- 1.2	0.4+- 0.6	1.3+- 0.8
437					0.6+- 0.6	0.3+- 1.2	0.6+- 0.6	0.9+- 0.7
443						0.3+- 1.1		
450						0.9+- 1.1		-0.8+- 0.9
457								1.6+- 0.9
463								0.3+- 0.8
470								0.9+- 0.8
477								0.4+- 0.8
484								0.7+- 0.8
492								0.8+- 0.8

Table III. 7. Laboratory cross sections at 84°.

LAB ANG = 120.0 CM ANG = 147.5

P	934	983	1034	K 1084	1134	1185	1235	1285
231				2.7+- 2.7	0.3+- 2.8	2.0+- 3.0	-1.2+- 3.2	
234				3.0+- 2.6	-4.0+- 2.5	5.0+- 2.6	-3.5+- 3.0	
238				0.5+- 2.2	1.9+- 2.3	-2.1+- 2.6	0.3+ 2.8	
241				1.7+- 2.3	-0.1+- 2.2	0.5+- 2.6	1.6+- 2.8	
245				-1.2+- 2.1	2.9+- 2.2	0.1+- 2.5	0.3+- 2.7	
249				1.4+- 1.9	-1.3+- 2.0	-0.1+- 2.5	1.7+- 2.7	
252				1.7+- 1.8	-0.2+- 1.9	1.0+- 2.1	-0.7+- 2.4	
260				2.4+- 1.7	-0.8+- 1.7	0.1+- 2.1	-1.5+- 2.4	4.5+- 2.4
263				2.2+- 1.7	-1.4+- 1.7	0.8+- 1.9	0.1+- 2.1	6.0+- 2.2
267				2.2+- 1.6	2.5+- 1.5	-1.3+- 1.9	0.9+- 2.2	2.8+- 2.5
271				-0.7+- 1.4	3.0+- 1.4	1.2+- 1.8	-1.4+- 2.2	1.6+- 2.4
275				-1.2+- 1.4	1.3+- 1.4	2.1+- 1.7	2.3+- 2.0	-1.0+- 2.1
279				-0.3+- 1.4	0.6+- 1.4	1.3+- 1.5	-0.5+- 1.8	1.4+- 2.1
284				-1.6+- 1.1	0.8+- 1.3	1.9+- 1.5	0.3+- 1.6	0.3+- 1.7
288							1.7+- 1.5	1.6+- 2.0
292							0.9+- 1.5	-2.1+- 1.8
296							0.6+- 1.4	1.2+- 1.6
301							0.4+- 1.4	-0.5+- 1.7
305							1.6+- 1.3	0.7+- 1.5
310							-0.5+- 1.3	0.4+- 1.5
315							-0.0+- 1.2	0.3+- 1.3

Table III. 8. Laboratory cross sections at 120°.

C. Center of Mass Cross Section

For purposes of interpretation it is generally convenient to express the cross section in the center of mass system. The laboratory cross section at each point could be multiplied by an appropriate kinematic factor to give the c. m. cross section at corresponding values of the c. m. kinematic variables. We chose a different approach which involved an alternative, and physically more illuminating, solution to the unfolding problem presented by equation (7) than that provided by equation (9).

Equation (7) may be rewritten in terms of the c. m. cross section. Defining the experimentally determined quantity

$$\bar{\sigma}(E_2, E_1, p_o, \theta_o) = \frac{\sigma^*(E_2, p_o, \theta_o) - \sigma^*(E_1, p_o, \theta_o)}{I(E_2, E_1, p_o, \theta_o)} ,$$

we have the following equation:

$$\bar{\sigma}(E_2, E_1, p_o, \theta_o) = \frac{1}{I(E_2, E_1, p_o, \theta_o)} \int_{k_m}^{E_2} dk\, R(k, E_1, E_2)\, J(k, p_o, \theta_o) \frac{d^2\sigma'}{dM^2 d\Omega'} \tag{10}$$

where θ' = π^- c. m. angle,

M = invariant mass of the undetected final state particles,

$\frac{d^2\sigma'}{dM^2 d\Omega'}(k, M^2, \theta')$ = c. m. cross section for π^- production per unit solid angle and per unit interval of M^2,

$J(k, p_o, \theta_o)$ = Jacobian which transforms this c. m. cross section into $\frac{d^2\sigma}{dpd\Omega}(k, p_o, \theta_o)$ in the laboratory system (see Section VI. A).

Instead of proceeding to solve equation (10) by expanding $\frac{d^2\sigma'}{dM^2 d\Omega'}$ in a power series in k as we did to obtain equation (9), we shall use an expansion in functions which have particular physical significance. We anticipate that the cross section will have a resonant shape as a function of M^2. Since M^2 is a linear function of k, this implies that the cross section will have a resonant behavior as a function of k near some value of k for each p and θ. We assume that this resonant behavior is the most rapidly varying part of the k dependence of the cross section, and choose an expansion in functions of M^2 and k which have the known resonant behavior or the behavior of a phase space background. That is, we take

$$\frac{d^2\sigma'}{dM^2 d\Omega'} = \sum_{i=1}^{n} A_i(k, \theta') \, g_i(M^2, k) \qquad (11)$$

where the g_i are functions which are discussed below. If we assume that the unknown coefficients $A_i(k, \theta')$ vary slowly with k over the region where $R(k, E_1, E_2)$ is large, equation (10) reduces to an algebraic equation:

$$\bar{\sigma}(E_2, E_1, p_o, \theta_o) = \sum_{i=1}^{n} A_i(\bar{k}, \bar{\theta}') \, F_i(E_2, E_1, p_o, \theta_o) \; . \qquad (12)$$

The functions F_i, defined by

$$F_i(E_2,E_1,p_o,\theta_o) = \frac{1}{I(E_2,E_1,p_o,\theta_o)} \int_{k_m}^{E_2} dk\, R(k,E_1,E_2)\, J(k,p_o,\theta_o)\, g_i(M^2,k)\ , \tag{13}$$

were evaluated numerically. A set of values for the A_i at a single point $(\bar{k}, \bar{\theta}')$ was then obtained by fitting the right hand side of equation (12) at fixed θ_o, E_1, and E_2 to the measured values of $\bar{\sigma}$ by the method of least squares. The values $\bar{k}$ and $\bar{\theta}'$ represent average values of the photon energy and π^- c.m. angle; for given θ_o, E_1, and E_2, we took $\bar{k}$ and $\bar{\theta}'$ to be the values obtained by averaging k_o and $\theta'(\theta_o, k_o, p_o)$ over the momenta p_o at which $\bar{\sigma}(E_2, E_1, p_o, \theta_o)$ was measured.

We must now specify the functions $g_i(M^2, k)$. The simplest model is that the most prominent dynamical features of the reaction are shown in the pseudo-two-body channels

$$\gamma + p \rightarrow \pi^- + N^*(1238)^{++} \tag{14a}$$

$$\rightarrow \pi^+ + N^*(1238)^{o} \tag{14b}$$

$$\rightarrow \rho^o + p, \tag{14c}$$

and that the M^2 dependence of any remaining contribution to the cross section can be adequately described by three-body invariant phase space for the reaction

$$\gamma + p \rightarrow \pi^- + \pi^+ + p\ . \tag{14d}$$

Rather than attempting to use a detailed model of the production mechanism to specify the M^2 dependence of reactions (14a) - (14c), we chose the phenomenological approach of using modified phase space calculations. This method has been summarized by Jackson.[28] For reaction (14a) this gives:

$$g_1(M^2, k) = N\left(\frac{p'}{4W}\right)\left[\frac{M_r}{\pi}\,\frac{\Gamma(M)}{(M_r{}^2 - M^2)^2 + M_r{}^2\,\Gamma(M)^2}\right] \qquad (15)$$

where M_r = mass of the resonance = 1238 MeV,

W = total c. m. energy,

N = normalization constant,

$\Gamma(M)$ = width of the resonance,

$p'(M^2, k)$ = π^- 3-momentum in the overall c. m. system.

The width function used was that obtained by Jackson from lowest-order perturbation theory:

$$\Gamma(M) = \Gamma_o \left(\frac{q}{q_r}\right)^3 \frac{\rho(M)}{\rho(M_r)} \qquad (16)$$

with $$\rho(M) = \frac{(M + M_p)^2 - m^2}{M^2}\,,$$

M_p = proton mass,

m = pion mass,

q = 3-momentum of the π^+ in the π^+-p c. m. system,

q_r = value of q at $M = M_r$,

Γ_o = width parameter = 123 MeV.

The normalization constant, N, was chosen arbitrarily since it could be considered part of the unknown coefficient $A_1(k, 0')$. For reaction (14d) we used the mass distribution calculated from three body invariant phase space:

$$g_2(M^2, k) = \frac{\pi}{4} \frac{p'}{W} \frac{q}{M} . \tag{17}$$

Reactions (14b) and (14c) require a modification of the calculation used to obtain g_2: a weighting factor giving the mass distribution of the N^{*o} or ρ^o is included in the integrand of the invariant phase space integral. The result in both cases may be expressed in the form

$$g(M^2, k) = \frac{\pi}{16W^2} \int_{M'^2_{min}}^{M'^2_{max}} dM'^2 \; f(M'^2) \tag{18}$$

where $f(M'^2)$ = mass distribution for the N^{*o} or ρ^o,

M'_{max} (min) = maximum (minimum) possible invariant mass of the N^{*o} or ρ^o for given M and k.

In the case of N^{*o} production, the limits on the mass are given by

$$M'^{2}_{\substack{max \\ min}} = M_p^2 + m^2 + 2(\omega'' E_p \pm p'' q) \tag{19}$$

where q, E_p = proton 3-momentum and total energy respectively in the $(\pi^+ p)$ c. m. system,

p'', ω'' = π^- 3-momentum and total energy respectively in the $(\pi^+ p)$ c. m. system;

for ρ^o production the limits are given by

$$M'^{2}_{\substack{max \\ min}} = 2m^2 + 2(\omega'' E_\pi \pm p'' q) \tag{20}$$

where E_π = π^+ total energy in the $(\pi^+ p)$ c. m. system.

Figure 7 shows the four mass distributions given above for two different photon energies, where a Breit-Wigner form has been used for $f(M^2)$, and the energy dependence of the width of this function has been ignored so that the integral in equation (18) could be evaluated in terms of elementary functions. Because the curve representing the "reflection of the ρ^o" is so similar to the nonresonant phase space curve, the ρ^o term was not included in the fitting function. This is also reasonable from a dynamical viewpoint, because bubble chamber studies have shown that ρ^o production is not the dominant part of the total cross section for k less than 1.3 GeV.[17, 19] The N^{*o} term has a much more striking mass spectrum than the ρ^o term; however, this term was also not included in the fitting function finally used. There were three reasons for this decision. In the first place, the bubble chamber

Figure 7

Missing mass distributions for the phenomenological model. $P(M^2)$ is the distribution function (normalized to unit area) for the square of the missing mass in $\gamma + p \rightarrow \pi^- + X$. The curves are for the specific models (a) $\gamma + p \rightarrow \pi^- + N^*(1238)^{++}$; (b) $\gamma + p \rightarrow \pi^- + \pi^+ + p$ (nonresonant); (c) $\gamma + p \rightarrow \pi^+ + N^*(1238)^o$; (d) $\gamma + p \rightarrow \rho^o + p$. Curve (d) is not shown at k = 900 MeV because this is below threshold for ρ^o production.

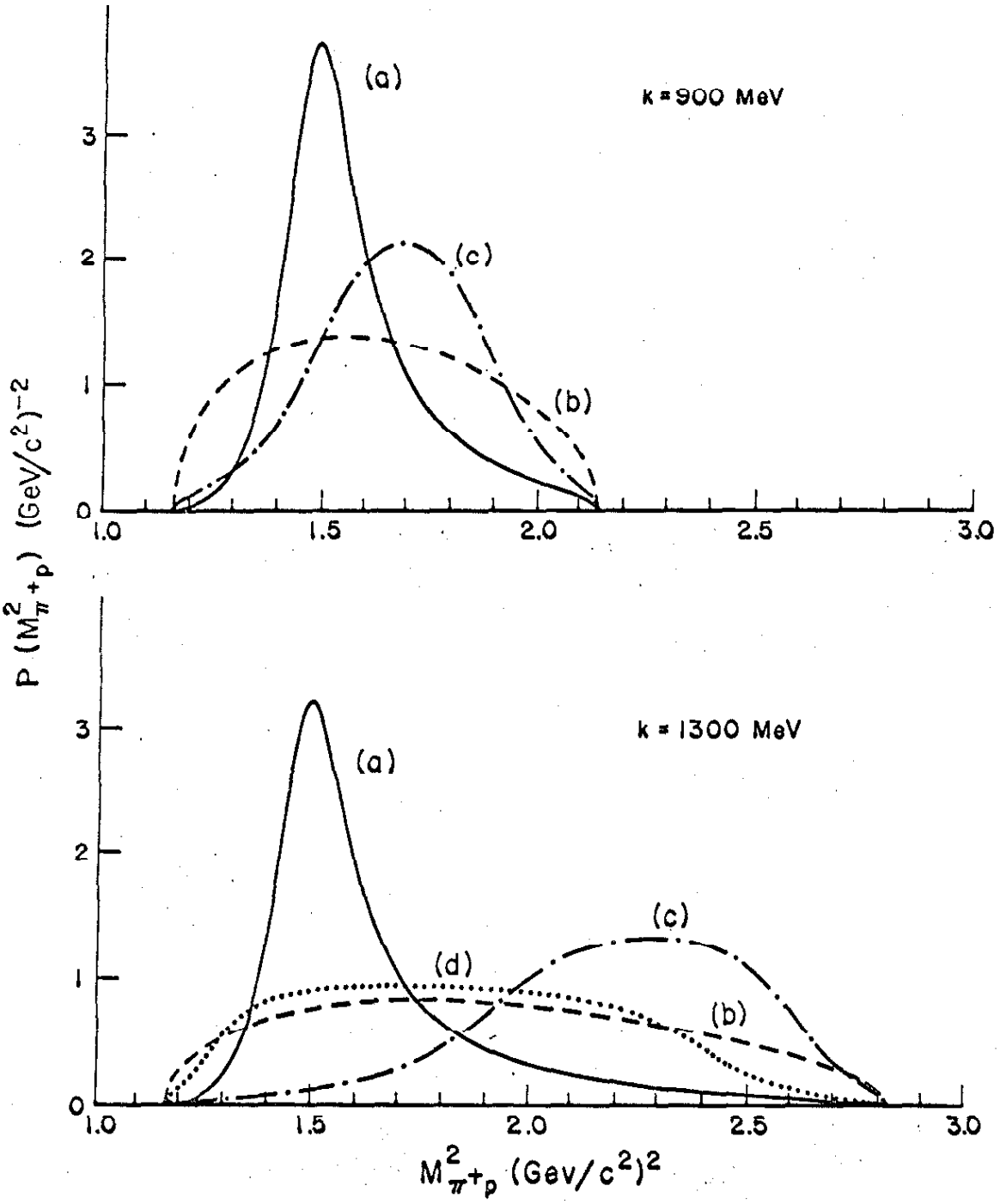
k = 900 MeV
(a)
(b)
(c)
k = 1300 MeV
(a)
(b)
(c)
(d)
P (M²π+p) (GeV/c²)⁻²
M²π+p (Gev/c²)²
0
1
2
3
1.0
1.5
2.0
2.5
3.0

Figure 7.

studies of the π^--p mass distribution in this reaction showed no significant enhancement in the $N^*(1238)^o$ region. In the second place, the N^{*o} term produces a peak in the π^+-p mass distribution close to the maximum kinematically allowed π^+-p mass, whereas our measurements were made within 250 MeV/c^2 of the minimum possible mass. This means that for $k \gtrsim 1$ GeV, the N^{*o} term peaks well above the maximum mass for which the cross section was measured, and is fairly uninteresting over the measured range. Finally, the data at $k_o = .934$ GeV, where this term seems most likely to contribute, were fitted with an expansion including the N^{*o} term; its coefficient was consistent with zero at each angle measured.

Thus, the final fits were made using only two terms in equation (12): the N^{*++} term given in equation (15) and the nonresonant phase space term given in equation (17). The upper smooth curve shown in each plot of Figure 6 is the sum of these two terms as determined by the fit. The lower smooth curve in each plot is the nonresonant phase space term alone. In the few cases where only one curve appears, the coefficient of one of the terms vanished.

In order to present the results of the fits in a meaningful way, we define c.m. angular distributions as follows:

$$\sigma_{\substack{R \\ NR}}(k,\theta') = \int_{M^2_{min}}^{M^2_{max}} dM^2 \left(\frac{d^2\sigma'}{dM^2 d\Omega'}\right)_{\substack{R \\ NR}} \tag{21}$$

where $\left(\frac{d^2\sigma'}{dM^2 d\Omega'}\right)_R$ = term in equation (11) from N^{*++} production,

$\left(\frac{d^2\sigma'}{dM^2 d\Omega'}\right)_{NR}$ = term in equation (11) from three body phase space.

$M_{max} = (W - m)$ and $M_{min} = (M_p + m)$ are respectively the maximum and minimum possible values of M. These angular distributions are easily evaluated, once the fitting parameters $A_i(k,\theta')$ have been determined, from the relation

$$\sigma_i(k,\theta') = A_i(k,\theta')\,\rho_i(k) \quad . \tag{22}$$

The functions $\rho_i(k)$, defined by

$$\rho_i(k) = \int_{M^2_{min}}^{M^2_{max}} dM^2\, g_i(M^2,k) \quad , \tag{23}$$

were evaluated numerically and tabulated once for use in analysis of all of the data. Since we know a priori that each of the $\sigma_i(k,\theta')$ should be positive, this constraint was placed upon the fit which determined the A_i. The method used to impose this constraint is described in Section VI. F. Actually, the unconstrained fits gave positive coefficients at all but a few points.

The angular distributions obtained in this way are plotted in Figure 8 and listed in Table IV. The angular distribution denoted by σ_C is the sum of the other two terms:

$$\sigma_C(k,\theta') = \sigma_R(k,\theta') + \sigma_{NR}(k,\theta') \quad . \tag{24}$$

Figure 8

Center of mass angular distributions of negative pions for all charged pion pair (x) and $N^*(1238)^{++}$ (o) photoproduction. The solid curves are Moravcsik fits to the corresponding sets of data. The dot-dash curve is from the Drell model, and the dotted curve is from the Stichel-Scholz calculation.

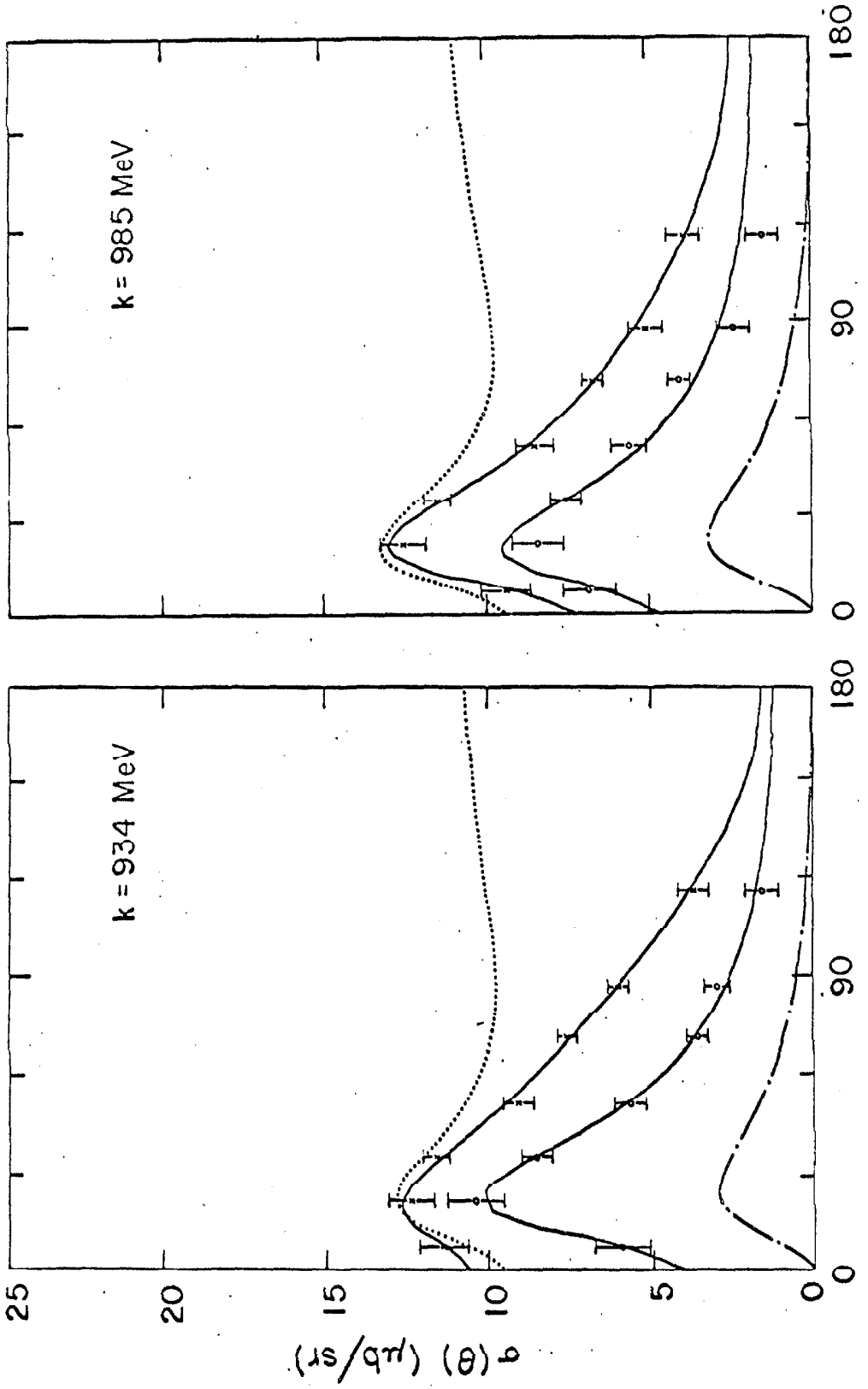

Figure 8.1. Center of mass angular distributions.

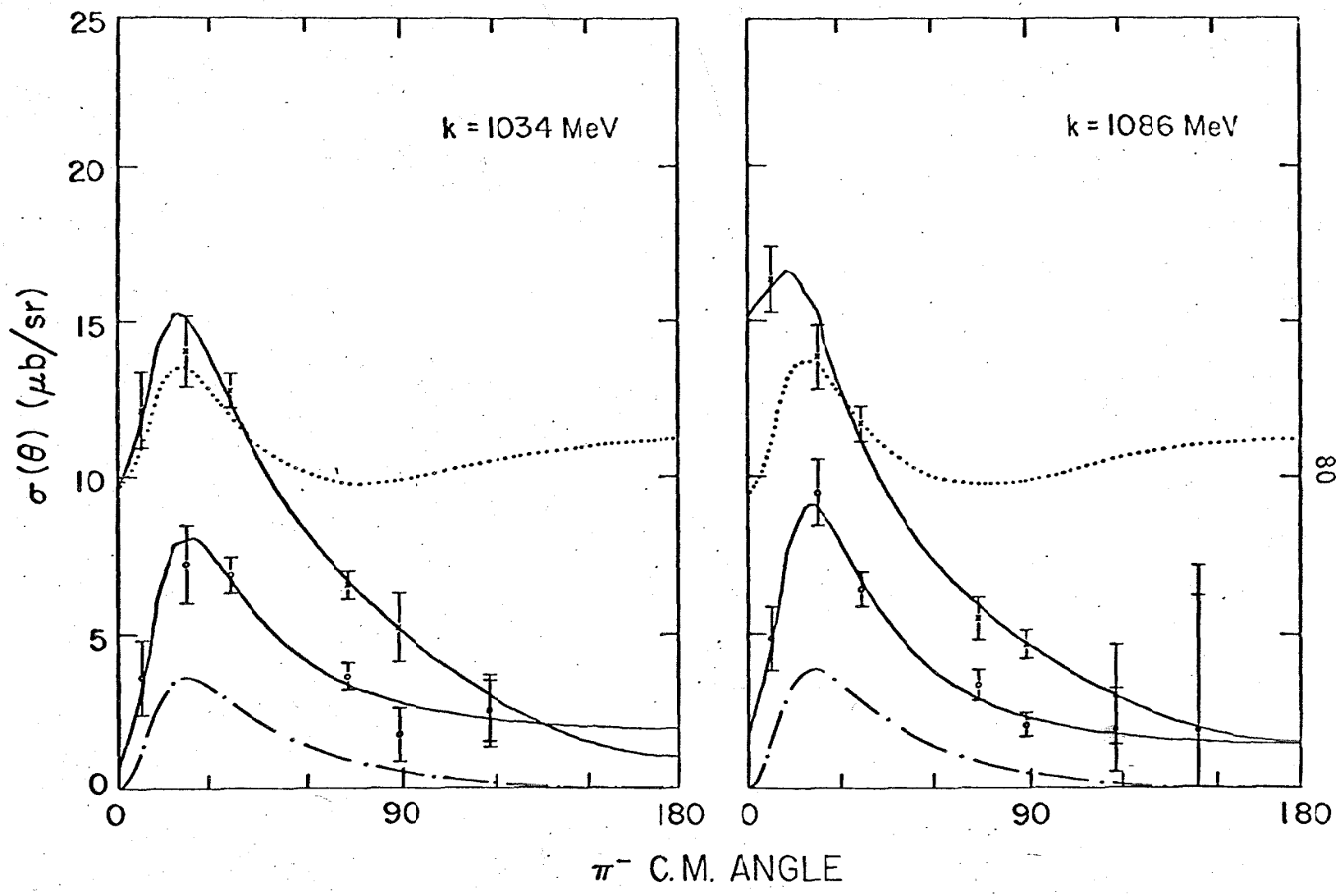

Figure 8.2. Center of mass angular distributions.

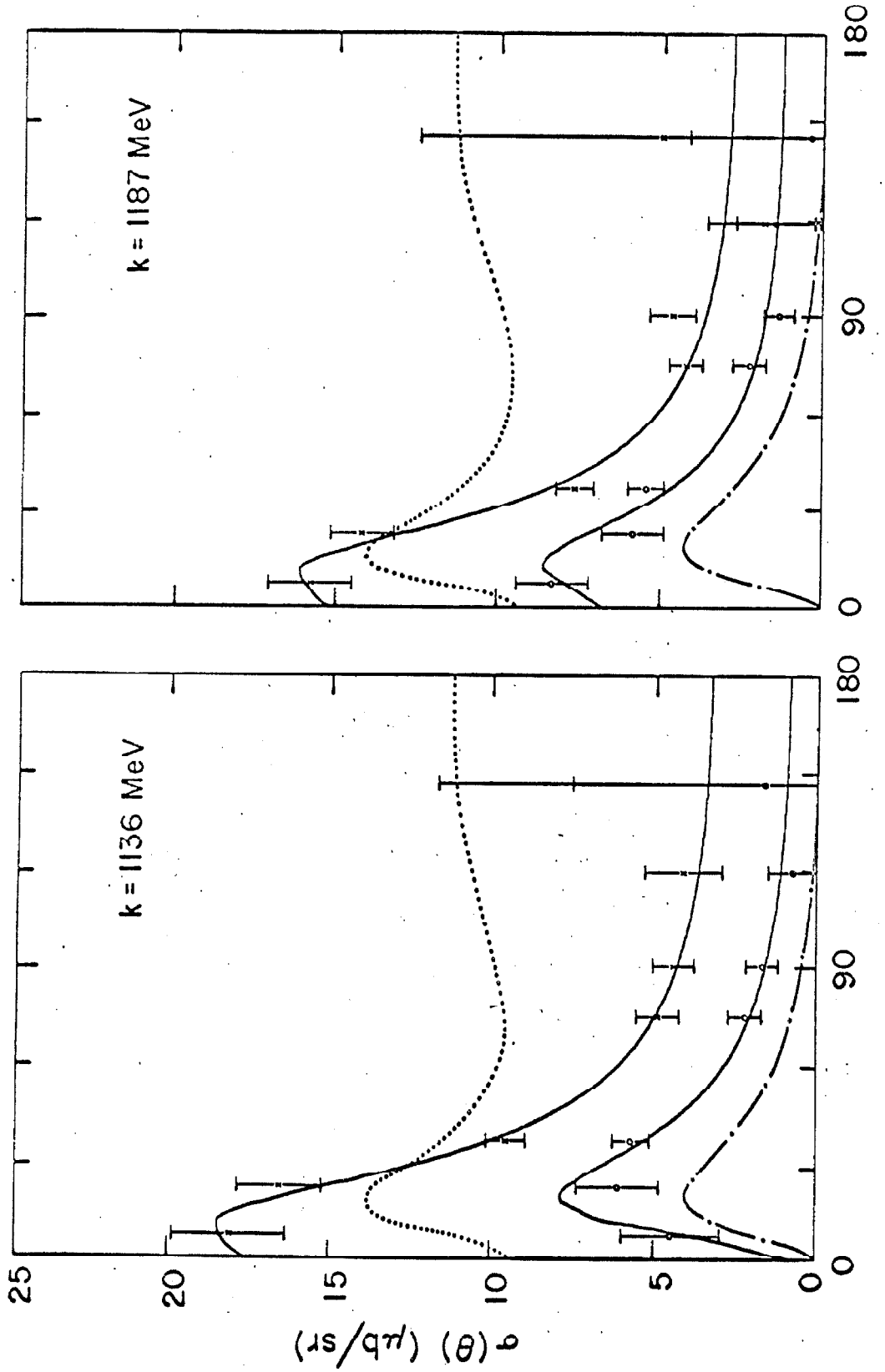

Figure 8.3. Center of mass angular distributions.

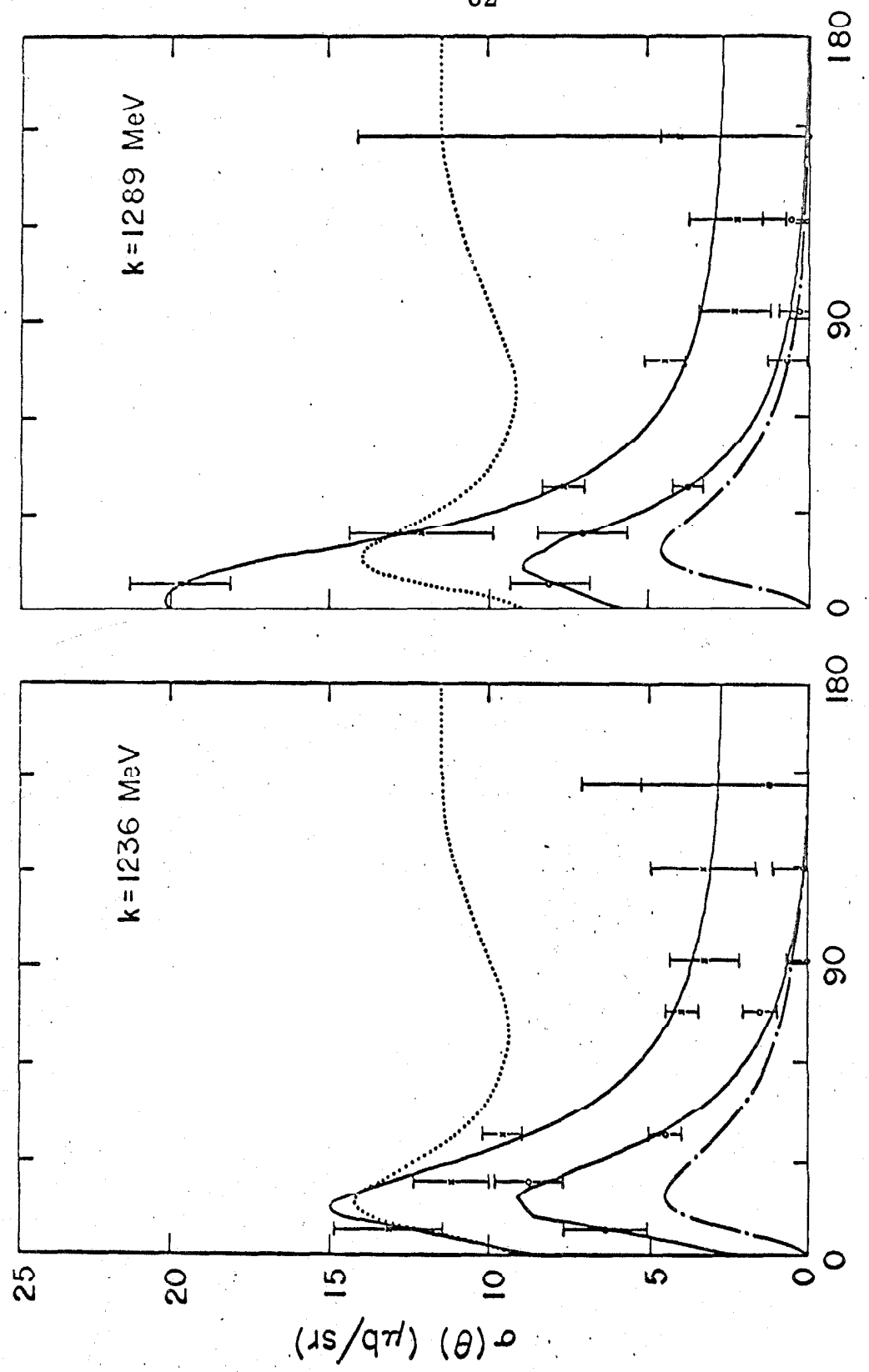

Figure 8.4. Center of mass angular distributions.

TABLE IV

Center of Mass Angular Distributions

K is the photon lab energy (MeV)

CM ANG is the π^- c. m. angle (degrees)

LAB ANG is the π^- lab angle (degrees).

σ_{NR}, σ_R, and σ_C are the differential cross sections defined in the text in units of μb/sr.

K	CM ANG	σ_{NR}	σ_R	σ_C
LAB ANG = 4.0				
936	7.1	5.5+- 1.3	5.9+- 0.8	11.4+- 0.8
985	7.2	2.6+- 1.3	6.8+- 0.8	9.4+- 0.8
1034	7.3	8.7+- 2.2	3.6+- 1.2	12.2+- 1.2
1086	7.4	11.7+- 1.7	4.8+- 1.0	16.5+- 1.1
1136	7.5	13.8+- 3.0	4.5+- 1.5	18.3+- 1.8
1187	7.7	7.6+- 2.0	8.3+- 1.1	15.9+- 1.3
1236	7.8	6.9+- 2.7	6.4+- 1.3	13.2+- 1.7
1289	7.9	11.8+- 2.4	8.2+- 1.3	19.9+- 1.6
LAB ANG = 12.0				
935	21.2	2.0+- 1.2	10.5+- 0.9	12.4+- 0.7
983	21.6	4.2+- 1.2	8.5+- 0.8	12.7+- 0.7
1034	21.9	6.9+- 2.0	7.2+- 1.2	14.1+- 1.2
1086	22.1	4.4+- 1.7	9.5+- 1.1	13.9+- 1.1
1135	22.5	10.6+- 2.2	6.1+- 1.3	16.7+- 1.3
1188	22.8	8.5+- 1.5	5.8+- 0.9	14.3+- 1.0
1236	23.1	2.5+- 1.9	8.8+- 1.1	11.3+- 1.2
1287	23.4	5.1+- 3.5	7.1+- 1.4	12.2+- 2.3
LAB ANG = 20.0				
936	34.8	3.1+- 0.6	8.6+- 0.5	11.7+- 0.4
984	35.4	4.0+- 0.6	7.6+- 0.5	11.6+- 0.4
1036	35.8	6.0+- 0.9	6.8+- 0.6	12.8+- 0.6
1086	36.3	5.4+- 0.9	6.4+- 0.6	11.8+- 0.6
1139	36.8	3.9+- 0.9	5.7+- 0.6	9.6+- 0.6
1187	37.3	2.2+- 0.9	5.4+- 0.5	7.6+- 0.6
1239	37.8	5.1+- 1.0	4.5+- 0.5	9.6+- 0.6
1289	38.3	3.9+- 1.0	3.8+- 0.5	7.7+- 0.7
LAB ANG = 30.0				
935	51.1	3.5+- 0.8	5.6+- 0.5	9.1+- 0.5
984	51.8	2.9+- 1.0	5.6+- 0.5	8.6+- 0.6

K	CM ANG	σ_{NR}	σ_R	σ_C
LAB ANG = 44.0				
934	71.6	4.0+- 0.5	3.5+- 0.3	7.6+- 0.3
983	72.6	2.7+- 0.5	4.1+- 0.3	6.7+- 0.3
1033	73.6	2.9+- 0.8	3.6+- 0.4	6.5+- 0.4
1085	74.2	2.1+- 1.1	3.3+- 0.5	5.4+- 0.7
1135	75.0	2.7+- 1.1	2.2+- 0.5	4.9+- 0.7
1188	75.8	2.0+- 0.8	2.2+- 0.5	4.2+- 0.5
1236	76.6	2.4+- 0.8	1.5+- 0.5	3.9+- 0.5
1285	77.4	3.9+- 1.1	0.7+- 0.6	4.5+- 0.6
LAB ANG = 56.0				
932	87.6	3.1+- 0.6	2.9+- 0.4	6.0+- 0.3
981	88.7	2.7+- 0.9	2.4+- 0.5	5.1+- 0.5
1032	89.5	3.5+- 1.9	1.7+- 0.9	5.2+- 1.1
1082	90.2	2.6+- 0.8	2.0+- 0.4	4.6+- 0.4
1133	91.0	2.8+- 1.0	1.7+- 0.5	4.4+- 0.6
1184	91.7	3.3+- 1.1	1.3+- 0.5	4.6+- 0.7
1234	92.5	3.2+- 1.6	0. +- 0.6	3.2+- 1.1
1283	93.3	2.0+- 1.7	0.3+- 0.6	2.3+- 1.1
LAB ANG = 84.0				
932	117.2	2.1+- 0.8	1.5+- 0.5	3.7+- 0.5
982	118.1	2.4+- 0.9	1.5+- 0.5	3.9+- 0.5
1033	118.7	0. +- 2.0	2.5+- 1.0	2.5+- 1.2
1082	119.5	1.1+- 2.8	1.8+- 1.3	3.0+- 1.6
1135	120.0	3.4+- 1.8	0.7+- 0.8	4.1+- 1.2
1184	120.7	0.4+- 2.8	1.5+- 1.2	1.8+- 1.7
1233	121.5	3.1+- 2.5	0.1+- 0.9	3.3+- 1.6
1287	121.9	1.7+- 2.3	0.6+- 0.9	2.2+- 1.5
LAB ANG = 120.0				
1082	146.6	0. +- 9.3	1.9+- 4.3	1.9+- 5.3
1131	147.1	0. +-16.0	1.6+- 6.0	1.6+-10.2
1180	147.6	4.6+-11.1	0.4+- 3.7	5.0+- 7.6
1230	147.9	0. +- 9.7	1.2+- 4.0	1.2+- 5.9
1283	148.3	4.1+-14.7	0. +- 4.7	4.1+-10.2

Table IV. Center of mass angular distributions.

Because the values of σ_R and σ_{NR} were correlated, the complete error matrix obtained in the least squares fit for the parameters $A_i(k,\theta')$ had to be used to evaluate the error in σ_C. The upper set of points in each plot of Figure 8 is σ_C, and the lower set of points gives the resonant term σ_R, corresponding to $N^*(1238)^{++}$ production only.

D. Total Cross Section

The total cross section for π^- production can be evaluated in the standard manner:

$$\sigma(k) = \int d\Omega' \, \sigma(k,\theta') \quad . \tag{25}$$

We obtain both the contribution of the N^{*++} and the complete total cross section by using $\sigma_R(k,\theta')$ and $\sigma_C(k,\theta')$ respectively in the integrand. In order to carry out the integral, smooth curves can be fitted to the angular distributions and then integrated. Since the OPE diagram (Figure 1) is expected to give an important contribution to the cross section, we follow Moravcsik's suggestion[29] and perform a fit in the following manner:

$$(1 - \bar{\beta} \cos\theta')^2 \, \sigma(k,\theta') = \sum_{i=0}^{n} B_i(\cos\theta')^i \quad . \tag{26}$$

The π^- velocity, $\bar{\beta}$, can be taken equal to the π^- c.m. velocity for which the missing mass is equal to 1238 MeV/c^2. This expansion

has two nice features: the data are fitted well with a low value of $\underline{n}$, and the total cross section can be evaluated analytically in terms of the coefficients B_i and elementary functions of $\bar{\beta}$.

Figure 9 shows the total cross sections obtained in this manner. In order to constrain the fitted curves to be well-behaved at backward angles, fake data points were inserted at c.m. angles of 150° and 180°. The value of the cross section at these points was taken equal to the measured value at 120° and the error bars were made large enough to overlap zero. This approach seemed justified since the bubble chamber studies showed the differential cross section to be quite flat for backward π^- angles from .85 to 1.5 GeV.[17] With this procedure, both the resonant and complete total cross sections were generally independent of the order of the fit for $n \geq 3$. The smooth curves in Figure 8 are the fitted curves used to obtain the total cross sections. These cross sections and the parameters B_i are also listed in Table V.

A number of comments should be made regarding these total cross sections. They are to some extent model dependent, since the quantities $\sigma_R(k,\theta')$ and $\sigma_{NR}(k,\theta')$ are model dependent. More precisely, $\sigma_R(k,\theta')$ and $\sigma_{NR}(k,\theta')$ were obtained by integration over some missing mass values where no measurements were made (see equation (21)). Only the shape of our phenomenological phase space model determined the cross section for such values of missing mass. The fraction of the complete total cross section which came from the missing mass range covered by the measurements varied smoothly from about 3/4 at the lowest energy to about 1/2 at the highest energy (see Section VI.D.6). The fractions for the N^* term alone were 7/8 and 3/4 at the same energies.

Figure 9

Total cross sections for $\gamma + p \rightarrow \pi^- + N^*(1238)^{++}$ and $\gamma + p \rightarrow \pi^- + \pi^+ + p$. The symbols indicate the source of the data:

X - this experiment

S - Stanford data[18]

C - CEA data[17]

D - DESY data[19, 34] .

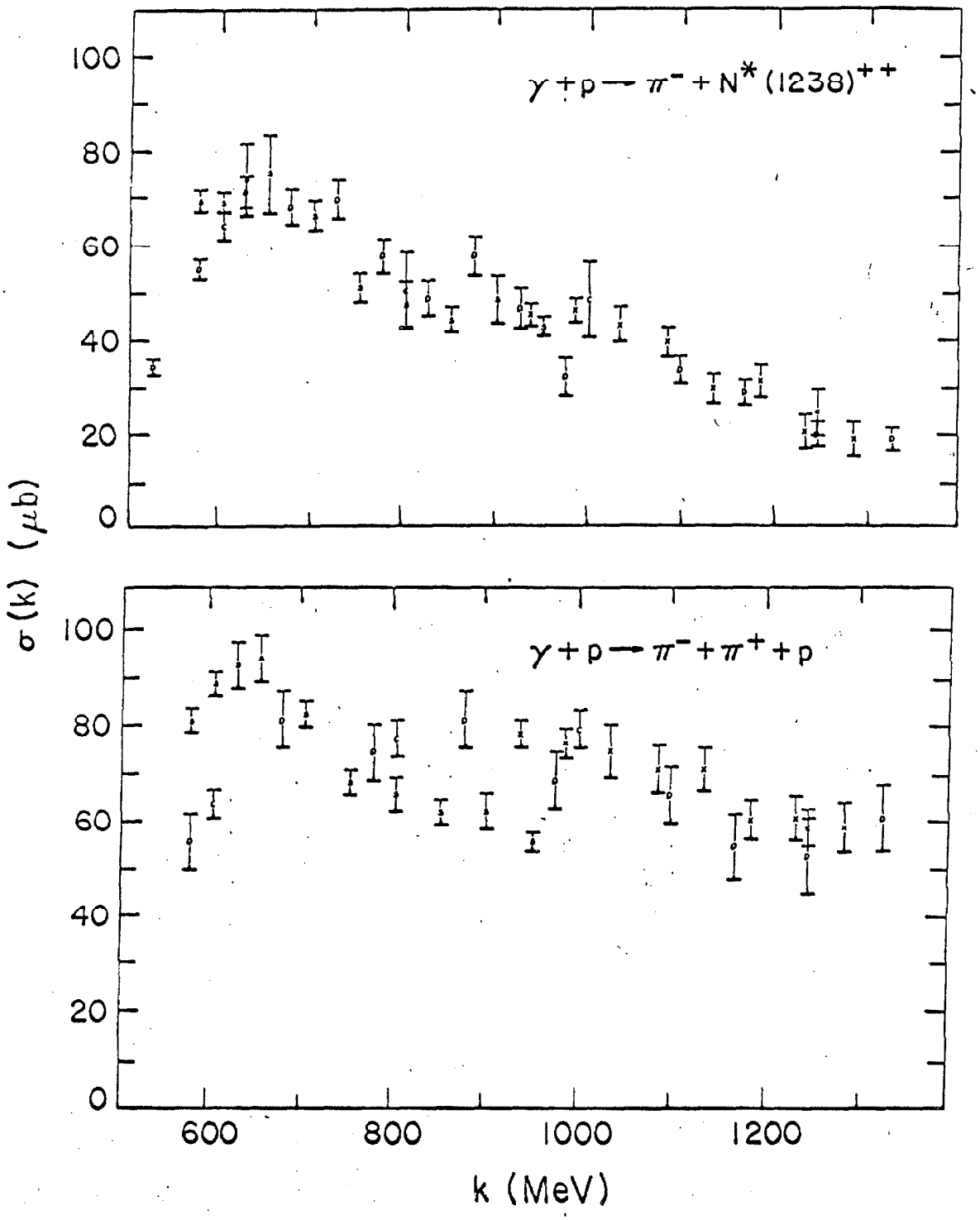

Figure 9. Total cross sections.

TABLE V

Moravcsik Coefficients and Total Cross Sections for
$\gamma + p \rightarrow \pi^- + N^*$ (σ_R) and $\gamma + p \rightarrow \pi^- + \pi^+ + p$ (σ_C)

		Moravcsik Coefficients		Total Cross Sections	
k(MeV)	Coeff.	σ_R(μb/sr)	σ_C(μb/sr)	σ_R(μb)	σ_C(μb)
934	B_0	2.58 ± .23	5.83 ± .21	45.0 ± 2.4	78.9 ± 2.9
	B_1	-2.25 ± .55	-5.94 ± .80		
	B_2	-0.30 ± .34	-2.87 ± 1.40		
	B_3		3.06 ± .76		
985	B_0	2.80 ± .24	5.36 ± .25	45.9 ± 2.5	76.9 ± 3.3
	B_1	-3.32 ± .56	-6.24 ± .89		
	B_2	0.55 ± .34	-0.70 ± 1.50		
	B_3		1.62 ± .80		
1034	B_0	2.74 ± .36	5.09 ± .42	42.9 ± 3.8	75.3 ± 5.7
	B_1	-3.56 ± .82	-4.56 ± 1.57		
	B_2	0.82 ± .48	-3.17 ± 2.54		
	B_3		2.69 ± 1.31		
1086	B_0	2.29 ± .29	4.67 ± .36	39.1 ± 3.2	71.5 ± 5.0
	B_1	-2.65 ± .67	-4.81 ± 1.47		
	B_2	0.37 ± .40	-1.86 ± 2.69		
	B_3		2.06 ± 1.44		
1136	B_0	1.59 ± .26	4.33 ± .42	29.2 ± 3.0	71.4 ± 4.5
	B_1	-1.63 ± .59	-6.23 ± .96		
	B_2	0.04 ± .35	1.95 ± .55		

TABLE V (cont.)

		Moravcsik Coefficients		Total Cross Sections	
k(MeV)	Coeff.	σ_R(μb/sr)	σ_C(μb/sr)	σ_R(μb)	σ_C(μb)
1187	B_0	1.77 ± .32	3.65 ± .39	30.8 ± 3.5	60.6 ± 4.2
	B_1	-2.35 ± .71	-5.30 ± .88		
	B_2	0.60 ± .41	1.69 ± .50		
1236	B_0	0.66 ± .32	3.69 ± .45	19.9 ± 3.5	61.1 ± 4.8
	B_1	0.20 ± .71	-5.26 ± 1.02		
	B_2	-0.86 ± .41	1.59 ± .58		
1289	B_0	0.65 ± .33	3.49 ± .50	18.2 ± 3.5	59.1 ± 5.2
	B_1	-0.14 ± .74	-5.24 ± 1.15		
	B_2	-0.50 ± .43	1.78 ± .67		

In addition, all negative pions detected have been included in these cross sections. It was shown in Section II. A. that several reactions which produce three pions, in particular (2c) and (2d), could produce negative pions which would be included in our results. The total cross section for these reactions has been measured by the bubble chamber groups.[17, 19] The contribution of these reactions to our total cross section was estimated, assuming that the π^- is produced isotropically in the c. m. system and that the missing mass distribution is described adequately by phase space at our energies (see Section VI. D. 6). The result of these considerations was that reactions (2c) and (2d) combined contributed about 1 μb to our total cross section at all energies. Because this is so small compared to other uncertainties in our total cross section, no correction was made for contamination from three pion production.

E. Error Summary

In this section we simply summarize the factors affecting the precision and accuracy of the measurements. These factors are discussed in detail in the Appendices. The dominant source of random error in our results was counting statistics: although the yield per equivalent quantum was generally measured with 5-10% error per channel of the spectrometer, the bremsstrahlung subtraction amplified this by a sizeable factor. Other sources of random error, such as beam monitoring and the energy stability of the synchrotron, contributed about a 1. 4% error in the yield, which was included in quadrature with the counting error in all results shown.

The remaining sources of error, which have been classified as systematic since they presumably do not vary from point to point, are tabulated below along with an estimate of their magnitude:

Decay correction	1%	
Nuclear scattering correction	3-4%	
Absolute quantameter calibration	3%	
Counter and electronic efficiency	2%	
Net hydrogen density	1%	
Shape of bremsstrahlung spectrum	2%	
Electron contamination (600 MeV/c spectrometer only)	2%	(30°, 44°)
	5%	(56°, 84°, 120°)
Internal inconsistency of data (1200 MeV/c spectrometer only)	4%	
Contamination from three pion production	2%	

If these errors are added in quadrature, we obtain an estimated normalization accuracy for our measurements of 7%.

IV. DISCUSSION OF RESULTS

A. Comparison with Other Experiments

The data presented in the previous sections show clearly the strong influence exerted by the pseudo-two-body channel

$$\gamma + p \rightarrow \pi^- + N^*(1238)^{++}$$

on photoproduction of charged pion pairs from 0.9 to 1.3 GeV. This is perhaps most evident in the π^- momentum spectra of Figure 6. The difference between the smooth curves shown in this figure is the contribution of the N^*: in general, it is most prominent at small angles, and decreases in relative magnitude at a fixed angle as the energy increases.

The phenomenological model used to fit these spectra is seen to represent the data well at all angles and energies. It should be kept in mind that the position and width of the resonance were not adjustable parameters in the fit. Although the peak in the resonance curve occurs at 1222 MeV, a lower mass than the 1238 MeV used for the "energy of the N^*" because of the energy dependence of the width (equation (16)), the location of the peak in the data generally coincides closely with that of the fitting function. Such differences between the location of a resonant peak in a production reaction and the theoretical parameters of the resonance are a common occurrence.[28]

In order to compare our results with previous work, the total cross sections obtained in other recent experiments have also been plotted in Figure 9. Both the complete total cross section for pion pair production and the total cross section for $N^*(1238)$ production

determined in this experiment are in good agreement with the CEA and DESY bubble chamber data. This agreement suggests that the model we used to extrapolate our measurements over the unobserved, but kinematically allowed, missing mass range did not introduce serious errors.

There seems to be substantial agreement between our results and the Stanford results for the resonant part of the total cross section, but there is significant disagreement on the complete total cross section. Although their experimental method was essentially identical to ours, they analyzed their data in a different manner. Their approach, in which they fit the yield at fixed momentum as a function of synchrotron energy, required that they make an arbitrary choice for the normalization of the nonresonant part of the cross section. The nonresonant fraction of the cross section increases as k increases; one would therefore expect a normalization error to affect their cross section most at the highest k they observed, which is just where our experiments overlap. Since the DESY and CEA results are closer to ours in this region, we are inclined to believe that the Stanford group underestimated the nonresonant part of the cross section. This interpretation is consistent with the fact that our experiments get the same result for the N^* total cross section, since there was no arbitrariness in their normalization of the N^* term.

When we look only at our total cross section values, we see a smooth decrease as k increases, with no evidence of structure around 1.05 GeV, where the $N^*(1688)$ shows up in single pion photoproduction. However, in a more speculative vein, if we take our data and the Stanford data for the N^* total cross section at face value, there is a definite bump, or at least a shoulder, at a slightly lower energy.

Going a step further, if we assume that the Stanford determination of the complete total cross section is systematically low from about 0.8 to 0.95 GeV, there may be a corresponding bump in the complete cross section for two pion production. Believing that it is risky to engage in phrenology on the results of a single experiment, and foolhardy to try it on the contact point of two experiments, we have not attempted a detailed analysis of these possible bumps. It is clear that a single, good resolution experiment including the range from 0.8 to 1.1 GeV is needed to settle the question of whether or not there is structure in the total cross section attributable to the presence of the $N^*(1688)$.

B. Comparison with Theoretical Models

We turn now to comparison of our results with predictions of the Drell, or one pion exchange, model. If we evaluate the contribution of the lower vertex in Figure 1 in the limit where the exchanged pion is on the mass shell, we obtain the following invariant cross section:

$$\frac{d^2\sigma}{dM^2dt} = \left(\frac{2\alpha}{\pi}\right) \frac{Mq}{(W^2-M_p^2)^2} \frac{1}{(t-m^2)^2} \left[\frac{1}{2} \sum_{\lambda} |\underline{\epsilon}^{\lambda} \cdot \underline{p}|^2\right] \sigma_{\pi p}(M) \qquad (27)$$

where α = fine structure constant,

$t = (\underline{p} - \underline{k})^2$,

$\underline{\epsilon}^{\lambda}$ = polarization 4-vector of the photon,

$\underline{p}, \underline{k}$ = 4-momenta of the π^- and photon respectively,

$\sigma_{\pi p}(M)$ = total cross section for π-p scattering at a π-p c.m. energy of M.

If we choose the Coulomb gauge, and use one of the relations

$$\frac{d^2\sigma'}{d\omega' d\Omega'} = \left(\frac{W^2 - M_p^2}{\pi}\right) p' \frac{d^2\sigma}{dM^2 dt} \tag{28a}$$

$$\frac{d^2\sigma}{d\omega d\Omega} = \left(\frac{W^2 - M_p^2}{\pi}\right) p \frac{d^2\sigma}{dM^2 dt} \tag{28b}$$

we can evaluate the cross section either in the c.m. (denoted by primes) or laboratory systems. In particular, in the c.m. system we obtain

$$\frac{d^2\sigma'}{d\omega' d\Omega'} = \left\{\frac{\alpha}{8\pi^2} \frac{\omega'(k' - \omega')}{k'^3} \left(\frac{\sin\theta'}{1 - \beta'\cos\theta'}\right)^2 \sigma_{\pi p}(M)\right\} \left[\frac{\beta'^3 Mq}{W(k' - \omega')}\right] \tag{29}$$

where β' = π^- c.m. velocity,

k' = photon energy in the c.m. system.

The factor in braces is exactly the result given by Drell, and the factor in square brackets is a kinematic factor of order unity which he ignored for the purposes of his argument. Thiebaux[30] added a correction factor to equation (29) based upon an approximate expression

for the off-shell pion-nucleon scattering amplitude obtained by Ferrari and Selleri.[31] Because this factor included the additional uncertainty of a pionic form factor, and because including it would not appreciably alter our conclusions regarding the Drell model, we have chosen to use equation (29) as it stands.

We are interested in equation (29) for M values near threshold, where $\sigma_{\pi p}(M)$ is dominated by scattering in the I = 3/2, J = 3/2 state. Since $\sigma_{\pi^+ p \to \pi^+ p} / \sigma_{\pi^- p \to \pi^- p} = 9$ for scattering in a pure I = 3/2 state, this model predicts a 9:1 ratio for $N^*(1238)^{++}$ production relative to production of the $N^*(1238)^0$ followed by decay into the $(\pi^- p)$ charge state. This is consistent with our finding that the "reflection of the N^{*0}" term was not needed to fit the missing mass spectra. Stronger evidence for the absence of N^{*0} production was obtained in the bubble chamber studies,[17] where the $(\pi^- p)$ mass distribution was directly observed. It should be noted that this prediction is not unique to the OPE model; the same conclusion is reached if one supposes the reaction to occur in an I = 1/2 state. From this point on, we shall consider only the OPE diagram in which the π^- is produced at the electromagnetic vertex.

The π^- momentum spectrum given by equations (27) and (28b) is compared with one of our experimental spectra at a point where the N^* is dominant in Figure 10. The bremsstrahlung spectrum has been folded into the theoretical cross section. As Kilner, Diebold and Walker observed,[11] the qualitative shape of the Drell cross section resembles the data very closely, but quantitatively it is too small.

One of the most characteristic features of the OPE model is the angular distribution of the π^-. If equation (29) is integrated over

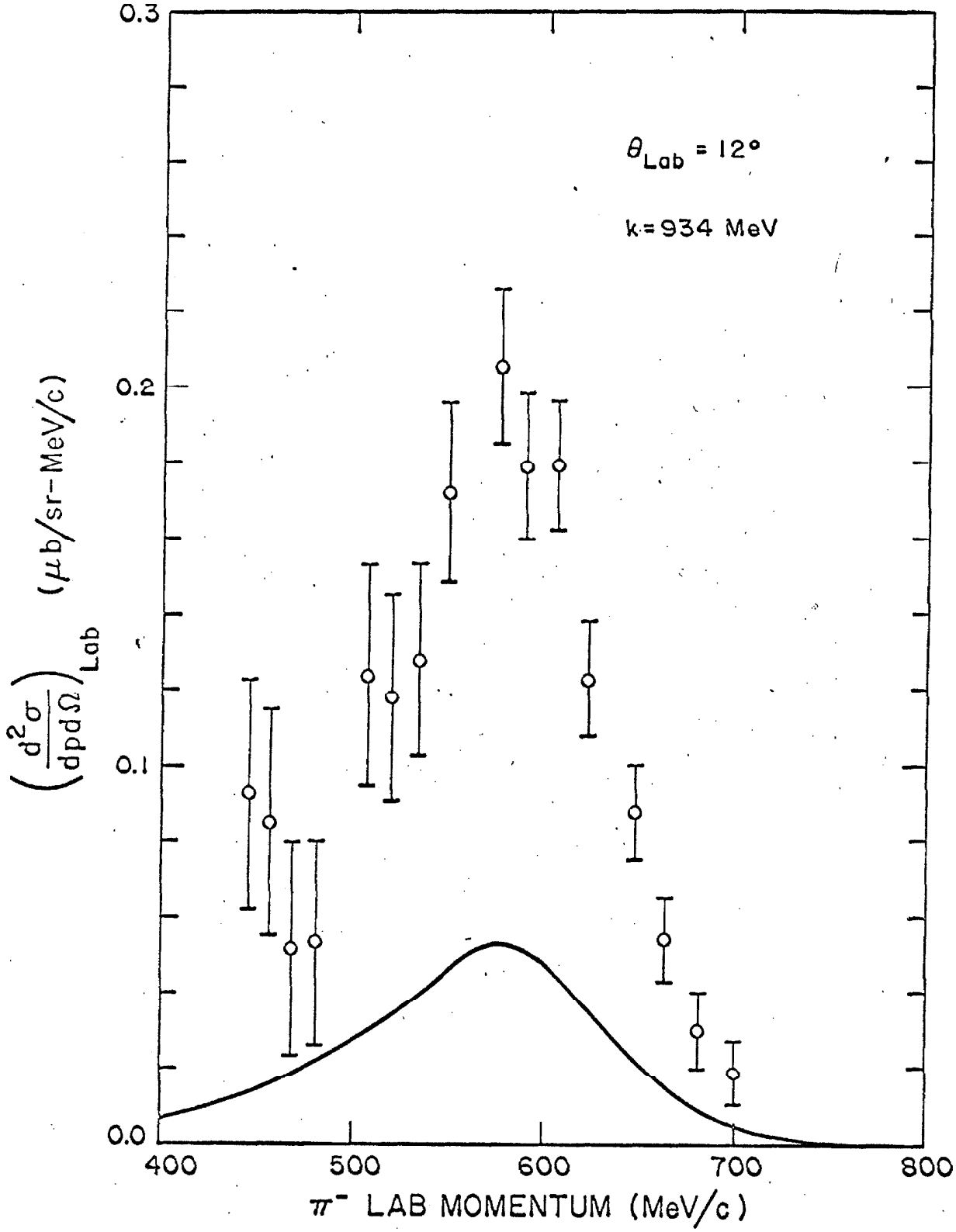

Figure 10. Comparison of a typical π^- momentum spectrum with the spectrum calculated from the Drell model.

π^- energy, the angular distribution obtained is dominated by the function $\sin^2\theta'/(1 - \bar{\beta}\cos\theta')^2$, where $\bar{\beta}$ can be taken as the π^- velocity for production of an N^* of mass 1238 MeV/c^2. This function is a maximum for $\theta' \approx m/\bar{p}$, where $\bar{p}$ is the π^- momentum corresponding to $\bar{\beta}$. The angle for the maximum is about 25° at k = .9 GeV and 17° at k = 1.3 GeV. The cross section vanishes at 0° and drops rapidly toward zero for $\theta' > m/\bar{p}$.

The c.m. angular distributions calculated from equation (29) are shown with the data in Figure 8. We see that the shape of the Drell curve is virtually the same as the behavior of the data, particularly the N^* part. The N^* data show the decrease in cross section predicted for $\theta' < m/\bar{p}$, as well as the rapid decrease at larger angles. That the Drell curve has the same shape as the N^* data at small angles can also be seen from the Moravcsik coefficients of Table V. These coefficients, determined largely by the small angle behavior, show that $\sigma_R(k,\theta')$ has essentially the shape

$$\sigma_R \propto \frac{1 - x}{(1 - \bar{\beta}x)^2}$$

$$\cong \frac{1}{2}\,\frac{(1 - x^2)}{(1 - \bar{\beta}x)^2} \qquad \text{for } x \cong 1$$

where $x = \cos\theta'$. Thus, at small angles the Moravcsik fit to the N^* data has nearly the shape of the Drell cross section.

Quantitatively, the Drell cross section is smaller than the N^* data at all energies, but it approaches the observed cross section as k increases toward 1.3 GeV. However, this quantitative agreement must

be regarded as accidental: the rapidly decreasing experimental cross section happens to become equal to the slowly changing OPE cross section for these values of k. The bubble chamber data at higher k show that the OPE model gives too large a result for $k > 1.8$ GeV.[17] Another way of stating this is that the OPE model does not give the observed shape of the total N^* cross section.

The simple OPE model has some additional deficiencies. Both major bubble chamber groups studying this reaction have found that the OPE model does not correctly describe the distributions of the N^* decay angles, angles which were not observed in this experiment. From a theoretical point of view, the OPE model alone is not acceptable because it is not gauge invariant. Mathews attempted to overcome the latter objection by calculating the amplitude for N^* production from the four Feynman diagrams shown in Figure 11.[32] In this calculation, the N^* was treated as a stable particle. The πNN^* coupling constant, f, is related to the width of the N^*, Γ, by

$$\frac{f^2}{4\pi} = \frac{3M}{q^3(E_N + M_N)}\Gamma \cong 18.9 \text{ GeV}^{-2}$$

where q = pion momentum in the N^* rest frame,

E_N = nucleon energy in the N^* rest frame,

M = N^* mass,

M_N = nucleon mass,

and a coupling of the form fq_μ has been assumed. Even when the coupling of the photon to the anomalous magnetic moments of the

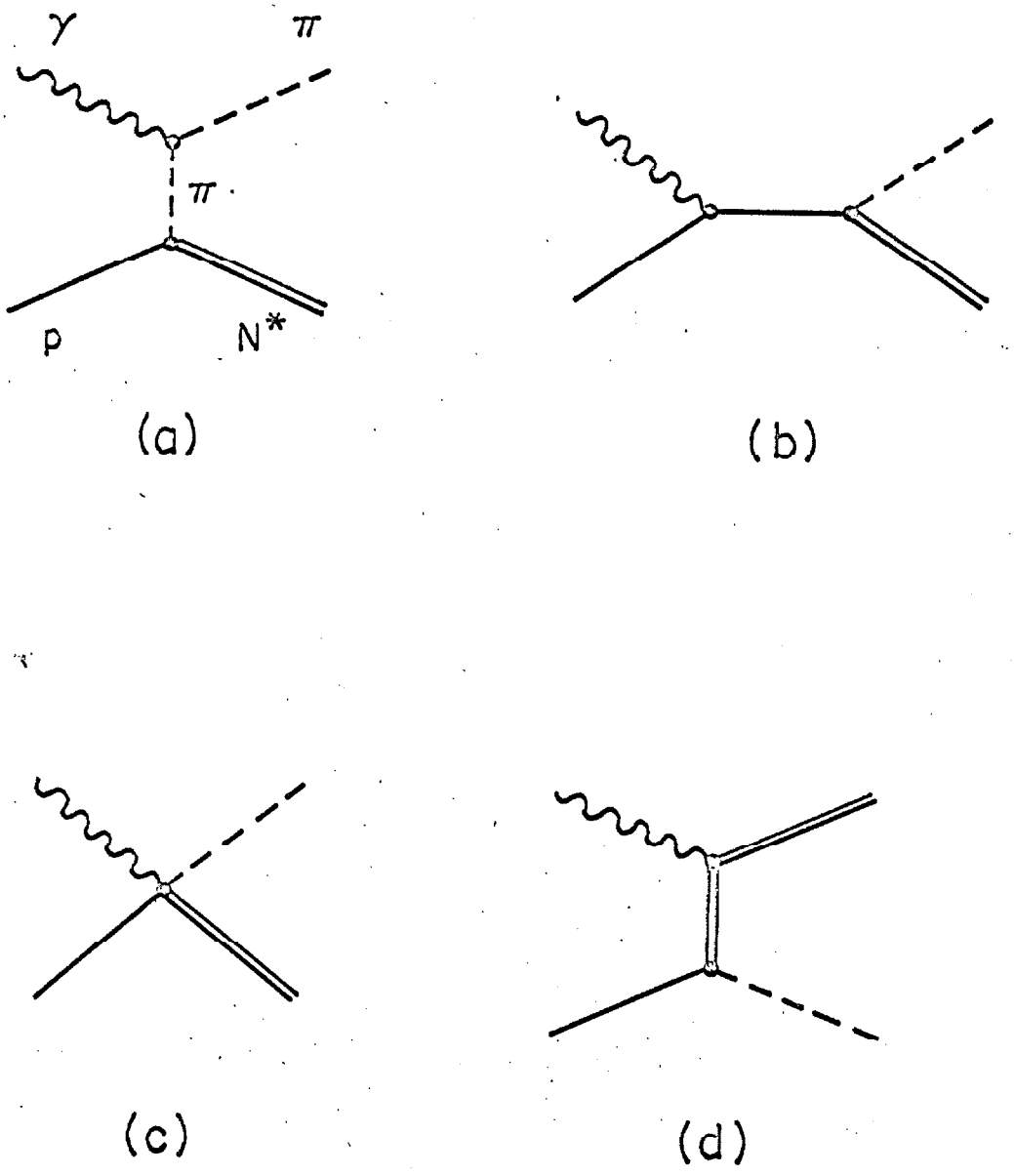

Figure 11. Diagrams used in the calculation of the gauge invariant Born approximation.

nucleon and the N^* is neglected, the calculated cross section is in serious disagreement with the observed π^- angular distributions in N^* production, being generally too large and increasing to very large values in the backward direction. Stichel and Scholz performed a similar calculation,[33] but kept what they asserted are the minimum contributions from diagrams 11(b) and 11(d) needed to achieve gauge invariance. Angular distributions calculated from the Stichel-Scholz amplitude, using the coupling constant given above, are also shown in Figure 8. While these curves have the proper shape in the forward direction, they have the wrong behavior at wide angles and are generally too large.

Finally, it is interesting to note that the DESY bubble chamber group recently reported that the Stichel-Scholz model with absorption corrections agreed fairly well with their N^* production data at small momentum transfers ($|t| < .3$ GeV^2); the comparison was made with the total cross section, production angular distribution, and N^* decay distributions.[34] In contrast, the CEA collaboration, with data quite similar to that from DESY, felt that modified OPE models were not adequate, and that resonances in the s channel must be included to describe their results.[17] However, they have not yet published the results of detailed calculations along these lines.

V. CONCLUSIONS

We have found that the "missing mass spectrometer" method used here is a particularly simple and successful technique for measuring the contribution of $N^*(1238)^{++}$ photoproduction to pion pair photoproduction from 0.9 to 1.3 GeV. The success of the technique is largely a result of the virtual absence of competing reactions which could produce undesired background. It is doubtful that this technique would be useful at higher energies, both because the N^* cross section becomes small and because ρ^0 production, which becomes dominant, could not readily be studied in this way.

The π^- momentum spectra, obtained at seven angles at each of eight photon energies from 0.93 to 1.29 GeV, clearly show the presence of the $N^*(1238)^{++}$ in the final state. This is particularly true at small π^- angles and the lower part of the energy range covered. A phenomenological model, using an incoherent sum of a Breit-Wigner shape for N^* production and a phase space shape for nonresonant production, fits these spectra well at all angles and energies, and permits separation of the $N^*(1238)^{++}$ contribution. No need was found for inclusion of an $N^*(1238)^0$ term in this model.

The total cross section for pion pair production decreases over the energy range investigated, although not as rapidly as the contribution of N^* production to the cross section. When our data are combined with those obtained at lower energies in other experiments, there is a suggestion that the third resonance, $N^*(1688)$, may be contributing, particularly to $N^*(1238)^{++}$ production. However, the magnitude of such an effect would be difficult to estimate because the relative normalization of independent experiments is of crucial importance.

The one pion exchange model, evaluated in the pole approximation limit, predicts many of the qualitative features of the reaction quite well, particularly for the $N^*(1238)$ part of the cross section. These features include the relative absence of $N^*(1238)^o$ production, the shape of the π^- momentum spectrum, and the angular distribution of the π^- produced in association with the $N^*(1238)^{++}$. Even the magnitude of the differential cross section for $N^*(1238)^{++}$ production is in fair agreement with this model for $k \geq 1.1$ GeV. It is perhaps most surprising that this model gives the correct behavior for the angular distribution at large π^- angles, for here the exchanged pion is certainly far off the mass shell and the pole approximation would not seem justified. The model does begin to have difficulties at large momentum transfers when additional terms are added to make the complete theory gauge invariant.

We thus conclude that much theoretical analysis remains to be done if we are to have a quantitative understanding of pion pair production in this energy range within the framework of a gauge invariant theory. It appears that the present data, including information on the N^* decay distributions obtained in the bubble chamber studies, would be sufficient to justify such analysis in the near future.

VI. APPENDIX

A. Kinematics

In this section we list many of the kinematic relations which were found useful in analyzing this experiment. Although we concern ourselves explicitly with the reaction $\gamma + p \rightarrow \pi^- + \pi^+ + p$, many of the equations below apply to a more general class of processes. The symbols used in these equations have the same meanings as those used in the text of this paper, but for convenience are summarized here:

m = pion mass,

M_p = proton mass,

β, p, ω, θ = π^- velocity (in units of $c = 1$), momentum, total energy, and angle relative to the incident photon respectively, all as measured in the laboratory system. Primes are used to denote the corresponding variables in the c. m. system.

γ = Lorentz factor of the $\pi^- = \omega/m$,

k = photon lab energy.

The total energy in the c. m. system, W, is given by the usual relation for photoproduction reactions:

$$W = (M_p^2 + 2kM_p)^{1/2} \quad . \tag{1}$$

The invariant mass, M, of all particles in the final state except the π^- can be expressed either in terms of π^- lab variables

$$M^2 = W^2 + m^2 - 2\omega [M_p + k(1 - \beta \cos\theta)] \tag{2}$$

or in terms of π^- c.m. variables

$$M^2 = W^2 + m^2 - 2\omega' W . \tag{3}$$

The velocity of the c.m. system in the laboratory, β_{cm}, is given by

$$\beta_{cm} = \frac{k}{k + M_p} , \tag{4}$$

and the Lorentz factor for the c.m. system is given by

$$\gamma_{cm} = \frac{k + M_p}{W} . \tag{5}$$

The c.m. angle of the π^- can be expressed in terms of these variables and the lab angle and velocity of the π^- as follows:

$$\tan\theta' = \frac{\sin\theta}{\gamma_{cm}(\cos\theta - \frac{\beta_{cm}}{\beta})} . \tag{6}$$

The π^- energy in the c.m. system can be obtained in terms of lab variables immediately from equations (2) and (3)

$$\omega' = \frac{\omega}{W} [M_p + k(1 - \beta \cos\theta)] \quad . \tag{7}$$

It is also useful to express the π^- c.m. momentum in terms of W and M:

$$p' = \frac{1}{2W} \left\{ [(W - m)^2 - M^2][(W + m)^2 - M^2] \right\}^{1/2} . \tag{8}$$

The magnitude of the 3-momentum of the π^+ in the π^+-p c.m. system, q, is a quantity which keeps appearing in phase space calculations:

$$q = \frac{1}{2M} \left\{ [M^2 - (M_p + m)^2][M^2 - (M_p - m)^2] \right\}^{1/2} . \tag{9}$$

The minimum photon energy required to produce a π^- at lab angle θ, $k_{th}(\theta)$, is given by

$$k_{th}(\theta) = \frac{2m(1 + \frac{m}{M_p})}{[1 - (\frac{m}{M_p} \sin\theta)^2]} \quad . \tag{10}$$

The minimum photon energy, $k_m(\theta, p, n)$, required to produce a π^- at lab angle θ with momentum p in the reaction $\gamma + p \rightarrow \pi^- + n\pi + N$ is given by

$$k_m(\theta, p, n) = \frac{m\left[\frac{M_N}{m}(\gamma + n) + \frac{1}{2}(n^2 - 1)\right]}{\left[\frac{M_N}{m} - \gamma(1 - \beta \cos\theta)\right]} \quad (n \geq 1) \tag{11}$$

where M_N is the nucleon mass. The laboratory cross section differential in π^- momentum and angle is related to the c. m. cross section differential in M^2 and angle in the following way:

$$\frac{d^2\sigma}{dp d\Omega}(k, p, \theta) = \frac{2\beta pW}{p'} \frac{d^2\sigma'}{dM^2 d\Omega'}(k, M^2, \theta') . \tag{12}$$

The factor $\left(\frac{2\beta pW}{p'}\right)$ is denoted by $J(k, p, \theta)$ in Section III. C.

B. Experimental Parameters

1. Photon Beam

The arrangement of apparatus in the laboratory is shown in Figure 3. The bremsstrahlung beam was produced in a tantalum radiator .193 radiation lengths thick and was collimated by a lead collimator having a rectangular cross section. The collimated beam had half-angles of 1.84×10^{-3} radians (in the plane of the electron orbit) by 2.21×10^{-3} radians, producing a beam spot at the liquid hydrogen target approximately 1 1/2 in. by 1 3/4 in. The central beam was not further collimated, but a number of lead scraping walls were placed along the beam line to remove photons and charged particles diverging from the beam line. During the 1965 phase of the experiment, a single sweeping magnet, located slightly down-

stream from the primary collimator, was used to remove charged particles from the beam line. Before the 1966 running began, a second sweeping magnet was installed closer to the hydrogen target. This second sweeping magnet had a beam path 30 in. long between its pole tips and was run at a central field of 13.5 kilogauss. Lead scraping walls placed at the entrance and exit of this magnet were designed so that the most energetic electrons entering the magnet would be swept away from the aperture in the exit wall. A helium bag was installed from the exit wall to the entrance window of the hydrogen target vacuum jacket; when taking data at 4^{o} and 12^{o}, a second helium bag was added from the hydrogen target to the 1200 MeV/c spectrometer.

The position of the photon beam at the hydrogen target was checked frequently by placing a 1/32 in. Cu radiator in the beam and taking a Polaroid picture of the ionizing particles produced. It was necessary to adjust the position of the tantalum radiator in the synchrotron slightly to keep the beam centered on the hydrogen target in the horizontal plane at all energies. The beam spot was kept centered to about 1/8 in.

There were two properties of the beam which had to be known accurately in order to minimize random errors in this experiment: the total energy in the bremsstrahlung beam during each run, and the change in the synchrotron energy from one run to the next. The bremsstrahlung subtraction amplified small errors in either of these quantities, causing large errors in the cross section. For example, in a typical case the π^- yield per unit beam energy increased by 20% when the synchrotron energy was raised 50 MeV. A random error of 2% in monitoring the total beam energy at one end point would produce a 10% error after the bremsstrahlung subtraction. A 10 MeV error in

the synchrotron energy change would produce a 20% error in the normalization of the cross section (see Section III. B). In addition, errors in our knowledge of the shape of the bremsstrahlung spectrum and the absolute calibration of the synchrotron energy would cause systematic errors in the cross section. The methods used to determine each of these properties of the beam are discussed below.

The synchrotron energy was measured with a beam energy meter which measured the field of the synchrotron magnet and was calibrated to read the electron energy. The electronic part of this meter was calibrated by H. A. Thiessen during this experiment,[35] with the result

$$E_{o_{TRUE}}/E_{o_{METER}} = 1.021 \pm .003 \quad ,$$

where E_o denotes the synchrotron energy. Excitation curves for the reaction $\gamma + p \rightarrow \pi^+ + n$ made by Thiessen and Ecklund with the magnetic spectrometers used in this experiment gave results in reasonable agreement with this value[24, 25]:

$$E_{o_{TRUE}}/E_{o_{METER}} = \begin{cases} 1.025 \pm .005 \text{ (600 MeV/c spectrometer)} \\ 1.025 \pm .005 \text{ (1200 MeV/c spectrometer)} \end{cases} .$$

The absolute energy calibration was therefore taken to be

$$E_{o_{TRUE}}/E_{o_{METER}} = 1.025 \pm .005 \quad .$$

As indicated above, control of the increment in synchrotron energy from one run to the next was more important for this experiment than knowing the absolute energy calibration. There were two sources of error in this increment: errors in selecting the synchrotron energy, and fluctuations of the energy about the selected value. The first kind of error was caused by nonlinearity of the beam energy meter. Thiessen found that the beam energy meter had a maximum error of 2 MeV for a change of 50 MeV.[35] The second kind of error was caused by shifts in the maximum synchrotron field from one machine cycle to the next, and by changes in the field during the part of the cycle when the bremsstrahlung beam was produced (the "dump"). The normal operating procedure for this experiment was to set the synchrotron magnetic field to give the desired energy at the middle of the beam dump as indicated by the beam energy meter, and to adjust the field for zero slope during the dump. Normally, this could be accomplished so that the beam energy meter indicated the same field at both ends of the dump; in the worst cases, the beam energy meter indicated a 2 MeV change from one end of the dump to the other. The synchrotron energy at the center of the dump seemed to wander by about 2 MeV over a period of a few cycles, and drifts from the desired value as large as about 4 MeV sometimes occurred before the synchrotron operator noticed them and made an appropriate adjustment. It should be noted that another potential source of energy variation, namely, the degradation of electron energy arising from multiple traversals of the radiator, was accounted for in the calculation of the shape of the bremsstrahlung spectrum. Finally, in order to be as insensitive as possible to long term instability of the beam energy meter, data which were to be subtracted were taken as close

in time as possible, i.e., our running procedure was to take energy scans at fixed p and θ.

The methods used to monitor the total beam energy were summarized in Section II. B, and have been described in detail by Thiessen.[24] The thin ion chamber, TC-1, and the electron probe in the synchrotron, 40 Mc probe, were usually calibrated with the quantameter before and after every run, or at least before and after every change of synchrotron energy. The average of the number of quantameter BIPS (beam integrator pulses) computed for each run from each of these monitors was used as the number of quantameter BIPS for that run. Whenever a discrepancy $\geq$ 2% between the results from these monitors occurred, an attempt was made to resolve it using the monitor telescope and/or beam catcher ion chamber readings. However, the latter monitors were generally less useful in this experiment than TC-1 and the 40 Mc probe for three reasons: (1) the beam catcher ion chamber was in the shadow of the 1200 MeV/c spectrometer for the majority of the running time; (2) neither of these monitors was in the beam when the quantameter was in place and so could not be calibrated directly; and (3) the good short term reproducibility of the monitor telescope at a given synchrotron energy was of diminished value because the synchrotron energy was changed so frequently. The random error in the yield arising from this beam monitoring procedure was estimated to be 1% on the basis of analysis of the Plexiglas target calibration runs (see Section VI. D. 1).

The absolute calibration of the quantameter was obtained from the relation:

$$U = \frac{13.10 \times 10^{18} \text{ MeV/coulomb}}{(P/T)} \times Q/BIP$$

where U = total energy in the bremsstrahlung beam per quantameter BIP,

P = pressure of the quantameter gas in mm of Hg,

T = absolute temperature of the quantameter gas in ^{o}K,

Q/BIP = charge (in coulombs) required to produce 1 BIP from the electronic integrator attached to the quantameter (No. 0628).

The numerical constant in the above relation was determined by Thiessen and Pine.[36] The value of P/T changed gradually over the period of this experiment; the value of Q/BIP was stable within a few tenths of one percent, except for a 1% change which occurred when the tubes in the integrator were changed. The values of P/T and Q/BIP used in reducing the data are given in the following table:

Run Number	P/T	Q/BIP
0-314 0-5064	2.455	2.225×10^{-7} (integrator scale 3)
315-1209 5065-5300	2.439	2.235×10^{-6} (integrator scale 4)
1210-1459 5301-5538	2.405	2.235×10^{-6} (integrator scale 4)
1460-1488 5539-5564	2.394	2.235×10^{-6} (integrator scale 4)
1489-1688 5565-5746	2.394	2.213×10^{-6} (integrator scale 4)

The major uncertainty in the absolute quantameter calibration was a 3% uncertainty in the calibration constant giving the energy per coulomb of charge.

It was important to know the shape of the bremsstrahlung spectrum in order to make an accurate analysis of the results of this experiment. F. Wolverton recently completed a study of this problem, and developed a theory of thick target bremsstrahlung which gives good agreement with spectral measurements presently available.[27] The beam spectrum is conventionally written in the form

$$N(k, E_o)dk = \frac{1}{E_o} \frac{B(k, E_o)}{k} dk$$

where $N(k, E_o)dk$ = number of photons with energy k to k + dk per unit energy in the beam,

E_o = synchrotron energy.

The function $B(k, E_o)$, conventionally normalized so that

$$\int_0^{E_o} \frac{dk}{E_o} B(k, E_o) = 1 ,$$

can be calculated for the beam after collimation by a rectangular collimator using the computer program, BPAK I, prepared by Wolverton. It was convenient to incorporate a correction for the nonuniform thickness of the hydrogen target into the evaluation of $B(k, E_o)$. This modified spectral function, designated by $\bar{B}(k, E_o)$, was defined by

$$\bar{B}(k, E_o) = \int dxdy \; b(k, E_o, x, y) \; \frac{T(x, y)}{D}$$

where x, y = rectangular coordinates in a plane normal to the photon beam with origin at the center of the hydrogen target,

$T(x, y)$ = thickness of the hydrogen target (in the direction of travel of the beam) at the point (x, y),

D = diameter of the hydrogen target,

$b(k, E_o, x, y)$ = differential beam spectral function.

$b(k, E_o, x, y)$ and $B(k, E_o)$ are related by

$$\int dxdy \; b(k, E_o, x, y) = B(k, E_o)$$

with $B(k, E_o)$ normalized in the conventional way. A detailed discussion of the evaluation of $\bar{B}(k, E_o)$ has been given elsewhere[37]; it was computed and tabulated using BPAK I, and in the data reduction was obtained by interpolation in the tables thus constructed.[38] Table VI gives the values of $\bar{B}(k, E_o)$ used in the analysis of all data in this experiment; Figure 5(a) is a graph of this function for $E_o = 1$ GeV.

2. Hydrogen Target

The liquid hydrogen target used in this experiment was used in many previous experiments in this laboratory, and was

	EO (MEV)							
K/EO	800	900	1000	1100	1200	1300	1400	1500
0.	1.430	1.433	1.435	1.437	1.439	1.441	1.443	1.446
0.100	1.237	1.236	1.237	1.237	1.238	1.239	1.241	1.243
0.200	1.109	1.110	1.110	1.111	1.111	1.112	1.113	1.115
0.300	1.015	1.015	1.016	1.016	1.017	1.018	1.019	1.020
0.400	0.946	0.946	0.947	0.947	0.948	0.949	0.950	0.951
0.500	0.898	0.899	0.899	0.900	0.901	0.901	0.901	0.902
0.600	0.869	0.870	0.870	0.870	0.870	0.871	0.871	0.871
0.700	0.856	0.856	0.855	0.855	0.855	0.855	0.855	0.855
0.800	0.850	0.849	0.848	0.848	0.848	0.847	0.847	0.846
0.840	0.846	0.845	0.845	0.844	0.843	0.843	0.842	0.841
0.880	0.838	0.837	0.836	0.836	0.835	0.834	0.833	0.832
0.900	0.831	0.830	0.829	0.828	0.827	0.826	0.825	0.824
0.920	0.818	0.818	0.817	0.816	0.815	0.814	0.812	0.811
0.940	0.798	0.797	0.797	0.796	0.795	0.794	0.793	0.791
0.950	0.781	0.782	0.782	0.781	0.780	0.779	0.778	0.776
0.960	0.758	0.759	0.760	0.760	0.759	0.758	0.757	0.756
0.970	0.722	0.725	0.727	0.728	0.728	0.727	0.727	0.726
0.980	0.658	0.665	0.670	0.673	0.675	0.676	0.676	0.676
0.985	0.602	0.613	0.621	0.626	0.630	0.632	0.634	0.635
0.990	0.505	0.524	0.538	0.548	0.556	0.561	0.565	0.569
0.992	0.443	0.467	0.485	0.498	0.509	0.516	0.522	0.527
0.994	0.352	0.384	0.408	0.427	0.441	0.452	0.461	0.468
0.996	0.211	0.254	0.287	0.313	0.334	0.351	0.365	0.376
0.998	0.	0.017	0.063	0.101	0.133	0.159	0.181	0.200
1.000	0.	0.	0.	0.	0.	0.	0.	0.

Table VI. The bremsstrahlung beam spectrum function $\bar{B}(k, E_o)$ for the radiator, collimator, and hydrogen target used in this experiment is tabulated for various values of E_o.

described most recently by Thiessen.[24] The parameters of the target used in the analysis of our data are shown in the following table:

Run Number	Target Diameter(cm)	Hydrogen Density(g/cm^3)
0-807 5000-5237	$7.597 \pm .040$	.0696
808-1688 5238-5746	$7.539 \pm .040$	.0696

The target diameter shown in the table was the diameter at liquid hydrogen temperature. The change in target size occurred because the original cup was broken on 24 September 1965 and was replaced with one of slightly different size. The hydrogen density shown was the net hydrogen density, i.e., the density of the liquid hydrogen minus the density of the hydrogen gas present in the target when "empty target" data were obtained.

A well-known eccentricity of this target was that it gradually accumulated a layer of opaque material on the walls of the cup containing the liquid hydrogen. To avoid difficulty from this potential source of background, the target was warmed up and cleaned at regular intervals, and empty target runs were usually made shortly before or shortly after the full target runs at the same points.

3. Spectrometers

We summarize here the parameters of both spectrometers used in this investigation. The magnet configurations, the counters

and their locations, and the electronics in each of these systems were identical to those described in detail by Ecklund[25] (for the 1200 MeV/c spectrometer) and Thiessen[24, 41] (for the 600 MeV/c spectrometer), with the few minor exceptions noted below.

Ecklund and Thiessen used the spectrometers to detect positive pions. The only change needed to detect negative pions was to reverse the magnet polarity. Because protons were thus eliminated, we were able to relax the time-of-flight and scintillator pulse-height requirements they set. The Plexiglas threshold Cherenkov counters they used to discriminate against protons were kept in the systems, but were not essential for this experiment.

The only significant change made in either spectrometer was a modification of the electronics connected with the FAN counters of the 1200 MeV/c spectrometer. The FAN counters were scintillators mounted against each pole tip of the magnet, used to veto events in which a charged particle scattered from a pole tip. During the first part of this experiment, the large electron flux at 4^{o} produced a much higher rate in the FANS than the phototubes could handle, so these counters were turned off and the FAN correction at 4^{o} was estimated from data at larger angles. In an effort to overcome this difficulty, a second sweeping magnet and several helium bags were added to produce a cleaner photon beam (see Section VI. B. 1). These measures reduced the electron counting rate in the spectrometer by roughly a factor of 4 at 4^{o}. Even with the accompanying reduction in FAN singles rates, the gain of the FAN phototubes sagged considerably. Therefore, the voltages on the last five dynodes of the FAN photomultiplier tubes were stabilized by putting an emitter follower on each dynode. The "base-boost" circuits used for this were previously designed and used by Marshall.[39] The FAN gain was then stable, but an appreciable

number of accidental FAN vetoes were observed at 4^{o}. The method used to correct for these accidental vetoes is discussed in Section D. 1 of the Appendix.

The basic properties of the spectrometers required to analyze the data are their momentum calibrations and their resolution functions. The methods used to determine these properties have been previously discussed,[25, 40, 41] so we shall give here only the results, beginning with the properties of the 1200 MeV/c spectrometer. The central field of each magnet was measured with a proton resonance magnetometer. Denoting the resonant frequency in megacycles/sec by F, the central momentum, p_o, was given by

$$\frac{p_o}{F} = \begin{cases} A & F \leq 30 \text{ Mc} \\ A + B\left(\frac{F - 30}{100}\right) + C\left(\frac{F - 30}{100}\right)^2 & F > 30 \text{ Mc} \end{cases}$$

where $A = 18.794 \text{ MeV/c - Mc}^{-1}$

$B = -9 \times 10^{-3} \text{ MeV/c - Mc}^{-1}$

$C = -4.937 \text{ MeV/c - Mc}^{-1}$.

At a given central momentum setting, the acceptance was divided into four channels by a counter hodoscope at the momentum focus. Since no attempt was made to unfold the effects of the finite widths of the spectrometer resolution functions, the only property of these functions we required was their area, $\Delta p \Delta \Omega$. Table VII gives the mean momentum, p_i, and total acceptance for each channel of the 1200 MeV/c spectrometer. This table was prepared for a

TABLE VII

Properties of the 1200 MeV/c Spectrometer

Channel	$(\frac{p_i - p_o}{p_o}) \times 10^2$ a)	$(\frac{\Delta p \, \Delta \Omega}{p_o}) \times 10^5$ b)
T	4.03	3.54
TC	1.23	3.34
BC	-1.41	3.17
B	-3.89	2.99
Total	0.0	13.04

a) p_o is the central momentum of the spectrometer, and p_i is the mean momentum of the channel.

b) The acceptance is given for a central field of 10 kilogauss and a 3 in. x 9 in. aperture counter (A1).

3 in. x 9 in. aperture-defining counter (A1). During the experiment, several aperture counters were used, and the acceptance for each was the value shown in Table VII multiplied by the ratio of the area of the counter to that of the 3 in. x 9 in. counter. These aperture counters and the correction factors used are listed below:

A1 Counter	Dimensions	Solid Angle Correction Factor
1	3 in. x 9 in.	1.000
2	3 in. x 6 in.	.667
3	2 3/4 in. x 12 in.	1.222
4	2 3/4 in. x 6 in.	.611
5	2 3/4 in. x 9 in.	.917

The momentum acceptance given in Table VII was for a central field of 10 kilogauss. According to Ecklund, these values changed by less than 0.4% at the peak field of about 15 kilogauss, so no field-dependent correction was made to the above values.

We now consider the properties of the 600 MeV/c spectrometer. The central momentum was related to the magnetometer frequency as follows:

$$\frac{p_o}{F} = A + BF + CF^2$$

where $A = 8.358$ MeV/c - Mc^{-1}

$B = 4.470 \times 10^{-3}$ MeV/c - Mc^{-2}

$C = -7.407 \times 10^{-5}$ MeV/c - Mc^{-3} .

The momentum acceptance of this spectrometer was divided into seven channels. The mean momentum and acceptance for each channel are given in Table VIII. These values were obtained for a 2 3/4 in. x 9 1/2 in. aperture counter, which was used throughout this experiment, and for a central field of 10 kilogauss. Thiessen found that a small correction had to be made to the acceptance at fields above 10 kilogauss. He expressed this correction in the form

$$\left(\frac{\Delta p\ \Delta\Omega}{p_o}\right) = \left(\frac{\Delta p\ \Delta\Omega}{p_o}\right)_{10\ kg} \left[1 - 0.0144\ \left(\frac{B-10}{5}\right)\right]$$

where B is the central magnetic field in kilogauss. It was convenient to express this correction in the form

$$\left(\frac{\Delta p\ \Delta\Omega}{p_o}\right) = \left(\frac{\Delta p\ \Delta\Omega}{p_o}\right)_{10\ kg} \left[1 - 0.0144\ \left(\frac{p_i - 368}{184}\right)\right]$$

for $p_i > 368$ MeV/c. In adopting this form, we first made the approximation that the central momentum was a linear function of the central field, and then replaced the central momentum by the mean momentum, p_i, of the channel of interest. Because the entire correction was 1.5% in the worst case, these approximations introduced negligible error.

TABLE VIII

Properties of the 600 MeV/c Spectrometer

Channel	$\left(\frac{p_i - p_o}{p_o}\right) \times 10^2$ a)	$\left(\frac{\Delta p \, \Delta\Omega}{p_o}\right) \times 10^5$ b)
A	-4.29	4.314
B	-2.96	4.324
C	-1.58	4.612
D	-0.13	4.800
E	1.38	4.976
F	2.92	5.000
G	4.52	5.359
Total	0.19	33.65

a) p_o is the central momentum of the spectrometer, and p_i is the mean momentum of the channel.

b) The acceptance is given for a central field of 10 kilogauss and a 2 3/4 in. x 9 1/2 in. aperture counter.

It should be noted that the spectrometer properties listed in Tables VII and VIII do not include corrections for nuclear scattering of pions or pion decay. These corrections are discussed in Sections VI. D. 3 and VI. D. 4 respectively. The effect of multiple coulomb scattering was investigated for the 600 MeV/c spectrometer by Thiessen,[24] and for the 1200 MeV/c spectrometer by Kilner.[42] Thiessen calculated the pion loss analytically and found it to be less than 0.5% for momenta greater than 200 MeV/c; Kilner used a Monte Carlo calculation and obtained a result consistent with no loss. Therefore, no multiple scattering correction was made to the total acceptances shown in Tables VII and VIII. However, the pions did suffer a small energy loss in traversing the matter of the hydrogen target and its walls. A constant momentum loss of 2.7 MeV/c was added to the momentum at the spectrometer to obtain the pion momentum in the hydrogen target.

C. Data Handling

1. General Plan

In this experiment, π^- yields were measured at some 257 different kinematic points as defined by the synchrotron energy, π^- angle, and spectrometer central momentum. Normally two, and in some cases as many as five, data runs were made at each of these points with the hydrogen target full, and at most of them there were one or more runs with the target empty. A total of nearly 10^6 π^- were detected. Even with the aid of a large computer, the tasks involved in manipulating the raw data to obtain cross sections occupied a major fraction of the experimenter's time. In this section we shall describe the methods used to organize and analyze the data.

The basic plan was to put the data into a form suitable for computer input with as few hand operations as possible, and to let the computer do all the rest of the work. A boundary condition for this plan was that data from both spectrometers should be presented to the computer in the same format, so that a single set of analysis programs could be used to handle all data.

When setting up a large scale data handling scheme, two of the major problems encountered are to decide whether to save some of the intermediate results, and to decide in what form the input data and any intermediate results are to be stored (cards, tapes, etc.). With regard to the first of these problems, it seems to be axiomatic that as long as the work remains unpublished the investigator will decide he wants to try something different at some point in the analysis. It is therefore economical to save some intermediate results, particularly those obtained from time-consuming operations, in a form which can easily be put back into the computer as a starting point for the subsequent manipulations.

The medium of communication with the computer in this investigation was punched cards, and the results of every major step in the analysis were punched onto cards. In retrospect, it is felt that this was a very satisfactory solution to the above problems for our purposes. Although some time had to be spent shuffling cards, the flexibility of the system and the ease with which the data could be rearranged and reanalyzed starting at any step as the analysis evolved were more than compensating advantages.

2. Preliminary Data Handling

In order to carry out this general plan, a certain amount of preliminary manipulation had to be performed on the raw data. The objective of this preliminary work was to put all of the kinematic, counting, and beam monitoring information needed to analyze each run into a form suitable for computer input and independent of which spectrometer was used to obtain the data.

A "run" consisted of data obtained with a single spectrometer within a period of an hour or two with fixed operating conditions of the synchrotron and spectrometer. In general, runs were taken with both spectrometers simultaneously. Runs were numbered sequentially for identification purposes: those from the 600 MeV/c spectrometer were numbered beginning with 1, whereas those from the 1200 MeV/c spectrometer were numbered starting with 5001.

Kinematic information was treated in the same way for both spectrometers: the information was recorded on coding sheets in a form suitable for punching by the professional key-punchers in the Computing Center. A single card was sufficient to contain all such information for each run.

The counting information, i.e., the number of pions in each momentum channel, was available in quite different forms from the two spectrometers. The 1200 MeV/c spectrometer data were recorded in data notebooks directly from the scalers in this system, and were then transferred to coding sheets for punching onto cards. The output from the 600 MeV/c spectrometer was a paper tape containing all the information from the data storage system.[24] Because paper tapes could not be read directly into the IBM 7094

computer, they were first copied onto magnetic tape, a peripheral service provided by the Computing Center. The 7094 was then used to read the magnetic tape, determine the number of pions observed in each momentum channel, and punch all this information onto one BCD card for each run.

Some of the programs used in the preliminary analysis of data from the 600 MeV/c spectrometer should be of use to future workers and will be mentioned briefly here. The program which actually read the magnetic tape and put the information into a form suitable for analysis with FORTRAN programs was subroutine UNPACK, which was written in the MAP language by a member of the Computing Center staff according to our specifications. A description of this program is contained in the Synchrotron Program Library, along with the specifications used to write the program.[43] These specifications include a description of the paper tape format. Subroutine SPCTRA was written to analyze pulse height spectra contained in the output from the data storage system, and a large package of subroutines was written to simplify the analysis of scaling information. These were all FORTRAN programs, and are also contained in the Synchrotron Program Library.[44]

The beam monitoring information was handled in a somewhat cumbersome way, largely for historical reasons. The method used to find the number of quantameter BIPS for each run was discussed in Section VI. B. 1, and this was the number actually required in the analysis of data. However, the output of one of the secondary monitors, usually the 40 Mc probe, was recorded in channel 0 of the memory of the Nuclear Data Pulse Height Analyzer, and was included on the punched card (COUNTS card) containing the counting information from the 600 MeV/c spectrometer. In order to

convert this number to quantameter BIPS, a calibration constant was put onto the card containing kinematic information: this constant was computed for each run so that when multiplied by the secondary monitor output recorded on the COUNTS card, the product would be the correct number of quantameter BIPS. To preserve the equivalence in handling of data from the two spectrometers, the same procedure was used for runs taken with the 1200 MeV/c spectrometer.

Thus, the first and most time-consuming step in the analysis of the data produced two punched cards for each run containing all of the essential information in a format which did not depend on which spectrometer was used for that run.

3. Cross Section Calculations

The objective of the data analysis was to evaluate the cross sections discussed in Section III. A large package of FORTRAN programs, written specifically for this experiment, was developed to accomplish this objective. In addition, Wolverton wrote a group of data reading programs which permitted convenient control over the sequence of all operations through the use of appropriate cards in the data deck itself.[45] Although this was the first experiment in which Wolverton's programs were used, they are completely general, and are recommended for use in other experiments.

The main steps in the analysis of the data are indicated schematically in Figure 12, along with the cards which were punched to store the results at each step. The 'KIN' cards were the set of two cards giving kinematic and counting information for each run described in the previous section. After reading the data from a

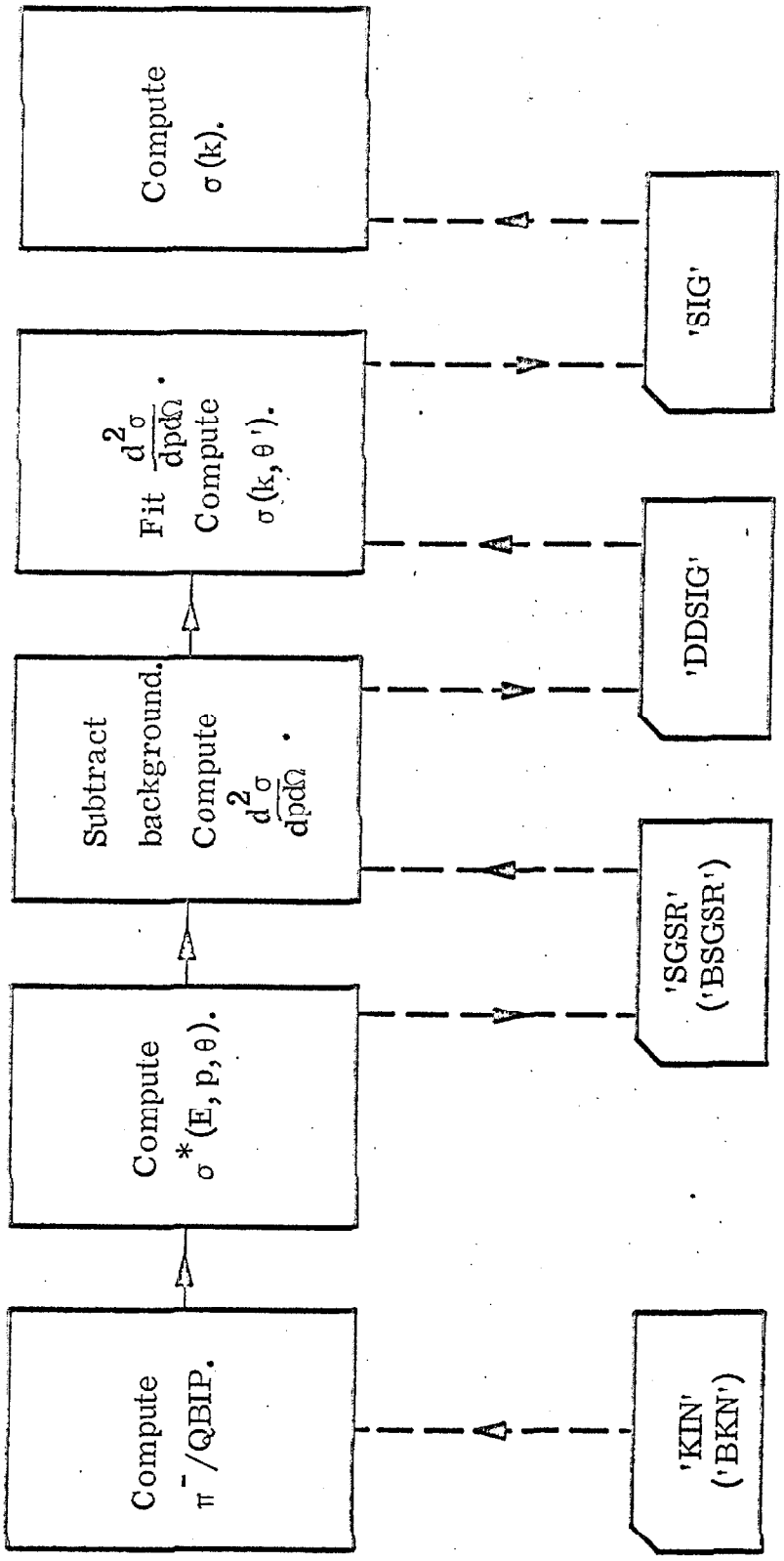

Figure 12. Simplified block diagram of data analysis. The punched cards containing intermediate results are also indicated.

single run, the yield per equivalent quantum, $\sigma^*(E_o, p, \theta)$, was computed; the kinematic parameters of the run and the value of σ^* for each channel, along with its statistical error, were then punched onto three 'SGSR' cards. If the run was made with the liquid hydrogen target empty, its initial set of cards were labelled 'BKN', and its normalized yield cards were called 'BSGSR'. After all data at a given angle and two successive synchrotron energies were read, with runs at the same momentum and energy being averaged together, empty target yields were subtracted from full target yields and the laboratory cross sections, $d^2\sigma/dpd\Omega$, were evaluated. These results, together with the momentum of each channel and other kinematic information, were punched onto four 'DDSIG' cards. The functions $F_i(E_2, E_1, p, \theta)$ needed to perform the fit which separated the resonant and nonresonant parts of the cross section (Section III. C) were then tabulated, and the least squares fit to the cross section was performed. The differential cross sections obtained from the fit, $\sigma_R(k, \theta')$, $\sigma_{NR}(k, \theta')$, and $\sigma_C(k, \theta')$, were punched onto a 'SIG' card. All of the above operations could be performed in a single computer job, or we could start with any intermediate set of cards and perform as many of the above steps as desired. The final step, in which all the 'SIG' cards at a given k were read, the total cross section evaluated, and the result punched onto a 'TXSC' card, was performed in a separate job.

The procedure used in the final analysis of all data was to evaluate $d^2\sigma/dpd\Omega$ separately for each batch of data at given k and θ (see Section III. A). This approach, designed to minimize errors which could result from systematic shifts if data obtained at different times were subtracted, was easily carried out with our data reduction system. In one job, all data were analyzed by batches to the point

where 'DDSIG' cards were punched. The 'DDSIG' cards for the same k and θ from different batches were then read in a second job, the cross sections were averaged together weighted by the reciprocals of their variances, and the remainder of the analysis was performed as described above.

D. Corrections

1. Pion Detection Efficiency

In this section we discuss corrections for effects which might all be described as inefficiencies in pion detection or identification. Pions produced in the hydrogen target by the reaction of interest were not all counted because some failed to traverse the complete counter system, either as a result of nuclear interactions or decay. Pions produced in the walls of the hydrogen target, pions produced by competing reactions in liquid hydrogen, and other particles indistinguishable from pions with our apparatus gave unwanted counts. Finally, the particle detectors and associated electronics had inefficiencies. Correction for competing sources of pions is discussed in paragraph 6 of this section. Particle identification ambiguities and detector inefficiencies are treated in this paragraph, and the other problems are discussed in the remainder of this appendix.

The efficiency of a counter is a property both of the nature of the counter response and of the requirements placed upon the response in order for it to be recorded as an event. There were a sufficient number of counters in each spectrometer to enable us to define a particle beam ignoring one counter; the gain of this counter and biases on its output were then adjusted, and its efficiency was

measured by observing the fraction of events in which its response was recorded. When this was done for the scintillation counters in the system, the observed efficiency was typically 99% or better. The "inefficient" events were investigated by looking at the counter output on an oscilloscope; it was generally found that no pulse occurred at all in these events. This suggested that such events were not caused by a single charged particle traversing all the counters. The efficiency of each scintillation counter, with the exception of the FANS, was therefore taken to be $(100 \pm 1)\%$.

The FANS were tested in a similar way, but required a somewhat more elaborate set-up to define a beam of particles through them. A small, well-collimated electron beam was produced by placing a pinhole collimator into the bremsstrahlung beam near the hydrogen target (with the hydrogen target raised out of the beam line). The spectrometer was placed slightly to one side of 0° so the resulting electron beam would pass through the FAN counter on one of the pole faces. A test counter narrower than the FAN counter was placed in the shadow of the last few inches of one finger of the FAN counter, and a particle beam was defined by requiring the test counter as well as the remaining counters in the spectrometer. The FAN counter efficiency for particles passing through the extreme end of one finger measured in this way was 90-95%. Because the FAN counters typically vetoed no more than 10-15% of the pion events, no correction was made for any inefficiency of the FAN counters.

The Plexiglas threshold Cherenkov counters had an inherent momentum-dependent efficiency. The bias on the output of this counter in the 1200 MeV/c spectrometer was sufficiently low that the measured efficiency was greater than 99% for pions of the lowest momentum detected; the counter was required in the logic

and assumed to have (100 ± 1)% efficiency. The Cherenkov counter in the 600 MeV/c spectrometer had an appreciable inefficiency at the lowest pion momentum detected, and was completely ignored when adding up the number of pions in all runs.

In the 1200 MeV/c spectrometer, the freon threshold Cherenkov counter (FC) was used to eliminate electrons. This counter was tested by placing the spectrometer at 0^{o} and setting up an electron beam in the manner described above. The observed inefficiency of FC for events triggering all the other counters in the system (except the FANS) was 0.05%. About half of the events not triggering FC produced large pulses in the last scintillator of the system (S3), which was preceeded by 1/2 in. of lead. This suggested that a majority of the inefficient events were electrons, i.e., the above inefficiency appeared to be real. The largest yield of electrons relative to pions occurred with the spectrometer at 4^{o}, a central momentum of 540 MeV/c, and a synchrotron energy of 900 MeV. Before the second sweeping magnet and helium bags were in the beam line, the ratio of electron to pion yield under these conditions was about 80 with the target empty and 45 with the target full. With FC rejecting all but .05% of the electrons, this implied a 4% contamination of the empty target pion yield and a 2 1/2% contamination of the full target yield. However, the absolute electron yield (in counts/BIP) with the target empty was 85% of the electron yield with the target full, whereas the empty target pion yield was only 45% of the full target value. Therefore, in the particle flux after empty target correction, the number of electrons was only about 11 times the number of pions; the measured net pion yield thus had an electron contamination of only 0.5%. Since the electron flux changed more slowly with synchrotron energy than the pion flux, the electron

contamination after the bremsstrahlung subtraction was even less than 0.5%. After the second sweeping magnet and helium bags were added, the ratio of electron to pion yield at the same kinematic point was only 25 with the target empty and 14 with the target full. The conclusion from all this was that there was no electron contamination of the yields measured with the 1200 MeV/c spectrometer, i.e., the freon Cherenkov counter effectively provided 100% rejection of electrons.

There was no counter on the 600 MeV/c spectrometer which distinguished between electrons and pions. The basic assumptions made in omitting a counter for this purpose were that there were few electrons present at lab angles of 30^{o} or greater where the 600 MeV/c spectrometer was used, and that at such angles and fixed momentum the electron yield would not be a sensitive function of the synchrotron energy. These assumptions were tested by measuring the e^- and π^- yields with the 1200 MeV/c spectrometer at a few of the points where the 600 MeV/c spectrometer was used to measure cross sections. The results of these measurements, together with the e^- yields at some additional points, are summarized in Table IX. Several distinctive features of the wide angle electron yield can be seen from this table. In contrast to the situation at small angles, almost all of the electrons were associated with processes originating in hydrogen; the empty target electron yield was generally only 10% of the full target value. At a given angle and momentum, there was no appreciable variation of the electron yield with synchrotron energy; in fact, the observed yields were statistically consistent with the hypothesis that the ratio e^-/QBIP was independent of E_o. Finally, except for points very close to the two pion threshold, the electron yield was less than 5% of the π^- yield at these angles wherever the 600 MeV/c spectrometer was used.

TABLE IX

Electron Yield at Some Large Angle, Low Momentum Points

θ (deg)	p_o (MeV/c)	E_o (MeV)	e^-/QBIP * Full Target	Empty Target	Net	$\frac{\pi^-}{QBIP}$ **
20	510	923	.142 ± .012	.033 ± .009	.109 ± .015	
"	"	974	.124 ± .015	.011 ± .008	.113 ± .017	
"	"	1025	.155 ± .015	.030 ± .009	.125 ± .017	
"	570	923	.122 ± .012	.022 ± .007	.100 ± .014	
"	"	974	.110 ± .014	.011 ± .008	.099 ± .016	
"	"	1025	.126 ± .013	.014 ± .005	.112 ± .015	
30	535	923	.060 ± .011	.008 ± .007	.052 ± .013	1.27
"	"	974	.078 ± .009	.005 ± .005	.073 ± .010	2.43
"	"	1025	.062 ± .011	.005 ± .005	.057 ± .012	3.37
"	600	923	.049 ± .006	.010 ± .007	.039 ± .009	
"	"	974	.042 ± .006	.000 ± .005	.042 ± .008	
"	"	1025	.049 ± .007	.010 ± .007	.039 ± .010	
"	670	974	.042 ± .006	.000 ± .005	.042 ± .008	
"	"	1025	.044 ± .006	.005 ± .005	.039 ± .008	
44	465	974	.073 ± .022	.000 ± .007	.073 ± .023	1.67
"	"	1025	.058 ± .018	.007 ± .007	.051 ± .019	1.96
"	520	923	.052 ± .012	.000 ± .007	.052 ± .014	.22
"	"	974	.048 ± .011	.007 ± .007	.041 ± .013	.62
"	"	1025	.029 ± .009	.007 ± .007	.022 ± .011	1.08
"	575	923	.043 ± .011	.007 ± .007	.036 ± .013	.02
"	"	974	.040 ± .010	.014 ± .010	.026 ± .014	.09
"	"	1025	.056 ± .012	.000 ± .007	.056 ± .014	.26
"	"	1076	.040 ± .009	.004 ± .004	.036 ± .011	.59
"	"	1128	.052 ± .011	.004 ± .004	.048 ± .012	1.07
"	"	1178	.057 ± .011	.003 ± .003	.054 ± .011	1.22

TABLE IX (cont.)

θ (deg)	p_o (MeV/c)	E_o (MeV)	e^-/QBIP * Full Target	Empty Target	Net	$\frac{\pi^-}{\text{QBIP}}$ **
44	655	1076	.034 ± .009	.009 ± .005	.025 ± .010	
"	"	1128	.036 ± .009	.009 ± .005	.027 ± .010	
"	"	1178	.048 ± .010	.003 ± .003	.045 ± .010	
"	"	1230	.033 ± .009	.003 ± .003	.030 ± .010	
"	"	1281	.036 ± .006	.009 ± .005	.027 ± .008	
"	"	1332	.041 ± .010	.007 ± .005	.034 ± .011	
"	735	1178	.026 ± .009	.013 ± .006	.013 ± .011	
"	"	1230	.018 ± .005	.000 ± .003	.018 ± .006	
"	"	1281	.035 ± .009	.000 ± .003	.035 ± .010	
"	"	1332	.057 ± .012	.006 ± .004	.051 ± .013	

* The electron counts are summed over momentum channels of the 1200 MeV/c spectrometer at lab angle θ, central momentum p_o, and synchrotron energy E_o.

$$1 \text{ QBIP} = 1.2 \times 10^{13} \text{ MeV}.$$

$$\frac{\Delta\Omega\Delta p}{p_o} = 1.59 \times 10^{-4}$$ for the 1200 MeV/c spectrometer since the 2 3/4 in. x 12 in. aperture counter was used.

** This is the number of π^- per QBIP after empty target subtraction, shown only for those points where data were also obtained with the 600 MeV/c spectrometer.

It would be very desirable to have a model which could account for the electrons at the points in Table IX, so that the electron yield at more backward angles and lower momentum could be estimated with some confidence. A possible source of electrons at wide angles is π^0 photoproduction, where one of the decay photons creates an electron by pair production. An estimate of the contribution from this source at $\theta = 44^0$, $p_0 = 465$ MeV/c, and $E_0 = 974$, using the fact that there were .03 radiation lengths of material between the center of the hydrogen target and the entrance to the spectrometer, gave an upper limit an order of magnitude smaller than the observed electron yield. Decay of the π^0 in the mode $\pi^0 \rightarrow \gamma + e^+ + e^-$, which occurs only 1% of the time, would make a smaller contribution. Furthermore, if π^0 production were the electron source, the electron yield would be expected to increase noticeably with synchrotron energy: as E_0 increased, more of the photons in the beam would have sufficient energy to produce a π^0 capable of giving an electron with the momentum accepted by the spectrometer. Another possible source of high momentum electrons at wide angles is pair production by the bremsstrahlung beam in liquid hydrogen. The contribution from this source was also estimated for $\theta = 44^0$, $p_0 = 465$, and $E_0 = 974$ MeV, and was found to be two orders of magnitude smaller than the observed electron yield. [46]

Lacking a satisfactory quantitative model for the source of the wide angle electrons, we were forced to adopt an empirical approach. In addition to the measurements shown in Table IX, there were some measurements of the electron yield at wide angles made by Thiessen with the 600 MeV/c spectrometer while this experiment was in progress. [24] His method was to count negatively charged

particles satisfying pion logic with the synchrotron energy set below threshold for π^- production from $\gamma + p \rightarrow \pi^- + \pi^+ + p$. His results suffered from the lack of positive identification of the negative particles, and were statistically poor because of a large empty target background, but they were the only available data for angles greater than 44^o. If the measurements in Table IX at 20^o, 30^o, and 44^o and momentum about 530 MeV/c are averaged over E_o and scaled by $\Delta\Omega\Delta p/p_o$ for the two spectrometers, they fall quite close to the smooth curve given by Thiessen in Figure 9 of his thesis. This gave us some confidence that his "negative field background" was primarily electrons, and that we could use his results at backward angles. Note that Thiessen also investigated one further possible source of the electrons: conversion of photons in the aperture counter. He found that such conversion could account for only a small fraction of the observed electron yield.

Consideration of all of the above data on the electron yield at wide angles leads us to the following conclusions with regard to its dependence on E_o, p_o, and θ. The measurements at $\theta = 44^o$, $p_o = 575$ MeV/c, and $p_o = 655$ MeV/c each covered a 250 MeV range of E_o with no strong evidence for any variation with E_o. A reasonable upper limit for any such variation at fixed momentum is

$$\left| \frac{1}{e^-/\mathrm{QBIP}} \frac{\Delta(e^-/\mathrm{QBIP})}{\Delta E_o} \right| \lesssim .05 \ (50\ \mathrm{MeV})^{-1} \ .$$

Because the E_o dependence is so slight, the momentum dependence can be investigated by averaging the results over E_o at fixed p_o. The result is consistent with the relation

$$\frac{1}{e^-/\mathrm{QBIP}} \frac{\Delta(e^-/\mathrm{QBIP})}{\Delta p_o} \approx -0.2 \ (100 \ \mathrm{MeV/c})^{-1} \ ,$$

at both 30^o and 44^o over the momentum range in Table IX. Finally, we adopt the approximate angular dependence found by Thiessen:

$$e^-/\mathrm{QBIP} \cong c \left[1 + 1.7 \frac{(\theta - 180^o)^2}{90^o} \right] \ ,$$

where c is a scale factor with the value 0.03 for the 600 MeV/c spectrometer. This gives roughly a factor of 2 decrease in the e^- yield in going from 44^o to 84^o.

The results in Table IX show that the π^- yield per equivalent quantum, σ^*, measured with the 600 MeV/c spectrometer at 30^o and 44^o must have had an e^- contamination of the order of 5% except near threshold. Since the π^- yield at fixed momentum changes by at least 20% for a 50 MeV increment in E_o, and since this is much greater than the change in e^-/QBIP for the same increment, the cross section had < 1% contamination arising from electrons. Close to threshold, the e^- yield became the major part of the total yield measured with the 600 MeV/c spectrometer. However, the π^- yield increases much more rapidly with E_o than the e^- yield, so again the cross section was not in error by more than a few percent.

The properties of the e^- yield determined above allow us to extend these conclusions to the 56^o, 84^o, and 120^o measurements with the 600 MeV/c spectrometer. The decrease in the e^- yield with increasing θ is matched by a corresponding decrease in the π^- cross section, so the relative magnitude of the contamination was

independent of angle. The "π^-" yields contained a contribution from electrons, varying from close to 100% near threshold to a few percent at large missing mass. The yields per equivalent quantum, shown in Table I, tended to approach small, non-zero values at the maximum p_o for given E_o because they were not corrected for this contamination. It is unfortunate that yield measurements with the 600 MeV/c were not carried below threshold in some cases, for this would have constituted a direct measurement of the electron yield. However, at $\theta = 84^o$, $p_o = 375$ MeV/c, and $E_o = 922$ MeV, we were just above the threshold of 882 MeV for this momentum and angle. The observed yield at this point, scaled to the aperture of the 1200 MeV/c spectrometer, gives an upper limit for the e^- yield of $(.03 \pm .01)$ counts/QBIP. This is quite consistent with the e^- yield measured with the 1200 MeV/c spectrometer at $\theta = 44^o$ and $p_o = 465$ MeV/c (see Table IX) if we use the angular dependence given by Thiessen.

In summary, the slow variation of the e^- yield with E_o prevented the occurrence of large errors in the cross section as a result of the inability to discriminate against electrons with the 600 MeV/c spectrometer. It did not seem reasonable to make a correction to the data on the basis of the available information, but it is felt that the cross sections measured with this spectrometer were systematically too large by no more than 2% at 30^o and 44^o, and by no more than 5% at 56^o, 84^o, and 120^o as a result of electron contamination.

We next consider accidental and dead time corrections. There were enough counters on the 1200 MeV/c spectrometer to eliminate accidental coincidences arising from uncorrelated events in the counters; this was the conclusion reached both by considering the known rates in the counters and the resolving times of the circuits,

and by measurements made with one or more counters delayed by a multiple of the period of the electrons in the synchrotron. The rates at the inputs of all coincidence circuits were sufficiently low that dead time corrections were negligible also.

The FAN veto circuit had an appreciable accidental rate when measurements were made at 4^{o} with the FAN counters on (see Section VI. B. 3), in the worst cases as high as 10% of the pion rate. To correct for these accidental vetoes, the accidental veto rate was monitored continuously. A TC-4 fast coincidence circuit ($FAN_D \cdot S1$), identical to the one used in the normal FAN logic ($FAN \cdot S1$), was added to the system. The FAN input to $FAN_D \cdot S1$ was delayed by 100 ns, so that all events vetoed by an output from this circuit were known to be accidentally vetoed. The number of pions in coincidence with the delayed FAN signal was scaled for each run, and this number was added to the net pion counts (which were vetoed by the $FAN \cdot S1$ output). The number of $FAN_D \cdot S1$ counts and $FAN \cdot S1$ counts in a given run were normally within 10% of each other, which gave us confidence that the number of pions in coincidence with the $FAN_D \cdot S1$ signal was a reasonably accurate measure of the number of pions accidentally vetoed by $FAN \cdot S1$. The average true FAN veto rate at 4^{o} determined in this way for each central momentum setting of the spectrometer was used as the FAN correction in the final analysis of all data obtained at 4^{o} when the FAN counters were turned off. This correction was determined independently for the full and empty target runs.

There was a correction applied to the data from the 1200 MeV/c spectrometer for what appeared to be correlated events in the counters of the momentum hodoscope, S2T, S2TC, S2BC, and S2B.

In addition to scaling the number of pions in each of these channels, the logical sum, (S2T + S2TC + S2BC + S2B), was also scaled. The sum of the number of pions in each individual channel always exceeded the number in the logical sum channel by about 2%. This phenomenon was investigated by Ecklund,[25] who found that occasionally a count would occur in two of the momentum channels from a single event. These pairs of counts generally occurred in adjacent channels, suggesting a charged secondary produced by scattering of the original particle was responsible for the spurious count. A correction was made for this effect by assigning the excess counts in each run

$$[(S2T) + (S2TC) + (S2BC) + (S2B)]_{\text{arithmetic sum}}$$

$$- [S2T + S2TC + S2BC + S2B]_{\text{logical sum}}$$

to the channels in the proportion

$$T : TC : BC : B = 1 : 2 : 2 : 1 \quad ,$$

and subtracting the numbers thus found from the counts in each channel. This proportion was chosen because the central channels (TC and BC) had twice as many adjacent channels as the highest and lowest channels.

The 600 MeV/c spectrometer was slightly susceptible to accidental coincidences in which one particle triggered the aperture counter and another triggered the remaining counters. The number of accidental coincidences of this type was monitored using

the same delayed coincidence technique described above for the FAN counters of the 1200 MeV/c spectrometer. The correction was made by reducing the observed number of pions by the number of events satisfying all the normal pion logic but in coincidence with a signal from the aperture counter delayed by 100 ns from its normal timing. The correction was rarely as much as 3%, and was normally less than 1%.

The momentum hodoscope of this spectrometer was also subject to "accidentals" or some kind of correlated particle events. However, the momentum channels of this spectrometer were defined by overlapping pieces of scintillator, with the consequence that if two particles passed through adjacent channels, the event would be recorded in only one channel. This type of event, which was the major source of "accidentals" in the hodoscope of the 1200 MeV/c spectrometer, caused only a slight redistribution but no excess of events in the 600 MeV/c spectrometer. The number of events in which a combination of hodoscope counters was triggered which could not be triggered by a single particle was very small; often there were no such events in a run, and rarely as many as 0.5%. No correction was included for such events.

No dead time correction was required for the fast electronics of the 600 MeV/c spectrometer. However, the data storage system required about 25 μs to record an event, which was a potential source of trouble at high trigger rates. The number of triggers of the data storage system which occurred while the system was busy with a previous event was scaled; this number was compared with the total number of triggers to determine the dead time correction. The correction was only about 1% for the Plexiglas target calibration runs (see Section VI. E. 1), and was completely negligible for all hydrogen target runs.

2. Empty Target Background

The walls of the liquid hydrogen target were a source of negative pions. The contribution from this source was eliminated by measuring the pion yield with liquid hydrogen removed from the target and subtracting the result from the yield with the target full. Because "ice" tended to accumulate on the target walls (Section VI. B. 2), background runs were normally taken within a week or so of the corresponding full target runs. The data were handled in batches, so that background runs could be subtracted from full target runs taken at the same time before results from different times were averaged.

Cross sections were measured at a large number of different kinematic points, and it seemed inefficient to measure the background at each point. Instead, the procedure adopted for a large part of the data was to measure the background at each angle and momentum but only in 100 MeV steps of E_o, i.e., the background was measured at only half of the points. At each of the points where the background was measured, the amount of synchrotron time spent with the target empty was about half of the time spent with the target full. The values of σ^* obtained with the target empty at given θ and E_o were averaged over all momentum channels and plotted versus p_o. A smooth curve was drawn through the data, and background at all points was taken from these smooth curves. For energies between the values of E_o for which empty target data were taken, the background was obtained by linear interpolation between the results at adjacent values of E_o. The statistical error assigned to the smoothed background values was taken to be the error in the measured value of σ^* after averaging over all momentum channels.

In order to put these results back into the computer, they were punched onto 'BSGSR' cards in the usual format, with background for the 600 MeV/c and the 1200 MeV/c spectrometers assigned "fake" run numbers starting with 4001 and 9001 respectively (see Section VI. C. 3).

Some representative values of the ratio of the empty target yield to the full target yield are shown in Figure 13. These curves were drawn for a fixed E_o near the middle of the range covered in this experiment, and were quite typical of the general situation. Near threshold, the empty target yield approached the full target yield. As p_o decreased, the fractional empty target rate dropped rapidly to a more or less constant value between 0. 1 and 0. 2. The measurements at 4^o presented a special problem because the empty target rate never dropped below 30% of the full target rate. The reason for this large background was investigated, and it was found that the entrance and exit windows of the hydrogen target vacuum jacket and some of the air path downstream from the hydrogen target were additional sources of pions visible to the spectrometer at this small angle. The helium bag placed in the beam line from the hydrogen target to the aperture of the 1200 MeV/c spectrometer during the second half of the experiment eliminated part of this additional source, reducing the pion background at 4^o by about 20%; the values shown in Figure 13 were obtained with this helium bag in place. Because the background at 4^o was such a large fraction of the full target rate, the empty target yield was measured at every point for data batches 2 and 3 at 4^o, and equal amounts of time were spent at each point with the target empty and full.

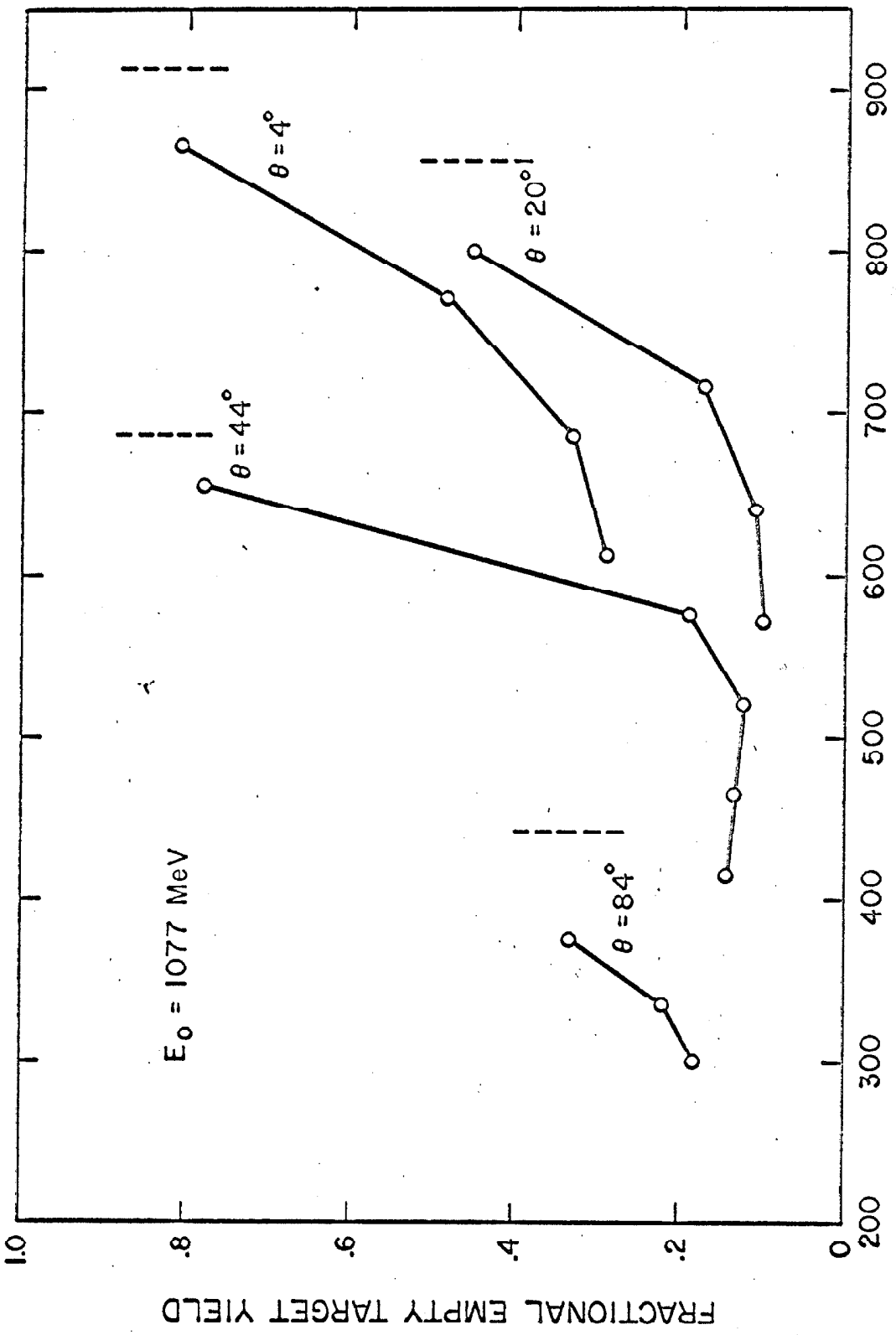

Figure 13. Fractional empty target π^- yield at some representative points. The dashed lines near the highest momentum point at each angle indicate the maximum π^- momentum which can be produced at that angle by a 1077 MeV photon in the reaction $\gamma + p \rightarrow \pi^- + \pi^+ + p$.

3. Nuclear Absorption

Some of the pions produced in the target were not counted because they suffered nuclear interactions in matter before traversing all of the counters in the spectrometer. The matter which the pions had to penetrate included liquid hydrogen, the walls of the target and its vacuum shield, several meters of air, and the counters in the spectrometer. Detailed tabulations of all material in each spectrometer were given by Thiessen and Ecklund. Each of these investigators discussed the absorption correction for the spectrometer he used, and evaluated the correction for detection of positive pions as a function of momentum. We consider the correction for negative pions for each spectrometer separately.

Most of the pion absorption in the 600 MeV/c spectrometer occurred in the rear counters. In order to find the loss in these counters, Thiessen (and the author) measured the fraction of pions (π^+) which counted in all counters except the last scintillator (S2) when additional absorbing material was inserted in the system at various distances from S2. The results of these measurements were tabulated by Thiessen. The pion loss for each of these configurations was also calculated by Thiessen, using published data for π^+ scattering from hydrogen and carbon. For the "best geometry" measurements (additional absorber farthest from S2), the measured attenuation was in excellent agreement with the calculated result for π^+ momentum from 300 to 570 MeV/c. In the normal configuration, all of the rear counters were close enough to S2 to constitute "bad geometry" scatterers. Thiessen defined a geometrical factor, η, for each counter as the ratio of the loss, measured when the distance from the absorber to S2 was the same

as the distance from that counter to S2, to the loss calculated for "good geometry". The known thickness and chemical composition of each counter were used to calculate the thickness in g/cm^2 of hydrogen and of complex nuclei. The heavy nucleus content was reduced to an equivalent thickness of carbon using an $A^{2/3}$ dependence for the cross section per nucleus. The carbon and hydrogen thicknesses of each counter were then multiplied by the geometrical factor, η, and summed to give the total effective mass of carbon and of hydrogen for the whole system. The hydrogen target, air, and aperture counter, for which the geometrical factors were all consistent with unity, were included in the sum. Published cross sections were then used to calculate the total π^+ loss due to nuclear absorption.

A similar procedure was adopted to evaluate the π^- absorption; the details of this calculation are shown in Table X. The results differed only slightly from those for π^+ absorption because the heavy nucleus total absorption cross section, which contributed most of the absorption, is nearly the same for π^+ and π^-. The hydrogen cross sections are also quite similar except at the lowest momenta observed with this spectrometer. The total absorption calculated for a pure pion beam was reduced by the fraction of events which were pions, since muons have much smaller interaction cross sections. The absorption obtained by linear interpolation in the final column of Table X was used to correct all data measured with the 600 MeV/c spectrometer. An additional correction of 3% was applied to the 30^o data; when the 600 MeV/c spectrometer was at this angle, the pions passed through the aluminum wall of the downstream snout of the hydrogen target at a small angle of incidence, giving a long additional path in aluminum. Because of the statistical

TABLE X

Calculation of Nuclear Absorption for the 600 MeV/c Spectrometer*

p (MeV/c)	σ_{abs} carbon (mb)	π^- - C absorption (%)	σ_a (π^--p) (mb)	π^- - p absorption (%)	π^- beam absorption (%)	Fraction of π^- in beam	Total absorption (%)
198	340[b]	6.85	22	.60	7.45	.79	5.9
233	360[b]	7.24	43	1.14	8.38	.80	6.7
259	360[f]	7.24	57	1.55	8.79	.82	7.2
282	355[f]	7.14	66	1.79	8.93	.83	7.4
305	355[f]	7.14	65	1.76	8.90	.84	7.5
332	350[c]	7.05	46	1.25	8.30	.85	7.1
354	325[c, d]	6.55	40	1.09	7.64	.85	6.5
376	325[c]	6.55	38	1.04	7.59	.86	6.5
398	300[f]	6.07	35	.96	7.03	.87	6.1
522	240[f]	4.89	27	.74	5.63	.89	5.0
625	230[e]	4.69	33	.90	5.59	.90	5.0
727	225[e]	4.59	43	1.14	5.73	.91	5.2

* Calculated for .458 g/cm^2 of hydrogen and 4.16 g/cm^2 carbon equivalent.

a G. Källén, Elementary Particle Physics (Addison-Wesley Publishing Company, Inc., Reading, Massachusetts, 1964), p. 73.

b R. L. Martin, Phys. Rev. 87, 1052 (1952).

c A. E. Ignatenko, et al., Soviet Phys. - JETP 4, 351 (1957).

d V. P. Dzhelepov, et al., Soviet Phys. - JETP 4, 864 (1957).

e M. Crozon, et al., C. R. Congrès International de Physique Nucléaire, 1964. Vol. 2, p. 222.

f Interpolated value.

errors in the π^+ absorption measurements, uncertainties in the appropriate cross section to use for absorption by heavy nuclei, and the lack of absorption measurements made directly with negative pions, an error of 50% of the correction was estimated for the absorption correction. This implies a 3-4% normalization error in the cross sections measured with the 600 MeV/c spectrometer.

Nuclear absorption in the 1200 MeV/c spectrometer also occurred mostly in the rear counters and in the 1/2 in. of lead placed ahead of the last scintillator (S3). Ecklund evaluated the loss for π^+ detection on the basis of the S3 efficiency for particles triggering all other counters, which was measured during his normal data runs, and some transmission measurements made by placing additional absorbers in the system. The loss produced by the remaining material in the system was calculated assuming the cross section for a nucleus of atomic weight A was given by $\sigma_e A^{2/3}$, and using a value for the cross section per nucleon, σ_e, deduced from his transmission measurements.

Published data for the absorption of pions in carbon show that the π^- absorption cross section is essentially constant (230 mb) over the entire momentum range of the 1200 MeV/c spectrometer,[47] and that the π^+ and π^- absorption cross sections differ at most by a few percent from 800 to 1200 MeV/c,[4-8] with the π^- cross section being the larger. Unfortunately, there did not seem to be enough published data for pion scattering from carbon in the "intermediate range" of 425 to 625 MeV/c to draw any firm conclusion, so we could only interpolate the results at higher and lower momenta and assume the cross sections are comparable for π^+ and π^- in this range also. The π^+ - p total cross section is

much larger than the π^- - p cross section at low momentum, but drops rapidly until they become equal at about 530 MeV/c. The π^- - p cross section then becomes the larger one, and remains roughly a factor of two larger from 700 to 1100 MeV/c.[49]

Since hydrogen constituted only about 10% of the mass of the absorbing material, it seemed reasonable to use the same correction for π^- absorption that Ecklund found for π^+ absorption. The correction was expressed in the form

$$C_{OBS} = (.956)\,[1 - (.117 - .056\,p)]\,C_{TRUE}$$

where C_{OBS} = measured number of events,

C_{TRUE} = number of events which would be measured with no nuclear absorption loss,

p = particle momentum in GeV/c.

The first factor above was the correction for absorption in liquid hydrogen, the target walls and shield, air, aperture counters A1 and A2, and the freon Cherenkov counter. Ecklund gave a slight angular and momentum dependence for this factor, but the variation was so small that we simply used the average value. The second factor above was the correction for absorption in counters S1, S2, and LC and the 1/2 in. of lead ahead of S3. The absorption correction for this spectrometer is seen to be about twice as large as that for the 600 MeV/c spectrometer, varying from 13.3% at 500 MeV/c to 10.5% at 1000 MeV/c.

As a check on the absorption correction for the 1200 MeV/c spectrometer, the "S3 miss rate" (fraction of pions triggering all counters except S3) was measured at 600 MeV/c using negative pions. The result, $(8.6 \pm 0.3)\%$, was somewhat higher than the value $(7.3 \pm 0.3)\%$ measured by Ecklund with positive pions, but consistent with our knowledge of the basic cross sections at this momentum. Ecklund estimated the accuracy of the absorption correction to be about 10% of the correction. Allowing some additional uncertainty for the extension of his results to negative pions, the error was estimated to be no greater than 25% of the correction, which implies a 3-4% normalization error in the π^- cross sections measured with the 1200 MeV/c spectrometer.

4. Pion Decay

The distance from the hydrogen target to the last counter of either spectrometer was sufficiently great that an appreciable fraction of the pions, typically 20%, decayed before reaching the last counter. Correction for this effect would be no problem except that essentially 100% of the decays proceed via $\pi^- \rightarrow \mu^- + \bar{\nu}$, and μ^- were indistinguishable from π^- in our apparatus. Therefore, it was necessary to determine the resolution function for muons, a complicated geometrical problem. This problem was studied extensively in the past by investigators of the reaction $\gamma + p \rightarrow \pi^+ + n$; a summary of their work was given by Thiessen.[24]

The decay correction has two effects on the spectrometer resolution: it changes the area of the resolution function, and it changes its shape. The most significant effect on the shape is to

add a long tail at high momentum. There is a cutoff on this tail, set by the kinematics of the pion production reaction and the synchrotron energy. For single π^+ photoproduction, the kinematic cutoff normally occurred for momenta only moderately greater than the central momentum, $\frac{p - p_o}{p_o} \lesssim .2$, because the synchrotron energy was kept only slightly greater than the photon energy of interest. However, in this experiment data were obtained under conditions where $\frac{p - p_o}{p_o}$ could be as large as 0.8: this had to be done in order to measure the cross section at large missing mass values (see Figure 2). There is a low momentum cutoff to the muon resolution function at $\frac{p - p_o}{p_o} \approx -.2$; this limit is set by the kinematics of pion decay and the spectrometer geometry, and so does not depend on the production reaction.

In the analysis of this experiment, no attempt was made to unfold the effects of the finite width of the momentum and angular resolution because the width of the photon energy resolution function determined the resolution in missing mass. Therefore, we were interested only in the change in area of the spectrometer resolution function resulting from pion decay. The method used to evaluate the correction was the same as that described by Thiessen, except that the kinematic conditions for two pion production were used to fix the high momentum cutoff of the muon acceptance. A Monte Carlo program for calculating the muon acceptance, written originally by Kilner[42] and modified by Thiessen, was used to calculate the acceptance for each spectrometer for larger values of $\frac{p - p_o}{p_o}$ than had been done by Thiessen and Ecklund. The solid angle for

accepting the decay muon from a pion with momentum p when the magnet is set at p_o, over the entire range of $\frac{p - p_o}{p_o}$ for which it has been calculated with this program, is shown for both spectrometers in Figures 14 and 15. These results were for a 3 in. x 9 1/2 in. aperture counter in the 600 MeV/c spectrometer, and a 3 in. x 9 in. aperture counter in the 1200 MeV/c spectrometer. It was assumed that the solid angle for some other aperture counter could be obtained by scaling according to the area of the counter. Furthermore, these results were obtained for the "central channel" of each spectrometer, i.e., for channel D of the 600 MeV/c spectrometer, and for a channel the size of BC centered on the central ray for the 1200 MeV/c spectrometer. It was assumed that the fraction of events which were muons in any other channel with mean momentum p_i was the same as that in the central channel would have been if the central magnet momentum were p_i:

$$\frac{\Delta\Omega(q, p_i)_{\mu,i}}{(\Delta\Omega\,\Delta p)_{\pi,i}} = \left.\frac{\Delta\Omega(q, p_c)_{\mu,c}}{(\Delta\Omega\Delta p)_{\pi,c}}\right|_{p_c = p_i}$$

where $q = \frac{p - p_i}{p_i}$

$\Delta\Omega(q, p_i)_{\mu,i}$ = muon solid angle for the i^{th} channel (given for the central channel in Figures 14 and 15),

$(\Delta\Omega\Delta p)_{\pi,i}$ = total pion acceptance of the i^{th} channel (given in Tables VII and VIII),

and the subscript c denotes the central channel.

Figure 14

600 MeV/c spectrometer resolution functions for pions which decay in flight. The data with error bars are the results from the Monte Carlo calculation. The smooth curve is obtained from a quadratic fit to the results as a function of P0 at each value of (P - P0/P0).

P0 = spectrometer central momentum.

P = pion momentum in the target.

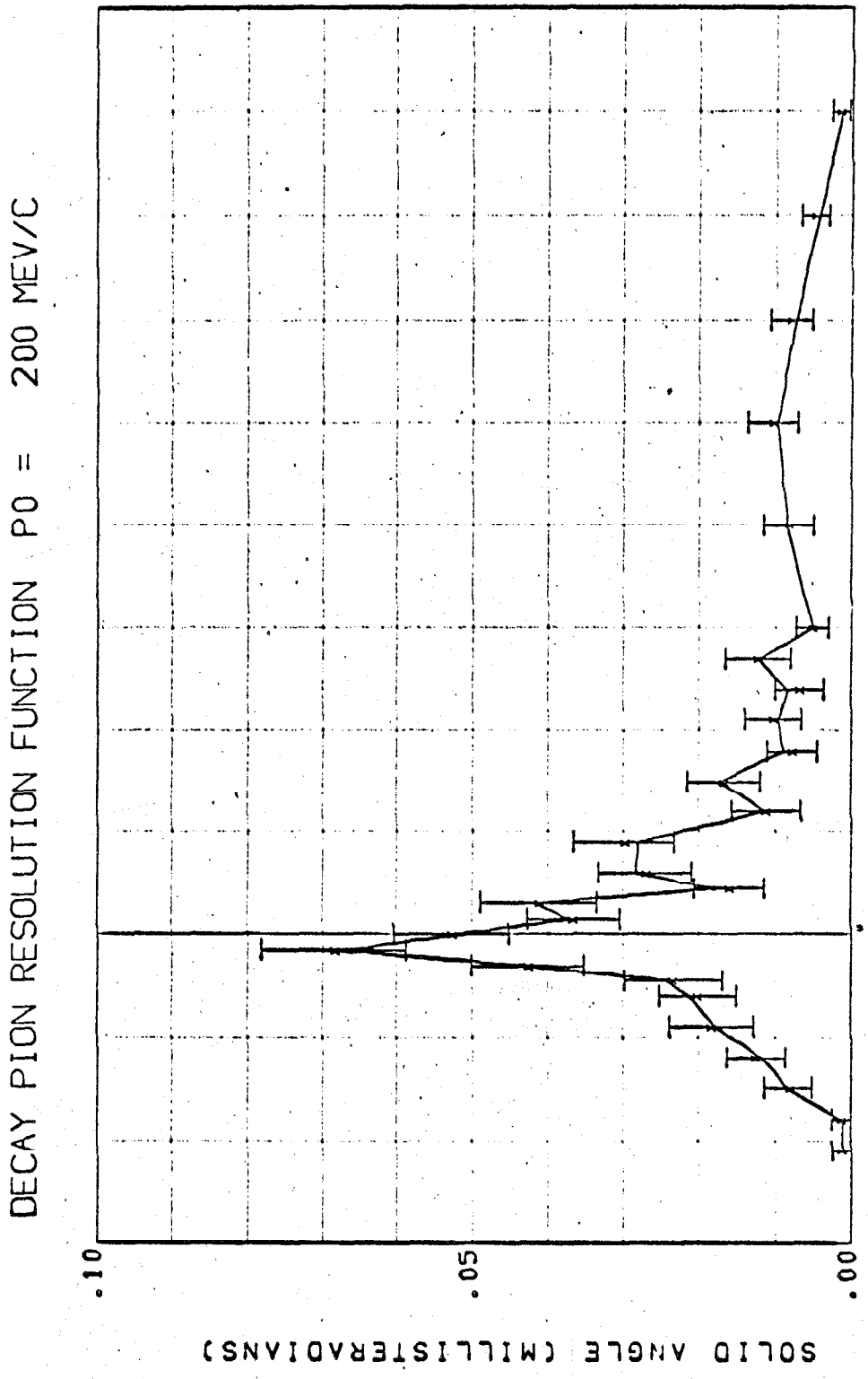

Figure 14.1. Decay pion resolution function for the 600 MeV/c spectrometer.

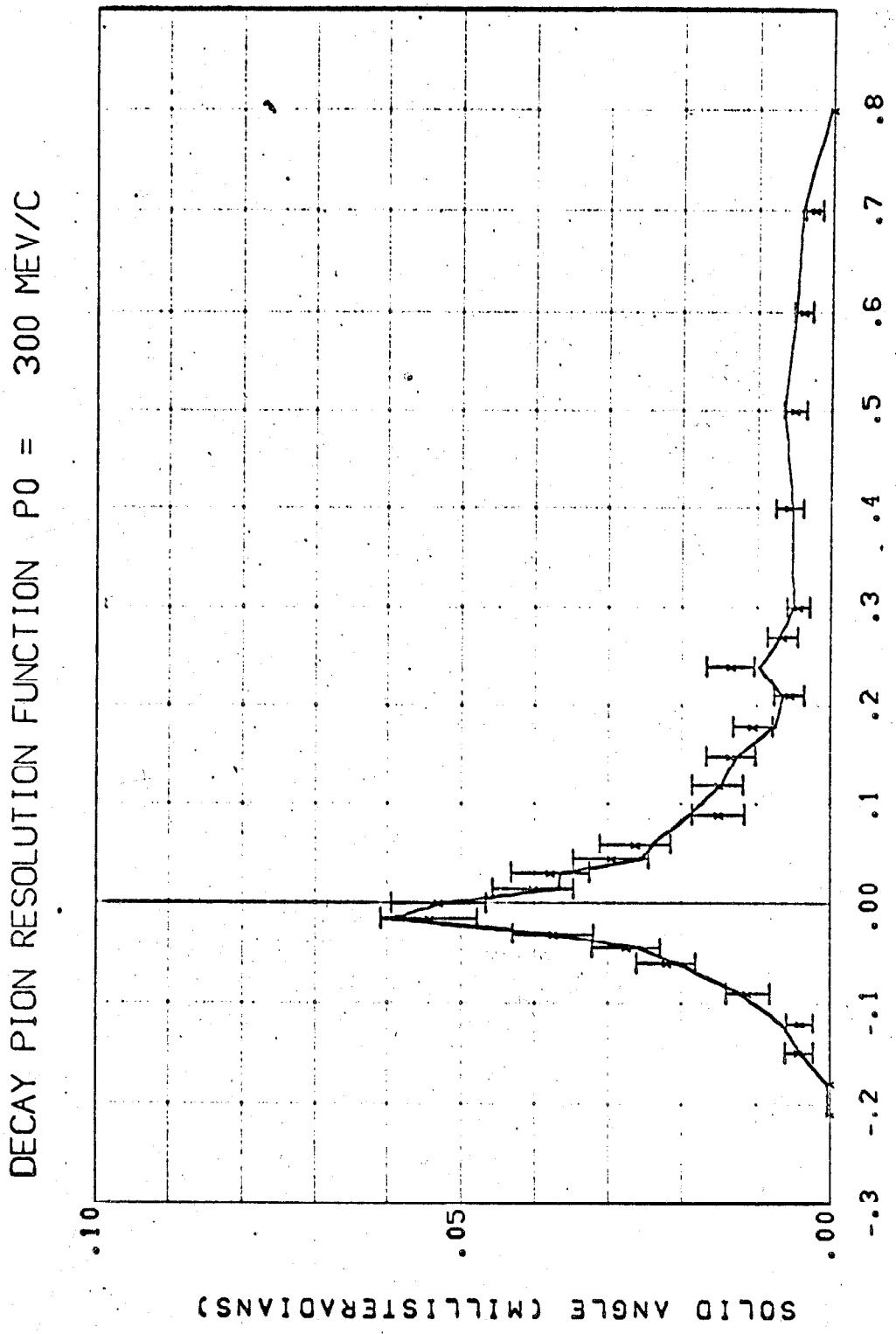

Figure 14.2. Decay pion resolution function for the 600 MeV/c spectrometer.

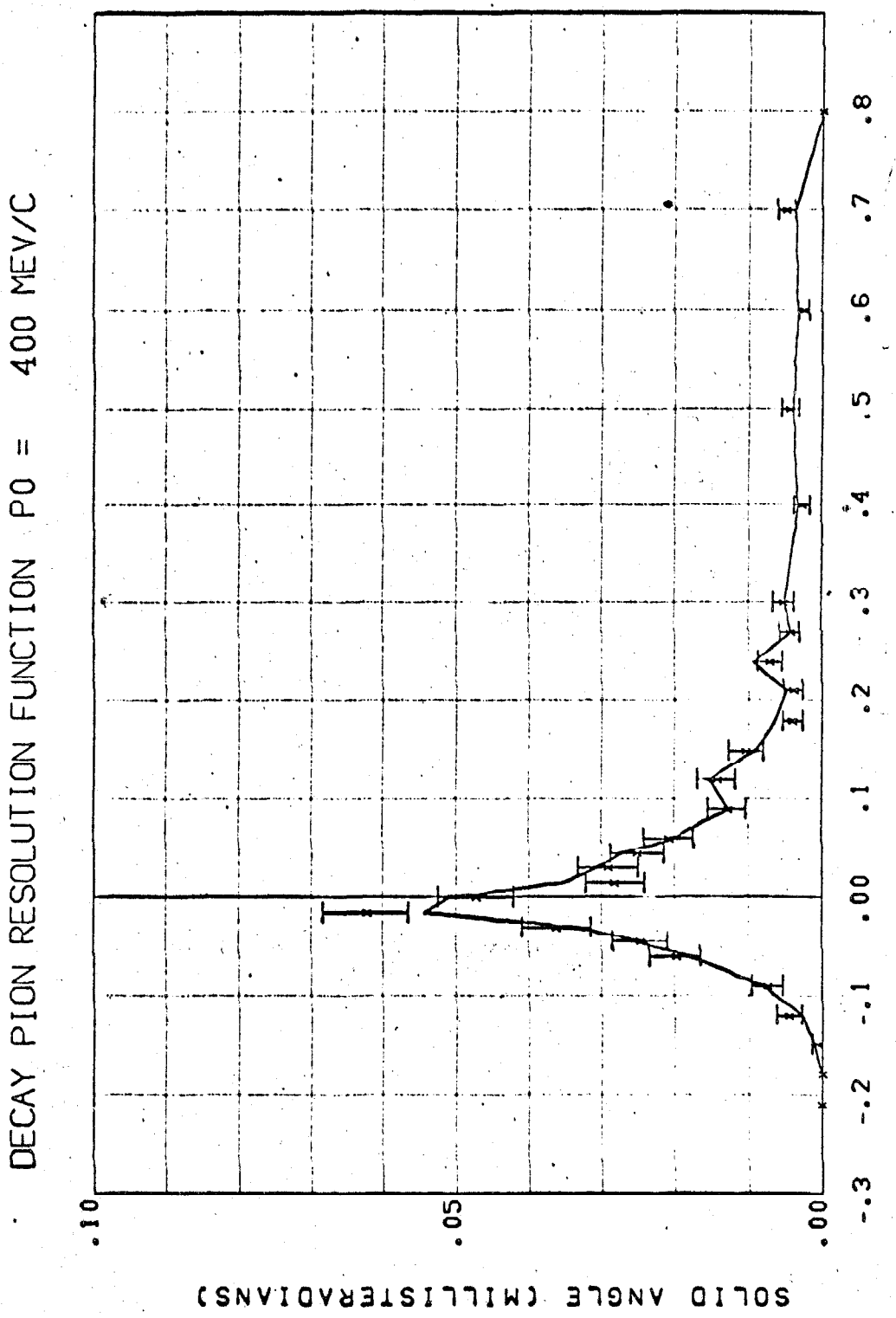

Figure 14.3. Decay pion resolution function for the 600 MeV/c spectrometer.

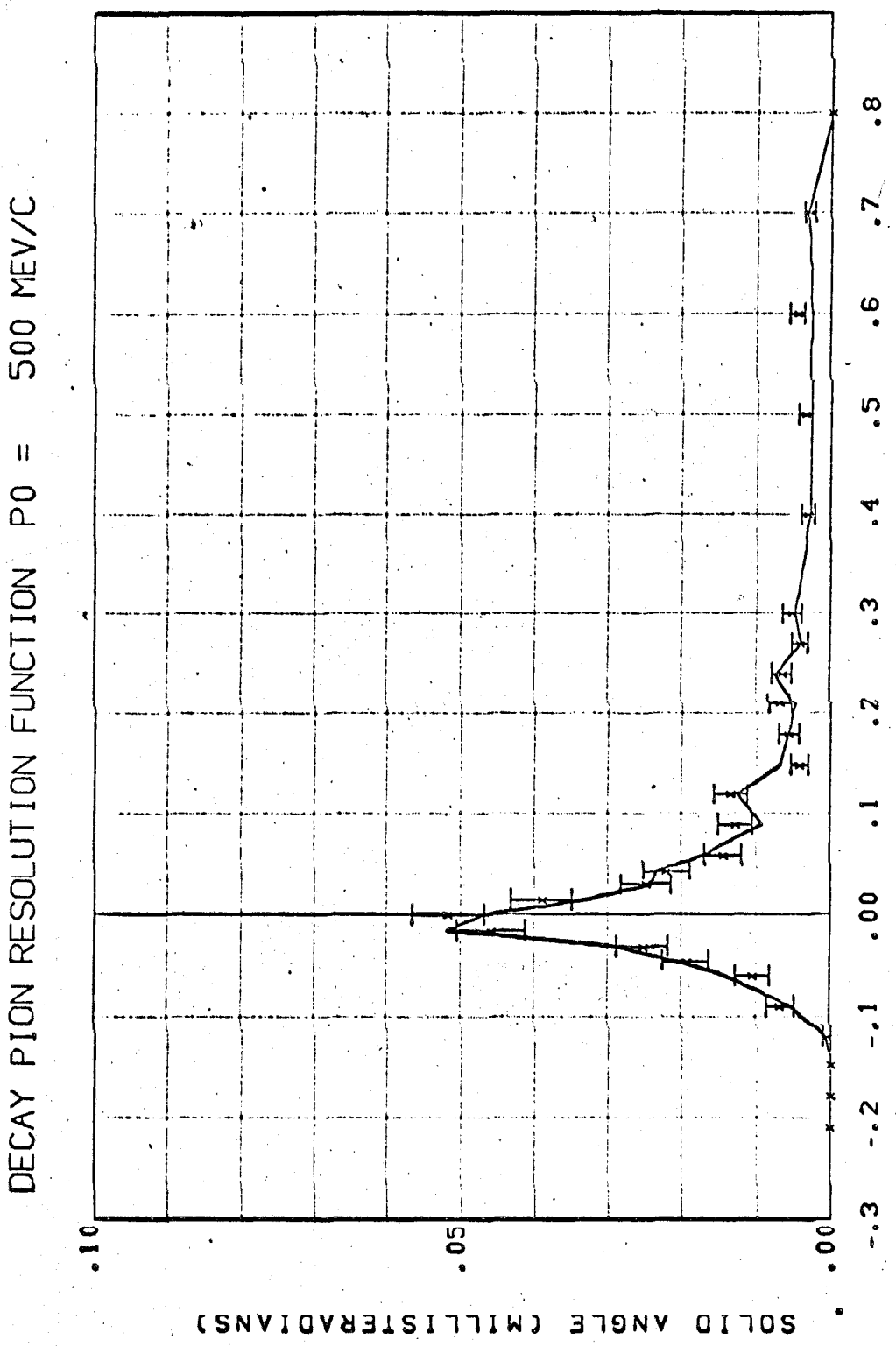

Figure 14.4. Decay pion resolution function for the 600 MeV/c spectrometer.

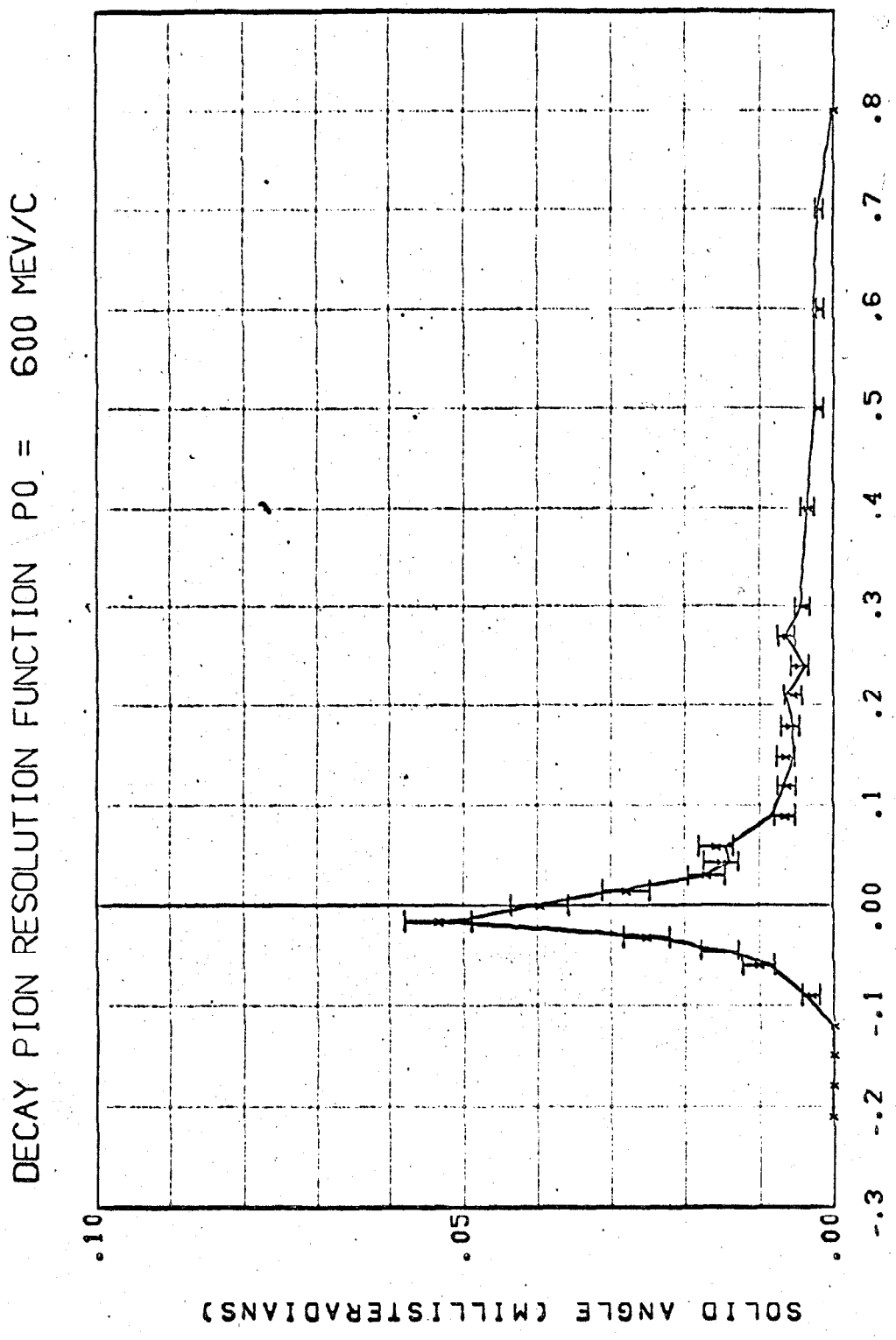

Figure 14.5. Decay pion resolution function for the 600 MeV/c spectrometer.

Figure 15

1200 MeV/c spectrometer resolution functions for pions which decay in flight. The data with error bars are the result from the Monte Carlo calculation. The smooth curve is obtained from a quadratic fit to the results as a function of P0 at each value of (P - P0/P0).

P0 = spectrometer central momentum.

P = pion momentum in the target.

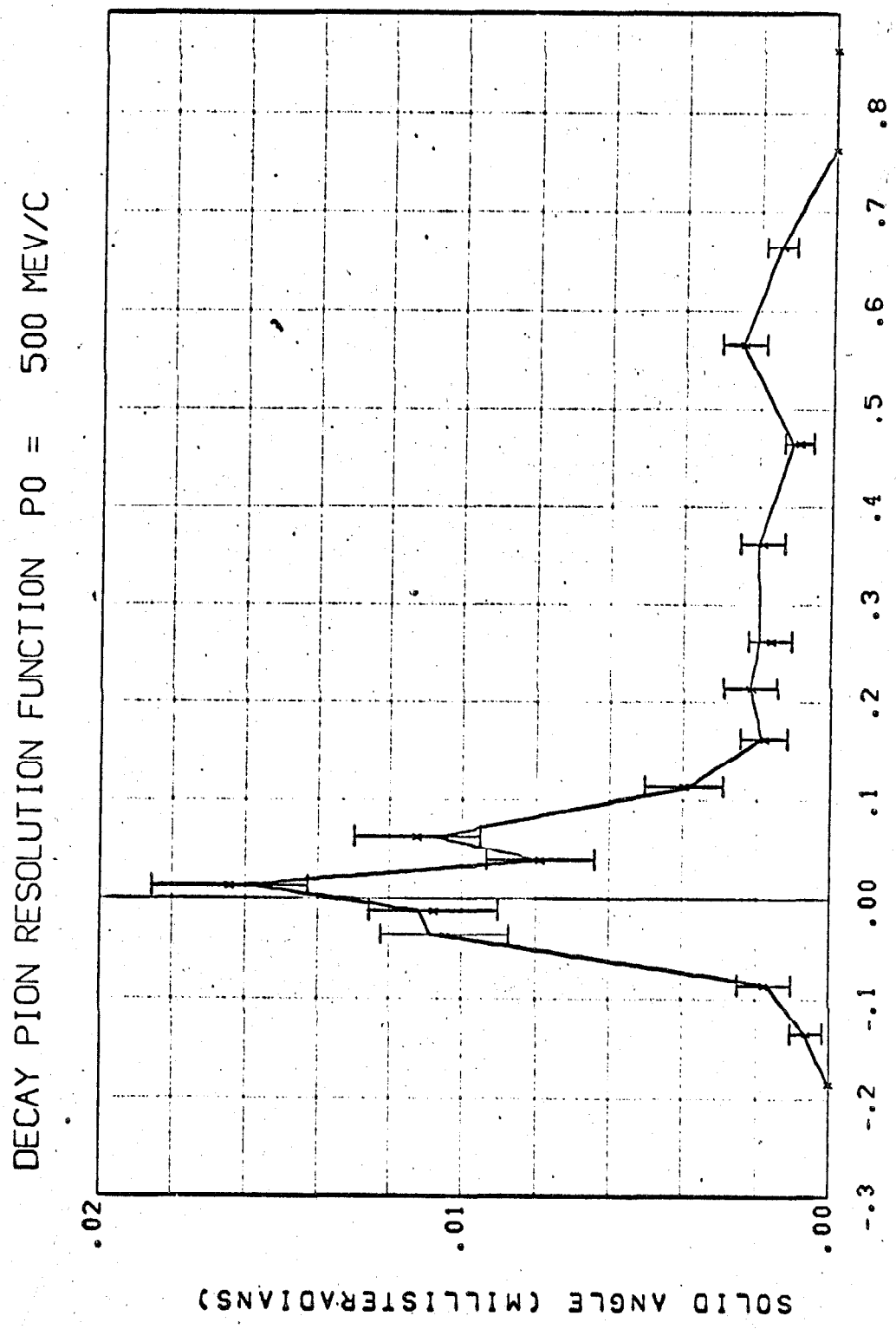

Figure 15.1. Decay pion resolution function for the 1200 MeV/c spectrometer.

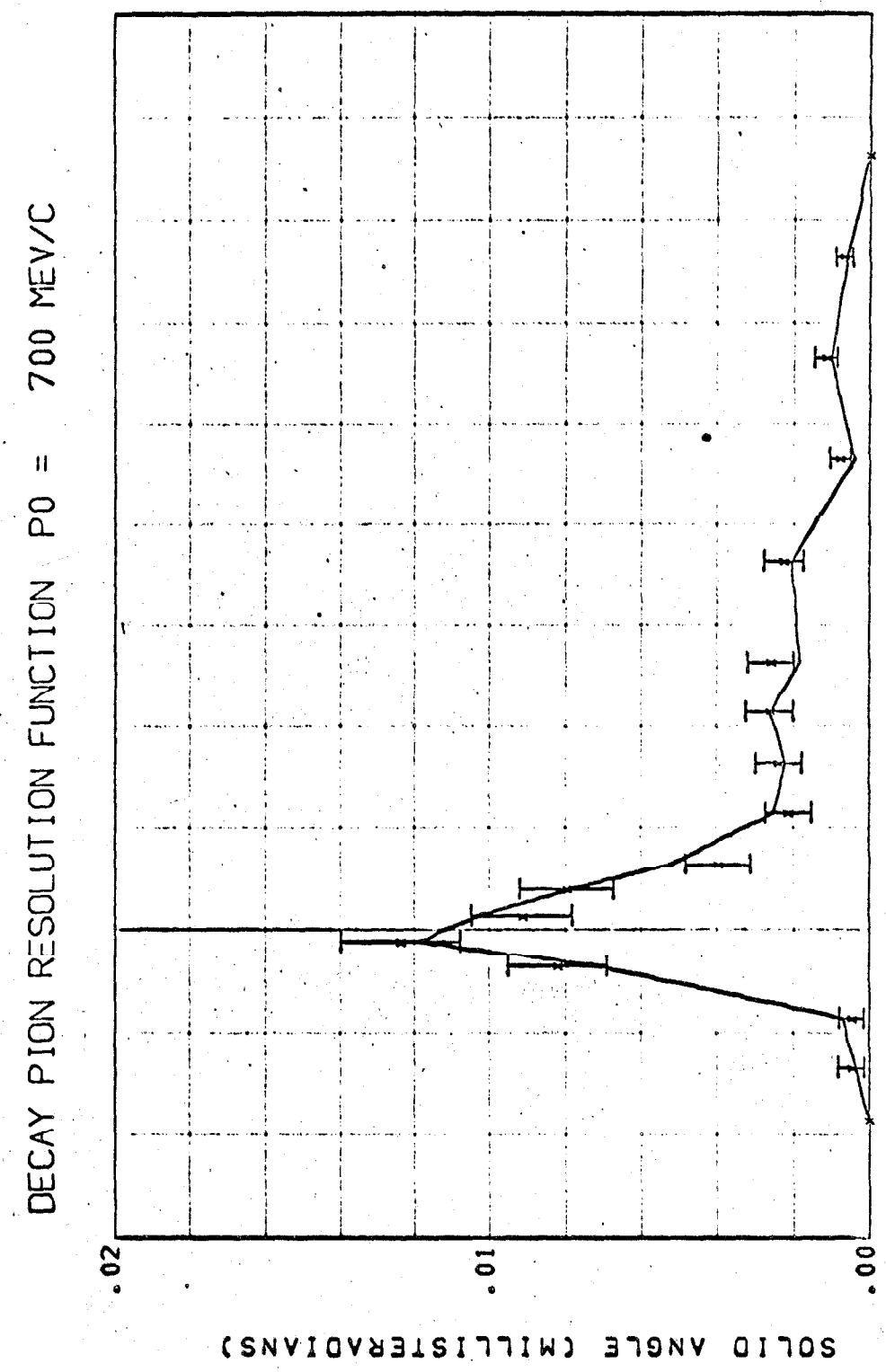

Figure 15.2. Decay pion resolution function for the 1200 MeV/c spectrometer.

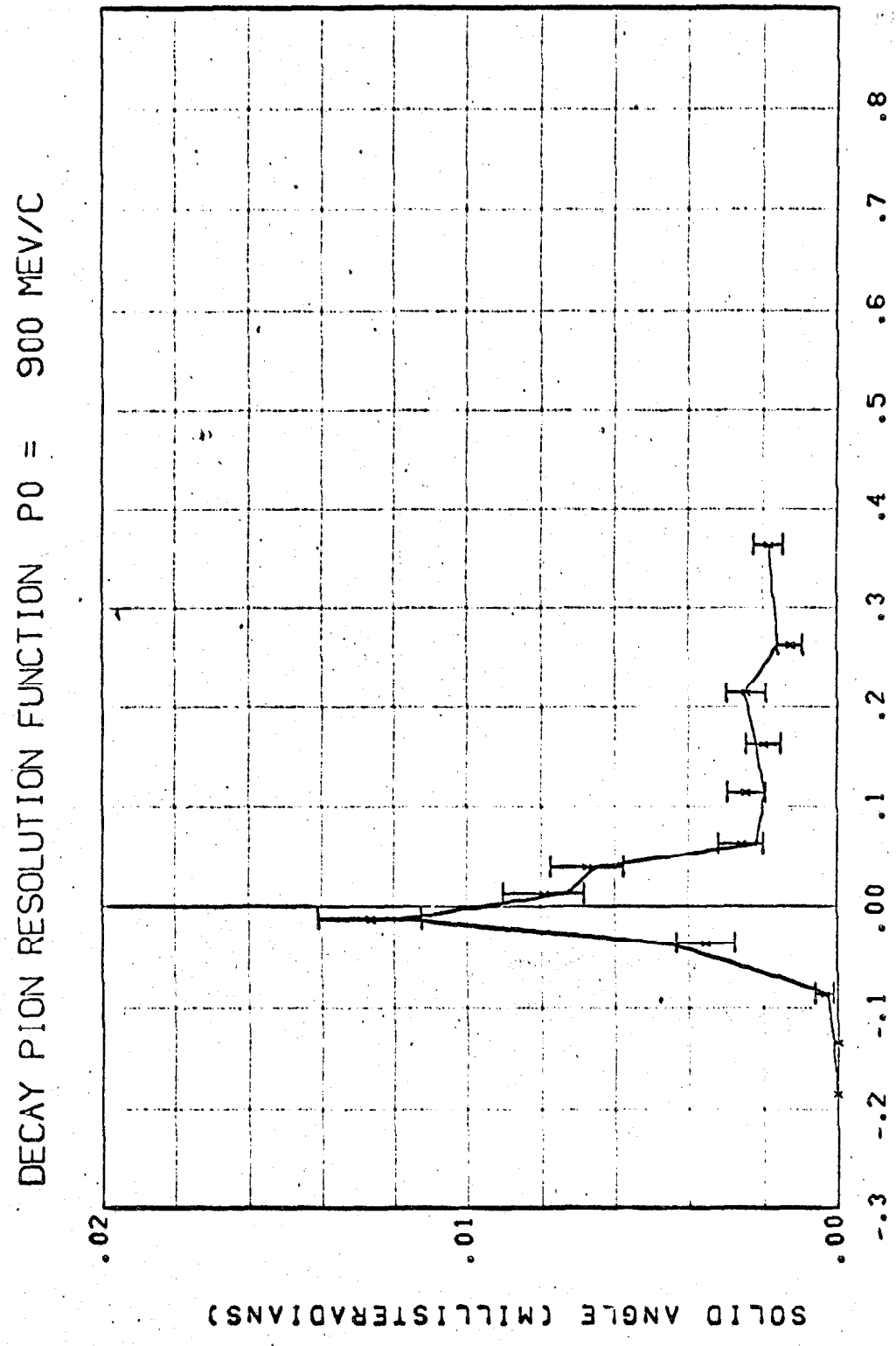

Figure 15.3. Decay pion resolution function for the 1200 MeV/c spectrometer.

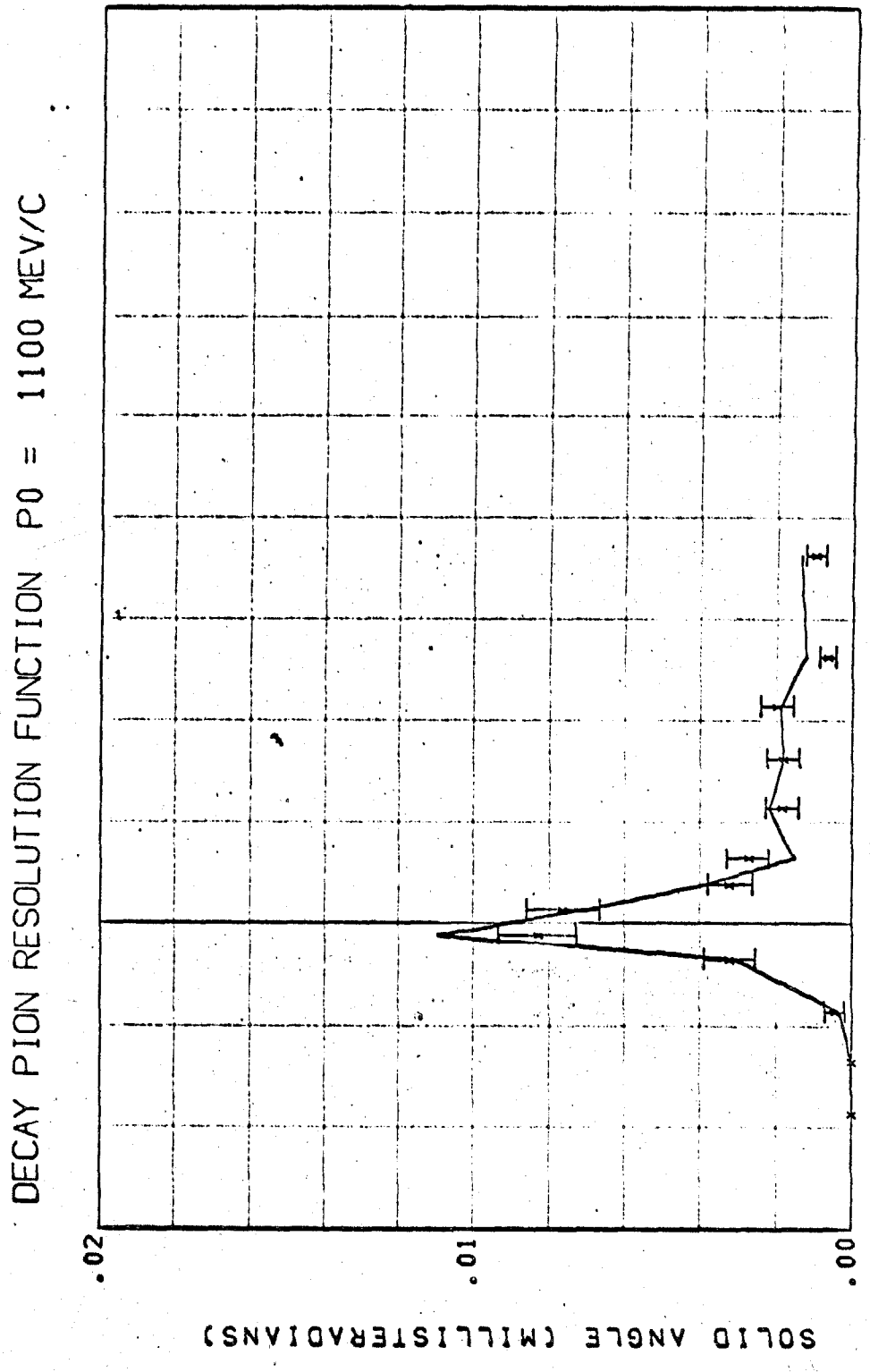

Figure 15.4. Decay pion resolution function for the 1200 MeV/c spectrometer.

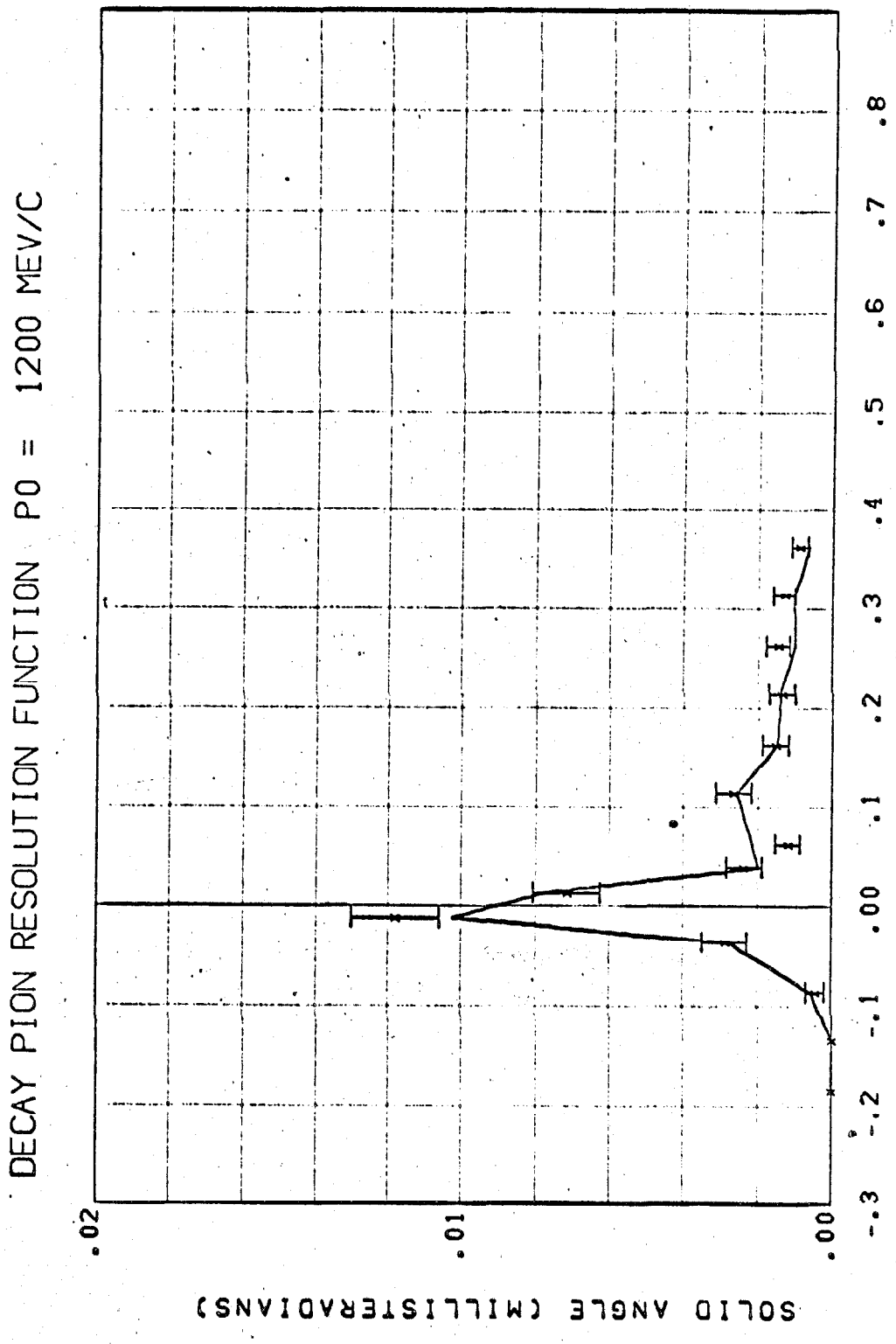

Figure 15.5. Decay pion resolution function for the 1200 MeV/c spectrometer.

The muon solid angle of the central channel was computed only for a small number of central momentum values. In order to obtain the solid angle for arbitrary central momentum, a quadratic function of p_o was fitted to the calculated values at each value of q:

$$\Delta\Omega(q, p_o)_{\mu,c} = A(q) + B(q)\, p_o + C(q)\, p_o^2 \ .$$

The parameters A, B, and C obtained from the data in Figures 14 and 15 are listed in Tables XI and XII.

Since we were only interested in the area of the resolution functions, the above relations were integrated over the momentum, p, to obtain finally:

$$\frac{\Delta\Omega\Delta p}{p_o}(q_{max})_{\mu,i} = \frac{(\Delta\Omega\Delta p/p_o)_{\pi,i}}{(\Delta\Omega\Delta p/p_o)_{\pi,c}}[a + bp_i + cp_i^2]$$

where $$a(q_{max}) = \int_{-\infty}^{q_{max}} A(q)\, dq$$

$$q_{max} = \frac{p_{max} - p_i}{p_i}$$

$p_{max}(E_o, \theta)$ = maximum π^- momentum which can be produced at lab angle θ when the synchrotron energy is E_o,

and $b(q_{max})$ and $c(q_{max})$ are defined analogously to $a(q_{max})$. The parameters a, b, and c were tabulated using trapezoidal integration of the values in Tables XI and XII, and linear interpolation in the resulting tables gave the total muon acceptance for arbitrary values of q_{max}.

Thus, the total acceptance of the i^{th} channel of either spectrometer, required in equation (6) of Section III. A, was obtained as follows:

$$(\Delta\Omega\Delta p)_i = p_o \left\{ \left(\frac{\Delta\Omega\Delta p}{p_o}\right)_{\pi,i} \exp\left(\frac{-mL}{p_i\tau}\right) + \left[\frac{\Delta\Omega\Delta p}{p_o}(q_{max})\right]_{\mu,i} \right\}$$

where p_o = spectrometer central momentum

p_i = mean momentum of the i^{th} channel

m = π^- mass

L = length of π^- flight path

$$= \begin{cases} 421 \text{ cm for the 600 MeV/c spectrometer} \\ 660 \text{ cm for the 1200 MeV/c spectrometer} \end{cases}$$

τ = π^- lifetime (2.55×10^{-8} sec).

Both the pion and muon acceptances in the above equation were adjusted for the size of the aperture counter actually used. The error in the total resolution function resulting from this method of calculating the decay correction was estimated to be 1%.

TABLE XI

Parameters for Evaluation of the Solid Angle for Detection of Muons in the Central Channel of the 600 MeV/c Spectrometer

$\frac{p - p_o}{p_o}$	A	$B(MeV/c)^{-1}$	$C(MeV/c)^{-2}$
- .21	.038 x 10^{-4}	- .170 x 10^{-7}	.180 x 10^{-10}
- .18	.037	- .165	.175
- .15	.218	- .829	.778
- .12	.271	- .932	.808
- .090	.333	- .922	.716
- .060	.176	.350	- .836
- .045	.128	.842	-1.36
- .030	.526	- .496	.030
- .015	.910	-1.45	1.34
0.0	.456	.543	-1.02
.015	.351	.196	- .476
.030	.499	- .352	- .322
.045	- .148	2.20	-2.86
.060	.382	- .550	.257
.090	.544	-1.60	1.38
.12	- .059	1.17	-1.61
.15	.299	- .744	.557
.18	.133	- .262	.219
.21	.209	- .723	.800
.27	.305	-1.17	1.29
.30	.042	.054	- .085
.40	.192	- .678	.696
.50	.197	- .609	.538
.60	.148	- .462	.432
.70	.041	.034	- .110
.80	.046	- .205	.218

TABLE XII

Parameters for Evaluation of the Solid Angle for Detection of Muons in the Central Channel of the 1200 MeV/c Spectrometer

$\frac{p - p_o}{p_o}$	A	$B(MeV/c)^{-1}$	$C(MeV/c)^{-2}$
- .186	0.	0.	0.
- .136	$.201 \times 10^{-5}$	$- .334 \times 10^{-8}$	$.137 \times 10^{-11}$
- .086	.643	-1.28	.659
- .036	2.52	-3.57	1.42
- .011	.608	1.50	- .964
.014	4.18	-6.83	3.33
.039	.243	1.92	-1.63
.064	3.51	-6.40	3.04
.114	1.05	-1.81	.958
.164	- .035	.657	- .420
.214	- .110	.975	- .639
.264	.165	.140	- .163
.364	- .015	.666	- .494
.464	.135	- .083	0.
.564	.558	- .634	0.
.664	.334	- .381	0.
.764	0.	0.	0.
.864	0.	0.	0.

5. Photon Beam Contamination

During the 1965 phase of this experiment, two characteristics of the photon beam line configuration were potential sources of systematic beam monitoring errors. There was a long air path and a liquid hydrogen target used by another experimental group (from UCLA) between our sweeping magnet and our hydrogen target; the sweeping magnet shown close to our hydrogen target in Figure 3 was not used in 1965. An appreciable number of pair-produced electrons could accumulate in the beam by the time it reached our hydrogen target. Since electroproduction cross sections are much smaller than photoproduction cross sections, these electrons would not contribute noticeably to pion production, yet their energy was included in the total beam energy measured by the quantameter. In addition, at that time the quantameter was inserted into the beam at the position of the large sweeping magnet shown in Figure 3; because there was a scraping wall between this position and our hydrogen target, it was possible that some of the beam energy recorded by the quantameter did not reach the hydrogen target.

The presence of such sources of error was suggested by analysis of the Plexiglas target calibration runs (see Section VI. E. 1) and of systematic shifts between the cross sections measured in 1965 and 1966 (see Section VI. E. 3). Both of these analyses suggested the cross sections were lower in 1965 by about 4%. In order to confirm that the electron content of the photon beam could have been of this magnitude in 1965, a test was conducted after the completion of the experiment. (The author is indebted to Mr. F. B. Wolverton for volunteering the synchrotron time necessary to make this test and

for assistance in performing it.) The UCLA hydrogen target, which was the target used in the K^+ photoproduction experiment by Groom and Marshall,[39, 50] introduced 6 in. (.018 radiation lengths) of liquid hydrogen and .03 in. (.002 radiation lengths) of Mylar into the photon beam. The test consisted of measuring the fraction of the beam energy contributed by electrons at the position of the second sweeping magnet shown in Figure 3. This was accomplished by measuring the ratio of the quantameter responses with the sweeping magnet on and off, using the thin ionization chamber, TC-1, as a monitor. The quantameter and TC-1 were located in the positions shown in Figure 3. Because the UCLA hydrogen target could not be filled at the time of the test, a 1/4 in. piece of Plexiglas (.017 radiation lengths) was used to simulate the target. The results of six runs of 10 TC-1 BIPS each made within a period of half an hour under conditions of virtually constant synchrotron beam intensity are shown below:

Run	Sweep Magnet	Q/TC-1
1	Off	2.198
2	Off	2.198
3	On	2.165
4	On	2.175
5	Off	2.201
6	On	2.169

The average difference between the runs with sweep magnet on and off was

$$\frac{(Q/TC-1)_{Off} - (Q/TC-1)_{On}}{(Q/TC-1)_{Off}} = .013 \pm .001 \ .$$

The fraction of the beam which was expected to produce pairs in the 1/4 in. of Plexiglas and 32 in. of air between the UCLA target and the sweep magnet was 1.6%, in good agreement with the above measurement.

In 1965, the entire 14 ft. (.015 radiation length) air path between the UCLA target and our target was an electron source, leading one to expect that about 2.7% of the beam at our target was electrons. In 1966, the second sweeping magnet and the He bag from the exit of this magnet to the hydrogen target guaranteed that the beam was virtually free of electrons. Because it was not easily possible to measure the additional error introduced by the scraping wall between the quantameter and the hydrogen target in 1965, it was decided that the observed 4.3% increase between 1965 and 1966 of the Plexiglas target calibration run yield measured with the 3 in. x 9 in. aperture counter in the 1200 MeV/c spectrometer constituted the best determination of the correction which should be applied to the data. Therefore, the 1965 data from both spectrometers were multiplied by a factor of 1.043, and an error of 2% was included in the overall systematic error as an estimate of the uncertainty in this procedure.

6. Contribution from Three Pion Production

We consider in this section the problem of evaluating the contribution made to our results by the following reactions:

$$\gamma + p \rightarrow \pi^- + \pi^+ + \pi^o + p \qquad (1)$$

$$\gamma + p \rightarrow \pi^- + \pi^+ + \pi^+ + n \ . \qquad (2)$$

At the photon energies used in this experiment, the total cross sections are as follows[19]:

k (Gev)	σ_1 (μb)	σ_2 (μb)
.8	0	4 ± 1
1.2	8 ± 2	20 ± 2
1.6	15 ± 2	32 ± 3

where σ_1 and σ_2 refer to the reactions in equations (1) and (2) above respectively.

We determined the pion pair total cross section from our measurements in the following manner:

$$\sigma_C = \int d\Omega' \int_{M^2_{min}}^{M^2_{max}} dM^2 \frac{d^2\sigma'}{dM^2 d\Omega'} \qquad (3)$$

where $M_{min} = M_p + m$

$M_{max} = M_{max}(k) = W - m$.

For the present purposes, it is convenient to rewrite equation (3) in the form

$$\sigma_C = \int d\Omega' \, [\, 1 + f(\Omega')\,] \int_{M^2_{min}}^{M_1^2} dM^2 \, \frac{d^2\sigma'}{dM^2 d\Omega'} \qquad (4)$$

where M_1 = maximum missing mass which the data included,

$$f(\Omega') = \frac{\int_{M_1^2}^{M^2_{max}} dM^2 \, \frac{d^2\sigma'}{dM^2 d\Omega'}}{\int_{M^2_{min}}^{M_1^2} dM^2 \, \frac{d^2\sigma'}{dM^2 d\Omega'}} \; .$$

It is understood that we are considering all variables at a fixed k. Equation (4) has the advantage that it expresses the cross section in terms of the quantity actually measured, $d^2\sigma'/dM^2 d\Omega'$ from M_{min} to M_1. The factor $f(\Omega')$ is a property of the fitting functions we chose. From equation (4), we see that if the measurements included a contribution from three pion production, the contamination produced in our total cross section would be

$$\sigma_{cont} = \int d\Omega' \, [1 + f(\Omega')] \int_{M^2_{min}}^{M_1^2} dM^2 \, \left(\frac{d^2\sigma'}{dM^2 d\Omega'}\right)_{3\pi} \qquad (5)$$

where $\left(\frac{d^2\sigma'}{dM^2 d\Omega'}\right)_{3\pi}$ = c. m. cross section summed over reactions (1) and (2).

Several approximations were made in evaluating equation (5). The factor $f(\Omega')$ was determined separately for the N^{*++} term and the three-body phase space term used in our fitting function: because the fitting function was explicitly independent of angle, f depended only on the photon energy. The two values of f at each energy were then averaged together, weighted by an appropriate factor which took account of the relative contributions of the corresponding terms to the total cross section at that energy.

In order to estimate the differential cross section for three pion production, we assumed that the π^- is produced isotropically in the c. m. system, and that the mass distribution of the nucleon and the other two pions does not differ significantly from phase space. These seem like reasonable assumptions at the low excitation energies involved here. We thus have

$$\left(\frac{d^2\sigma'}{dM^2 d\Omega'}\right)_{3\pi} \cong \frac{1}{4\pi}\, \sigma_{TOT}^{3\pi}\, P(M^2) \qquad (6)$$

where $\sigma_{TOT}^{3\pi}$ = sum of the total cross sections for reactions (1) and (2),

$P(M^2)$ = invariant mass distribution of the undetected ($N_{\pi\pi\pi}$) system in reactions (1) and (2).

$P(M^2)$ is assumed to be normalized so that

$$\int_{(M_p + 2m)^2}^{M^2_{max}} dM^2 \, P(M^2) = 1 \, . \qquad (7)$$

The phase space prediction for $P(M^2)$ may be written as follows[51]:

$$P(M^2) = C \, R_2 \, (W;M, m) \, R_3 \, (M;M_p, m, m) \qquad (8)$$

where C = normalization constant

$R_n(Y;m_1, m_2, \ldots m_n)$ = invariant phase space for n particles having total energy in their c. m. system of Y and individual masses of $m_1, \ldots m_n$.

The two factors appearing in equation (8) are as follows:

$$R_3 \, (M;M_p, m, m) = \int_{(2m)^2}^{(M-M_p)^2} dX^2 \, R_2 \, (M;X, M_p) \, R_2 \, (X;m, m) \qquad (9)$$

$$R_2 \, (Y;m_1, m_2) = \frac{\pi}{2Y^2} \left\{ [\, Y^2 - (m_1+m_2)^2][Y^2 - (m_1-m_2)^2] \right\}^{1/2} . \qquad (10)$$

Note that $R_3 \, (M;M_p, m, m)$ is independent of k; although it could be expressed in terms of elliptic integrals, it was easier to evaluate it numerically as a function of M.

The results of the calculations described above are summarized in the following table:

k (GeV)	y_R	f_R	f_{NR}	$\bar{f}$	g	$\sigma_{TOT}^{3\pi}$ (μb)	σ_{cont} (μb)
0.9	.57	.14	.68	.32	.070	10	0.9
1.0	.55	.28	1.03	.53	.038	16	0.9
1.1	.55	.31	1.33	.64	.023	22	0.8
1.2	.50	.37	1.76	.83	.015	28	0.8
1.3	.32	.37	2.00	1.18	.011	33	0.8

In this table, y_R is the fraction of the total cross section contributed by the N^{*++} term, as estimated from the total cross section data. f_R and f_{NR} are the factors $f(\Omega')$ defined in equation (4) for the N^{*++} term and the three-body phase space term respectively. $\bar{f}$ is the average of these quantities weighted in a manner appropriate to their relative contributions to the total cross section. g is the fraction of the phase space for reactions (1) and (2) included by our measurements, defined by

$$g = \int_{(M_p+2m)^2}^{M_1^2} dM^2 \, P(M^2) \quad . \tag{11}$$

$\sigma_{TOT}^{3\pi}$ was estimated at each energy from the results quoted at the beginning of this paragraph. All of these calculations were done for $M_1 = 1.30$ GeV/c^2.

The results in the above table show that three pion production made a negligible contribution to our data, giving less than 1 μb to the total cross section at all energies. In terms of the

calculation, this occurred because the factor g was so small, a consequence of the fact that the ($N\pi\pi$) mass distribution in the four-body final state increases very slowly near its low mass limit.

E. Errors

1. Equipment Monitoring

This experiment was performed during three intervals of synchrotron time spaced out over a 15-month period. At the beginning of each of these intervals, about a week was devoted to testing the operation of both spectrometers; all necessary gain, bias, and timing adjustments were made to give optimum system performance. In order to be sure that the systems continued to operate normally, two kinds of daily checks were performed: a short calibration run was made at the beginning of the day, and the pulse-height spectrum in each counter was observed during one of the normal runs or the calibration run. Whenever the spectrum revealed the gain of a counter had deviated appreciably from its nominal value, appropriate adjustments were made to return to the normal condition. On the few occasions when a gross malfunction of a spectrometer occurred, it was revealed in the calibration run and corrections were made before any time was wasted taking data. An equally valuable result of the calibration runs was that they were the best source of information on random errors and on the long term stability of everything associated with the experiment, notably the spectrometers, the beam monitors, and the synchrotron energy meter. The purpose of this section is to describe the calibration

runs and their implications concerning the precision and accuracy of the measurements.

The parameters for the calibration run were chosen with the primary purpose of counting a large number of pions in a short period of time under easily reproducible conditions. The hydrogen target was raised out of the beam line and replaced with a Plexiglas cylinder, which was machined to a 3 in. diameter to simulate the geometry of the hydrogen target. The operating conditions for each spectrometer are summarized below:

Spectrometer	Lab Angle (Degrees)	Central Momentum (MeV/c)	Pions per 100 Quantameter BIPS
600 MeV/c	31.00	570	9×10^3
1200 MeV/c	26.13	600	3×10^3

(3 in. x 9 in. aperture)

The synchrotron beam energy meter was always set at 900 MeV for these runs; the runs were roughly 100 quantameter BIPS long, requiring about 20 minutes at a typical beam intensity. The above table shows that the counting errors for each run were about 1% and 2% for the 600 MeV/c spectrometer and 1200 MeV/c spectrometer respectively.

Since the calibration runs were performed under conditions essentially identical to those of normal runs, they provided a detailed test of all phases of spectrometer operation. The counting rates of all coincidence circuits were monitored, as were the singles rates in many counters. The FAN efficiency was monitored by watching

the fraction of pions vetoed by FAN counts. The operation of the momentum hodoscope was checked by computing the fraction of pions in each channel. For the 1200 MeV/c spectrometer, the efficiency of the freon Cherenkov counter was checked by computing the ratio of electrons to pions; the Plexiglas Cherenkov counter efficiency was monitored by recording the ratio of pion events having counts in the counter to the total number of pions. Finally, the overall efficiency of the spectrometers and the stability of the beam monitors were checked by computing the total number of pions per quantameter BIP.

At the end of the experiment, the calibration data were reanalyzed. Those calibration runs which had revealed equipment malfunctions were ignored. For all others, the number of pions per quantameter BIP was computed including several corrections. Because the size of a quantameter BIP changed at various times due to changes in the P/T ratio and in the integrator (see Section VI. B. 1), the results were normalized to the size of the BIP during August 1965. The number of BIPS in each run, before correction, was computed using TC-1 and the 40 Mc probe as secondary monitors, since the normal data runs were treated in this way (see Section VI. B. 1). The number of pions counted by the 600 MeV/c spectrometer was corrected for accidental coincidences (typically a 1-2% correction), for the dead time of the data storage system (typically a 0. 5 - 1% correction), and for multiparticle events in the momentum hodoscope (an almost constant 0. 4% correction). In addition, the number of pions counted by each spectrometer was corrected for accidental FAN vetoes. During the last part of the experiment, the accidental FAN veto rate of the 1200 MeV/c spectrometer was monitored continuously (see Section VI. D. 1), so the correction was easily made. For the rest of the 1200 MeV/c spectrometer data, and all

of the 600 MeV/c spectrometer data, the correction was made by assuming the accidental veto rate was proportional to the beam intensity, and normalizing the correction to the veto rate measured once with the FAN signal delayed by 100 ns. As a measure of average beam intensity, I_B, for each run we used

$$I_B = \frac{\text{QBIPS}}{\text{GATES} \times T_D}$$

where QBIPS = number of quantameter BIPS in the run,

GATES = number of beam pulses in the run,

T_D = duration of the beam spill for each pulse.

The FAN accidental correction was typically 1-3% for the 600 MeV/c spectrometer, and 0.5 - 1% for the 1200 MeV/c spectrometer. There was some uncertainty in making this correction to the 1965 measurements because no direct measure of accidental FAN vetoes was made under the conditions of a calibration run in 1965.

The results of the calibration run analysis are summarized in Table XIII. In this table, N is the number of calibration runs used in the analysis, and $\overline{R}$ is the mean value of the ratio π^-/QBIP (1 QBIP = 1.200×10^{13} MeV). The error quoted for $\overline{R}$ is the standard deviation of the mean. ΔR is the rms fluctuation of (π^-/QBIP) about $\overline{R}$. $(\Delta R/\overline{R})_{\text{expected}}$ is the rms fluctuation of (π^-/QBIP) calculated on the basis of counting statistics alone. $(\Delta R/\overline{R})_{\text{excess}}$ is the random fluctuation in (π^-/QBIP) which must be added in quadrature with $(\Delta R/\overline{R})_{\text{expected}}$ to give the observed value, $(\Delta R/\overline{R})_{\text{obs}}$.

TABLE XIII

Summary of Plexiglas Target Calibration Runs

Spectrometer	Aperture size (in. x in.)	Dates	N	$\bar{R}$	ΔR	$(\frac{\Delta R}{\bar{R}})_{obs}$ (%)	$(\frac{\Delta R}{\bar{R}})_{exp}$ (%)	$(\frac{\Delta R}{\bar{R}})_{excess}$ (%)
600 MeV/c	2-3/4 x 9-1/2	8/24 - 10/2/65	23	$92.23 \pm .33$	1.58	1.72	1.0	1.4
600 MeV/c	2-3/4 x 9-1/2	5/13 - 8/22/66	53	$92.53 \pm .22$	1.56	1.69	1.0	1.4
1200 MeV/c	3 x 9	8/24 - 10/2/65	16	$27.20 \pm .18$	.72	2.65	2.0	1.7
1200 MeV/c	3 x 9	5/25 - 6/2/66	4	$28.40 \pm .29$	.58	2.04	1.8	1.0
1200 MeV/c	3 x 6	8/24 - 10/2/65	8	$18.22 \pm .15$	.43	2.36	2.0	1.3
1200 MeV/c	2-3/4 x 12	5/13 - 8/22/66	23	$36.24 \pm .12$	.57	1.57	1.6	0.0
1200 MeV/c	2-3/4 x 6	5/13 - 8/22/66	27	$18.09 \pm .09$	.49	2.71	2.3	1.4
1200 MeV/c	2-3/4 x 9	5/13 - 8/22/66	4	$27.49 \pm .17$	.34	1.24	2.0	0.0

A number of conclusions may be drawn from the information in Table XIII. There was almost uniformly a 1.4% rms fluctuation in (π^-/QBIP) in addition to that expected on the basis of counting statistics alone. One possible source of such random errors was the beam monitoring. The rms beam monitoring fluctuations could be independently evaluated because the beam catcher ion chamber (BC) was used to monitor the beam during all calibration runs as well as TC-1 and the 40 Mc probe. BC is known to be a very stable monitor, showing only a slow drift relative to the quantameter as a function of time. If P/T corrections are made to the responses of BC and the quantameter, they remain in good agreement over long periods of time.[40] We therefore adopted the attitude that BC could be regarded as an "absolute" standard for the beam monitoring, and that the ratio (QBIPS/BC), where QBIPS was the number of quantameter BIPS determined by comparison of TC-1 and the 40 Mc probe directly with the quantameter, could be used to investigate the random errors in this normal beam monitoring procedure. The same ion current integrator was always used to record both the quantameter and BC outputs, so changes in the integrator would not affect their ratio. The temperature and pressure of the gas in BC were not recorded during the experiment. In order to correct for the known slow drift of BC relative to the quantameter, the ratio (QBIPS/BC) was averaged over the first 14 calibration runs (centered around 3 September 1965) and over the last 14 calibration runs (centered around 5 August 1966). The difference in these averages showed that (QBIPS/BC) decreased by ($.31 \pm .04$)%/month. The rms fluctuation of (QBIPS/BC), when its average value was taken to decrease linearly with time with the above slope, was found to be 1.0% for the 76 calibration runs in

which BC was recorded. Thus, random errors in beam monitoring apparently did not cause all of the excess fluctuation in (π^-/QBIP).

Another possible source of random fluctuation in (π^-/QBIP) was a variation of the synchrotron energy, E_o. The Plexiglas ($C_5H_8O_2$) target contained roughly equal numbers of neutrons and protons, most of them bound in nuclei. The neutrons were a source of negative pions via the reaction $\gamma + n \rightarrow \pi^- + p$; the yield of π^- at given momentum and angle from this source is not expected to be sensitive to small changes in E_o. However, assuming the proton contribution comes from free protons, the yield from $\gamma + p \rightarrow \pi^- + \pi^+ + p$ is expected to change by roughly 10% for a 1% change in E_o. This may be seen by considering equation (4), Section III. A, and noting that k_m was about 100 MeV less than E_o for the conditions of the calibration run. As a test of the sensitivity of the π^- yield to E_o during the calibration runs, E_o was deliberately lowered by 10 MeV ($\approx$ 1%) for one calibration run. The π^- yield measured by each spectrometer was (5 $\pm$ 1)% lower than normal for this run. This is consistent with what we would expect if the neutrons and protons in the Plexiglas contributed roughly equally to the π^- yield. Furthermore, this implies that an rms fluctuation in E_o of 0.2% (2 MeV) could account for a 1% fluctuation in (π^-/QBIP). A fluctuation in E_o of this magnitude seems quite consistent with the changes observed by watching the beam energy meter. We conclude that we can account for all of the random fluctuations observed in the calibration runs.

We next consider systematic changes; unfortunately, the situation here was not as fully understood. The 600 MeV/c spectrometer showed remarkable reproducibility from 1965 to 1966: Table XIII shows that $\overline{R}$ differed by only (0.3 $\pm$ 0.4)% during these

two running periods. There were two discrepancies, however, in the 1200 MeV/c spectrometer data: $\overline{R}$ measured with the 3 in. x 9 in. aperture counter increased by (4.3 ± 1.2)% between 1965 and 1966, and $\overline{R}$ measured with aperture counters 2-3/4 in. wide was larger than expected on the basis of $\overline{R}$ measured with the 3 in. wide aperture counter at the same time.

The second discrepancy is shown more clearly in the following table:

Ratio	Observed Value	Expected Value
$\frac{\overline{R}(3 \times 6)}{\overline{R}(3 \times 9)}$	.670 ± .007 (1965 data)	.667
$\frac{\overline{R}(2\text{-}3/4 \times 12)}{\overline{R}(3 \times 9)}$	1.276 ± .009 (1966 data)	1.222
$\frac{\overline{R}(2\text{-}3/4 \times 6)}{\overline{R}(2\text{-}3/4 \times 12)}$	.499 ± .003 (1966 data)	.500
$\frac{\overline{R}(2\text{-}3/4 \times 9)}{\overline{R}(2\text{-}3/4 \times 12}$	.759 ± .005 (1966 data)	.750

In this table, $\overline{R}$ (a x b) denotes the average value of (π^-/QBIP) measured with the aperture counter with the indicated dimensions. The expected value of each ratio is simply the ratio of the areas of the two aperture counters. We see that for aperture counters of the same width (first dimension shown), the ratios behaved exactly as expected, but that in going from the 3 in. x 9 in. aperture to the

2-3/4 in. x 12 in. aperture there was a $(4.3 \pm .7)\%$ deviation from the expected ratio.

Several possibilities were explored in seeking an explanation for these systematic changes. The temporal change might have been caused by a change in the synchrotron energy. However, a change in E_o of almost 1% would have been required to produce the 4% shift observed, and such a large shift seems extremely unlikely. Another possible cause might have been a change in the momentum calibration of the 1200 MeV/c spectrometer. In fact, the rear counters of this spectrometer were removed and remounted with a new supporting rack between the 1965 and 1966 running. It is believed that the position of the momentum hodoscope (S2) was reproduced to within 0.1 in. Since the dispersion of this spectrometer was such that a change in position of 1 in. at the focus corresponded to a 2% change in momentum, the momentum calibration was reproduced to within 0.2%. The sensitivity of the pion yield to the spectrometer momentum could be obtained from the calibration run data for the individual momentum channels. Comparing the average yields measured in the two most widely separated channels (S2T and S2B), it was found that

$$\frac{\Delta \sigma^*}{\sigma^*} = 3.2 \frac{\Delta p}{p}$$

for the conditions of the calibration run, where σ^* is the normalized yield defined in Section III. A. Thus, a 0.2% change in momentum could not have produced the change in yield between 1965 and 1966.

A possible source of difference between the 1965 and 1966 yields was electron contamination of the photon beam in 1965. This source was not considered at first because it did not show up in the 600 MeV/c spectrometer calibration data. However, initial analysis of the hydrogen target data showed the 1966 cross section measurements with this spectrometer were several percent higher than those in 1965 (see Section VI. E. 3), and direct investigation of the electron component of the photon beam showed that a contamination of the order of 3% was likely during 1965 (see Section VI. D. 5). It was, therefore, concluded that electron contamination of the photon beam in 1965 was the probable source of the 4. 3% depression of the 1200 MeV/c spectrometer calibration run yield, and that some other factors must have conspired to mask this effect in the 600 MeV/c spectrometer calibration data.

No satisfactory explanation was found for the failure of the scaling law for aperture counters of different width in the 1200 MeV/c spectrometer. The data suggest that some counter other than the aperture counter (A1) was determining the horizontal aperture, so that the spectrometer was not 100% efficient for particles passing through the wider apertures. The only other counter which was close to limiting the horizontal aperture was the final scintillator (S3). To test whether S3 was limiting the horizontal aperture, the fraction of particles triggering all counters except S3 was measured with the 3 in. x 9 in. A1 and immediately thereafter with the 2-3/4 in. x 12 in. A1. The S3 "miss rates" observed were (8. 3 $\pm$. 4)% and (8. 9 $\pm$. 4)% respectively. These measurements showed that S3 was not limiting the horizontal aperture to any appreciable extent.

A calculation of the loss expected from S3 due to multiple scattering in all the matter of the spectrometer system, assuming the photon beam was uniformly distributed in intensity over a 1-1/2 in. wide spot, gave a value of 0.5% at a momentum of 600 MeV/c for a 3 in. wide aperture counter. This was an upper limit since the photon beam intensity was actually more concentrated near the center of the spot. Thus, according to this calculation, multiple scattering losses could cause the S3 efficiency to differ at most by 0.5% for 3 in. and 2-3/4 in. apertures, a result consistent with the measured miss rates.

The inefficiency of the second scintillator (A2) was measured with the 3 in. x 9 in. A1 and found to be 0.6%. Since this many "inefficient" events could have been caused by accidental coincidences between A1 and the remaining counters, A2 was essentially 100% efficient. The FAN veto rate with the 3 in. x 9 in. A1 was $(9.3 \pm .2)\%$, and with the 2-3/4 in. x 12 in. A1 it was $(7.2 \pm .2)\%$. However, one would expect a higher FAN veto rate with a wider A1 just because more of the particles scattered from the pole tips would pass through the aperture counter. It is therefore likely that the higher FAN veto rate observed with the wider A1 was not a result of the FANS overlapping the aperture counter.

We were forced to conclude that there was a $(4.3 \pm 0.7)\%$ discrepancy of unknown origin between the effective solid angles of the 1200 MeV/c spectrometer when aperture counters of different width were used. Further evidence for such an effect was seen in the data from the hydrogen target; this additional evidence and the normalization finally adopted for all of the data are discussed in Section VI. E. 3.

2. Checks of the Data Analysis

Many numerical operations were necessary to reduce the raw data from this experiment to cross sections. The many computer programs used to perform these operations constituted a potential source of errors as large as any of those of experimental origin. In this section we shall describe briefly some of the tests made to give us confidence in the accuracy of the results from the computer.

The value of the yield per equivalent quantum, σ^*, for each momentum channel was calculated by hand for one run with each spectrometer. After correcting a number of small errors and one major error in programs which had been considered previously debugged, the computer results agreed with the hand calculation to about 0.1%, which was consistent with the number of figures retained in each calculation. In general, one more figure was retained in writing and punching computed results than the number of figures which were physically significant in order to guard against cumulative roundoff errors. The σ^* values for a number of full target and empty target runs at the same point were averaged together and the empty target correction was made. This time the results of the computer calculation and the hand calculation agreed on the first try. Finally, the normalizing factor $I(E_2, E_1, p_o, \theta_o)$, evaluated numerically with the computer, was used to calculate the laboratory cross section $d^2\sigma/dpd\Omega$ by hand. Again, the computer and hand calculations agreed.

The accuracy of the remaining steps in the data reduction depended on the accuracy with which various integrals were evaluated. The fitting functions $F_i(E_2, E_1, p_o, \theta_o)$ used to obtain the c.m. cross

sections had to be evaluated by numerical integration (see equation (13), Section III. C), as did the moments of the bremsstrahlung spectrum needed to find $I(E_2, E_1, p_o, \theta_o)$ and k_o. All of the numerical integrals were performed using the Gauss-Legendre quadrature technique. The basic computer program for the quadrature integration simply contained a table of the coefficients and roots of Legendre polynomials needed in the quadrature formula.[52] This program was tested by evaluating several elementary integrals for which the quadrature should give exact answers: it was found to do so to the eight significant figures retained by the computer. The calculation of the zeroth, first and second moments of the beam spectrum was tested first by using a rectangular form for the spectral function, $\bar{B}(k, E_o)$, for which the moments could be calculated analytically. In this case, the numerical evaluation agreed with the exact answer to 1 part in 10^7. Using the real shape of $\bar{B}(k, E_o)$, the numerical evaluation was tested by increasing the number of steps in the quadrature to two and three times as many as normally used. All these moments of the beam spectrum varied by less than 0.1% in these tests. Similar tests were performed on the functions $F_i(E_2, E_1, p_o, \theta_o)$: the answers here also varied by $< 0.1\%$ when the number of steps in the quadrature was increased beyond the number finally adopted.

One other potential source of error in data handling was in the transfer of information from data books to punched cards. All beam monitoring information on the punched cards was compared with the data books at the end of the experiment; only a few errors were discovered (out of nearly 1400 runs), and these runs were reanalyzed. In addition, the σ^* values obtained in all runs at each kinematic point were checked for gross differences which would be

indicative of copying errors as well as equipment or experimenter malfunction.

We therefore believe that our results are free from appreciable errors introduced in the data handling processes.

3. Systematic Error Analysis

The calibration runs made to check the functioning of the apparatus on a daily basis revealed some systematic differences between measurements made at different times and with slightly different spectrometer configurations, as discussed in Section VI. E. 1. In an effort to identify the causes of these changes, the data taken with the hydrogen target were also analyzed carefully for systematic shifts. When this analysis was completed, it was decided that a small renormalization of part of the 1200 MeV/c spectrometer data was desirable to achieve internally consistent results. The purpose of this section is to describe the analysis for consistency and the readjustment made.

Most of the cross sections obtained in this experiment were measured at least twice, at times separated by as much as a year. The following scheme was adopted to describe systematic changes quantitatively with relatively few parameters. Consider the yields measured at a given synchrotron energy and spectrometer angle. At each momentum there is some "true" yield, $\mu_i(E_o, \theta)$, and in the absence of systematic changes the measured yield $\sigma^*(E_o, \theta, p_i)$ is assumed to be normally distributed about this mean. However, suppose that at a given time, all the measurements at this E_o and θ are shifted by the same factor, $k^{(j)}$, as a result of a systematic change in conditions. Then the yields measured at the

j^{th} time would be normally distributed about the mean values $k^{(j)}\,\mu_i(E_o,\theta)$. In principle, we must allow a different factor $k^{(j)}$ for each set of measurements made, although we certainly hope the $k^{(j)}$ are all close to, or equal to, unity. The basic problem in the data analysis is then to determine the "true" values, $\mu_i(E_o,\theta)$, and, as a measure of the consistency of the data, the factors $k^{(j)}$.

The standard approach to the solution of this problem is the method of maximum likelihood. Assuming a normal distribution for the errors, the likelihood function for the complete set of measurements at angle θ and energy E_o may be written as follows:

$$L = \prod_{j=1}^{m} \prod_{i=1}^{n} (2\pi\ \sigma_i^{(j)2})^{-1/2} \exp\left\{ - \frac{(\chi_i^{(j)} - \mu_i k^{(j)})^2}{2\sigma_i^{(j)2}} \right\}$$

where $\chi_i^{(j)}$ = value of $\sigma^*(E_o,\theta,p_i)$ measured at the j^{th} time,

$\sigma_i^{(j)}$ = standard deviation of $\chi_i^{(j)}$.

The subscript $\underline{i}$ runs over all momenta for which the cross section was measured at that E_o and θ. The solution to the problem is the set of values $\hat{\mu}_i$ and $\hat{k}^{(j)}$ which maximize L. It is difficult to write the $\hat{\mu}_i$ and $\hat{k}^{(j)}$ as explicit functions of the $\chi_i^{(j)}$, but the following sets of coupled equations converge quickly to a solution when iterated:

$$\hat{k}^{(j)} = \frac{\sum_{i=1}^{n} \left(\frac{\hat{\mu}_i}{\sigma_i^{(j)}} \right)^2 \left(\frac{\chi_i^{(j)}}{\mu_i} \right)}{\sum_{i=1}^{n} \left(\frac{\hat{\mu}_i}{\sigma_i^{(j)}} \right)^2} \qquad j = 1, \ldots, m$$

$$\hat{\mu}_i = \frac{\sum_{j=1}^{m} \left(\frac{\hat{k}^{(j)}}{\sigma_i^{(j)}} \right)^2 \left(\frac{\chi_i^{(j)}}{\hat{k}^{(j)}} \right)}{\sum_{j=1}^{m} \left(\frac{\hat{k}^{(j)}}{\sigma_i^{(j)}} \right)^2} \qquad i = 1, \ldots, n .$$

The obvious starting point for an iterative solution is

$$\hat{k}^{(j)} = 1 \qquad j = 1, \ldots, m .$$

When these values are used for the $\hat{k}^{(j)}$, $\hat{\mu}_i$ is simply the commonly used average of the $\chi_i^{(j)}$ where each measurement is weighted by the reciprocal of its variance.

The above formalism was used to study the results of a preliminary analysis of the data. The comparison was made between the σ^* values obtained in 1965 and those obtained in 1966. The ratios $[\hat{k}(1966)/\hat{k}(1965)]$ were averaged over energy and angle, giving average increases of $(8.3 \pm 0.9)\%$ and $(1.4 \pm 0.5)\%$ for the 1200 MeV/c and 600 MeV/c spectrometers respectively from 1965 to 1966. This analysis was made on the data before correction for electron contamination of the photon beam had been made (Section

VI. D. 5). After correction for the electron contamination, the 1200 MeV/c spectrometer data were still about 4% higher in 1966 than in 1965, consistent with the shift observed in the calibration runs when we switched from a 3 in. to a 2 3/4 in. wide aperture counter; the 600 MeV/c spectrometer data were then a few percent higher in 1965 than in 1966.

The discrepancy in the 1200 MeV/c spectrometer data was investigated further by computing the χ^2 probabilities for each kinematic point. If the systematic shift were due to a change in the pion momentum or synchrotron energy calibrations, one would expect the points with low χ^2 probability to occur predominantly near the reaction threshold, where the yield is most sensitive to pion momentum and synchrotron energy. Such a trend was not evident among the points with low probability, suggesting that the systematic change was due to an acceptance or efficiency change. However, no satisfactory quantitative explanation for this shift was found, as discussed in Section VI. E. 1. Since not all cross sections were measured both in 1965 and 1966, it was decided to renormalize all data obtained with this spectrometer in one year so as to obtain an internally consistent set of measurements. The question of which year to choose as the standard was decided by comparison with 600 MeV/c spectrometer data. In 1966, the cross section was measured at $\theta = 30^{\circ}$, $p_0 = 535$ MeV/c, and $E_0 = 922$, 973, and 1025 MeV simultaneously with both spectrometers. These measurements showed the 1200 MeV/c spectrometer σ^* values were $(5.2 \pm 1.5)\%$ higher than those from the 600 MeV/c spectrometer. Therefore, the 1965 normalization of the 1200 MeV/c spectrometer data was chosen as the standard, and the 1966 values were lowered by 4.3%,

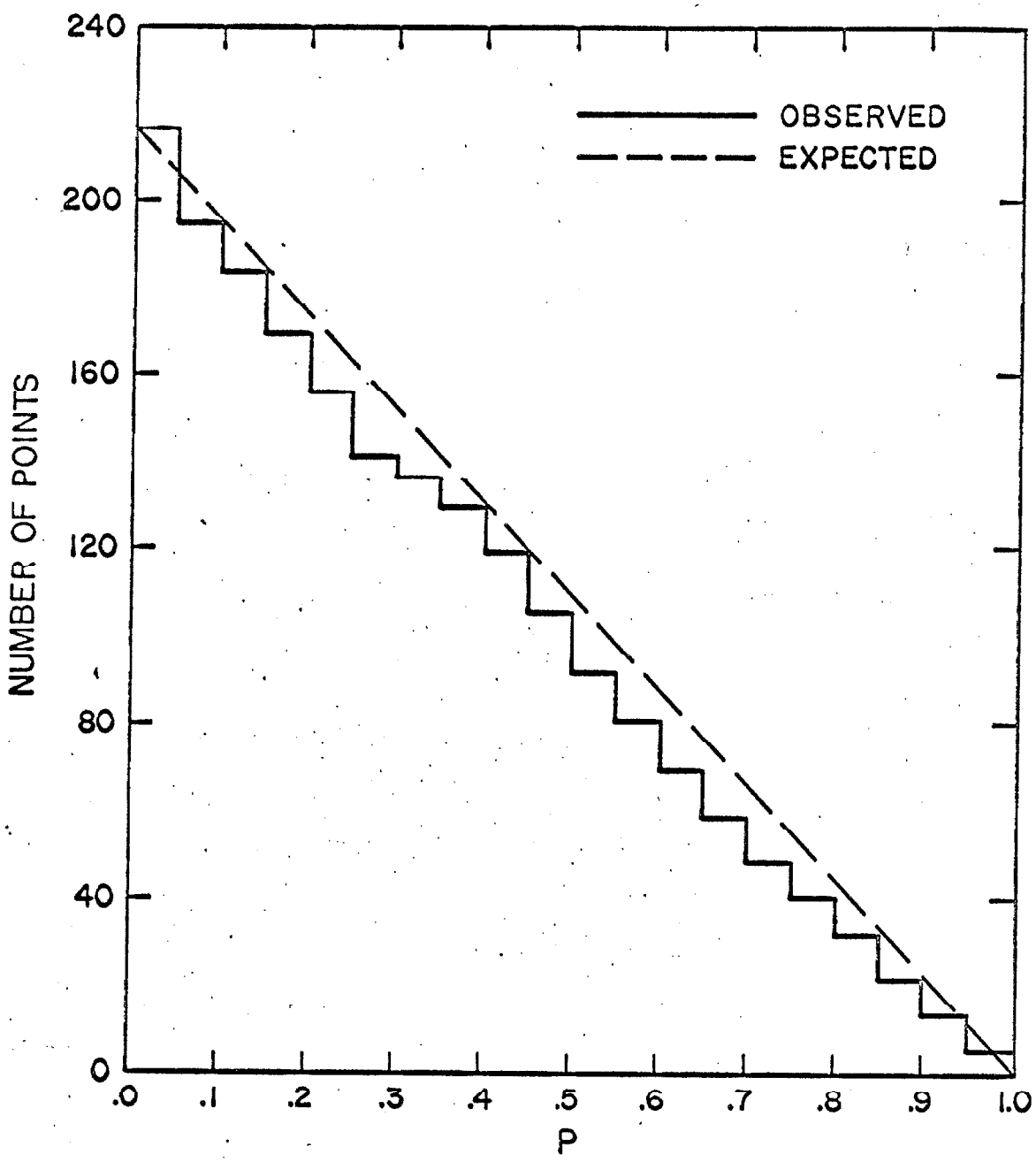

Figure 16. Integral χ^2 distribution for the π^- yields at all kinematic points. The observed and expected number of points having χ^2 probability greater than P are shown as a function of P.

the discrepancy between the two sets of measurements determined in the calibration runs.

The internal consistency of the data after the final analysis was performed is illustrated in Figure 16. The probability for obtaining a χ^2 value greater than or equal to the observed value was determined for all measurements of σ^* at each kinematic point. The number of pions was summed over all momentum channels at a given central momentum for this analysis. The random error of each measurement included the counting error and a 1.4% error due to beam monitoring and synchrotron energy fluctuations. The observed and expected χ^2 integral probability distributions are shown in Figure 16. Although there appears to be an excess of points in the low probability range and a corresponding depletion at high probability, this figure shows that no serious internal inconsistencies remain in the data. A possible systematic error of 4% was assigned to the results obtained with the 1200 MeV/c spectrometer to allow for the uncertainty in the way in which the data were renormalized.

F. Least Squares Fitting with Constraints

When fitting the phenomenological model to the laboratory cross sections (Section III. C), we were faced with the problem of fitting subject to the constraint that all coefficients be positive. A method was devised to handle this problem, and it will be described here.

The general formalism for least squares fitting of data was expressed in concise form by Mathews and Walker,[53] and we shall use their notation. We wish to add to the usual problem of minimizing χ^2, constraints of the form

$$a_i \geq b_i \text{ (or } a_i \leq b_i) \quad i = 1, \ldots, m, \tag{1}$$

where the a_i are the n parameters to be determined ($n \geq m$), and the b_i are constants. We denote the least squares solution obtained with no constraints by $\hat{a}_i$:

$$\hat{a} = M^{-1} X \tag{2}$$

where $\hat{a}$ is the n-component vector of the parameters, M is the symmetric n x n matrix defined by Mathews and Walker depending upon the standard deviations of the measurements and the values of the fitting functions, and X is the n component "data" vector depending upon the measurements, their standard deviations, and the fitting functions. At this point, it is useful to note that χ^2, the function which is minimized in the fit, can be expressed for a general parameter vector, a, in the form

$$\chi^2(a) = \chi^2_{min} + (a - \hat{a})^+ M (a - \hat{a}) \tag{3}$$

where χ^2_{min} is the value of χ^2 obtained in the unconstrained least squares fit.

We now suppose the unconstrained solution violates k of the constraints expressed by equation (1), i. e., suppose

$$\hat{a}_i < b_i \qquad i = 1, \ldots, k. \tag{4}$$

The minimum χ^2 solution satisfying the constraints will be denoted by $\hat{\hat{a}}$. This solution is achieved by taking

$$\hat{\hat{a}}_i = b_i \qquad i = 1, \ldots, k \tag{5a}$$

and minimizing χ^2 with respect to the remaining a_i, $i = k+1, \ldots, n$. The result of requiring

$$\frac{\partial \chi^2}{\partial a_i} = 0 \qquad i = k+1, \ldots, n$$

can be expressed as follows:

$$\hat{\hat{a}}_i = \hat{a}_i + [(M^r)^{-1} T]_{i-k} \quad i = k+1, \ldots, n \tag{5b}$$

where M^r is a "reduced" M matrix

$$M^r_{\mu\nu} = M_{\mu+k, \nu+k} \qquad \mu, \nu = 1, \ldots, n-k$$

and T is an (n - k) component vector

$$T_\mu = - \sum_{j=1}^{k} M_{\mu+k, j} (b_j - \hat{a}_j) \ .$$

M^r is a symmetric (n - k) x (n - k) matrix by virtue of the properties of M. T expresses the amount by which the constraint-violating parameters had to be shifted to satisfy the constraints.

That the solution expressed by equation (5) is one of minimum χ^2 subject to satisfying the constraints originally violated is clear from equation (3): the surfaces of constant χ^2 are concentric hyperellipsoids in the parameter space, centered at $\hat{a}$. The constraints initially violated tell us that the desired solution is where one of these hyperellipsoids is tangential to the hyperplane defined by equations (5a), and this is just the condition imposed by (5b). It is possible that equation (5b) violates some of the original m constraints not violated by $\hat{a}$: in this case, the corresponding parameters must be added to (5a) and calculation of (5b) repeated. This process of "receding from the absolute minimum" in order to satisfy the constraints must terminate in no more than m steps.

All of this formalism is simply stated and visualized in the case of interest for this experiment, a two parameter fit. Our constraints had the form

$$a_i \geq 0 \qquad i = 1, 2 \ . \tag{6}$$

The surfaces of constant χ^2 were ellipses in the (a_1, a_2) plane. At a few kinematic points, the center of this family of ellipses, i.e., the least squares solution $(\hat{a}_1, \hat{a}_2)$, lay in a region where one of the parameters was negative. If $\hat{a}_1$ was the negative parameter, equation (5) specified the desired solution as

$$\hat{\hat{a}}_1 = 0$$

$$\hat{\hat{a}}_2 = \hat{a}_2 - \frac{(M^{-1})_{21}}{(M^{-1})_{11}} \hat{a}_1 \ . \tag{7}$$

If $\hat{a}_2$ was the offending parameter, the subscripts 1 and 2 were interchanged in equation (7). The errors quoted for the parameters were obtained from M^{-1} in the usual way, since this matrix still specified the structure of the constant $-\chi^2$ surfaces.

REFERENCES

1. V. A. Peterson and L. G. Henry, Phys. Rev. 96, 850 (1954).
2. M. Sands, M. Bloch, J. G. Teasdale, and R. L. Walker, Phys. Rev. 99, 652 (1955).
3. V. Z. Peterson, Bull. Am. Phys. Soc. Ser. II 1, 173 (1956).
4. R. M. Friedman and K. M. Crowe, Phys. Rev. 105, 1369 (1957).
5. M. Bloch and M. Sands, Phys. Rev. 108, 1101 (1957).
6. W. M. Woodward, R. R. Wilson, and P. D. Luckey, Bull. Am. Phys. Soc. Ser. II 2, 195 (1957).
7. M. Bloch and M. Sands, Phys. Rev. 113, 305 (1959).
8. D. D. Elliott, Ph. D. Thesis, California Institute of Technology (1959).
9. J. M. Sellen, G. Cocconi, V. T. Cocconi, and E. L. Hart, Phys. Rev. 113, 1323 (1959).
10. B. M. Chasan, G. Cocconi, V. T. Cocconi, R. M. Schectman, and D. H. White, Phys. Rev. 119, 811 (1960).
11. J. R. Kilner, R. E. Diebold, and R. L. Walker, Phys. Rev. Letters 5, 518 (1960).
12. D. McLeod, S. Richert, and A. Silverman, Phys. Rev. Letters 7, 383 (1961).
13. R. DelFabbro, M. dePretis, R. Jones, G. Marini, A. Odian, G. Stoppini, and L. Tau, Phys. Rev. Letters 12, 674 (1964).

14. R. DelFabbro, M. dePretis, R. Jones, G. Marini, A. Odian, G. Stoppini, and L. Tau, Phys. Rev. 139, B701 (1965).

15. M. Beneventano, R. Finzi, L. Paoluzi, F. Sebastiani, M. Severi, and F. Villa, Nuovo Cimento 38, 1054 (1965).

16. A. Kusumegi, Y. Kobayashi, Y. Murata, H. Sasaki, K. Takamatsu, and A. Masaike, "Proceedings of the International Symposium on Electron and Photon Interactions at High Energies, Vol. II," Hamburg (1965).

17. H. R. Crouch, et. al., "Proceedings of the International Symposium on Electron and Photon Interactions at High Energies, Vol. II," Hamburg (1965).

18. J. V. Allaby, H. L. Lynch, and D. M. Ritson, Phys. Rev. 142, 887 (1966).

19. U. Brall, et al., Nuovo Cimento 41, 270 (1966).

20. L. J. Fretwell, Ph. D. Thesis, California Institute of Technology (1967).

21. R. E. Cutkosky and F. Zachariasen, Phys. Rev. 103, 1108 (1956).

22. R. R. Wilson, Phys. Rev. 110, 1212 (1958).

23. S. D. Drell, Phys. Rev. Letters 5, 278 (1960).

24. H. A. Thiessen, Ph. D. Thesis, California Institute of Technology (1967).

25. S. D. Ecklund, Ph. D. Thesis, California Institute of Technology (1967).

26. R. R. Wilson, Nuclear Instruments I, 101 (1957).

27. F. B. Wolverton, "Thick Radiator Bremsstrahlung. Angular Dependence of the Spectrum for Electron Energies Greater than 300 MeV," unpublished (1966).

28. J. D. Jackson, Nuovo Cimento 34, 1644 (1964).

29. M. J. Moravcsik, Phys. Rev. 104, 1451 (1956).

30. M. L. Thiebaux, Phys. Rev. Letters 13, 29 (1964).

31. E. Ferrari and F. Selleri, Nuovo Cimento 21, 1028 (1961).

32. J. Mathews, private communication.

33. P. Stichel and M. Scholz, Nuovo Cimento 34, 1381 (1964).

34. German Bubble Chamber Collaboration, paper submitted to the XIIIth High Energy Physics Conference, Berkeley (1966).

35. H. A. Thiessen, "A Recalibration of the Beam Energy Meter," CTSL Internal Report No. 21, unpublished (1966).

36. H. A. Thiessen and J. Pine, "Calibration of the South Quantameter," CTSL Internal Report No. 22, unpublished (1966).

37. M. G. Hauser, "Calculation of Effective Bremsstrahlung Spectrum for a Rectangular Collimator and a Cylindrical Hydrogen Target," CTSL Internal Report No. 26, unpublished (1966).

38. M. G. Hauser, "BR/Function to Obtain Synchrotron Beam Spectrum by Table Interpolation," unpublished (1966). This program write-up has been placed in the Synchrotron Program Library.

39. J. H. Marshall, Ph.D. Thesis, California Institute of Technology (1965).

40. C. Peck, Ph.D. Thesis, California Institute of Technology (1964).

41. H. A. Thiessen, "Calibration of the 600 MeV/c Magnet," CTSL Internal Report No. 27, unpublished (1966).

42. J. R. Kilner, Ph.D. Thesis, California Institute of Technology (1963).

43. M. G. Hauser, "UNPACK/Magnetic Tape Reading Subroutine," unpublished (1964). H. A. Thiessen and M. G. Hauser, "Specifications for Preliminary Data Handling," unpublished (1964).

44. M. G. Hauser, "SPCTRA/Pulse Height Analyze, Print, and Plot Subroutine," unpublished (1965). H. A. Thiessen, "Logic Subroutine Package for Translating the Output of the Scaling Adapter for the Nuclear Data Pulse Height Analyzer," unpublished (1965).

45. F. B. Wolverton, "RDR/Data Reading Program," unpublished (1965). This program and the associated ones, RDA, MCW, DIC, CAL, and DUM, are in the Synchrotron Program Library.

46. P. V. C. Hough, Phys. Rev. 74, 80 (1948).

47. M. Croyon et al., C. R. Congrès Internationale de Physique Nucléaire, 1964, Vol. 2, p. 222.

48. A. Abashian, R. Cool, and J. W. Cronin, Phys. Rev. 104, 855 (1956).

49. G. Källén, Elementary Particle Physics (Addison-Wesley Publishing Company, Inc., Reading, Massachusetts, 1964), p. 72.

50. D. E. Groom, Ph.D. Thesis, California Institute of Technology (1965).

51. R. Hagedorn, Relativistic Kinematics (W. A. Benjamin, Inc., New York, 1964), Chap. 7, p. 96.

52. M. G. Hauser, "AINTEG/Gauss Quadrature Integration Function," unpublished (1965). This program is in the Synchrotron Program Library.

53. J. Mathews and R. L. Walker, Mathematical Methods of Physics (W. A. Benjamin, Inc., New York, 1965), Chap. 14, p. 365.